

Tailored Devices for Integrated Quantum Photonics

*A synergetic circle of technology development,
simulation and benchmarking*

Der Naturwissenschaftlichen Fakultät
der Universität Paderborn
zur Erlangung des Doktorgrades

Dr. rer. nat.

vorgelegt von

Laura Padberg

aus Brilon

2022

Contents

Summary	1
Zusammenfassung	3
1 Preface	5
2 Introduction	9
3 Fundamental Theory	13
3.1 Integrated Optics	13
3.1.1 Waveguides	14
3.1.2 Directional Coupler	18
3.2 Nonlinear Optics	22
3.2.1 Nonlinear Material Response	23
3.2.2 Three-Wave Mixing	23
3.2.3 Phase Matching	26
3.2.4 Quantum Dispersion Engineering	31
3.3 Nonlinear Materials	35
3.3.1 Potassium Titanyl Phosphate	35
3.3.2 Lithium Niobate On Insulator	45
4 Technology	53
4.1 Potassium Titanyl Phosphate	53

4.1.1	State of the Art: Periodically Poled Waveguides in KTP	54
4.1.2	In-house Technology	56
4.2	Lithium Niobate On Insulator	68
4.2.1	State of the Art: Periodically Poled Waveguides in LNOI	68
4.2.2	In-house Technology	71
4.3	Characterisation	72
4.3.1	State of the Art: Material and Optical Characterisation	72
4.3.2	In-house Characterisation	74
5	Technology Results	89
5.1	Potassium Titanyl Phosphate	89
5.1.1	Periodic Poling	89
5.1.2	Waveguides	105
5.2	Lithium Niobate On Insulator	119
5.2.1	Wafer Quality	119
5.2.2	Periodic Poling	120
5.2.3	Waveguides	139
5.2.4	Modelling of LNOI Structures	154
5.2.5	Couplers	161
5.3	Final Remarks	165
6	Tailored Waveguide Sources	167
6.1	Potassium Titanyl Phosphate	167
6.1.1	State of the Art: Decorrelated Sources in KTP	167
6.1.2	KTP Source	169
6.2	Lithium Niobate On Insulator	178
6.2.1	State of the Art: Sources in LNOI	178
6.2.2	LNOI Source	178
7	Conclusion and Outlook	183
7.1	Conclusion	183

7.2 Outlook	184
Acknowledgements	187
A Appendix	189
A.1 Patents	189
A.2 Publications	189
A.3 Conference Contributions	191
B References	193

Summary

Integrated quantum optics is an emerging research field with the potential to revolutionise our society by providing previously unattainable applications. Integrated devices serve as the foundation for many quantum optical applications. In this thesis, we investigate the fabrication technologies for nonlinear integrated devices, which are essential to generate photonic quantum states. This research focuses on novel developments on two material systems for realising periodically poled waveguides in potassium titanyl phosphate (KTP) and lithium niobate on insulator (LNOI). Both materials have unique dispersion properties that allow for high integration densities and photon pair generation. However, the fabrication of these devices is challenging. Detailed investigations of the periodic poling behaviour and waveguides in KTP were conducted, resulting in a reliably established technology to fabricate periodically poled waveguides in KTP. Furthermore, this thesis shows the development of fabrication techniques for periodically poled waveguides in LNOI. Using these new technology approaches devices from both materials were fabricated and nonlinear optically characterised, demonstrating the desired functionality. This work lays the foundation for the fabrication of quantum optical devices in KTP and LNOI.

Zusammenfassung

Die integrierte Quantenoptik ist ein aufstrebendes Forschungsfeld, welches unsere Gesellschaft revolutionieren wird, indem sie bisher unerreichbare Anwendungen ermöglicht. Die Basis für viele quantenoptischen Anwendungen bilden integrierte Bauelemente. In dieser Dissertation wurden die Technologien entwickelt, die notwendig sind, photonische Quantenzustände zu erzeugen und hohe Integrationsdichten von Komponenten zu ermöglichen. Diese Arbeit konzentriert sich auf neuartige Entwicklungen zur Realisierung von periodisch gepolten Wellenleitern in zwei Materialsystemen, Kaliumtitanylphosphat (KTP) und Lithiumniobat auf einem Isolator (LNOI). Beide Materialien zeichnen sich durch einzigartige Dispersionseigenschaften aus, die hohe Integrationsdichten und Photonenpaarquellen ermöglichen. Jedoch ist die Herstellung dieser Bauteile herausfordernd. Es wurden detaillierte Untersuchungen zum Polungsverhalten und Wellenleitern in KTP durchgeführt, wodurch nun periodisch gepolter Wellenleiter in KTP verlässlich hergestellt werden können. Darüber hinaus wird die Entwicklung von Herstellungstechniken von periodisch gepolten Wellenleitern in LNOI gezeigt. Unter Verwendung der neuen Technologien wurden Bauelemente in beiden Materialien hergestellt und nichtlinear optisch charakterisiert, wodurch die gewünschten Funktionalitäten nachgewiesen wurden. Diese Arbeit stellt die Grundlagen zur Herstellung von quantenoptischen Bauelementen in KTP und LNOI dar.

*Everyone knew it was impossible.
until a fool who did not know
came along and did it.*

Albert Einstein

Preface

The work of this doctoral thesis has been performed during the years 2017-2022 in the integrated quantum optics (IQO) group of Prof. Dr. Christine Silberhorn at Paderborn University. The starting point of this thesis was the fabrication of tailored periodically poled waveguides in potassium titanyl phosphate (KTP) for quantum optical applications, but we extended this topic after one year with the development of a novel technology for periodically poled waveguides in lithium niobate on insulator (LNOI).

During the first year I continued the work from my master thesis of corrugated waveguides in KTP. In both the EU and the US, we patented the process for producing waveguides made of materials from the KTP family [1, 2]. I have further developed and optimised the technology for periodically poled waveguides in KTP for advanced devices. By implementing investigation pulses and preconditioning pulses, I could establish a reliable periodic poling process in KTP. Additionally, I investigated the back-switching of domains in KTP and established the periodic poling of rubidium doped KTP (RbKTP), a crystal of the same crystal family, but with much more stable domain behaviour. In the last years of my work our main objective was to exploit the unique dispersion properties of (Rb)KTP and develop the technology to overcome limitations of commercial state of the art sources and realise a high-quality source of pure heralded single photons at telecommunication wavelengths around 1550 nm [3].

Within one year of starting my PhD, we decided to extend our material portfolio by adding LNOI as a new material platform for our research. LNOI offers the possibility of high-performance integrated nano-photonic components as well as modulators operating at CMOS compatible voltages, due to the high index contrast between lithium niobate and silicon dioxide/air. Our group has a lot of experience with conventional lithium niobate, particularly titanium in-diffused waveguides and bulk poling. This prior knowledge aided me understanding the material properties. Nevertheless the required structures differed strongly from those of conventional lithium niobate. As a result, simultaneously to the optimisation of the (Rb)KTP technology, I started to develop an entirely new technology for LNOI from scratch. For this reason, I spent the

following years developing the process for periodic poling and waveguide fabrication in LNOI. We are highly fortunate in this technology that a major part of the following projects is based on my development on LNOI and without my preliminary work the entry into this topic, would not have been possible.

The technology is the foundation for any quantum optics application. Future quantum networks will depend on reliable integrated devices. Fabrication and optimisation of such integrated optical devices is challenging and the arising challenges of the underlying technology are significantly more complicated and time-consuming. It requires a deep understanding of the material properties to determine which process steps have the most impact and should be improved. To be able to build high-performance devices, numerous process steps have to be established and optimised. I would like to emphasise that, in order to overcome the aforementioned challenges, a full understanding of the fundamental physics underlying the sample fabrication process, as well as the simulation and characterisation, is required.

Therefore, I expanded my personal portfolio by adding simulations in (Rb)KTP and LNOI to my comprehensive technological knowledge. I used the pre-existing simulation tools and procedures to comprehend the geometrical influence on the modes. I gained a deeper insight into the quantum optical implications, e.g., the term decorrelation and its importance. My direct engagement in the fabrication of devices resulted in a thorough understanding of waveguide processing and its limitations. This aided the simulations in overcoming the difficulties posed by the fabrication process for nonlinear systems. This was a key aspect in my ability to adjust the simulations to our technological constraints. At the same time, the simulations have evolved my understanding of key features that I need to optimise in the technology for efficient and unique sources.

For a synergetic environment of design modelling, fabrication, and application and to enable the realisation of future quantum optical systems, I have started to establish the optical characterisation of LNOI. This was challenging as we were not familiar with these strongly confining and geometrically very small waveguide structures compared to conventional lithium niobate waveguides. I built a new setup that was mechanically stable and reproducible for efficient waveguide coupling. The analysis and work towards determining the losses of these waveguides stimulated interesting discussions and a collaboration with the group of Prof. Dr. Thomas Pertsch (Friedrich-Schiller-University - Jena).

This thesis focuses on the technological development of (Rb)KTP and LNOI processing and the sources I have directly developed and implemented. This research has resulted in the following patents and papers:

Padberg *et al.*, Patent: Herstellung von Wellenleitern aus Materialien der KTP-Familie, Az. 10 2018 108 636.9. (2018)

We patented the fabrication of corrugation free waveguides in materials from the

KTP family. I fabricated the periodic poling, the rubidium-exchanged waveguides and optimised the corrugation effect.

Padberg *et al.*, Patent: Production of waveguides made of materials from the KTP family, US 11.181.802 B2 (2021)

We patented the fabrication of corrugation free waveguides in materials from the KTP family. I fabricated the periodic poling, the rubidium-exchanged waveguides and optimised the corrugation effect.

Padberg *et al.*, “Characterisation of width-dependent diffusion dynamics in rubidium-exchanged KTP waveguides”, *Opt. Express*, 28(17), 24353-24362. (2020)

We showed that the waveguide depth depends on the width of the waveguide and that narrower waveguides are deeper. We demonstrated that we can model the diffusion introducing stress in the waveguides. I fabricated the waveguide samples, characterised the diffusion process and developed the model.

Padberg *et al.*, “Decorrelated photon pair source at 1550 nm in periodically poled Rb doped KTiOPO₄ waveguides”, in preparation (2022)

We will demonstrate a decorrelated type II photon pair source at 1550 nm with indistinguishable photons. I fabricated the periodic poling the rubidium-exchanged waveguides and performed the linear and nonlinear optical characterisation of this device.

The applications that evolved as a result of the innovative technology capabilities, go far beyond the scope of this written thesis. The following papers partly presented here benefited strongly from the technology:

Padberg *et al.*, “DC ionic conductivity in KTP and its isomorphs: properties, methods for suppression and its connection to gray tracking.”, in preparation (2022)

We investigated the DC conductivity in KTP and its isomorphs. Furthermore, we introduced a method to reduce the overall ionic conductivity in KTP by a potassium nitrate treatment and showed that a thermal treatment in oxygen rich atmosphere removes gray tracking from KTP crystals. I was partly involved in the fabrication and characterisation of those samples.

Brockmeier *et al.*, “Non-Invasive Visualization of Ferroelectric Domain Structures on the Non-Polar y-Surface of KTiOPO₄ via Raman Imaging”, *Crystals* 11(9), 1086 (2021)

We showed that it is possible to visualise domain grids of the non-polar y-surface of KTP via confocal Raman-spectroscopy. This gave us insights into the domain-growth. I fabricated the periodically poled KTP sample that was investigated in this work.

Eigner *et al.*, “Spatially single mode photon pair source at 800 nm in periodically poled Rubidium exchanged KTP waveguides”, *Opt. Express* 28(22), 32925-32935 (2020)

We realised single mode waveguides in periodically poled KTP for frequency-non-degenerate type II parametric down-conversion to generate photon pairs at around 800 nm. I was partly involved in the fabrication of those samples.

Eigner *et al.*, “Periodically poled ridge waveguides in KTP for second harmonic generation in the UV regime”, *Opt. Express* 26(22), 28827-28833 (2018)

We have demonstrated the first periodically poled ridge waveguides in KTP. Moreover, we analysed a type-II second harmonic generation at around 800 nm. I was partly involved in the fabrication of those samples.

Ansari *et al.*, “Heralded generation of high-purity ultrashort single photons in programmable temporal shapes”, *Opt. Express* 26(3), 2764-2774 (2018)

We fabricated and demonstrated a source of nearly pure single photons in arbitrary temporal shapes heralded from a parametric down-conversion. I modelled and fabricated the KTP waveguide sample.

Volk *et al.*, “Fabrication of low-loss Rb-exchanged ridge waveguides in z-cut KTiOPO₄”, *Opt. Mater. Express* 8(1), 82-87 (2018)

We reported on the first realisation of ridge waveguides in planar exchanged waveguides, single mode at 1550 nm, in z-cut KTP. I fabricated the planar waveguide sample and characterised the diffusion.

Padberg *et al.*, Patent: Gradientenfilter zur strahlversatzfreien, wellenlängenselektiven Modifikation der Lichteigenschaften, Az. 10 2019 130 532.2 (2018)

We patented the concept of a gradient filter for beam offset-free, wavelength-selective modification of the light properties. I contributed to the modelling of the coating layer design.

*It isn't what we say or think
that defines us. but what we do.*

Jane Austen

Introduction²

The first quantum computer in Germany, launched by IBM in June 2021, sparked a lot of excitement. Quantum computing is a rapidly-emerging technology that can solve certain classes of problems that go far beyond the capabilities of classical (super) computers by exploiting the peculiar laws of quantum mechanics. Quantum computing as well as quantum communication will revolutionise our society by offering previously unattainable benefits, e.g., new tools to secure bank transactions [4] or encrypt communications [5]. However, the realisation of a quantum computer is a daunting challenge and requires a wide range of complimentary skills. Different approaches to building a functional quantum computer are pursued, e.g., trapped ions [6], superconducting qubits [7], and photonics [8]. The latter is appealing because the only known way to share quantum information in a quantum internet is by means of photons. Light-based quantum computers would seamlessly integrate into such an architecture. In addition, photonic quantum computers could leverage the power of the classical photonics industry for mass production, given that quantum-compatible materials and process steps can be developed. Without much thought, one will come to the conclusion that a practical photonic quantum computer must be realised with integrated photonics and will require optimised sources of quantum light, reconfigurable photonic integrated circuits with feed-forward, and efficient detection and data analysis. Our expertise covers two key building blocks: quantum state generation and device integration.

Fundamental for the realisation of complex photonic systems for quantum communication or quantum computation applications is the generation and the interference between different quantum states of light [9–11]. It is desirable to generate quantum states of light with unique properties, e.g., pure indistinguishable photons, in a controlled manner. For this reason, we need to create quantum light sources which are bright and efficient in a classical way, but at the same time generate pure and indistinguishable photons to exploit their quantum character. Such photons can be generated directly with single photon sources such as atoms, ions, or quantum dots. More commonly, however, they are generated by first generating a photon pair and then detecting one of the pair photons to herald the presence of the other. An established standard for the generation of photon pairs are parametric down-conversion (PDC) sources. By engineering the PDC source it is possible to generate separable two-photon states for heralding pure

single photons [12–15]. A material of choice for such applications is potassium titanyl phosphate (KTiOPO_4 , KTP), whose unique dispersion properties allow for the generation of spectrally pure heralded single photons in the telecommunication wavelength regime [16]. The same holds for rubidium doped KTP (RbKTP) a crystal of the same crystal family.

Besides the generation of quantum light, a key component for integrated quantum optical applications is integration. With time, systems are becoming increasingly complex as they grow in size. In order to handle this, it requires integration, followed by miniaturisation. In order to obtain compact footprint devices, guiding structures must be integrated into crystals in photonic integrated circuits (PIC). Waveguide structures allow for a high mode confinement, leading to longer interaction length, higher energy densities [17] and a better mode overlap for the fields involved. As a result, the efficiency of the devices increases several orders of magnitude [18]. Moreover, integration on one chip enables one to build optical networks with low losses, a large number of optical modes, and excellent stability. One of the most versatile and attractive materials for photonics is lithium niobate (LiNbO_3 , LN) with its exceptional electro-, nonlinear- and acousto-optic properties. Within the past few years, devices based on thin-film LN (lithium niobate on insulator, LNOI), have outperformed their legacy counterparts realised in conventional LN with a complete set of integrated optical components and unprecedented performances, e.g., record-efficiency wavelength converters with conversion efficiencies up to $\eta_0 = 33000 \text{ \%}/(\text{W}\cdot\text{cm}^2)^1$ [20].

Motivated by these observations, this work has embarked on a mission to lay the technological foundations to design future integrated quantum optical applications and make them feasible. Our key goals are to enable waveguiding and single photon generation in KTP and LNOI, which can be accomplished by conserving energy and momentum. In order to fulfil phase matching, we will take advantage of quasi-phase matching. The overarching goal of this work is to develop a synergetic environment of design modelling, fabrication, and application, to enable future ideas for quantum optical systems.

This thesis is organised in five parts to reflect the various aspects of our efforts. In Chapter 3 “Fundamental Theory”, we introduce basic theoretical concepts from the fields of integrated optics, nonlinear optics and nonlinear materials to form a solid basis to understand the results of this work. Subsequently, in chapter 4 “Technology”, we focus on the state of the art fabrication techniques for quasi-phase matching and waveguides in KTP and LNOI devices. Afterwards, we present our techniques for the in-house fabrication of KTP and introduce the state of the art of characterisation methods in terms of material and optical characterisation. Chapter 5 “Novel Developments” is devoted to our developed techniques for optimising and increasing the quality of periodically poled waveguides in RbKTP. For LNOI we show the development of a new technology and the

¹For example, in buried waveguides formed by annealed and reverse proton exchange in periodically poled conventional lithium niobate a high conversion efficiency was demonstrated with $150 \text{ \%}/(\text{W}\cdot\text{cm}^2)$ [19].

important intermediate steps to achieve a reliable and high quality technology. Then, in chapter 6 “Tailored Waveguide Sources”, we apply our knowledge and techniques to demonstrate and analyse the performance of our in-house fabricated sources in RbKTP and LNOI. We discuss the state of the art of unique sources in both materials and we present the analysis of our periodically poled waveguides in RbKTP and LNOI. Finally, in chapter 7 “Conclusion and Outlook”, we conclude this thesis and identify potential future directions and extensions of our work.

*It's dangerous to go alone!
Take this.*

The Legend of Zelda

Fundamental Theory

Contents

3.1	Integrated Optics	13
3.2	Nonlinear Optics	22
3.3	Nonlinear Materials	35

Integrated quantum optics involves topics related to the fields of integrated optics, nonlinear optics and therefore, nonlinear materials. In this chapter, we introduce the theoretical concepts necessary to discuss the results of this work and we present our notation. First, we provide a mathematical description of the integrated optical elements relevant in this work, namely optical waveguides and directional couplers. Then, we introduce nonlinear optics, discussing light-matter interaction and three-wave mixing interactions, phase matching and dispersion engineering. Finally, we describe two nonlinear materials used in this thesis, potassium titanyl phosphate (KTP) and lithium niobate on insulator (LNOI) and address their properties in the context of integrated nonlinear optics.

3.1 Integrated Optics

Every integrated device relies on light guiding structures. Waveguides confine light in small cross-sections, enabling us to control the propagation direction and spatial structure of the light fields. This allows for the realisation of complex circuits [21] and the tailoring of specific applications like a decorrelated source with a wavelength at 1550 nm [16]. It is fundamental to precisely model device behaviour. In the following, we start with the simplest type of waveguides, a straight waveguide structure and its description.

3.1.1 Waveguides

A fundamental element of integrated optics is a waveguide, because it allows for almost lossless routing of light between different parts of an integrated device. A dielectric waveguide consists of a dielectric material referred to as the core surrounded by another dielectric material called cladding with a lower refractive index. Therefore, the light is trapped in the core through total internal reflection. For a full-field description of a straight, dielectric waveguide we have to solve Maxwell's equations by analytical or numerical methods.

3.1.1.1 Mathematical Description

The properties of light inside a waveguide can be derived from Maxwell's equations [22]. Here, we consider the most common type of waveguides, in a lossless, dielectric, non-magnetic and non-conducting medium. Thus, the equations simplify to

$$\nabla \times \mathbf{H} = \frac{\partial \mathbf{D}}{\partial t} \quad (3.1)$$

$$\nabla \times \mathbf{E} = -\frac{\partial \mathbf{B}}{\partial t} \quad (3.2)$$

$$\nabla \cdot \mathbf{H} = 0 \quad (3.3)$$

$$\nabla \cdot \mathbf{D} = 0, \quad (3.4)$$

where \mathbf{H} is the magnetic field vector, \mathbf{D} is the electric displacement vector, \mathbf{E} is the electric field vector, \mathbf{B} is the magnetic induction vector and t is the time. The constitutive equations are given by

$$\mathbf{D} = \epsilon_0 \cdot \epsilon_r(\mathbf{r}) \cdot \mathbf{E} \quad (3.5)$$

$$\mathbf{B} = \mu_0 \cdot \mu_r \cdot \mathbf{H}, \quad (3.6)$$

where ϵ_0 and ϵ_r are the permittivity of free space and the relative permittivity tensor depending on the space r . Furthermore, μ_0 and μ_r are the permeability of free space and permeability tensor of the material. The two Maxwell's equations can be rewritten as

$$\nabla \times \mathbf{H} = \epsilon_0 \cdot \epsilon_r(\mathbf{r}) \cdot \frac{\partial \mathbf{E}}{\partial t} \quad (3.7)$$

$$\nabla \times \mathbf{E} = -\mu_0 \cdot \mu_r \cdot \frac{\partial \mathbf{H}}{\partial t}. \quad (3.8)$$

If we apply the curl operator on equation 3.8 and use equation 3.7 we get

$$\nabla \times (\nabla \times \mathbf{E}) + \mu_0 \cdot \mu_r \cdot \epsilon_0 \cdot \epsilon_r(\mathbf{r}) \cdot \frac{\partial^2 \mathbf{E}}{\partial t^2} = 0. \quad (3.9)$$

We can expand the first term as

$$\nabla \times (\nabla \times \mathbf{E}) = \nabla \cdot (\nabla \cdot \mathbf{E}) - \nabla^2 \cdot \mathbf{E}. \quad (3.10)$$

Using equation 3.4 and 3.5 we can rewrite

$$\nabla \cdot \mathbf{D} = 0 = \nabla \cdot [\epsilon_0 \cdot \epsilon_r(\mathbf{r}) \cdot \mathbf{E}] = \epsilon_0 \cdot [\nabla \cdot \epsilon_r(\mathbf{r}) \cdot \mathbf{E} + \epsilon_r(\mathbf{r}) \cdot \nabla \cdot \mathbf{E}] \quad (3.11)$$

$$\Rightarrow \nabla \cdot \mathbf{E} = - \left(\frac{\nabla \cdot \epsilon_r(\mathbf{r})}{\epsilon_r(\mathbf{r})} \right) \cdot \mathbf{E}. \quad (3.12)$$

Therefore, equation 3.9 with help of equation 3.10 can be written as

$$\nabla^2 \cdot \mathbf{E} + \nabla \cdot \left[\left(\frac{\nabla \cdot \epsilon_r(\mathbf{r})}{\epsilon_r(\mathbf{r})} \right) \cdot \mathbf{E} \right] - \mu_0 \cdot \mu_r \cdot \epsilon_0 \cdot \epsilon_r(\mathbf{r}) \cdot \frac{\partial^2 \mathbf{E}}{\partial t^2} = 0. \quad (3.13)$$

A similar equation can be deduced for the magnetic field vector \mathbf{H}

$$\nabla^2 \cdot \mathbf{H} + \left[\left(\frac{\nabla \cdot \epsilon_r(\mathbf{r})}{\epsilon_r(\mathbf{r})} \right) \times (\nabla \times \mathbf{H}) \right] - \mu_0 \cdot \mu_r \cdot \epsilon_0 \cdot \epsilon_r(\mathbf{r}) \cdot \frac{\partial^2 \mathbf{H}}{\partial t^2} = 0. \quad (3.14)$$

These standard electromagnetic wave equations are satisfied by monochromatic plane wave solutions

$$\Psi = A \cdot e^{i(\omega \cdot t - \mathbf{k} \cdot \mathbf{r})}, \quad (3.15)$$

where A is the amplitude and ω the frequency of the wave. The magnitude of the wavevector \mathbf{k} is defined as

$$|\mathbf{k}| = \omega \sqrt{\mu \epsilon}. \quad (3.16)$$

The electromagnetic wave given in 3.15 is called a plane wave, whose wavefronts travel in the direction of \mathbf{k} with a velocity v , whose magnitude is

$$v = \frac{\omega}{|\mathbf{k}|} \quad (3.17)$$

and with a wavelength λ of

$$\lambda = \frac{2\pi}{|\mathbf{k}|} = 2\pi \frac{v}{\omega}. \quad (3.18)$$

The phase velocity v depends on the medium and therefore, can be described by the permittivity and permeability as

$$v = \frac{1}{\sqrt{\mu_r \mu_0 \epsilon_0 \epsilon_r}}. \quad (3.19)$$

The velocity of light in vacuum is

$$c = \frac{1}{\sqrt{\mu_0 \cdot \epsilon_0}}, \quad (3.20)$$

whereas in a medium we have

$$v = \frac{c}{n}. \quad (3.21)$$

The refractive index n of the material is defined as

$$n = \sqrt{\mu_r \epsilon_r} \quad (3.22)$$

Non-magnetic materials have a material permeability of $\mu_r = 1$ and we can simplify the refractive index for a lossless medium to

$$n = \sqrt{\epsilon_r}. \quad (3.23)$$

With equations 3.15 and 3.20 we can write the wave equations 3.13 and 3.14 as

$$\nabla^2 \cdot \mathbf{E} + \nabla \cdot \left[\left(\frac{\nabla \cdot \epsilon_r(\mathbf{r})}{\epsilon_r(\mathbf{r})} \right) \cdot \mathbf{E} \right] + \frac{\omega^2}{c^2} \cdot \epsilon_r(\mathbf{r}) \cdot \mathbf{E} = 0 \quad (3.24)$$

$$\nabla^2 \cdot \mathbf{H} + \left[\left(\frac{\nabla \cdot \epsilon_r(\mathbf{r})}{\epsilon_r(\mathbf{r})} \right) \times (\nabla \times \mathbf{H}) \right] + \frac{\omega^2}{c^2} \cdot \epsilon_r(\mathbf{r}) \cdot \frac{\partial^2 \mathbf{H}}{\partial t^2} = 0. \quad (3.25)$$

If we now make some approximations, we can further simplify the wave equations. We assume a lossless medium and thus, can use equation 3.23. Moreover, we consider waveguides with a refractive index that varies slowly compared to the optical wavelength and therefore, $\nabla \cdot \epsilon(\mathbf{r}) \approx 0$. This is true for weakly guiding waveguides, where in the guiding region the refractive index increase is relatively small. Next, we assume that the geometry is invariant on the z -axis and this allows us to write for the electric and magnetic fields

$$\mathbf{E}(\mathbf{r}) = E(x, y) \cdot e^{-i \cdot \beta \cdot z} \quad (3.26)$$

$$\mathbf{H}(\mathbf{r}) = H(x, y) \cdot e^{-i \cdot \beta \cdot z}. \quad (3.27)$$

With these approximations and with

$$\nabla \cdot \mathbf{E}(\mathbf{r}) = \nabla_{xy}^2 \cdot \nabla_z^2 \cdot E(x, y) \cdot e^{-i \cdot \beta \cdot z} = \left(\nabla_{xy}^2 \cdot E(x, y) - \beta^2 \cdot E(x, y) \right) \cdot e^{-i \cdot \beta \cdot z} \quad (3.28)$$

we can simplify the wave equations 3.24 and 3.25 further to

$$\left(\nabla_{xy}^2 + \frac{\omega^2}{c^2} \cdot n^2(x, y) - \beta^2 \right) \cdot E(x, y) = 0 \quad (3.29)$$

$$\left(\nabla_{xy}^2 + \frac{\omega^2}{c^2} \cdot n^2(x, y) - \beta^2 \right) \cdot H(x, y) = 0. \quad (3.30)$$

The solutions of these equations are a set of modes with field distributions of $\mathbf{E}_m(x, y)$ and their corresponding propagation constants β_m . Waveguides with only one solution, guide only one mode and are called single-mode waveguides. For confined modes, the field amplitude must decrease exponentially outside of the waveguide. Each mode is

associated with an effective refractive index of $n_{\text{eff}} = \beta \cdot \frac{c}{\omega} = \beta \cdot k_0$, which describes the propagation of the light mode inside a waveguide. The wavevector in vacuum is k_0 . With this, we can define the propagation constant as

$$\beta = k_0 n_{\text{eff}} = \frac{2 \cdot \pi \cdot n_{\text{eff}}}{\lambda_0}. \quad (3.31)$$

In weakly guiding waveguides, modes can be classified in two different types. On the one hand, there are quasi-transverse electric modes (quasi-TE or qTE), which have their electrical field perpendicular to the incidence plane and have a predominant field component of E_y . On the other hand, modes with a predominant field component of H_y are called quasi-transverse magnetic modes (quasi-TM or qTM) [22].

In the case of strongly guiding waveguides, i.e. a high index change between the refractive index of the waveguides and the cladding, these approximations are not valid. The polarisations are no longer decoupled and more complex modes can arise, such as hybrid modes, where the magnitudes of the amplitudes of the field components are comparable. As a result, these equations cannot be solved analytically and necessitates numerical approaches, which will be briefly discussed in the following part.

3.1.1.2 Numerical Methods

To solve the wave equations, a number of numerical methods have been evolved.

Marcatili's Method

An elementary approach is Marcatili's method [23], which describes the propagation of light in a rectangular dielectric waveguide. The light is guided by total internal reflection because the waveguide's core has a higher refractive index than its surrounding materials. This method approximates the waveguide as two planar waveguides and neglects at the same time the corner regions. The mode can be described as standing waves in both the x- and y-directions in the waveguide its core. The field decays exponentially in both horizontal and vertical directions outside the core. The propagation constant of the waveguide is defined as $\beta^2 = k_0^2 - k_x^2 - k_y^2$, where k_0^2 is the wavevector of the core of the waveguide and k_x, k_y correspond to the wavevectors of the standing waves along the x- and y-direction. Nevertheless, this method works best for low-index-contrast, multimode and step index waveguides. For weakly guiding waveguides or waveguides with more complex geometry, variations of this method exist, but they are usually less accurate.

Finite Element Method

For a precise calculation of the waveguide modes, solving the full numerical model using the finite element method (FEM) is required. FEM is a prominent technique for solving partial differential equations (PDE) [24] numerically. The FEM breaks a big system into smaller simpler sections called finite elements in order to solve a problem. This is

accomplished by discretising in the spatial dimensions. This is done through the creation of a mesh and the problem is solved inside each element of the mesh. For the final calculation, all sets of element equations are systematically recombined into a global system of equations. FEM can be used to investigate problems in complex domains. However, because the numerical implementation of FEMs is rather complicated, simpler and faster methods for solving Maxwell's equations are commonly implemented.

Finite Difference Method and Finite Difference Time Domain

For structures with simple geometry, finite difference methods (FDM) are more convenient [24]. FDM solves ordinary differential equations (ODE) or partial differential equations using finite differences to approximate derivatives. The spatial domain is discretised into a rectangular mesh, or broken down into a finite number of steps. By solving algebraic equations involving finite differences and values from neighbouring points, it is possible to approximate the value of the solution at these discrete points. The time-dependent solution of Maxwell's equation can be solved using an extended FDM techniques, called finite difference time domain (FDTD). At a given point in time, the electric and magnetic field vector components in a volume of space are solved. Therefore, FDM and FDTD are two of the most widely used methods for calculating the spatial modes and the propagation of light in a wide range of media.

3.1.2 Directional Coupler

A directional coupler is an optical component, which couples light between two waveguides and is a key component for optical splitters and switches. Guided modes have an evanescent field exponentially decreasing outside of the waveguide region. We can use this evanescent field to excite modes in an adjacent waveguide. If the distance between these two parallel waveguides is sufficiently small, the evanescent fields of the two waveguides overlap. This allows the field propagating inside of one the waveguides to couple to the other waveguide. The efficiency of the coupling is quantified by the coupling ratio, which depends on the length of the coupler and the coupling coefficient. The coupling coefficient describes how well the modes of the two waveguides interact. It is related to the distance between the two waveguides in the coupling region and the overall shape of the coupler. Figure 3.1 shows a directional coupler.

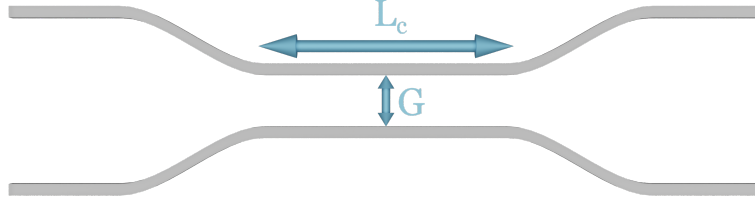


Figure 3.1 – Schematic of a directional coupler consisting of two waveguides. In the coupling region the two waveguides are separated by a gap G over a coupling length L_c , allowing a coupling between the adjacent waveguides.

For simplicity, this section focuses on two waveguides, which are identical and guide only the fundamental mode. Light can couple between the waveguides in the coupling region with a gap G and coupling length L_c . Before and after the coupling region the waveguides are separated by bendings.

The coupling between the two waveguides can be described with the coupled mode theory [25]. We consider two electromagnetic modes a and b with frequencies ω_a and ω_b and complex amplitudes A and B . In the presence of a perturbation the complex amplitudes are no longer constant but depend on the propagation direction z

$$\frac{dA}{dz} = \kappa_{ab} B e^{-i\Delta z} \quad (3.32)$$

$$\frac{dB}{dz} = \kappa_{ba} A e^{+i\Delta z}, \quad (3.33)$$

where κ_{ab} and κ_{ba} are the coupling coefficients. Here, the phase-mismatch $\Delta = \beta_b - \beta_a$ depends on the propagation constants of the two modes and on the spatial variation of the coupling perturbation. If we consider a co-directional coupler, the modes a and b propagate in the same direction. The power of these two modes are $|A(z)|^2$ and $|B(z)|^2$ and their sum is conserved over the entire coupling region with

$$\frac{d}{dz} (|A(z)|^2 + |B(z)|^2) = 0. \quad (3.34)$$

This is satisfied when

$$\kappa_{ab} = -\kappa_{ba}^*. \quad (3.35)$$

If the power is injected in one waveguide with mode b at $z = 0$ we have

$$b(0) = B_0 \quad (3.36)$$

$$a(0) = 0. \quad (3.37)$$

With these conditions the solutions for the equations 3.32 and 3.33 are

$$A(z) = B_0 \frac{2\kappa_{ab}}{(4\kappa^2 + \Delta^2)^{\frac{1}{2}}} e^{-i\Delta \frac{z}{2}} \sin \left[\frac{1}{2} (4\kappa^2 + \Delta^2)^{\frac{1}{2}} z \right] \quad (3.38)$$

$$B(z) = B_0 e^{i\Delta \frac{z}{2}} \left\{ \cos \left[\frac{1}{2} (4\kappa^2 + \Delta^2)^{\frac{1}{2}} z \right] - i \frac{\Delta}{(4\kappa^2 + \Delta^2)^{\frac{1}{2}}} \sin \left[\frac{1}{2} (4\kappa^2 + \Delta^2)^{\frac{1}{2}} z \right] \right\} \quad (3.39)$$

where $\kappa^2 = |\kappa_{ab}|^2$. If the phase-mismatch is $\Delta = 0$, which means the two modes have equal propagation constants, the power P_i is completely transferred periodically between the modes a and b

$$P_A = |A(z)|^2 = B_0^2 \sin^2(\kappa z) \quad (3.40)$$

$$P_B = |B(z)|^2 = B_0^2 \cos^2(\kappa z) \quad (3.41)$$

with a period of

$$z = L_x = \frac{\pi}{2\kappa}, \quad (3.42)$$

where L_x is the cross-over length. Figure 3.2 shows the power of the modes depending on the length z for a perfectly phase matched system.

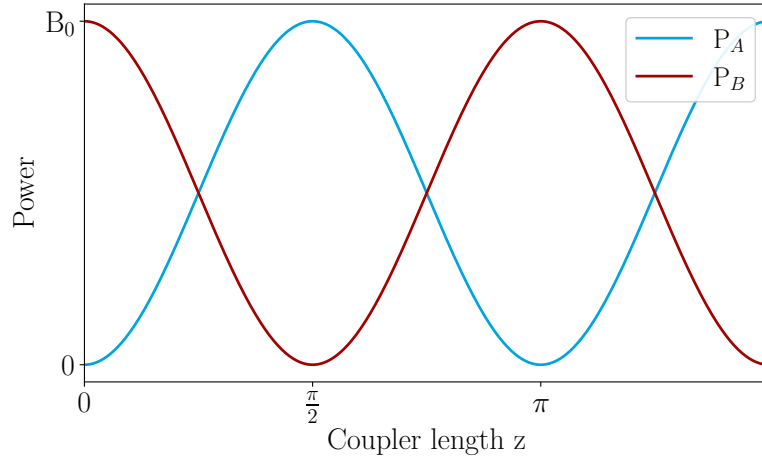


Figure 3.2 – Following equations 3.40 and 3.41, the power of mode a is minimal, when mode b has maximal power. The intersection point of both is referred to as 50:50 splitting ratio.

Using the supermode approach, we can calculate the coupling coefficient κ to describe the coupling behaviour. In this approach the coupler with the two waveguides is treated as a single structure. The eigenmodes of this structure are the symmetric and antisymmetric mode shown in figure 3.3. These two modes have slightly different propagation constants $\beta_{\text{symmetric}}$ and $\beta_{\text{antisymmetric}}$.

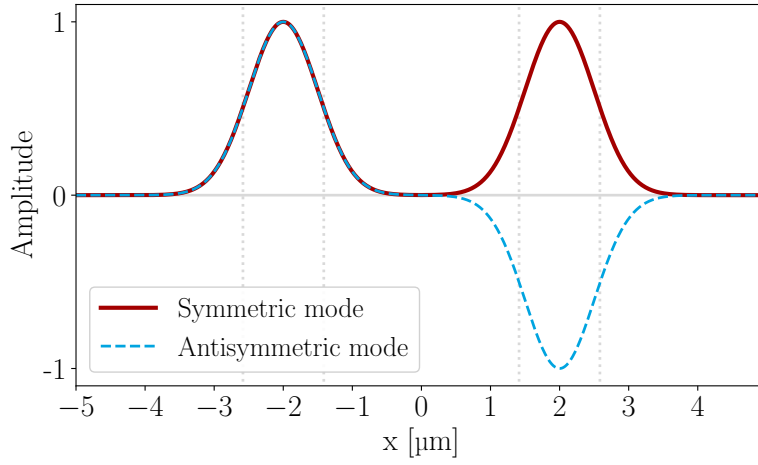


Figure 3.3 – Symmetric and antisymmetric mode of a directional coupler. The dotted lines indicate the two waveguides.

If we now excite the mode a in the waveguide, this field can be described as the sum of the symmetric and antisymmetric modes of the compound structure. The mode b can be described as the difference of symmetric and antisymmetric mode. Figure 3.4 shows the modes in the two waveguides as a sum or difference of the symmetric and antisymmetric mode.

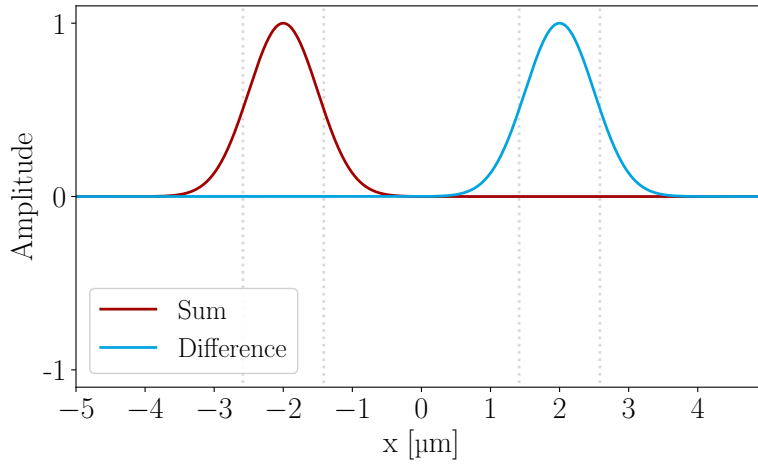


Figure 3.4 – Sum and difference fields of the symmetric and antisymmetric mode of a directional coupler shown in figure 3.3. The dotted lines indicate the two waveguides.

When launching light at $z = 0$ into mode a , this corresponds to exciting the symmetric and antisymmetric mode with equal weight and in phase. As they travel along the

waveguide, they change their relative phase and are out-of-phase at

$$z = L_x = \frac{\pi}{\beta_{\text{symmetric}} - \beta_{\text{antisymmetric}}}. \quad (3.43)$$

This means we have the difference between the two supermodes and we get mode b . After half a period the total power from mode a is transferred to mode b as described by equations 3.40 and 3.41.

Using $\beta_i = \frac{2\pi \cdot n_i}{\lambda}$ [26] and $\Delta n = n_{\text{symmetric}} - n_{\text{antisymmetric}}$, where $n_{\text{symmetric}}$ and $n_{\text{antisymmetric}}$ are the effective refractive indices of the symmetric and antisymmetric mode, we can rewrite equation 3.43 and define the cross-over length as

$$L_x = \frac{\lambda}{2 \cdot \Delta n}. \quad (3.44)$$

Therefore, we can calculate with equations 3.42 and 3.44 the coupling coefficient κ as

$$\kappa = \frac{\pi \Delta n}{\lambda}. \quad (3.45)$$

With this directional coupler it is possible to achieve different power splitting ratios of the coupler by precisely tuning the coupling length L_c . All coupling ratios are possible, in particular 100 % coupling from one waveguide to the other or 50 % : 50 % splitting.

In this section, we introduced linear optical components and their mathematical description. Nonlinear effects enable us to use a variety of further possible applications. Therefore, we introduce the concepts of nonlinear optics in the next section.

3.2 Nonlinear Optics

Nonlinear optics is the study of phenomena that arise as a result of intense light modifying the optical characteristics of a material system. Generally, only laser light is strong enough to observe nonlinear effects. The interaction between the laser light and the material can lead to the generation of new optical fields at new frequencies, allowing for novel applications such as nonlinear frequency conversion [27] or single photon generation via parametric down-conversion [28]. Therefore, the mathematical description of nonlinear processes, especially second-harmonic generation, is covered in this chapter. Moreover, we introduce two different types of phase matching and outline the concept of dispersion engineering. All of these descriptions generally begin with bulk media, but can be adapted to waveguides, since they achieve a stronger nonlinear interaction by increasing the field confinement and overcoming diffraction, which gives a longer interaction length [17].

3.2.1 Nonlinear Material Response

Since the origin of nonlinear optics is the response of the material in a nonlinear manner in the presence of an intense light field, the dipole moment per unit volume, or in other words the polarisation $\mathbf{P}(t)$, depends on the strength $\mathbf{E}(t)$ of the light field. $\mathbf{P}(t)$ can be expressed as a power series of $\mathbf{E}(t)$ [29]

$$\mathbf{P}(t) = \epsilon_0 [\chi^{(1)}\mathbf{E}(t) + \chi^{(2)}\mathbf{E}^2(t) + \chi^{(3)}\mathbf{E}^3(t) + \dots] \quad (3.46)$$

$$= \underbrace{\mathbf{P}^{(1)}(t)}_{\mathbf{P}_{\text{linear}}} + \underbrace{\mathbf{P}^{(2)}(t) + \mathbf{P}^{(3)}(t) + \dots}_{\mathbf{P}_{\text{nonlinear}}}, \quad (3.47)$$

where $\chi^{(m)}$ is the susceptibility tensor of m -th order with the rank m . If the strength of the electric field is relatively small, we only have a linear response with $\mathbf{P}_{\text{linear}}$. The linear susceptibility $\chi^{(1)}$ is related to the refractive index through [30]

$$\chi^{(1)} = n^2 - 1. \quad (3.48)$$

$\mathbf{P}^{(2)}(t)$ is referred to as the second order nonlinear polarisation and $\mathbf{P}^{(3)}(t)$ as the third-order nonlinear polarisation. The magnitude of the higher order terms of χ decreases relatively quick. As a result, terms of $\mathbf{P}^{(3)}(t)$ and higher can be neglected, unless the light intensity is very strong. Thus, we only consider in the following the second order nonlinear polarisation, which depends quadratically on the electric field. Therefore, the three-wave mixing processes are discussed in more detail in the next section.

3.2.2 Three-Wave Mixing

In the following, we briefly outline different three-wave mixing processes. Therefore, we assume an electric field as a monochromatic plane wave propagating only along the z -direction:

$$\mathbf{E}_i(t, z) = E_i \cdot e^{i(\omega_i t - \beta_i z)} + c.c. \quad (3.49)$$

with ω_i as the frequency, E_i as the amplitude and β_i the propagation constant of the light field. If we now consider two electric fields $\mathbf{E} = \mathbf{E}_1(t, z) + \mathbf{E}_2(t, z)$ exciting the nonlinear

material and use equation 3.47, we can calculate the nonlinear polarisation

$$\begin{aligned}
 \mathbf{P}^{(2)}(t, z) = \epsilon_0 \chi^{(2)} & \left[\underbrace{\left(E_1^2 \cdot e^{i \cdot (2 \cdot \omega_1 \cdot t - 2 \cdot \beta_1 \cdot z)} + c.c. \right)}_{\text{second-harmonic generation}} + \underbrace{\left(E_2^2 \cdot e^{i \cdot (2 \cdot \omega_2 \cdot t - 2 \cdot \beta_2 \cdot z)} + c.c. \right)}_{\text{second-harmonic generation}} \right. \\
 & + 2 \cdot \underbrace{\left(E_1 \cdot E_2 \cdot e^{i \cdot [(\omega_1 + \omega_2) \cdot t - (\beta_1 + \beta_2) \cdot z]} + c.c. \right)}_{\text{sum-frequency generation}} + 2 \cdot \underbrace{\left(E_1 \cdot E_2^* \cdot e^{i \cdot [(\omega_1 - \omega_2) \cdot t - (\beta_1 - \beta_2) \cdot z]} + c.c. \right)}_{\text{difference-frequency generation}} \\
 & \left. + 2 \cdot \epsilon_0 \chi^{(2)} \underbrace{\left[E_1 \cdot E_1^* + E_2 \cdot E_2^* \right]}_{\text{optical rectification}} \right] \quad (3.50)
 \end{aligned}$$

Each expression has been labelled with the name of the physical process it describes in this equation. We can distinguish between second-harmonic generation (SHG), sum-frequency generation (SFG), difference-frequency generation (DFG), and optical rectification (OR), which we do not consider in this work. If we consider this interaction in terms of field exchange between the various frequency components of the field, the nonlinearity induces two fields to combine into one field. In the case of two fields with identical frequency ω it results in a field with twice the original frequency $2 \cdot \omega$. This is called second-harmonic generation. For two fields with different frequencies, a sum- or difference frequency field is generated. Therefore, there are three different process, which can be distinguish because of the energy conservation:

$$\begin{aligned}
 \omega_3 &= 2 \cdot \omega_{1/2} && \text{Second-Harmonic Generation} \\
 \omega_3 &= \omega_1 + \omega_2 && \text{Sum-Frequency Generation} \\
 \omega_3 &= \omega_1 - \omega_2 && \text{Difference-Frequency Generation}
 \end{aligned}$$

These processes can be further categorised into types depending on the polarisation of the involved fields. In this thesis, we define these types as:

- type 0 - all the three fields have the same polarisation
- type I - the two input fields have the same polarisation
- type II - the two input fields have orthogonal polarisation

Taking a quantum approach of light-matter interaction, there is a fifth process possible called spontaneous parametric down-conversion (SPDC or PDC). PDC can be considered as the inverse process of sum-frequency [30]. In this case, one photon decays into two daughter photons with the sum of their frequencies equal to the frequency of the first photon.

3.2.2.1 Nonlinear Susceptibility

If we consider a three-wave mixing process and the nonlinear polarisation $\mathbf{P}^{(2)}(t, z)$, the second order nonlinearity $\chi^{(2)}$ only exists in non-centrosymmetric crystals [29]. If the frequencies of a considered process are far away from the resonance frequencies of the optical medium and if Kleinman's symmetry condition is valid, we can simplify the susceptibility and introduce the tensor

$$d_{ijk} = \frac{1}{2} \chi_{ijk}^{(2)}, \quad (3.51)$$

where we can further simplify the tensor assuming d_{ijk} is symmetric in the two last indices. Therefore, we can introduce a contracted matrix d_{il} , in which the indices jk are combined to l as

jk	11	22	33	23, 32	31, 13	12, 21
1	1	2	3	4	5	6

With this notation it is possible to represent the nonlinear susceptibility tensor as a 3×6 matrix. The tensor with its elements can be described as

$$d = \begin{pmatrix} d_{11} & d_{12} & d_{13} & d_{14} & d_{15} & d_{16} \\ d_{21} & d_{22} & d_{23} & d_{24} & d_{25} & d_{26} \\ d_{31} & d_{32} & d_{33} & d_{34} & d_{35} & d_{36} \end{pmatrix}. \quad (3.52)$$

We can describe the nonlinear polarisation for three-wave mixing with $\omega_3 = \omega_1 + \omega_2$ by

$$\begin{pmatrix} P_x(\omega_3) \\ P_y(\omega_3) \\ P_z(\omega_3) \end{pmatrix} = M \cdot \epsilon_0 \cdot \begin{pmatrix} d_{11} & d_{12} & d_{13} & d_{14} & d_{15} & d_{16} \\ d_{21} & d_{22} & d_{23} & d_{24} & d_{25} & d_{26} \\ d_{31} & d_{32} & d_{33} & d_{34} & d_{35} & d_{36} \end{pmatrix} \cdot \begin{pmatrix} E_x(\omega_1)E_x(\omega_2) \\ E_y(\omega_1)E_y(\omega_2) \\ E_z(\omega_1)E_z(\omega_2) \\ E_y(\omega_1)E_z(\omega_2) + E_z(\omega_1)E_y(\omega_2) \\ E_x(\omega_1)E_z(\omega_2) + E_z(\omega_1)E_x(\omega_2) \\ E_x(\omega_1)E_y(\omega_2) + E_y(\omega_1)E_x(\omega_2) \end{pmatrix} \quad (3.53)$$

M is the multiplicity factor and depends on the involved process. $M = 2$ for SHG and for all other processes $M = 1$. The nonlinear susceptibility and therefore, the simplified tensor is constrained by the given nonlinear crystal and its symmetry properties.

During this thesis we use two crystals: lithium niobate and potassium titanyl phosphate. The tensors for these two crystals are described in detail in sections 3.3.1.2 and 3.3.2.2.

3.2.3 Phase Matching

Phase matching is a condition and if it is fulfilled, the generated wave maintains a fixed phase relation with respect to the nonlinear polarisation. As a result, the generated wave is able to extract energy most efficiently from the incident waves.

The wave equation for nonlinear optical media can be derived from Maxwell's equations with $\mathbf{D} = \epsilon_0 \epsilon_r \cdot \mathbf{E} + \mathbf{P}$ and is given by [29]

$$\nabla^2 \mathbf{E}(\mathbf{r}) - \frac{\epsilon_r}{c^2} \cdot \frac{\partial^2 \mathbf{E}}{\partial t^2} = \frac{1}{\epsilon_0 \cdot c^2} \frac{\partial^2 \mathbf{P}_{\text{nonlinear}}}{\partial t^2}. \quad (3.54)$$

Next, we consider sum-frequency generation ($\omega_3 = \omega_1 + \omega_2$) in a lossless nonlinear optical medium and assume a plane wave with the amplitude A_i as

$$\mathbf{E}_i(t, z) = A_i \cdot e^{i(\beta_i z - \omega_i t)} + c.c., \quad (3.55)$$

assuming the amplitude is depending on z . Solving the wave equation and applying the slowly varying amplitude approximation [29] we get for the coupled wave equation of the generated field

$$\frac{dA_3}{dz} = \frac{2 \cdot i \cdot d_0 \omega_3^2}{\beta_3 c^2} \cdot A_1 \cdot A_2 \cdot e^{-i \Delta \beta \cdot z}, \quad (3.56)$$

where

$$\Delta \beta = \beta_3 - \beta_2 - \beta_1 \quad (3.57)$$

is the phase mismatch. The effective nonlinear coefficient d_0 can be calculated by equation 3.52 depending on the involved type of process. The amplitude of the sum-frequency field at the end of a nonlinear medium with length L is given by

$$A_3(L) = \frac{2 \cdot i \cdot d_0 \cdot \omega_3^2 \cdot A_1 \cdot A_2}{\beta_3 \cdot c^2} \int_0^L e^{-i \Delta \beta \cdot z} dz = \frac{2 \cdot i \cdot d_0 \cdot \omega_3^2 \cdot A_1 \cdot A_2}{\beta_3 \cdot c^2} \left(\frac{e^{-i \Delta \beta \cdot L} - 1}{-i \cdot \Delta \beta} \right). \quad (3.58)$$

Thus, we obtain for the intensity [29]

$$I_3 = \frac{8 \cdot d_0^2 \cdot \omega_3^2 \cdot I_1 \cdot I_2}{n_1 \cdot n_2 \cdot n_3 \cdot \epsilon_0 \cdot c^2} \cdot L^2 \cdot \text{sinc}^2 \left(\frac{\Delta \beta \cdot L}{2} \right). \quad (3.59)$$

Figure 3.5 shows the effect of the wavevector mismatch on the efficiency of the process.

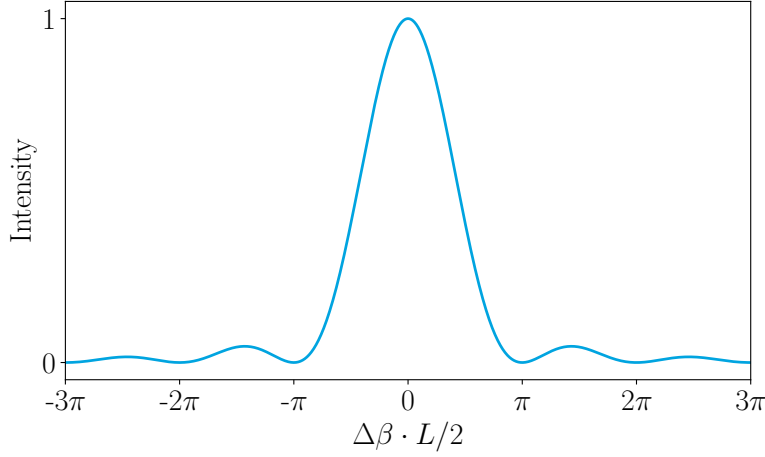


Figure 3.5 – Intensity of the three-wave mixing conversion process. The intensity depends on the phase mismatch between the involved waves. At zero phase mismatch, the intensity is maximal, and significantly decreases for increasing mismatch.

In the case of

$$\Delta\beta = 0, \quad (3.60)$$

we have perfect phase matching and the converted intensity reaches its maximum. In the case of SHG, $\mathbf{P}_{\text{nonlinear}}$, which generates a field at ω_3 , propagates with speed $\beta_1 + \beta_2$, since it depends on the other two fields. The generated wave at ω_3 propagates at β_3 . After a coherence length L_{coh}

$$L_{\text{coh}} = \frac{\pi}{\Delta\beta}, \quad (3.61)$$

$\mathbf{P}_{\text{nonlinear}}$ is out of phase, with a phase mismatch equal to π , with the field generated at ω_3 . Thus, these fields interfere destructively. In general, it is difficult to fulfil the phase matching condition $\Delta\beta = 0$, because normally the refractive index of lossless materials is decreasing with higher wavelength, which is called normal dispersion. Therefore, the phase matching condition has to be described as a function of the wavelength dependent refractive index

$$\Delta\beta = 2\pi \left(\frac{n_1(\lambda_1)}{\lambda_1} + \frac{n_2(\lambda_2)}{\lambda_2} - \frac{n_3(\lambda_3)}{\lambda_3} \right). \quad (3.62)$$

However, there are two common techniques to achieve phase matching called birefringent phase matching and quasi-phase matching.

3.2.3.1 Birefringent Phase Matching

Birefringent phase matching uses the birefringence of a crystal to achieve phase matching. If possible, this is achieved by properly choosing the polarisation of the three interacting fields, to counteract the effect of dispersion in the crystal. However, this technique requires tuning in order to reach the desired phase matching condition, by modify refractive index seen by light. This can be accomplished by changing the temperature or the angle of the crystal. Nevertheless, the allowed processes are highly limited due to the dispersion characteristics of nonlinear crystals. Note that angle tuning is not suitable in waveguides. Moreover, birefringent phase matching makes use of different polarised fields and excludes the d_{33} coefficient of the nonlinear susceptibility. However, the d_{33} coefficient uses three fields with equal polarisation and is the highest coefficient for our chosen materials KTP and LNOI.

3.2.3.2 Quasi-Phase Matching

To be more flexible in the choice of polarisation and wavelengths involved in the three-wave mixing process, one can engineer the material nonlinearity via quasi-phase matching. As described in equation 3.61, the fields propagating in a waveguide interfere destructively after a coherence length, which is the length over the accumulated phase mismatch is equal to π . This situation for second-harmonic generation is illustrated by the red curve in figure 3.6. It shows the intensity of the generated second-harmonic (SH) light field as a function of the propagation length. For a non-phase matched case the intensity grows and decays periodically along the length of the interaction with a period twice the coherence length.

As discussed in section 3.2.3.1 the phase mismatch can be compensated by birefringent phase matching. In this case the second-harmonic field grows linearly with the propagation length and thus, the intensity growth quadratically. The blue curve in figure 3.6 shows the condition of perfectly, i.e. birefringent, phase matched process.

If birefringent phase matching is not feasible, another technique is quasi-phase matching (QPM). In QPM the relative phase between the involved fields is periodically inverted. One way to introduce a phase shift is to change the sign of the nonlinear coefficient. Unlike birefringent phase matching, QPM necessitates the structuring of the nonlinear material. Ferroelectric materials possess a spontaneous polarisation. By inverting the spontaneous polarisation periodically, the sign of the nonlinear coefficient is also periodically switched. This is called periodic poling. The green curve in figure 3.6 shows the case, where the spontaneous polarisation is switched every coherence length. This situation is called first-order QPM.

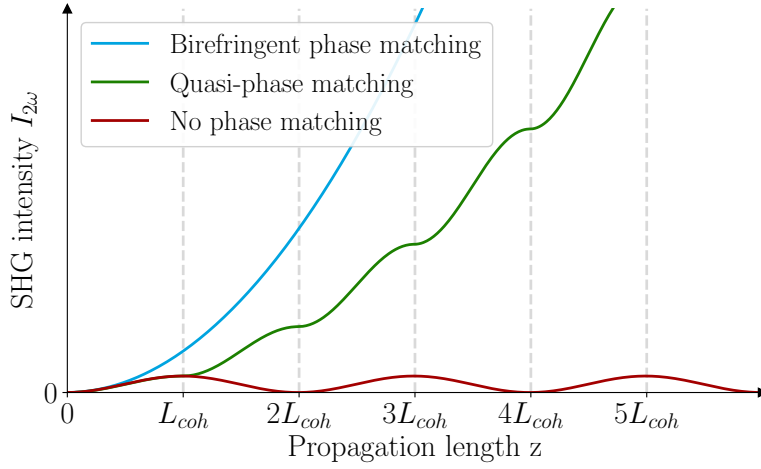


Figure 3.6 – Second-harmonic intensity for three different phase matching conditions depending on the propagation length. The red curve is ascribed to the situation of a non-zero phase mismatch. In contrast, the blue curve describes the conversion for perfect phase matching, here realised by birefringent phase matching processes. For quasi-phase matching (green), the efficiency is reduced assuming the same tensor strength.

Third-order QPM is given, when every third L_{coh} the spontaneous polarisation is inverted. More generally, modulating the crystal with a period of $2 \cdot m \cdot L_{\text{coh}}$, where m is an integer, this is called m -th order QPM. Even though the second-harmonic intensity for first-order QPM shown in figure 3.6 grows slower as for the birefringent case, the greatest advantage of QPM is the broader versatility of processes and the possibility to use the d_{33} coefficient in KTP and LNOI.

In a mathematical description the nonlinear coefficient d is a function of the propagation direction z . The green curve in figure 3.6 assumes the case of quasi-phase matching with periodic modulation of the nonlinear coefficient simplified by a square-wave function as [29]

$$d(z) = d_0 \cdot \text{sign} \left[\cos \left(\frac{2 \cdot \pi \cdot z}{\Lambda} \right) \right], \quad (3.63)$$

where Λ the poling period, corresponding to twice the coherence length

$$\Lambda = 2 \cdot L_{\text{coh}}. \quad (3.64)$$

The periodic spatial variation can be expressed in terms of a Fourier series

$$d(z) = d_0 \sum_{m=-\infty}^{\infty} G_m e^{i\beta_G z}, \quad (3.65)$$

where β_G is the grating vector given by

$$\beta_G = \frac{2 \cdot \pi \cdot m}{\Lambda}. \quad (3.66)$$

The Fourier coefficients G_m are given by [31]

$$G_m = \frac{2}{m \cdot \pi} \sin(m \cdot \pi \cdot D), \quad (3.67)$$

where D is the duty cycle defined as

$$D = \frac{l_{\text{poled}}}{\Lambda} \quad (3.68)$$

with l_{poled} as the length of the inverted spontaneous polarisation, see figure 3.13.

The coupled wave equations using the slowly varying amplitude approximation for the QPM case results in [29]

$$\frac{dA_3}{dz} = \frac{2 \cdot i \cdot d_{\text{eff}} \cdot \omega_3^2}{\beta_3 \cdot c^2} \cdot A_1 \cdot A_2 \cdot e^{-i \cdot \Delta\beta_{\text{QPM}} \cdot z}, \quad (3.69)$$

where d_{eff} the nonlinear coefficient according to

$$d_{\text{eff}} = d_0 \cdot G_m \quad (3.70)$$

and the wavevector mismatch for m -th order is given by

$$\beta_{\text{QPM}} = \beta_3 - \beta_2 - \beta_1 - \beta_G. \quad (3.71)$$

Comparing the coupled wave equation 3.69 for QPM with the previously introduced equation 3.56, both equations are formally identical, but involve modified values for the nonlinear coefficient and the wavevector mismatch.

For an optimum duty cycle the sine factor from equation 3.67 is unity. This results in a nonlinear coefficient of [31]

$$d_{\text{eff}} = \frac{2}{m \cdot \pi} \cdot d_0. \quad (3.72)$$

Therefore, the conversion intensity, which is formally analogous to equation 3.59, is given by

$$I_{\text{QPM}} = \frac{8 \cdot d_{\text{eff}}^2 \cdot \omega_3^2 \cdot I_1 \cdot I_2}{n_1 \cdot n_2 \cdot n_3 \cdot \epsilon_0 c^2} \cdot L^2 \cdot \text{sinc}^2\left(\frac{\Delta\beta_{\text{QPM}} \cdot L}{2}\right) = \left(\frac{2}{m \cdot \pi}\right)^2 I_3 \quad (3.73)$$

and thus, the intensity is reduced by $\left(\frac{2}{m \cdot \pi}\right)^2$ compared to a birefringent phase matched efficiency.

The highest intensity can be achieved for an odd number of $m=1$. For this condition an optimum duty cycle is given for 50 % ($D = 0.5$).

To find the correct poling period for a given process, one can solve the phase matching equation 3.71, i.e. set $\beta_{\text{QPM}} = 0$ find β_G and thus, Λ . Given a specific process with known wavelength the period for the modification of the nonlinear medium can be calculated from

$$\Delta\beta_{\text{QPM}} = 0 = 2\pi \left(\frac{n_1(\lambda_1)}{\lambda_1} + \frac{n_2(\lambda_2)}{\lambda_2} - \frac{n_3(\lambda_3)}{\lambda_3} - \frac{m}{\Lambda} \right). \quad (3.74)$$

$$\Rightarrow \Lambda = \frac{m}{\frac{n_1(\lambda_1)}{\lambda_1} + \frac{n_2(\lambda_2)}{\lambda_2} - \frac{n_3(\lambda_3)}{\lambda_3}}. \quad (3.75)$$

By periodically poling the material with the period Λ we can realise many different of processes. One method to fully explore the potentials of a material is to do dispersion engineering.

3.2.4 Quantum Dispersion Engineering

Dispersion engineering is a valuable tool that allows for modification of the dispersion properties by changing the waveguide geometry or refractive index modification. It can be used for engineering and optimising sources for quantum optical applications, such as the generation of pure heralded single photons at telecom wavelengths for quantum communication [16]. The heart of many quantum optical experiments is parametric down-conversion [32], a genuine quantum process that is often harnessed for generating photon pairs and, where we can detect one photon to herald the second one.

3.2.4.1 Parametric Down-Conversion

Parametric down-conversion is a nonlinear quantum optical process and is a powerful approach to generate quantum states. By using dispersion engineering, the possibilities of PDC can be increased even further. For PDC one pump photon of energy $\hbar\omega_p$ decays into two daughter photons, namely signal and idler with energy $\hbar\omega_s$ and $\hbar\omega_i$, such that energy is conserved $\hbar\omega_p = \hbar\omega_s + \hbar\omega_i$. At the same time momentum conservation $\Delta\beta(\omega_s, \omega_i) = \beta_p(\omega_s + \omega_i) - \beta_s(\omega_s) - \beta_i(\omega_i) - \beta_{\text{QPM}}$ has to be satisfied.

PDC can be described by the semi-classical Hamiltonian [33]

$$\hat{H} = C \int \int d\omega_s d\omega_i f(\omega_s, \omega_i) \hat{a}_s^\dagger(\omega_s) \hat{a}_i^\dagger(\omega_i) + h.c., \quad (3.76)$$

where C is a coupling constant related to the conversion efficiency of the process [34] and $f(\omega_s, \omega_i)$ is the joint spectral amplitude (JSA) describing the spectral correlations of the down-converted photon pair with a classical pump field. The operators $\hat{a}_s^\dagger, \hat{a}_i^\dagger$ are

the photon creation operators for signal and idler.

The JSA is related to the purity of heralded photons and the best way to visualise the properties of a source depending on the phase matching and the pump. It is possible to tailor the phase matching condition, by waveguide engineering and therefore, modifying the effective refractive index of a material due to diffusion or changes in the geometry of the waveguide. Therefore, one needs to figure out first, what are interesting objectives in the JSA and then how to modify it through dispersion engineering.

3.2.4.2 Joint Spectral Amplitude

In a PDC process the momentum and energy conservation between the three interacting fields define the spectral properties of the generated photon pair. These spectral properties can be described by the joint spectral amplitude function. The JSA $f(\omega_s, \omega_i)$ is the product of the pump envelope function $\alpha(\omega_s + \omega_i)$ and the phase matching function $\Phi(\omega_s, \omega_i)$ [35]

$$f(\omega_s, \omega_i) = \alpha(\omega_s + \omega_i) \cdot \Phi(\omega_s, \omega_i). \quad (3.77)$$

The pump envelope function represents the energy conservation condition $\hbar\omega_p = \hbar\omega_s + \hbar\omega_i$ and describes the spectral amplitude of the pump beam [36]

$$\alpha(\omega_s + \omega_i) = e^{-\frac{(\omega_s + \omega_i - \omega_p)^2}{2\sigma^2}}, \quad (3.78)$$

where $\omega_p, \omega_s, \omega_i$ are the frequencies of the pump photon and the generated photons signal and idler. The pump is generally assumed to exhibit a Gaussian frequency spectrum with width σ .

The phase matching function depends on the momentum mismatch, the periodic poling and the length of the waveguide L and is given by

$$\Phi(\omega_s, \omega_i) = \text{sinc}\left(\frac{L \cdot \Delta\beta(\omega_s, \omega_i)}{2}\right) e^{-i\frac{L \cdot \Delta\beta}{2}}. \quad (3.79)$$

The pump, the phase matching and the JSA function can be directly evaluated in a two-dimensional representation plotted in the (ω_s, ω_i) frequency plane [37]. Figure 3.7 shows an example for the pump envelope function, the phase matching function and resulting JSA of a PDC process.

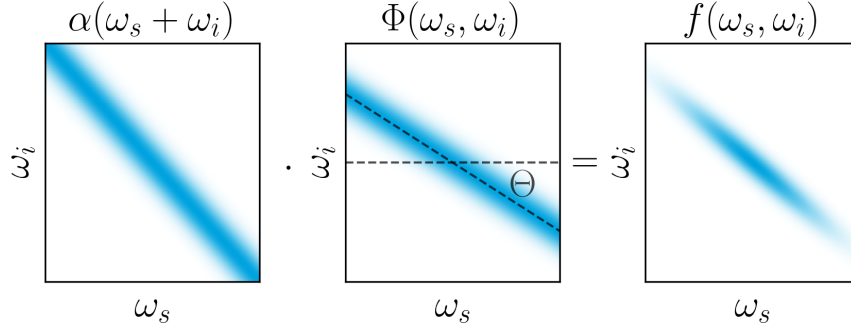


Figure 3.7 – Schematic illustration of the joint spectral amplitude for a PDC process. The JSA is a product of the pump envelope function and the phase matching function. The latter is determined by the used phase matching processes and the dispersion of the used system.

The angle of the pump envelope function is always aligned along -45° due to energy conservation, while the width of the function is given by the spectral width of the applied pump laser. On the other hand, the width of the phase matching function is given by the length of the nonlinear crystal and the angle Θ for PDC is defined by [38]

$$\Theta = -\arctan\left(\frac{v_{g,p}^{-1} - v_{g,s}^{-1}}{v_{g,p}^{-1} - v_{g,i}^{-1}}\right), \quad (3.80)$$

where $v_{g,p/s/i} = \left[\frac{\partial \beta_{p/s/i}}{\partial \omega_{p/s/i}}\right]^{-1}$ is the group velocity of pump, signal and idler, respectively.

The objective of device engineering is to specifically design a sources with a desired two-photon spectrum, e.g., the implementation of a quantum pulse gate (QPG) [39]. This is possible by engineering the angle of the phase matching function, the sample length and the pump bandwidth. While the last two can be chosen rather freely, the first one is extremely dependent on the material and waveguide geometry. Among all possible PDC processes, the most interesting ones are the spectrally decorrelated ones, as they allow for the generation of pure heralded single photons. It can be shown that these states can be obtained for two different group velocities configurations [40], namely symmetric group velocity matching (sGVM) and asymmetric group velocity matching (aGVM).

In the case of sGVM the group velocity of the pump field lies equidistant between the group velocities of signal and idler. This results in an angle of the phase matching function of $+45^\circ$ [41]. In addition to being decorrelated, PDC photons generated with sGVM can be also spectrally indistinguishable if they are spectrally degenerate [16], i.e. they have the same central wavelength. The decorrelation facilitates the generation of spectrally pure heralded single photons in short pulses, without the need for spectral filtering. This increases the source brightness significantly, because no filtering means no

additional losses. The indistinguishability, meaning the photons must have the same wavelength, polarisation, and temporal and spatial extent, is especially relevant in light of future quantum networks, where many photons should interfere and thus, need to be indistinguishable. Figure 3.8 shows an example of a symmetric group velocity matched PDC process.

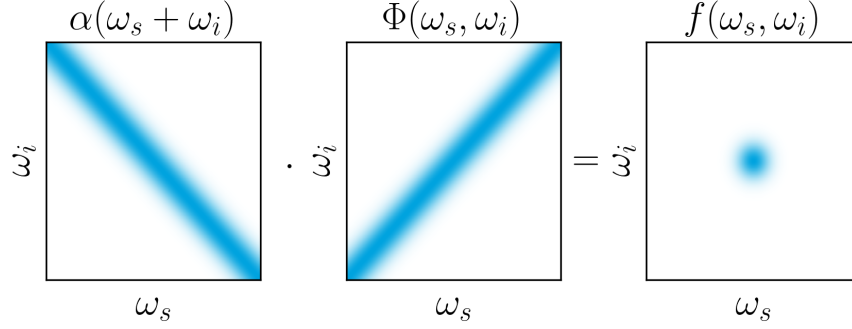


Figure 3.8 – Schematic of a joint spectral amplitude for a symmetric group velocity matched process. Here, the phase matching function exhibits an angle of -45° , resulting in a circular JSI shape.

For aGVM the group velocity of the pump field is equal to the group velocity of one of the other two fields. In this case, phase matching function is aligned with the respective axes and has an angle of 0° or 90° . Using the aGVM condition, it is possible to build sources of highly pure heralded single photons [42]. By spectrally shaping the pump pulses, used to drive these sources, it becomes possible to generate photons with programmable spectra, which can be adapted for multiple applications, e.g., optimum light-matter interaction, spectral information encoding or metrology tasks. Figure 3.9 shows an example of an asymmetric group velocity matched PDC process with an angle of 0° .

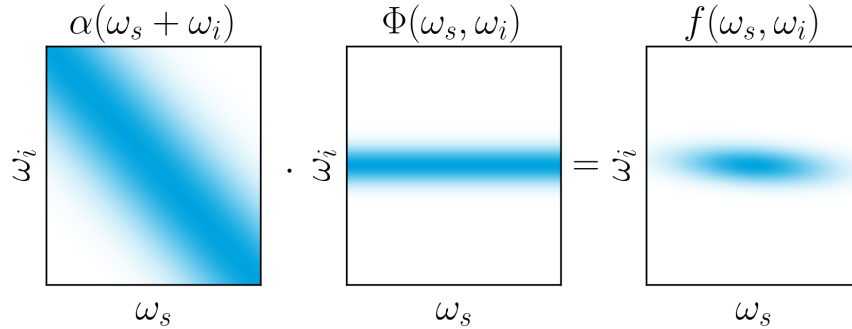


Figure 3.9 – Schematic of a joint spectral amplitude for an asymmetric group velocity matched process. Here, the phase matching function exhibits an angle of 0° , resulting in an elliptical JSI shape under 0° .

All these kinds of dispersion engineering can be realised in $\chi^{(2)}$ nonlinear materials. Therefore, we discuss in the following section two suitable materials with unique properties.

33 Nonlinear Materials

The material systems analysed in this thesis are lithium niobate on insulator (LNOI) and potassium titanyl phosphate (KTP), both with exceptional properties. They both possess a large optical nonlinearity and large electro-optic coefficients. Their broad transparent wavelength range and their potential for phase matching enables the possibility for various frequency generation process. Therefore, we present in this section the relevant properties of this material for this work. Moreover, we introduce the concept of phase matching in each material. Finally, we describe the types of waveguides for the different material systems and show theoretical models to describe the waveguides.

33.1 Potassium Titanyl Phosphate

Potassium titanyl phosphate (KTiOPO_4 , KTP) is a nonlinear material with an unique composition of properties that makes the material suitable for nonlinear optics. In 1890, Ouvrard was the first who synthesised it [43]. However, it was not until 1976 that Zumsteg et al. [44] discovered the optical nonlinearity of the material. KTP possesses a wide transparency range from 350 nm to 4500 nm [45] as well as large nonlinear optical coefficients [46]. Moreover, KTP features large electro-optical coefficients [46], which are necessary for electro-optic modulation and switching. In addition, the crystal has a high optical damage resistance and exhibits low photorefractive [47] allowing for high optical intensities inside the material even at room temperature. The realisation of waveguides in KTP, allows for nonlinear processes with high power density, large field overlap, and long interaction length. Furthermore, KTP displays a significant anisotropy in domain growth [48], which aids the periodic poling of small periods.

These characteristics are critical for efficient frequency conversion across the whole transparency range. In particular, the unique dispersion properties of KTP allow for the generation of separable decorrelated photon pairs at telecom wavelength [16]. This section provides an overview of the crystallographic structure, the optical properties and the feasibility for quasi-phase matching and waveguide fabrication.

33.1.1 Crystallographic Structure of KTP

Potassium titanyl phosphate belongs to the family of isomorphic compounds and its generic composition is described by the general formula MTiOXO_4 , where M can be potassium (K), rubidium (Rb), thallium (Tl), ammonium (NH_4) or caesium (Cs), while

X can be phosphorus (P) or arsenic (As). All crystals of this family possess an orthorhombic structure and belong to the space group $Pna2_1$ and to the non-centrosymmetric point group $mm2$ at room temperature [49], as initially specified by Tordjman et al. in 1974 [50].

The crystallographic structure was determined in 1971 by Masse and Grenier [51]. The lattice constants are $a = 12.819 \text{ \AA}$, $b = 6.399 \text{ \AA}$ and $c = 10.582 \text{ \AA}$, where c is the polar axis [52]. The crystallographic directions a , b , c correspond to the optical axes x , y , z [52]. Figure 3.10 shows the unit cell in a KTP lattice.

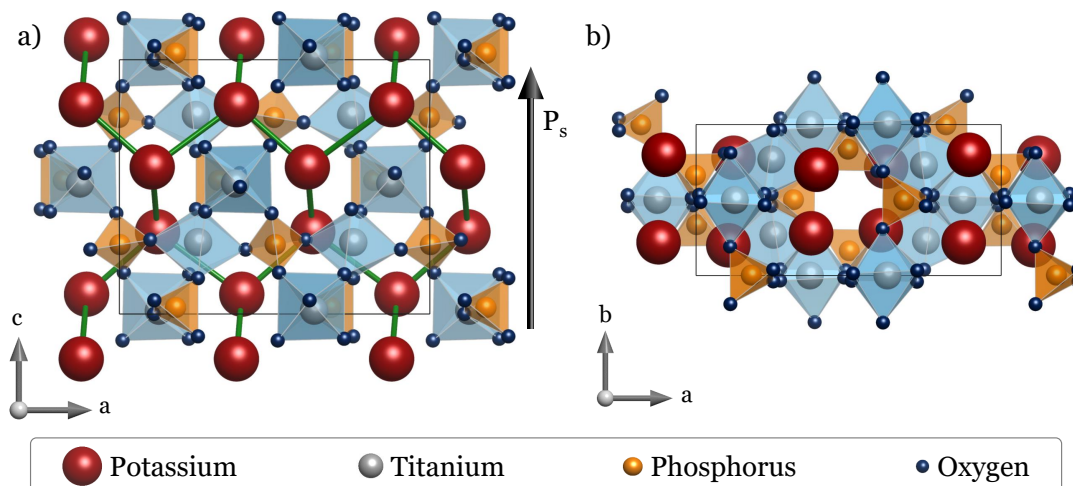


Figure 3.10 – Crystal structure of KTP. Here the a - c plane is depicted in a), indicating the permanent polarisation within the crystal. In b), the crystal structure is shown in its a - b plane. A comparison of the relative positions of all constituent species indicates that KTP in fact is a biaxial crystal [53].

The unit cell consists of 64 atoms divided into four subgroups of 16 atoms each. Each subgroup possesses two inequivalent sites for titanium, phosphorus and potassium atom and ten inequivalent sites for oxygen. The crystal contains helical chains of TiO_6 octahedra aligned along the $[011]$ and $[0\bar{1}1]$ directions and linked at two corners by alternately changing long and short $\text{Ti}(1)\text{--O}$ bonds [54]. The octahedra form a two dimensional network in the b - c plane and are interconnected by PO_4 tetrahedra. This particular arrangement of octahedra and tetrahedra creates quasi-one-dimensional channels along the c -axis. Such a channel is marked in green in figure 3.10. Inside these channels are two inequivalent cages, which are occupied by potassium. With respect to the oxygen, these are either eightfold or ninefold coordinated and denoted as $\text{K}(1)$ and $\text{K}(2)$, where the volume of cage $\text{K}(1)$ is 25 % larger as $\text{K}(2)$ [55]. The potassium ions are weakly bonded to both the octahedral and the tetrahedral groups and have an increased mobility inside the channels along the c -direction. Therefore, they provide special material properties, e.g., ionic conductivity or a large anisotropic domain growth.

Ionic Conductivity

Since stoichiometric KTP cannot be grown, it possesses a high concentration of K-vacancies, which allows the K-ions to move inside the quasi-one-dimensional channels. This hopping mechanism of the ions results in an ionic conductivity [56]. The conductivity along the c -directions is three orders of magnitude higher than in the other two directions [49].

When the crystal is exposed to a high voltage along the c -axis, this results in a non-negligible ionic conductivity, which is inhomogeneously distributed over the wafer, and hence, this affects the homogeneity and the quality of the QPM grating negatively. There are two techniques to achieve a permanent reduction of the ionic conductivity. One option is to perform a potassium treatment, in which the crystal is immersed in a pure potassium nitrate (KNO_3) bath. This decreases the amount of K-vacancies, which were formed during the crystal growth. The conductivity of the entire substrate is reduced and homogenised as a result of this procedure [57]. Another possibility to reduce the ionic conductivity is to insert larger ions, e.g., rubidium, inside the crystalline structure. This is independent of the Rb incorporation mechanism, e.g., crystal growth or ion-exchange [58]. The radius of the transported ion has a significant impact on ionic conductivity. Because the activation energy for hopping of larger ions is higher, the ionic conductivity is smaller in doped crystals compared to pure KTP [59].

The ionic conductivity of the material strongly depends on the concentration of the rubidium ions in the material. KTP possess a ionic conductivity in the order of $1 \cdot 10^{-5} \frac{\text{S}}{\text{cm}}$ [60]. With a small amount of rubidium doping (1.5 % of rubidium), the conductivity is reduced by one order of magnitude to $1 \cdot 10^{-6} \frac{\text{S}}{\text{cm}}$ [60]. Rubidium titanyl phosphate (RbTiOPO_4 ; RTP) has the highest possible amount of rubidium and therefore, has the lowest ionic conductivity with $1 \cdot 10^{-12} \frac{\text{S}}{\text{cm}}$ [48].

KTP and RbKTP

During this work we use RbKTP crystals, which are 1.5 % rubidium doped KTP. The general formula $\text{Rb}_x\text{K}_{(1-x)}\text{TiOPO}_4$ describes the amount of doping in the crystal. For $x = 0$ it is a pure KTP crystal and for $x = 1$ it forms a rubidium titanyl phosphate (RbTiOPO_4 ; RTP) crystal. In our case of RbKTP x is equal to 0.015.

RbKTP is commercially available and has similar transmission and nonlinear properties as flux-grown KTP [61]. Nonetheless, the ionic conductivity is lower and therefore, aids the homogeneity of the poling. Since there is no distinct variation of the optical properties and fabrication process of waveguides or periodic poling, we use KTP for describing the properties and use their notation interchangeable.

33.12 Optical Properties of KTP

To predict and fabricate samples for specific applications it is necessary to know the optical properties of a material. KTP has a wide transparency window ranging from UV to IR with cut-off limits at 350 nm and 4500 nm [62]. Moreover, we need to know the dispersion properties and the nonlinear coefficients.

Dispersion Properties

To correctly design QPM processes, it is necessary to know the dependence of the refractive index of a material from the wavelength of the incident light, i.e. the dispersion properties of the material. KTP is a biaxial birefringent material and the refractive index n can be describes in the form of a Sellmeier equation as [63]

$$n_i^2(\lambda) = A + \frac{B}{\lambda^2 - C} + \frac{D}{\lambda^2 - E}. \quad (3.81)$$

Here λ is the wavelength in μm and A, B, C, D and E are the Sellmeier coefficients. The Sellmeier coefficients are listed in table 3.1.

Table 3.1 – Sellmeier coefficients for KTP crystals [63].

	A	B	C	D	E
n_x	3.29100	0.04140	0.03978	9.35522	31.45571
n_y	3.45018	0.04341	0.04597	16.98825	39.43799
n_z	4.59423	0.06206	0.04763	110.80672	86.12171

The fact that refractive indices change very little with temperature indicates that they are not critically temperature dependent [54].

Optical Nonlinearity

KTP is a non-centrosymmetrical crystal and thus, possesses second order nonlinearity. Moreover, KTP belongs to the crystal class $mm2$ and the nonlinear tensor described by equation 3.52 simplifies to

$$d = \begin{pmatrix} 0 & 0 & 0 & 0 & d_{15} & 0 \\ 0 & 0 & 0 & d_{24} & 0 & 0 \\ d_{31} & d_{32} & d_{33} & 0 & 0 & 0 \end{pmatrix}. \quad (3.82)$$

The values for the nonlinear coefficient in KTP are given in table 3.2

Table 3.2 – Nonlinear coefficients for KTP for different wavelengths. All values are in $\frac{\text{pm}}{\text{V}}$.

Wavelength	d_{31}	d_{32}	d_{33}	d_{24}	d_{15}
532 nm [64]	1.4	2.65	10.7	2.65	1.4
1064 nm [65]	2.4	4.4	16.9	7.9	6.1

The allowed processes in KTP depending on the polarisation of the involved fields given by the tensor in equation 3.82 are

- type 0 - all the three fields have the same polarisation along z-direction ($zz \rightarrow z$)
- type I - the two input fields are polarised along x-direction and result in a field, which is polarised along the z-direction ($xx \rightarrow z$)
- type I - the two input fields are polarised along y-direction and result in a field, which is polarised along the z-direction ($yy \rightarrow z$)
- type II - the two input fields are polarised along y- and z-direction and result in a field, which is polarised along the y-direction ($yz \rightarrow y$)
- type II - the two input fields are polarised along x- and z-direction and result in a field, which is polarised along the x-direction ($xz \rightarrow x$)

To achieve these processes, we need to fulfil energy and momentum conservation. For the phase matching conservation we would like to use quasi-phase matching, which can be achieved by periodic poling of the material.

3.3.13 Periodic Poling of KTP

The necessity of phase matching and the concept of quasi-phase matching was explained in section 3.2.3.2. One possibility to achieve QPM is via periodic poling of the material. In the following, we will describe the fundamental aspects necessary for periodic poling, namely the formation of the spontaneous polarisation, polarisation reversal and ferroelectric domains.

Spontaneous Polarisation

KTP is at room temperature, and below the Curie temperature of $\approx 945^\circ\text{C}$, a ferroelectric crystal. The crystal is non-centrosymmetric and hence, possesses a spontaneous polarisation and a $\chi^{(2)}$ nonlinearity along the c -direction. The spontaneous polarisation is formed by the sum of all dipole moments in each unit cell. This means that the ions must be in a non-symmetrical position inside the unit cell. The origin of the spontaneous polarisation in KTP is still not fully understood yet. There exist two main

theories to explain the spontaneous polarisation in KTP. As explained in the last chapter the unit cell of KTP consists of TiO_6 octahedra linked at two corners by alternately changing long and short Ti–O bonds. The displacement of the Ti atoms introduces a dipole moment along the c axis and therefore, a spontaneous polarisation, which is responsible for the nonlinearity [44]. The second source for the nonlinearity is attributed to the various K–O bonds and PO_4 groups [66]. The calculated chemical bonds in KTP indicate that not only the Ti–O bonds contribute to the spontaneous polarisation, but all constituent chemical bonds do. Until now, it is still unknown, which factor has the highest influence on the nonlinear characteristics.

Polarisation Reversal

Ferroelectric materials like KTP possess a spontaneous polarisation and it can be reversed, e.g., by applying an external electric field. A reversal of the spontaneous polarisation in KTP corresponds to a reversal of the crystallographic structure. Since the spontaneous polarisation is linked to the Ti–O bonds, a reversal changes the short Ti–O bonds to long and vice versa [67]. Moreover, the alkali (potassium or rubidium) ions shift along the z-direction, the ninefold coordinated ions become eightfold coordinated and vice versa.

The polarisation reversal in ferroelectric materials depends on the strength of the applied electric field and is usually described using a hysteresis loop, which is shown in figure 3.11.

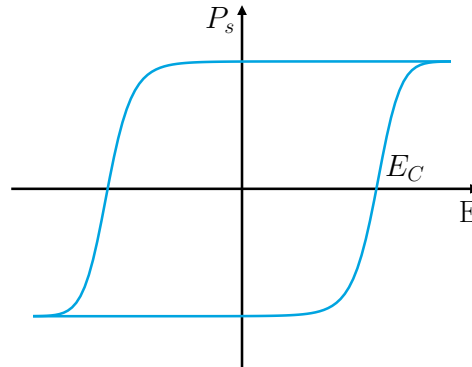


Figure 3.11 – Hysteresis loop of the spontaneous polarisation of a ferroelectric material. The spontaneous polarisation is inverted above the coercive field strength E_C . At vanishing applied fields, the system remains in either one of two polarisation states with inverted sign.

At zero applied electric field, the polarisation has two possible values, corresponding to the opposite orientations of the spontaneous polarisation. If we apply a small electric field to the crystal the material behaves like an ordinary dielectric, but the spontaneous polarisation can be reversed, if one exceeds the so called coercive field strength E_C . The

coercive field strength is defined as the field, at which half of the polarisation is reversed. This is an important parameter for periodic poling and the value is determined by the vacancies of the potassium ions, impurities and the amount of doping with rubidium ions [48]. For KTP the coercive field strength is $2.1 \frac{\text{kV}}{\text{mm}}$ [48] and for RbKTP it is $4.2 \frac{\text{kV}}{\text{mm}}$ [68].

Further investigations showed that a double inversion of the spontaneous polarisation before the actual periodic poling results in a reduction of the coercive field strength. In the following, we refer to this procedure as preconditioning, in which the spontaneous polarisation is switched back and forth once, which corresponds to a complete hysteresis cycle. After preconditioning the coercive field strength in KTP reduces to $1.7 \frac{\text{kV}}{\text{mm}}$ [68], whereas RbKTP reduces after preconditioning to $3.6 \frac{\text{kV}}{\text{mm}}$ [68].

Ferroelectric Domains

A ferroelectric domain is a region in a crystal, which has a uniformly oriented spontaneous polarisation. The border of two domains, in which the spontaneous polarisations are oriented differently, is called domain wall. The crystalline structure is disturbed by a domain wall in a narrow region. Figure 3.12 shows two domains with opposite spontaneous polarisation indicated as arrows and separated by a domain wall.

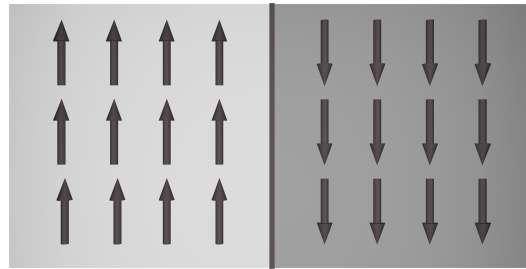


Figure 3.12 – Schematic representation of two domains with opposite spontaneous polarisation. The polarisation in each domain is indicated by arrows. The domains are separated by a so called domain wall.

The angle between the orientation of the spontaneous polarisation of neighbouring domains characterises the domain walls. During this thesis we only refer to domains with 180° domain walls, meaning a 180° inversion of the spontaneous polarisation.

In general, the polarisation reversal by an applied electric field starts with nucleation points, which are nano-domains. These domains are crystalline regions with nanometric dimension, possessing opposite polarisation as the surrounding area. These nucleation points grow and form new antiparallel domains. As many domains grow, they merge and form even larger domains. The domains can grow along the z -axis as well

as on the other two axis. The sideways motion of the domains is referred as domain broadening. Due to the crystallographic structure the domain formation speed along the z-axis is two orders of magnitude larger than along the other two directions. This is equally true for the anisotropy of ionic conductivity. The domain growth speed along the y-direction is 30 times larger than along the x-axis [48]. This anisotropy of the domain growth allows for the fabrication of small domains without huge domain broadening and therefore, it allows for short poling periods.

Periodic Poling

To achieve QPM the nonlinearity and thus, the spontaneous polarisation has to be inverted periodically. This is possible by a periodically structured contact while applying an electric field. This periodic contact is defined by the poling period given in equation 3.75. We use KTP z-cut, which is defined by the axis perpendicular to the largest sample surface. The material is poled with a periodic pattern on the -z-surface due to the enhanced domain nucleation on this side and a full contact on the +z-surface.

As described in section 3.2.3.2 the highest conversion intensity is achieved with a duty cycle of 0.5, which corresponds to a ratio of 1:1 for the initial domain to the inverted domain. Figure 3.13 shows the poling period and the domains for a perfect duty cycle of 1:1.

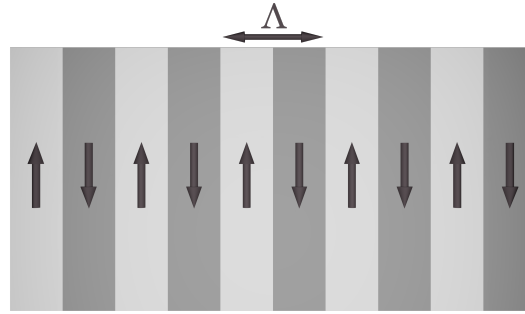


Figure 3.13 – Schematic representation of periodically inverted system. Here the spontaneous polarisation is inverted periodically with a period Λ and a duty cycle of 1:1.

Since the domain growth is the slowest along the x-axis and thus, mostly controllable during periodic poling, it is favourable to use the x-direction as the propagation axis for waveguides in KTP.

3.3.1.4 Waveguides in KTP

A major advantage of waveguides for nonlinear processes over bulk crystals is the strong confinement of the modes and therefore, a high field overlap over a long interaction

length. For the confinement it is necessary to have an increased refractive index inside the waveguide. Local exchange of alkali ions in molten nitrates, e.g., rubidium, caesium or thallium, in the KTP crystal, allows for the increasing of the refractive index in the exchanged regions and therefore, waveguiding [69]. A rubidium-potassium exchange in a KTP crystal is used to produce the waveguides in this work. As described in section 3.3.1.1 there are two inequivalent sites for the potassium ions. The rubidium ions with a larger radius than potassium ions preferentially occupy the larger K(2) cage [49].

Modelling of Exchanged Waveguides

The rubidium-potassium exchange takes place in a rubidium nitrate melt, which represents an infinite bath. The diffusion of the rubidium ions can be described by Fick's first law with the diffusion current density $j(z)$ as [70]

$$j(z) = -D \cdot \nabla c(z). \quad (3.83)$$

The concentration of the in-diffused rubidium ions is $c(z)$ and D is the diffusion coefficient. The minus sign denotes that diffusion is happening from high to low concentrations. The temporal change in the concentration in a particular region is depending on the divergence of the particle currents flowing in and out of a volume is described by the continuity equation

$$\frac{\partial c}{\partial t} + \nabla \vec{j} = 0. \quad (3.84)$$

Inserting Fick's first law into the continuity equation yields Fick's second law as

$$\frac{\partial c}{\partial t} = \nabla (D \cdot \nabla c(z)), \quad (3.85)$$

where t is the exchange time and z the exchange depth. If the diffusion coefficient D is concentration-dependent, the equation must be written in one dimension as the following [70]:

$$\frac{\partial c}{\partial t} = \frac{\partial}{\partial z} \left(D \cdot \frac{\partial c}{\partial z} \right). \quad (3.86)$$

If we assume a diffusion coefficient independent of the concentration, we can simplify equation 3.86 to

$$\frac{\partial c}{\partial t} = D \cdot \frac{\partial^2 c}{\partial z^2}. \quad (3.87)$$

When considering an infinite bath, it is reasonable to suppose that there are enough rubidium ions present to keep the concentration of the bath constant. Thus, the concentration c_0 at the interface between crystal and melt at $z = 0$ does not change

$$c(z = 0, t) = c_0. \quad (3.88)$$

Moreover, the initial concentration at the beginning of the diffusion should be

$$c(z, t = 0) = 0. \quad (3.89)$$

If we solve the diffusion equation 3.87, we obtain [71]

$$c(z, t) = c_0 \cdot \operatorname{erfc}\left(\frac{z}{2 \cdot \sqrt{D \cdot t}}\right) = c_0 \cdot \operatorname{erfc}\left(\frac{z}{d}\right), \quad (3.90)$$

where $d = 2 \cdot \sqrt{D \cdot t}$ is the well-known penetration depth.

The in-diffusion of rubidium ions increases the refractive index in the doped region. The simplest model proposed to describe Rb diffusion in KTP is a linear dependence of the refractive index on the rubidium concentration described in equation 3.90. This leads to a refractive index increase Δn_{wg} described by

$$\Delta n_{\text{wg}}(y, z, \lambda) = \Delta n_0(\lambda) \cdot \Pi_{\left[-\frac{w}{2}, \frac{w}{2}\right]}(y) \cdot \operatorname{erfc}\left(\frac{z}{d}\right), \quad (3.91)$$

where Δn_0 is the refractive index increase at the surface and $\Pi_{\left[-\frac{w}{2}, \frac{w}{2}\right]}$ is a box function with width w along the y-direction. However, it was known that this model was only a rough approximation [44]. Later on, we will discuss our findings, which improve upon this model.

We describe the refractive index of our waveguides n_{wg} by adding the refractive index increase due to the waveguide to refractive index of bulk KTP n_{bulk} and get [72]

$$n_{\text{wg}}(y, z, \lambda) = n_{\text{bulk}} + \Delta n_{\text{wg}}(y, z, \lambda) \quad (3.92)$$

$$n_{\text{wg}}(y, z, \lambda) = n_{\text{bulk}} + \Delta n_0(\lambda) \cdot \Pi_{\left[-\frac{w}{2}, \frac{w}{2}\right]}(y) \cdot \operatorname{erfc}\left(\frac{z}{d}\right). \quad (3.93)$$

We use a model for $\Delta n_0(\lambda)$ provided by Callahan et al. [72] as

$$\Delta n_0(\lambda) = A + B \cdot \lambda + C \cdot \lambda^2 + F \cdot e^{-\frac{\lambda \cdot 10^3 - 350}{G}}, \quad (3.94)$$

with the parameters given in table 3.3 with λ in μm .

Table 3.3 – Sellmeier coefficients for the refractive index increase of Rb-exchanged waveguides in KTP [73].

	A	B	C	F	G
Δn_y	26.76947	-10.9737	2.29268	$2.24595 \cdot 10^{-2}$	44.62477
Δn_z	29.0816	-6.5850	2.13894	$9.60547 \cdot 10^{-3}$	39.20047

It has to be noted that the equation 3.94 and the parameters have been modified by Dr. M. Santandrea [73]. Moreover, it has to be noted that this model is the only model provided in literature. We use this model, but one has to be aware that deviations might occur, due to fabrication differences.

33.2 Lithium Niobate On Insulator

In the past few years a new material platform, called lithium niobate on insulator (LNOI), had enormous progress in the fabrication of nano-structured elements. LNOI became commercial available in the last few years and is a thin-film of lithium niobate (LiNbO_3 , LN) on an insulator layer of silicon dioxide (silica, SiO_2) and a handle [74]. Figure 3.14 shows the layer stack of LNOI.

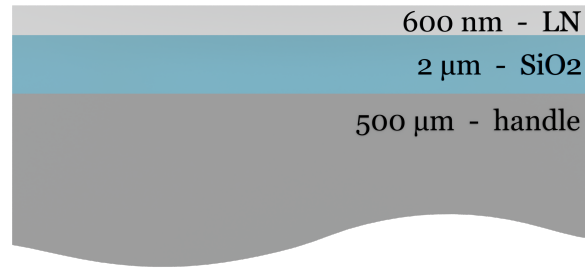


Figure 3.14 – Schematic representation of the layer stack of LNOI. The typically used three layer system consists of a thick handle substrate, an insulating layer of SiO_2 and the lithium niobate thin-film.

Lithium niobate was first reported by Zachariasen in 1928 [75] and its ferroelectric properties were discovered in 1949 by Matthias and Remeika [76]. Due to its remarkable electro-, nonlinear-, and acousto-optic properties, as well as its large transparency window and relatively high refractive index, LN is one of the most versatile and appealing materials for photonics [77].

Besides the unique optical properties, LNOI provides the possibility for high mode confinement and low bending radii due to the high refractive index contrast between the thin-film and the insulator/air. For this reason, the LNOI platform is an excellent choice for integrated quantum optical applications. Furthermore, because the effective refractive index is highly dependent on the waveguide geometry due to the high mode confinement, it provides a lot of possibilities for dispersion engineering. Within the past few years, the first photon pair sources have been developed in LNOI [78–80].

LNOI is commonly fabricated via a smart cut technique. In the first step a cleavage plane is defined by a high dose implantation of He^+ ions. After that, the crystal is bonded upside down to a SiO_2 coated handle. During thermal annealing the substrates split along the cleavage plane and defining the thin-film of LN. Ion-implanted crystal defects are reduced due to an additional annealing step [74].

Since all the light-matter interaction will happen in the thin-film of lithium niobate, the optical properties of conventional lithium niobate are comparable to LNOI. Therefore, we introduce in the following the crystallographic and optical properties of LN. More-

over, we give an insight into periodic poling and waveguide fabrication in LNOI.

3.3.2.1 Crystallographic Structure of LN

Lithium niobate belongs to the trigonal crystal class and exhibits a three-fold rotation symmetry along the crystallographic and optical c -axis. The crystallographic a - and b -axes are perpendicular to the c -axis and form a 120° angle. LN is a member of the point group $3m$ and the space group $R3c$ [81]. The lattice constants are $a = 5.148 \text{ \AA}$, $b = 5.148 \text{ \AA}$ and $c = 13.863 \text{ \AA}$ [82]. Figure 3.15 shows the unit cell in a LN lattice and the 120° degree angle between the crystallographic axes a and b .

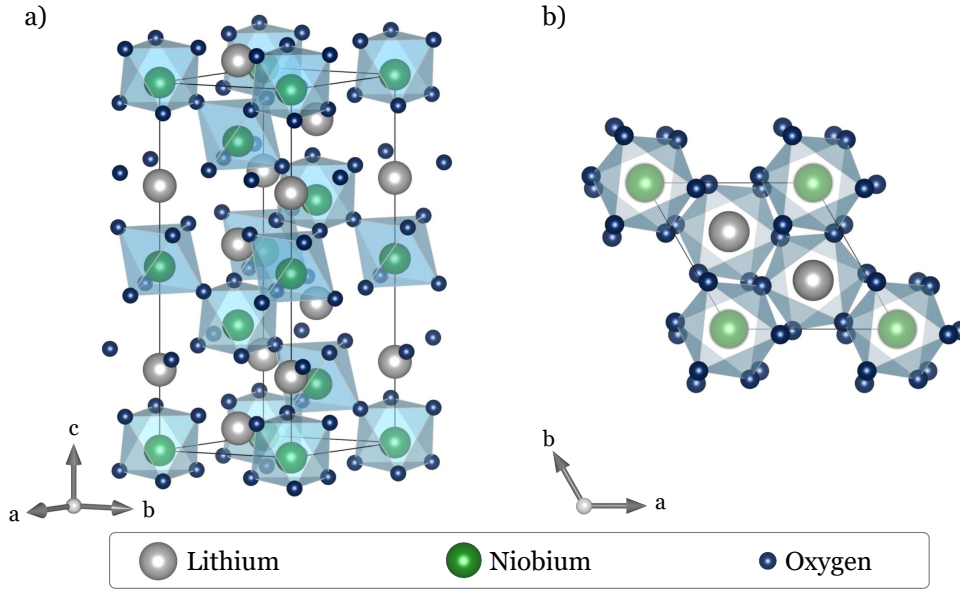


Figure 3.15 – a) Schematic of the crystal structure of lithium niobate. b) Atomic positions indicated within the a - b plane. The sequence of atomic positions within the a - and b -direction is identical, whereas it differs significantly from the c -axis. Consequently, the LN is an uniaxial crystal [53].

The unit cell of LN consists of lithium, niobium and oxygen atoms. These atoms are arranged in an alternating pattern along the c -axis, sequentially Nb^{5+} - Li^+ - vacancy - Nb^{5+} - Li^+ - ... [81]. Each Nb^{5+} is surrounded by six oxygen atoms organised in a slightly distorted octahedra. The NbO_6 octahedra share oxygen atoms diagonally at their corners, resulting in a hexagonal unit cell with 16 octahedra.

In this thesis we use congruent lithium niobate and magnesium oxide (MgO) doped lithium niobate. The congruent lithium niobate has a slight lithium deficiency with a Li/Nb ratio of 0.94553 compared to the stoichiometric material ($=1$). In case of MgO

doped material magnesium ions replace the niobium and lithium sites simultaneously [83].

3.3.2.2 Optical Properties of LN

Analogous to KTP it is necessary to know the optical properties of LN. Lithium niobate possesses comparable to KTP a wide transparency window ranging from UV to IR with cut-off limits at 320 nm and 5000 nm [84]. In the following, we introduce the dispersion properties and the nonlinear coefficients of LN.

Dispersion Properties

Lithium niobate is a uniaxial birefringent material and the extraordinary refractive index n_e is along the crystallographic c -axes and corresponds to the optical z -axis. It can be described by [85]

$$n_e^2(\lambda, T) = A_{1,e} + B_{1,e} \cdot f + \frac{A_{2,e} + B_{2,e} \cdot f}{\lambda^2 - (A_{3,e} + B_{3,e} \cdot f)^2} + \frac{A_{4,e} + B_{4,e} \cdot f}{\lambda^2 - A_{5,e}^2} - A_{6,e} \cdot \lambda^2, \quad (3.95)$$

where λ is the wavelength in μm , $A_{i,e}, B_{i,e}$ are the Sellmeier coefficients and $f = (T - 24.5)(T + 570.82)$ is a function of the temperature T in degree Celsius. The ordinary refractive index n_o of LN is characterised by [86]

$$n_o^2(\lambda, T) = A_{1,o} + \frac{A_{2,o} + B_{1,o} \cdot F}{\lambda^2 - (A_{3,o} + B_{2,o} \cdot F)^2} + B_{3,o} \cdot F - A_{4,o} \cdot \lambda^2, \quad (3.96)$$

where $F = (T - 24.5)(T + 549)$ and the wavelength λ is in μm .

The Sellmeier coefficients of congruent LN for equations 3.95 and 3.96, and the Sellmeier coefficients for 5 % MgO doped LN for equation 3.95 are presented in table 3.4.

Table 3.4 – Sellmeier coefficients for congruent LN crystals [85, 86] and for 5 % MgO doped LN [87].

n_0	congruent LN	5 % MgO doped LN	n_e	congruent LN	5 % MgO doped LN
$A_{1,o}$	4.9048	5.653	$A_{1,e}$	5.35583	5.756
$A_{2,o}$	0.11775	0.1185	$A_{2,e}$	0.100473	0.0983
$A_{3,o}$	0.21802	0.2091	$A_{3,e}$	0.20692	0.2020
$A_{4,o}$	0.027153	89.61	$A_{4,e}$	100	189.32
$A_{5,o}$	-	10.65	$A_{5,e}$	11.3493	12.52
$A_{6,o}$	-	$1.97 \cdot 10^{-2}$	$A_{6,e}$	$1.5337 \cdot 10^{-2}$	$1.32 \cdot 10^{-2}$
$B_{1,o}$	$2.2314 \cdot 10^{-8}$	$7.941 \cdot 10^{-7}$	$B_{1,e}$	$4.6390 \cdot 10^{-7}$	$2.860 \cdot 10^{-6}$
$B_{2,o}$	$-2.9671 \cdot 10^{-8}$	$3.134 \cdot 10^{-8}$	$B_{2,e}$	$3.8620 \cdot 10^{-8}$	$4.7 \cdot 10^{-8}$
$B_{3,o}$	$2.1429 \cdot 10^{-8}$	$-4.641 \cdot 10^{-9}$	$B_{3,e}$	$-8.9 \cdot 10^{-9}$	$6.113 \cdot 10^{-8}$
$B_{4,o}$	-	$-2.188 \cdot 10^{-6}$	$B_{4,e}$	$2.657 \cdot 10^{-5}$	$1.516 \cdot 10^{-4}$

Optical Nonlinearity

Lithium niobate is a non-centrosymmetric crystal. It possesses a second order nonlinearity and belongs to the crystal class $3m$. Consequently the nonlinear tensor is defined as

$$d = \begin{pmatrix} 0 & 0 & 0 & 0 & d_{31} & -d_{22} \\ -d_{22} & d_{22} & 0 & d_{31} & 0 & 0 \\ d_{31} & d_{31} & d_{33} & 0 & 0 & 0 \end{pmatrix}. \quad (3.97)$$

The values for the nonlinear coefficient are given in table 3.5

Table 3.5 – Nonlinear coefficients for LN. All values are in $\frac{\text{pm}}{\text{V}}$.

Wavelength	d_{33}	d_{31}	d_{22}
1064 nm [88]	27.2	4.35	2.1

In LN the allowed processes are

- type 0 - all the three fields have the same polarisation along z-direction (zz \rightarrow z)
- type 0 - all the three fields have the same polarisation along y-direction (yy \rightarrow y)
- type I - the two input fields are polarised along x-direction and result in a field, which is polarised along the y-direction (xx \rightarrow y)
- type I - the two input fields are polarised along x-direction and result in a field, which is polarised along the z-direction (xx \rightarrow z)
- type I - the two input fields are polarised along y-direction and result in a field, which is polarised along the z-direction (yy \rightarrow z)
- type II - the two input fields are polarised along y- and z-direction and result in a field, which is polarised along the y-direction (yz \rightarrow y)
- type II - the two input fields are polarised along x- and z-direction and result in a field, which is polarised along the x-direction (xz \rightarrow x)
- type II - the two input fields are polarised along x- and y-direction and result in a field, which is polarised along the x-direction (xy \rightarrow x)

In LN it is possible to achieve these processes via quasi-phase matching and therefore, periodic poling of the material.

33.23 Periodic Poling of LNOI

One possibility to achieve quasi-phase matching in LNOI is periodic poling of the material, exploiting its ferroelectric properties. The formation of the spontaneous polarisation and the polarisation reversal in LN, will be described in the following part.

Spontaneous Polarisation

Below the Curie temperature of $\approx 1150^\circ\text{C}$ [89] and thus, at room temperature LN is a ferroelectric crystal and possesses a spontaneous polarisation along the c -axis. The spontaneous polarisation is created by a slightly shifted position of the lithium and niobium atoms along the c -axis with respect to the oxygen octahedra. This leads to a non-inversion symmetry and therefore, to spontaneous polarisation of the crystal. Figure 3.16 shows the position of the Li^+ and Nb^{5+} ions, which are slightly shifted from the centres of the oxygen planes.

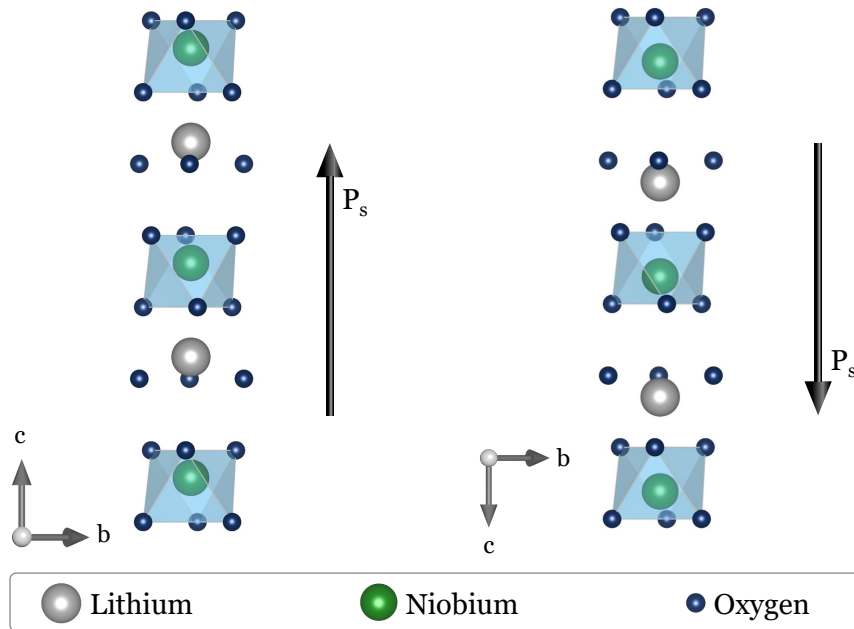


Figure 3.16 – Schematic representation of the differently polarised domains in LN. Depending on the direction of the positions of the lithium and niobium atoms with respect to the oxygen octahedra, a different sign of the spontaneous polarisation is induced [53].

Polarisation Reversal

Since LN is a ferroelectric crystal, an external electric field can be used to invert the spontaneous polarisation. By applying an electric field along the z-direction higher than the coercive field strength, the lithium and niobium atoms are displaced in the direction of the electrical field. This results in a reversal of the crystallographic structure and therefore, a reversal of the spontaneous polarisation in LN.

For conventional z-cut LN, periodic poling is a well-established method. Electric field pulses are applied to a periodic structure on the +z-surface. However, new strategies had to be created due to the unique structure of LNOI, which made the use of traditional poling approaches difficult. We use x-cut LNOI, which can be poled with a pair of periodic electrodes on the +x-surface, to invert the domains along the z-direction.

As introduced in section 3.3.1.3, the applied electric field has to be higher than the coercive field strength of the material. The coercive field strength required for poling varies with the material composition and is for lithium niobate $21 \frac{\text{kV}}{\text{mm}}$ [90]. Doping with 5 mol% MgO decreases the required coercive field to $6.8 \frac{\text{kV}}{\text{mm}}$ [91]. Thin-film x-cut LNOI has been shown to require a larger coercive field than bulk crystals of the same material around $30\text{--}48 \frac{\text{kV}}{\text{mm}}$ for both undoped and doped LNOI [92–95]. The origin of the increased field could be due to Li^+ out-diffusion within annealing during the LNOI fabrication [96], because the coercive field increases with decreasing Li^+ concentration. Another assumption for the increased coercive field is due to the bonding interface between the thin-film LN and the SiO_2 insulation layer [95] the domain inversion gets hindered.

3.3.2.4 Waveguides in LNOI

The high refractive index contrast in LNOI revolutionised the conventional lithium niobate platform with titanium in-diffused weakly confined waveguides. Large-scale implementation necessitates the high-density integration of compact and low-loss nano-structured components, which development in LNOI started only about a decade ago [96].

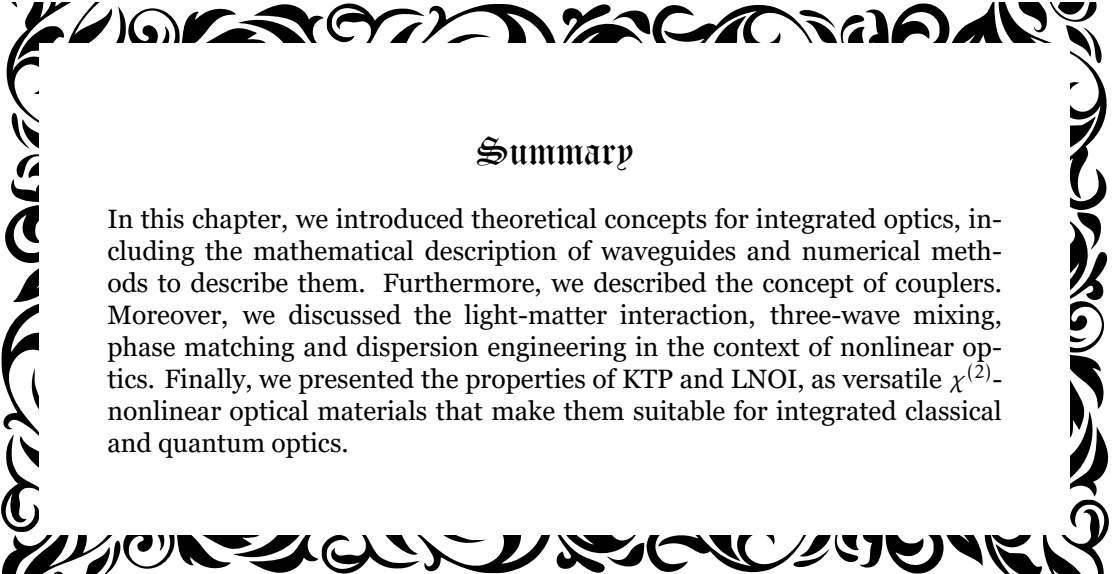
The high refractive index contrast in LNOI enables waveguides with sub-micrometer cross-sections and is a magnitude smaller than titanium in-diffused waveguides in LN [97, 98]. Therefore, the bending radii in LNOI are in the range of tens of micrometers, whereas bending radii of titanium in-diffused waveguides in LN are in the range of tens of millimetres [99].

Waveguides in LNOI are fabricated by nano-structuring of the thin-film. This creates ridge waveguides with large index contrast and strong mode confinement [100]. The cross-section of a typical LNOI waveguide has slanted sidewalls and a slab. The sidewalls are introduced due to limitations in the dry etching process. The slab is desirable,

e.g., in electro-optical modulators, because it increases the microwave field inside the LN thin-film. It can also help reduce optical losses by decreasing the overlap of the optical mode with etched sidewalls.

However, the fabrication is a challenging task, since this crystalline material is mechanically hard and chemically inert. Nevertheless, there are several fabrication methods, to selectively remove the LN material, e.g., dicing [101], wet or dry etching [102].

In LNOI the refractive index contrast is roughly an order of magnitude larger than titanium in-diffused waveguides [100]. This allows for a dense integration and much more important it allows for the tuning of the effective index of a waveguide mode by changing the waveguide geometry. This precise control of the modal properties is needed to enable tailored quantum optical applications. To model waveguides in LNOI and do dispersion engineering, we cannot solve the wave equations analytically and therefore, we need to use a numerical approach, which is introduced in section 4.3.2.2.



Summary

In this chapter, we introduced theoretical concepts for integrated optics, including the mathematical description of waveguides and numerical methods to describe them. Furthermore, we described the concept of couplers. Moreover, we discussed the light-matter interaction, three-wave mixing, phase matching and dispersion engineering in the context of nonlinear optics. Finally, we presented the properties of KTP and LNOI, as versatile $\chi^{(2)}$ -nonlinear optical materials that make them suitable for integrated classical and quantum optics.

*It's still magic.
even if you know how it's done.*

Terry Pratchett

Technology

Contents

4.1	Potassium Titanyl Phosphate	53
4.2	Lithium Niobate On Insulator	68
4.3	Characterisation.	72

The main focus of this work is to optimise the fabrication of poled structures and waveguides in nonlinear optical materials for quantum optical applications. To this aim, we will discuss in this chapter the techniques for periodic poling, waveguide fabrication and characterisation of KTP and LNOI devices. For each material we give an overview about the state of the art of periodic poling and waveguide fabrication. Afterwards, we present for each material our techniques for the fabrication process. Then, we introduce the state of the art of characterisation methods in terms of material and optical characterisation and our techniques to analyse our devices.

4.1 Potassium Titanyl Phosphate

We introduced the properties of KTP in section 3.3.1. In particular, the wide transparency range from 350 nm to 4500 nm [45], the large nonlinear optical coefficients [46] as well as the unique dispersion properties make the material highly interesting for quantum optical applications. To take full advantage of the KTP capabilities, dispersion engineered processes can be tailored by means of quasi-phase matching. Within the past years versatile integrated and dispersion engineered sources have been developed, e.g., a source for the generation of a separable photon pair state at telecom wavelength [16] or the generation of highly pure single photons in programmable temporal shapes [42]. However, this platform presents open challenges in the fabrication stage, in particular regarding reproducibility and the stability of periodically poled domains. This means that each device needs to be produced and optimised individually.

4.1.1 State of the Art:

Periodically Poled Waveguides in KTP

One key component for quantum optical applications are photon pair sources. For the development of such sources, there are two major components necessary to achieve efficient devices. On the one hand, waveguide fabrication for the passive routing and on the other hand, the periodic poling for the phase matching. Therefore, the technology for periodically poled waveguides has to be developed. In the following, we describe the state of the art of phase matching techniques via periodic poling and waveguide fabrication techniques in KTP.

4.1.1.1 Phase Matching Techniques

Over the years various approaches have been developed for quasi-phase matching in KTP. One approach to produce domain inversion is using a scanning electron beam [103]. By bombarding the -c-surface with electrons an electric field is formed on the -c-surface of KTP, which induces the domain reversal process. However, the procedure is prone to stitching errors due to the limited size of the writing fields of the electron beam.

One chemical method to achieve QPM is via periodically segmented waveguides. In this method, a waveguide is defined by a periodic segmented exchange of rubidium. Since the ion-exchange is performed in a nitrite melt of rubidium and barium, the ferroelectric domains in the exchanged regions are inverted, which results in the waveguide being periodically poled [104]. The main pitfall of this method is that the domain inversion is sensitive to the melt composition used for the exchange [105]. Moreover, segmented waveguides have the disadvantage that the guiding and phase matching properties cannot be optimised at the same time. Since they are non-continuous waveguides and the light diverges from the exchanged to the non-exchanged region, large losses are to be expected with this technique.

The most common and most effective method to create periodic domain structures is by applying an electric field. This technique is commonly referred to as periodic poling. A possible way to achieve periodic poling is to exploit the difference of coercive field strength between KTP and periodically Rb-exchanged KTP. By periodically exchange Rb, one can spatially structure the coercive field strength needed to invert the domains. Therefore, the application of an uniform electric field, with magnitude that lies in between the coercive field strength of KTP and Rb-exchanged regions, allows one to pole exclusively the non-exchanged regions, thus, achieving periodic poling [106]. The main drawback of this technique is that the exchanged regions act as a segmented waveguide and have the same drawbacks such as segmented waveguides.

Another approach to use electric field poling is by using an periodic insulation mask and thus, effectively increasing the resistivity of the regions below the insulation mask. In

this way, periodic domain inversion can be achieved by applying an electric field, above the coercive field strength [107]. This technique has the advantage to fabricate periodic structures reproducible and flexible. In KTP, however, periodic poling is difficult due to the high ionic conductivity acting against the electric field. Because of the high conductivity and in order to be able to periodically pole KTP at room temperature with a 1:1 duty cycle, an optical monitoring of the domain inversion is necessary. The optical monitoring will be introduced in section 4.1.2.1.

4.1.1.2 Waveguide Fabrication Techniques

A key component for integrated devices are waveguides. In the following, we present different methods to fabricate waveguides in KTP. One possible technique to produce planar waveguides is by He⁺-ion implantation. The implanted ions create an optical barrier several micrometers beneath the surface with a decreased refractive index [108]. Disadvantages of this method are the one dimensional confinement and the high losses. Another versatile and flexible method is femtosecond laser writing. The material characteristics can be modified with a laser beam focused into the KTP material, while the sample moves underneath the beam [109]. In this way, it is possible to create guiding structures by two or more parallel written tracks [110]. Femtosecond written waveguides give the possibility to write the waveguides below the surface of the sample and reduce the losses induced by surface contamination [111]. The disadvantages of this type of waveguides are the low mode confinement and irregularities in the symmetry of the spatial modes.

Analogue to LNOI, KTP on SiO₂ is a relatively new material and offers a strong mode confinement after dicing or etching [112]. Nevertheless, this material is still unexplored and the waveguides have high losses.

Another type of optical waveguides in KTP are based on a local exchange of the potassium (K) ions with rubidium (Rb), caesium (Cs) or thallium (Tl) ions [69]. The refractive index in the exchanged regions is increased. The dielectric characteristics, as well as ionic conductivity and coercive field strength, are all affected by the exchanged alkali ion.

One possibility to produce ridge waveguides is by doing a planar exchange, for an optical boundary in the depth and subsequent dicing for a larger refractive index contrast along the lateral direction [113]. Despite that, the waveguides are brittle due to the Rb-exchange and can be easily destroyed by mechanical stress, e.g., during the dicing process [114]. Another disadvantage of these waveguides are the increased losses due to the side wall roughness of the ridges.

Channel waveguides via local ion-exchange are an excellent choice for guided optics because of their high quality, symmetric spatial mode profile and low losses [42]. For this reason, we use this method for our waveguide fabrication.

4.1.2 In-house Technology

In the following section we introduce our technologies for periodic poling and waveguide fabrication in KTP. The in-house technology of KTP is a continuously developing process over the last decade and forced us to optimise existing setups and procedures and develop new approaches for periodically poled waveguides.

We introduced different techniques for periodic poling in KTP in section 4.1.1.1. Our long term experience in periodic poling of conventional lithium niobate encouraged us to use electric field poling for KTP. Over the last years we gained a lot of knowledge in the poling of bulk KTP and thus, we produce waveguides in periodically poled material. The drawback of this approach is possible corrugated waveguides. However, we have already resolved this issue [115] and we developed a technology to create high quality devices for frequency conversion applications or single photon sources.

4.1.2.1 Periodic Poling

We describe in the following our processes and setup for inverting periodically the spontaneous polarisation of KTP. To this aim, we require a periodic electrical contact, which we achieve by using an periodic insulation structure, on which we deposit a uniform electrode. By applying several high voltage pulses to the electrical contacts we can invert the spontaneous polarisation. To have a switch-off criterion, once the periodic poling has a 1:1 duty cycle, we use an optical monitoring technique. Below, we will go through each step in detail in order to achieve periodic poling in KTP.

Periodic Photoresist Fabrication via Mask-Lithography

Before any fabrication steps, we have to prepare our samples. We use 1 mm thick z-cut KTP or RbKTP wafers and dice them along the crystallographic axes with a sample size of 10 mm in x-direction and 6 mm in y-direction. The sample has a uniform spontaneous polarisation/domain and the top of the sample is the negative z-surface. Afterwards, the samples are polished at the end-facets for light propagation along the x-axis. After that the samples are cleaned and thus, immersed in four different chemical solutions for 10 min at 40 °C in an ultrasonic bath. The chemical solutions are in order acetone and isopropyl alcohol (IPA) to remove anorganic residuals, water, tickopur (3 % in water) and water to degrease the surface and ammonia solution (water, hydrogen peroxide (H_2O_2) and ammonium hydroxide (NH_4OH) with volume ratio of 70:20:10) to remove organic residuals. In the following, this procedure will be referred to as cleaning procedure.

For periodic poling we need an insulation mask, which spatially structures the coercive field strength needed to invert the domains. Figure 4.1 shows a scheme of all the process

steps involved in the fabrication of a periodic photoresist structure with gold-palladium layers for a good contact during poling.

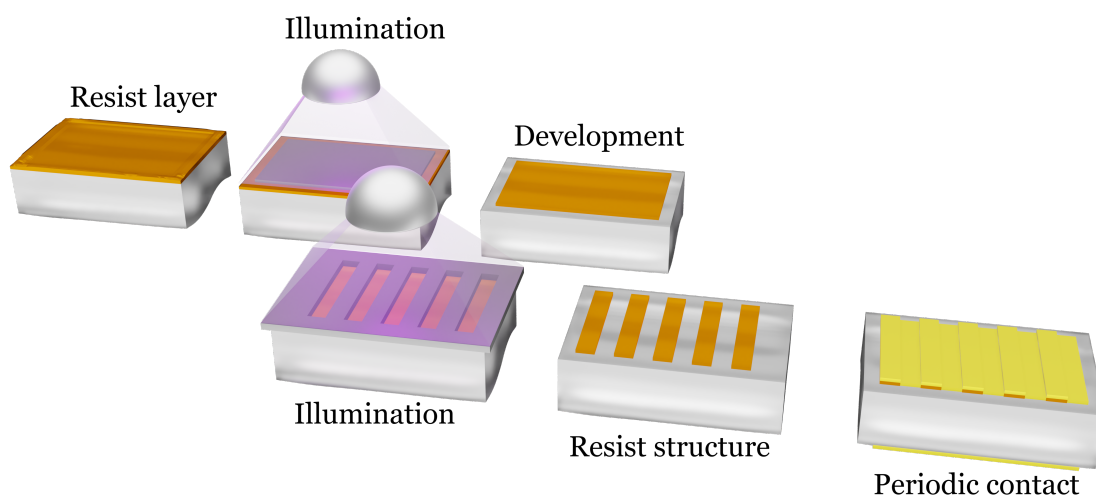


Figure 4.1 – Process steps for fabricating a periodic resist structure with gold-palladium layers to improve electrical contact.

The process starts with rinsing the sample with isopropyl alcohol and drying it with nitrogen for a good adhesion between the sample and the resist. We spin-coat a positive resist (AZ 4533 - MicroChemicals) at 6000 rounds per minute (rpm) for 3 seconds on the -z-surface, because the domain nucleation is more favourable on this side [48]. The resist is softbaked in a preheated oven at 105 °C for 30 min in order to reduce the solvent content and to stabilise the resist. This results in a 2.5 µm thick resist layer, which is sufficient to insulate the sample and prevent domain inversion beneath the resist. Due to the thickness of the resist and the small dimensions of the samples, a bulge is formed on the outer parts of the photoresist. This is problematic because it generates a relatively wide gap between the photo-mask and the inner area of the sample. We solve this by a double step lithography [115]. In the first step, only the outer parts of the photoresist are exposed. By developing the sample, we can remove the bulges, thus, providing better adhesion of the photoresist mask during the second step. The second step consists of illuminating the remaining photoresist with the desired poling pattern. We expose the photoresist for 80 s. During development (AZ 826 MIF - MicroChemicals) all the exposed areas vanish. A hardbake at 100 °C for 2 h, 120 °C for 3 h and 140 °C for 1 h increases the resistance of the photoresist to the electrolyte used as an electrode during periodic poling. To achieve a good electrical contact with the exposed KTP regions, we sputter (Quorum Technologies SC7640) a 60 nm thin layer of gold-palladium (Au/Pd) on both sides of the sample.

Poling Holder and Setup

For the poling, we place the sample in a poling holder. The holder is split in two parts, each with electrical connections to the circuit. The sample is held in place between the two holder sections by screws. Figure 4.2 shows the poling holder with a KTP sample. The holder is designed to only cover the top and bottom of the sample and leave the input and output end-facets along the x-direction accessible.

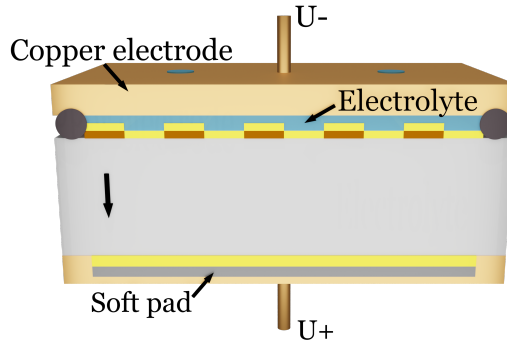


Figure 4.2 – Sketch of the used poling holder for KTP. The KTP crystal is situated between two copper electrodes and is contacted via an electrolyte from the top and an electrically conductive soft pad from the backside. The sample itself is deposited with Au/Pd for a good electrical contact. The direction of spontaneous polarisation is shown by the arrow in the KTP sample.

The bottom part of the sample is placed on a soft-pad, containing silver coated copper particles, providing an electrical contact. Moreover, the pad distributes the forces during fixing the sample and therefore, lowers the risk of breaking or damaging the sample. The top part of the sample is electrically contacted via an electrolyte sealed with an o-ring. The electrolyte is a solution of 89 % water, 10 % isopropyl alcohol and 1 % potassium chloride. IPA reduces the surface tension, such that the solution flows better between the resist stripes. With this design the applied high voltage (High voltage amplifier Trek 20/20C) is directly connected to the sample.

The sample holder is attached to a three-axis tower, allowing for the alignment for the optical monitoring and the switch-off criterium during poling.

Optical Monitoring

As explained in section 3.2.3.2 the highest conversion intensity is achieved with a perfect 1:1 duty cycle. To monitor the duty cycle as poling occurs, we use an optical monitoring system developed by Karlsson et al. [116, 117] based on the electro-optical effect. When an electric field is applied to a sample in the z-direction, the y- and z-components of the incident field undergo a relative phase shift due to the electro-optical effect. The

induced phase retardation Γ can be described by:

$$\Gamma = \frac{2 \cdot \pi}{\lambda} \cdot E_z \cdot L \cdot \left(\frac{n_y^3}{2} \cdot r_{23} - \frac{n_z^3}{2} \cdot r_{33} \right) \quad (4.1)$$

where λ is the wavelength of the laser, E_z is the applied electric field along the z-direction, L the length of the crystal, n_y and n_z are the refractive indices along y- and z-axis and r_{23} and r_{33} the electro-optic coefficients of KTP.

The phase retardation is only observed during the change of the electric field. In combination with a linear polariser the differential phase retardation results in an intensity modulation, which can be represented as

$$I \propto (1 - \cos \Gamma). \quad (4.2)$$

We use a He-Ne laser ($\lambda = 633 \text{ nm}$), which is linearly polarised 45° to the y- and z-axis of the crystal. The beam is launched along the x-axis of the crystal with the help of two lenses. Therefore, we set for the refractive index $n_y = 1.771$ and $n_z = 1.865$ [63] and for the electro-optic coefficients $r_{23} = 15.7 \frac{\text{pm}}{\text{V}}$ and $r_{33} = 36.3 \frac{\text{pm}}{\text{V}}$ [46] for KTP. We use a linear polariser orthogonal to the laser beam after the sample and a photo diode to measure the transmitted intensity. Figure 4.3 shows our setup for the optical monitoring.

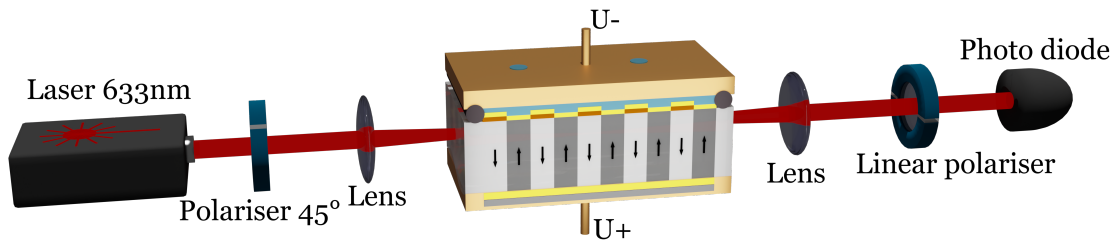


Figure 4.3 – Illustration of the used optical monitoring setup. Here, diagonally polarised light is launched into the crystal. The domain inversion leads to a phase retardation and therefore, in a variation of the detected optical signal in the photo diode, depending on the status of the periodic domain inversion.

When a continuously changing electric field below the coercive field is applied to a crystal, the phase retardation inside the crystal is translated through the linear polariser into an intensity modulation. The modelled optical signal for a 10 mm long sample is shown in figure 4.4.

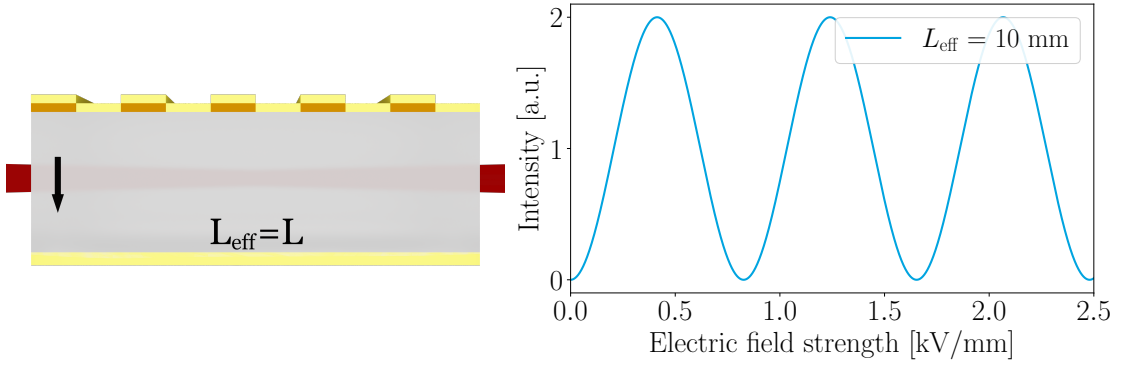


Figure 4.4 – Modelled optical signal during the optical monitoring process of an unpoled 10 mm long KTP crystal. The intensity that is detected by the photo diode in the setup is modulated upon changing the applied electric field.

An external field above the coercive field strength leads to an inversion of the spontaneous polarisation and therefore, a change in the sign of the electro-optic tensor elements. For the length x , describing the inverted domains in a crystal, the phase retardation can be written as the following

$$\Gamma_{\text{pol}} = \frac{2 \cdot \pi}{\lambda} \cdot E_z \cdot \left[\underbrace{\left(\frac{n_y^3}{2} \cdot r_{23} - \frac{n_z^3}{2} \cdot r_{33} \right) \cdot (L - x)}_{\text{initial domain}} + \underbrace{\left(-\frac{n_y^3}{2} \cdot r_{23} + \frac{n_z^3}{2} \cdot r_{33} \right) \cdot x}_{\text{inverted domain}} \right]. \quad (4.3)$$

This expression can be simplified to

$$\Gamma_{\text{pol}} = \frac{2 \cdot \pi}{\lambda} \cdot E_z \cdot \left(\frac{n_y^3}{2} \cdot r_{23} - \frac{n_z^3}{2} \cdot r_{33} \right) \cdot \underbrace{(L - 2x)}_{L_{\text{eff}}}. \quad (4.4)$$

As a result, the accumulated phase retardation is reduced, resulting in a shorter effective length L_{eff} , which is the difference between the poled and unpoled areas. Figure 4.5 shows an effective length of 5 mm, which corresponds to a quarter inversion of the crystal.

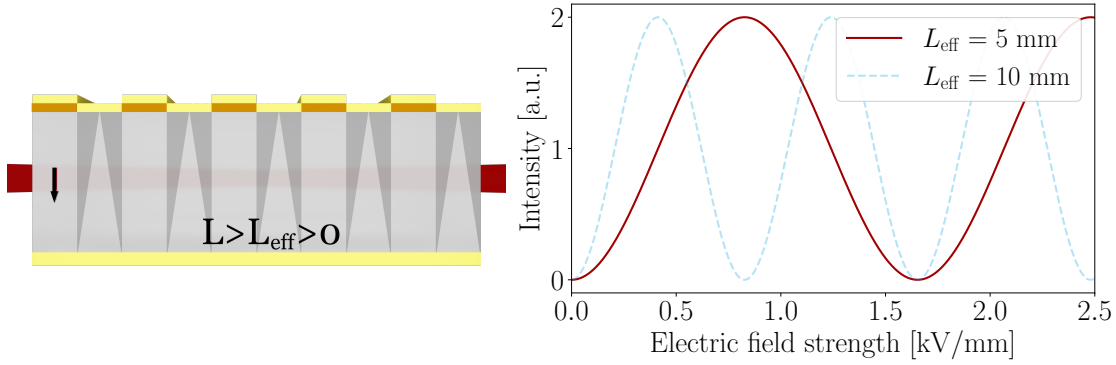


Figure 4.5 – Modelled detected signal of the optical monitoring process for a partly poled KTP crystal with an effective length of 5 mm.

As more and more domains are inverted, the total phase retardation reduces, and it becomes equal to 0 when half of the sample is completely poled. This usually means that poling has been achieved with 1:1 duty cycle in the monitored region. This is a switch-off criterion and we stop applying the pulses. Figure 4.6 shows that the oscillations vanish for a poled sample with a 1:1 duty cycle.

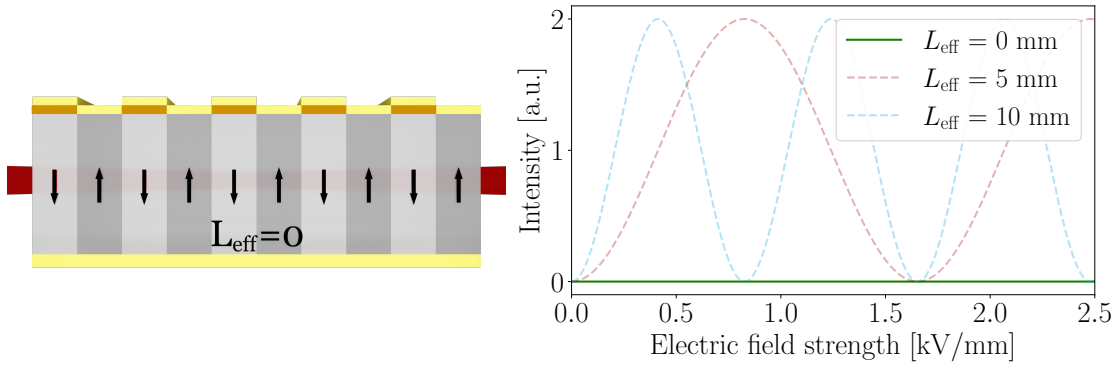


Figure 4.6 – Modelled detected signal of the optical monitoring process for a periodically poled KTP sample with an effective length of 0 mm and a 1:1 duty cycle.

It has to be mentioned that the effective length can be negative. This is the case if more than half of the crystal is inverted and the oscillations start again. The effective length L_{eff} will be equal to $-L$ if the spontaneous polarisation is completely reversed, resulting in a maximum amount of oscillations.

It is important to note that this technique is an average method and thus, the intensity modulation does not spatially resolve the domain duty cycle. Inhomogeneous pol-

ing can be caused by inhomogeneous ionic conductivity, inhomogeneous shielding of the applied field by ionic space charges, or variations in sample thickness. We want to emphasise at this point that KTP is known for its spatial inhomogeneities in the crystal structure [68, 118] and this can cause inhomogeneities in the poling and therefore, overpoling, perfect poling and underpoling in different areas. This is not possible to detect via optical monitoring. This is also valid for RbKTP. Despite these limitations, optical monitoring is a versatile technology that is well suited for periodic poling of KTP.

Periodic Poling Process

The purpose of the optical monitoring technique is to identify a switch-off criterion that can be utilised to precisely terminate the poling process. The full cover metal electrode on both sides of the sample allows for nearly similar electric field components in the poled and unpoled regions in the crystal. With the electric field over the whole sample it is possible to determine the poling result, when the crystal with a periodic insulation structure is poled with a 1:1 duty cycle.

Once the electrode structure and the monitoring are defined, the number of variables to optimise is still quite large, e.g., poling pulse shape or the magnitude of the electric field. The shape of the poling pulse is trapezoidal with a rise and fall time of 1 ms, as shown in figure 4.7. In the following, the voltage in the plateau area is referred to as plateau voltage, and the time of the plateau area as the plateau time. The plateau time and the plateau voltage of the poling pulse need to be tailored for each poling period and sample, due to small variations in the commercially available crystals.

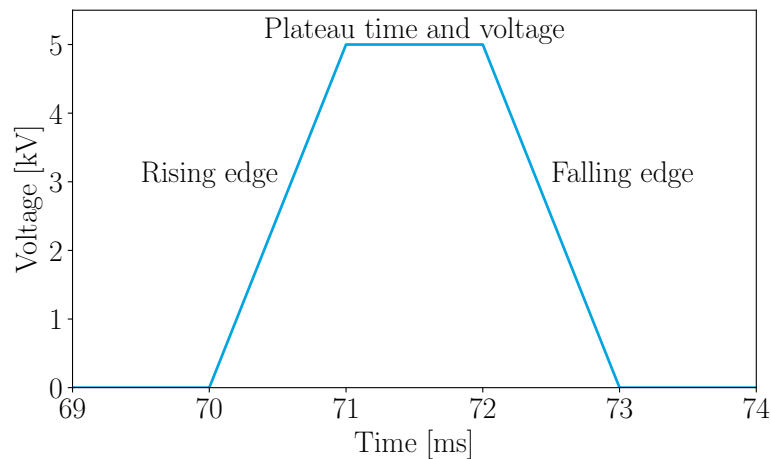


Figure 4.7 – Illustration of the poling pulse shape above the coercive field strength with a rise and fall time of 1 ms.

Several poling pulses are necessary for the successful periodic poling of a sample. To analyse our poling process we record simultaneously the voltage and the current pro-

vided by the amplifier as well as the optical signal, used for the optical monitoring technique. Domain inversion occurs primarily during the plateau area, if the voltage is larger than the coercive field strength of KTP or RbKTP. Due to the changing of the electric field strength, we can observe in the rising and falling edge an intensity modulation in the form of oscillations.

Investigations during this thesis have shown, the poling pulse alone is not sufficient to analyse the oscillations properly. Therefore, we expanded the pulse with two inspection pulses, one before and one after the actual poling pulse, which is shown in figure 4.8.

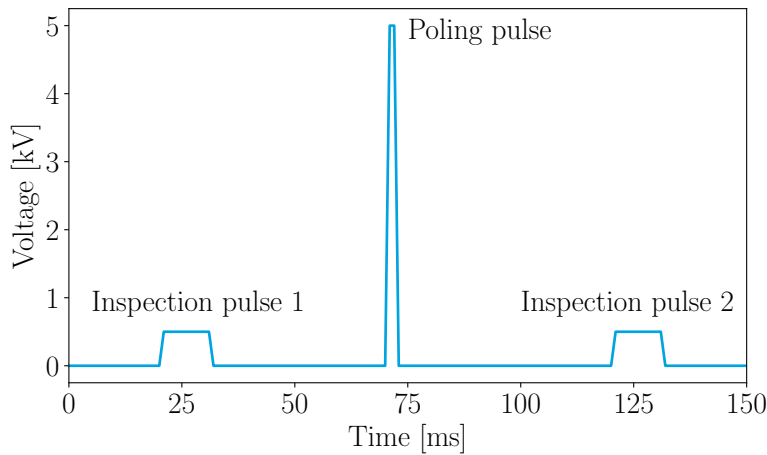


Figure 4.8 – Illustration of the pulse shape with two inspection pulses for the optical monitoring before and after the poling pulse.

These inspection pulses are well below the coercive field strength with 0.5 kV and do not influence the poling behaviour of the samples. We use these pulses to observe the poling progress especially the oscillations directly before and after the poling pulse. Because of heating of the samples, the oscillations continue a short amount of time in the plateau region, therefore, we enlarged the plateau time of the inspection pulses to 20 ms to distinguish between the oscillations of the rising and falling edge. In section 5.1.1.2 we give an insight into the advantages of this technique.

We must find a balance between pulse length and number of pulses, when we pole our samples. It is known that longer pulses lead to more homogeneous poling [118], but at the same time it is harder to inspection the poling process and analyse the change in the oscillations. Therefore, we decide for each material and sample individually.

After the poling, we remove the sample from the holder, etch the gold-palladium electrodes in an ammonia solution and place the sample overnight in TechniStrip (TechniStrip NI555 - MicroChemicals), to dissolve the resist from the sample surface. In the end, we clean the samples in a subsequent cleaning procedure.

4.1.2.2 Waveguide Fabrication

In the following, we describe our fabrication for Rb-exchanged channel waveguides in KTP. For a selective Rb-exchange we use a slit mask on the surface of KTP defining the waveguides. The confinement of the waveguides is achieved due to the increased refractive index in the exchanged regions. The geometry of the waveguides depends on the structure of the exchange mask and the parameters for the exchange process, e.g., melt composition, exchange time or temperature. Therefore, we introduce our recipe to produce optimised channel waveguides in KTP for our devices.

Mask Definition via Mask-Lithography

Independent of whether the samples are periodically poled or not, the first step is to clean the samples in a cleaning procedure. This allows for a good adhesion of a subsequently deposited layer. For the exchange of the waveguides we prepare a titanium mask on the surface to define the exchanged regions. If we pole the sample, we produce the exchange mask on the initial -z-side of KTP, because the poling mask was defined on that side and related to that the domains are more homogeneous on that side. Figure 4.9 shows the steps to produce a titanium mask and prepare the samples for the Rb-exchange.

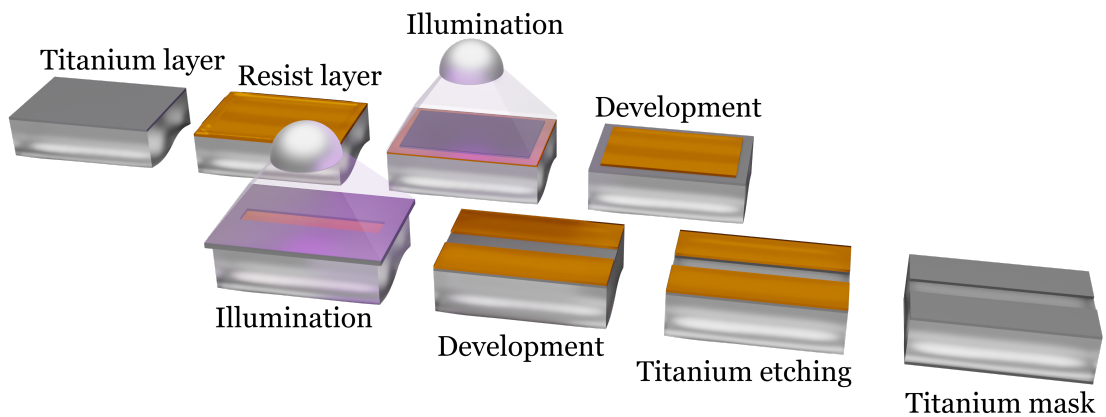


Figure 4.9 – Stepwise illustration of the KTP waveguide mask fabrication process. Titanium stripes are defined by means of mask-lithography and selective wet chemical etching. The titanium stripes act as a solid mask for rubidium in-diffusion into the substrate.

The first step after cleaning is to deposit (LAB 750 - Leybold) a titanium layer with a thickness of 80 nm. Afterwards, we rinse the sample with acetone and IPA to allow a good adhesion of the photoresist. We spin-coat a layer of positive photoresist (AZ 1518 - MicroChemicals) at 6000 rpm for 3 seconds on the titanium layer. After the

softbake for 30 min in a preheated oven at 105 °C, we remove the bulge as described in section 4.1.2.1. With illumination for 18 s via mask-lithography and subsequent development (AZ 726 MIF - MicroChemicals) we transfer the slits from the photo-mask into the resist layer via mask-lithography (MA 6/BA 6 - Karl Suss). In a mixture of H₂O, H₂O₂, NH₄OH and EDTA (ethylenediaminetetraacetic acid) (weight ratio 100:10:5:2.5) we etch the exposed titanium in the photoresist slits at 40 °C to enhance the etching. This creates trenches in the titanium layer, defining the waveguide width during the Rb-exchange. Afterwards, we remove the photoresist and deposit a second layer of titanium on the backside of the sample to prevent the penetration of rubidium ions during the exchange. The larger radii of the Rb-ions, compared to the K-ions, modify the size of the unit cell, causing it to expand macroscopically and thus, cause a bending of the sample. This bending could cause a higher probability of breaking during the end-facet polishing.

We use different photo-masks to define our waveguide width, the two common variations on the samples are waveguides with widths between 1.5 µm and 4.5 µm in 0.5 µm steps, or waveguides with widths between 2.0 µm and 3.5 µm in 0.5 µm for a smaller width variation.

Rubidium Exchange

For the rubidium exchange the samples are immersed in a melt composed of rubidium nitrate (RbNO₃), potassium nitrate (KNO₃) and barium nitrate (Ba(NO₃)₂) above 330 °C for more than 40 min to produce single-mode waveguides at 1550 nm. The exchange process and hence, the waveguide properties are defined by the melt composition, exchange time, and temperature. The higher the temperature and longer the exchange time, the higher is the rubidium concentration at the surface and the deeper are the waveguides. We use the RbNO₃ to increase the refractive index in the KTP crystal [69] allowing wave guiding. The KNO₃ is used as a buffer to reduce the exchange rates and achieve a homogeneous exchange on the surface [119], whereas the Ba(NO₃)₂ serves as a catalyst for the exchange to get deeper waveguides [120], [121]. We have different melt compositions, our commonly used melt is composed of 88 % RbNO₃, 11 % KNO₃ and 1 % Ba(NO₃)₂ with an exchange temperature of 358 °C for 43 min.

Due to the thermal expansion of KTP and the holder at high temperatures, we must secure the sample with platinum or gold wire to allow enough room for expansion during the exchange. It is critical that the wire maintains the sample in place while not being overly tight, as this will cause the sample to break during expansion.

For the exchange we melt our chosen mixture in a ceramic crucible on a hot plate, which is insulated with aluminium foil to keep the melt at a constant temperature. A steel-covered thermocouple in a ceramic thermal protection tube is used to keep track of the temperature. The melt has a temperature change of less than 2 °C, which is within the error tolerance of the thermocouple. The crucible is covered with a lid during the ex-

change process to keep the temperature conditions consistent. The sample holder is held in place by a rack consisting of two threaded rods and a crossbeam. We use a grip to precisely and carefully lower the sample holder in the melt. Figure 4.10 shows the setup for the Rb-exchange.

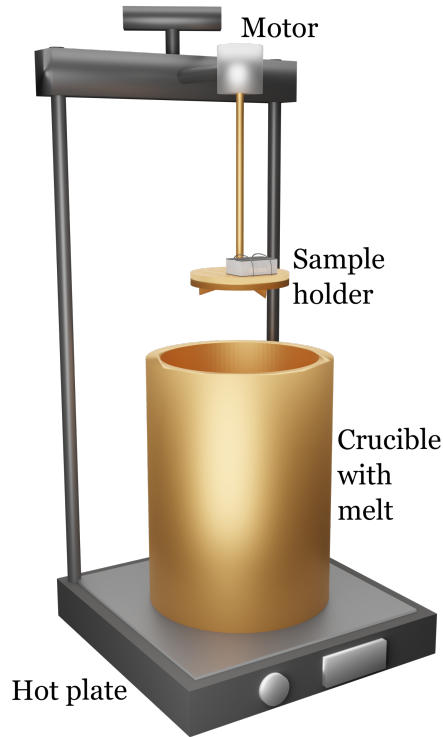


Figure 4.10 – Schematic of the setup for the Rb-exchange for waveguide fabrication in KTP.

The temperature gradient, which is present, is a crucial parameter that could cause the samples to break. Therefore, we use an optimised procedure to slowly increase the temperature, while lowering the sample holder stepwise before immersing it in the melt. For each step we wait for 10 min that the sample holder and the samples can assimilate the ambient temperature. The first step is slightly above the crucible edge, then slightly below. At this point we close the lid to stabilise the temperature fluctuations. Then, we lower the holder in the middle of the crucible, slightly above the melt and finally with the holder slightly touching the melt to equalise both temperatures. Then, we immerse the sample into the melt.

During the exchange, the holder rotates at six rounds per minute. The holder has on the backside melt mixer to mix the melt during rotation. This allows for a homogeneous temperature distribution and at the same time a constant melt composition at the exchange areas of KTP, to ensure a homogeneous in-diffusion of the rubidium. After a fixed exchange time, we stop the diffusion process by moving the holder to the

middle height of the crucible. After 10 min, we move the holder slightly below the crucible edge for 10 min before raising it slightly above the edge. Once the holder has reached a temperature of 100 °C, we carefully immerse the holder in 80 °C water. The sample can gently cool down to room temperature in the water, and the leftover melt components on the sample and holder dissolve in the water.

After the exchange, we remove the titanium mask in an ammonia solution and clean the sample with a final cleaning procedure. The final procedure to use the waveguides for linear and nonlinear measurements is to do the end-facet polishing.

End-Facet Polishing

We use chemical mechanical polishing (CMP) to prepare our end-facets. During polishing, material is removed chemically and mechanically. Without a suitable second sample on the top surface of the waveguide sample, the edges of our waveguide sample rounds. As a result, the edge is rounded 1 μm - 2 μm [115], while the waveguide is just 8 μm deep. This makes coupling without high in-coupling losses impossible. Therefore, we press a second sample made of the same material on the top surface of our waveguide sample. At the same time, the highest pressure is on the slightly higher waveguides than the bulk material. This results in a bonding effect and we destroy the waveguides, when we remove the second sample [68]. We use a thin layer of photoresist between the two samples to relieve the pressure.

Altogether this assembly is mounted in a polishing holder. It is important to mount the samples parallel to the holder sides that the sample end-facet is adjusted perpendicular to the waveguide, to allow for 0° incidence of light. This holder is placed in a second holder on a polishing plate. The two holders and the plate rotate independently to allow for a homogeneous polishing without any directional dependency. An aqueous solution of the SF1 polishing solution (Logitech Limited) drips on the polishing plate at a rate of about 1 drop per second, forming a thin layer. One end-facet requires several hours of polishing. The last step is to clean the sample in a cleaning procedure.

4.2 Lithium Niobate On Insulator

In section 3.3.2 we discussed the exceptional optical properties of lithium niobate for quantum optical applications. However, high integration density for compact and low-loss devices requires a sophisticated fabrication technology for the LNOI platform. The development of such compact devices only started about a decade ago [122] and within the past few years breakthroughs in the technology enabled the fabrication of versatile integrated optical components in LNOI [94, 95, 123–129].

4.2.1 State of the Art:

Periodically Poled Waveguides in LNOI

Waveguides and QPM are the backbones of devices for integrated quantum optical applications. The optimisation of the technology and fabrication techniques for these two components is fundamental for the efficiency of the devices. In the following, we describe the state of the art of phase matching and waveguide fabrication techniques in LNOI.

4.2.1.1 Phase Matching Techniques

A major challenge in fabricating quantum optical devices is to achieve momentum conservation, which means in this context phase matching. There are several techniques to engineer conditions, under which the phase mismatch is compensated.

Birefringent phase matching is a traditional method for phase matching. Since LN is a negative uniaxial crystal, type I and II phase matching can be used. Nevertheless, it is rarely used in waveguide geometries since the possible conversion frequencies are limited and the largest component of the $\chi^{(2)}$ tensor is not accessible.

One way to access the largest nonlinear tensor component is modal phase matching [130]. In this case, the phase mismatch is compensated by different spatial mode profiles. Because of an overlap integral being zero of even and odd modes, the fundamental and third-order modes are often used [131]. A huge disadvantage of this technique is a lower mode overlap between the fundamental mode and a higher order spatial mode [132].

Cyclic phase matching [133] can be used in microring or microdisk resonators, when the crystallographic axis is not the symmetry axis, which is true for x-cut LNOI. As light propagates through the resonator, the effective refractive index of the in-plane polarised light oscillates between the ordinary and extraordinary values [134]. The refractive index varies with an angle between the crystallographic axis and the propagation vector in the period of 2π . There are four positions in every round trip, where there is perfect phase matching [135]. Nevertheless, the conversion efficiency can be constructively and

destructively in different phase matched position and this would lead to a wavelength-dependent gain profile [133].

Metasurface-assisted phase-matching-free conversion [136] is a technique without structuring the lithium niobate but metasurfaces on top of a waveguide consisting of densely packed arrays of optical antennas. The pump light at a fundamental mode is converted, e.g., to its second-harmonic fundamental mode and the metasurface couples the second-harmonic light into higher-order spatial modes. Collecting higher-order modes is generally inefficient and a disadvantage of this method.

Another method to introduce phase matching by structuring the waveguide is to periodically vary the waveguide width. This perturbation introduces a periodic modulation of the refractive index along the propagation direction, giving an additional momentum and compensating the phase mismatch [130]. One drawback of this method are the added losses due to the perturbation of the waveguide.

Currently, quasi-phase matching is the most popular phase matching technique. QPM allows for using the same spatial modes and the largest element of the $\chi^{(2)}$ tensor. To achieve QPM the sign of the $\chi^{(2)}$ material must be inverted periodically. This can be achieved by inverting the ferroelectric domains, e.g., by applying high voltage pulses. For periodic poling of bulk materials, this process is fully established, but in case of LNOI the technology had to be developed in recent years. In z-cut LNOI the thin-film can be either periodically poled before or after bonding to SiO_2 and substrate layer. Before bonding, the conventional lithium niobate is poled traditionally and then bonded on to the substrate via smart-cut technique [74]. Another method is to do the poling after bonding and it is directly performed on the thin-film, e.g., by using an atomic force microscope (AFM) tip [137, 138] or focused ion beam [137] to locally invert the spontaneous polarisation. Another way is by electric-field poling directly through the hole wafer stack [132]. In x-cut LNOI periodic poling can be achieved using two electrodes on the surface of the material. Poling can be done before and after waveguide fabrication. Before waveguide fabrication the poling process can be tracked in-situ monitoring of the ferroelectric domains by second-harmonic confocal microscopy [139]. After waveguide fabrication the process can be actively monitored through the optical signal [140]. In x-cut samples poling periods with electric field poling of $2.8\text{ }\mu\text{m}$ over 5 mm [141] have been shown. Also periods as short as 600 nm over $50\text{ }\mu\text{m}$ with electric-field poling [141] and as short as 200 nm consistent over 3 mm length with focused ion beam poling [137] have been demonstrated. One disadvantage of periodically poled gratings in x-cut samples is that only linear gratings are possible, while in z-cut LNOI the domains are formed normal to the plane and can form arbitrary shapes (e.g., radial gratings) [132].

In order to take full advantage of the unique capabilities of LNOI, we decided to use electric field poling in x-cut LNOI in our technology. Periodic poling of x-cut LNOI has the advantage of directly structuring a periodic mask on the surface and thus, predefine the domain growth direction between the electrodes. Furthermore, we decided to use optical-lithography, to enable a high flexibility in the structure design with low fabrication time, which allows for a broad geometry evaluation and optimization. This allows for tailoring the periodic poling structures for quantum optical applications.

4.2.1.2 Waveguide Fabrication Techniques

The key component of integrated devices are waveguides. In this section we present different approaches to form waveguides in LNOI.

Rip loaded waveguides are a heterogeneous approach to avoid structuring the thin-film of LN. For these type of waveguides a strip of material, which is easy to etch or deposit, is patterned on the plain LNOI. These strip-loaded waveguides confine the light either in the strip or in the lithium niobate film by adjusting the thickness and width of strip [142]. One drawback of this method is that the nonlinear interaction strength is restricted, since the spatial modes only partially overlap with the lithium niobate layer [143].

There are two methods to mechanically process LNOI waveguides. Ridge waveguides are fabricated by diamond blade dicing [101, 144, 145]. These waveguides have propagation losses of less than 3 dB/cm [101], but due to the width of the diamond they are limited in realisation of complex components such as couplers. Another mechanical approach is chemical mechanical polishing (CMP) [124]. In this process a chromium mask is formed by femtosecond laser ablation and the uncovered lithium niobate is removed by CMP. This method results in sub-nanometer surface roughness and propagation losses as low as 0.027 dB/cm [124]. One drawback of this method are the shallow sidewalls limiting the minimum bending radius.

Wet etching in HF:HNO_3 [97] or ion-beam-enhanced KOH-etching [146] [147] are other possibilities to form waveguides in LNOI. A disadvantage of wet etching is the different etching behaviour depending on the crystallographic structure [97]. Therefore, it is problematic to achieve homogeneous bending structures or non-corrugated waveguides in periodically poled material.

Another technique well known from the conventional lithium niobate channel waveguides are proton exchanged waveguides [148–150]. These waveguides as well as waveguides formed by Helium implantation [151] suffer from a relatively low index contrast and mode confinement in the lateral direction.

Due to the difficulties of mechanical processes, wet etching or exchanged waveguides, a convenient method in realising complex photonic structures is dry etching. Dry etching is a very efficient, precisely controllable process and well-known from semiconductor technology. Although historically lithium niobate was considered as difficult to etch, the breakthroughs of the last years have shown an impressive progress in lithium niobate dry etching technology [123]. At an early stage focus ion beam milling has been used to pattern LNOI. However, this technique is time consuming and only suitable for small areas [152, 153]. At present there are two major techniques in dry etching: reactive-ion etching (RIE) and pure physical etching. Both processes require a patterned structure, which serves as a mask during the dry etching, where the mask is transferred onto the lithium niobate thin-film. In the case of RIE, fluorine gases can be used to form volatile compounds with niobium [154], but at the same time it forms non-volatile lithium fluoride (LiF) [155]. This effect can be reduced with a proton exchange, which leads to a lower lithium concentration in the material [154, 156]. Nevertheless, the LiF redeposi-

tion is highly resistant to further etching and introduces as a result sidewall roughness [157]. One of the most widely used dry etching techniques currently is pure physical etching with an Ar^+ plasma [74]. Pure physical etching exhibits two challenges. First the etch selectivity between dry etching mask and lithium niobate is low (around 1:1), which limits the resulting etching depth. Second, due to redeposition the sidewalls are not vertical [158]. Nevertheless, the lithium niobate redeposition layer can be smooth, which does not result in significant scattering loss and the transmission losses can be as low as 0.027dB/cm [123]. To further reduce the redeposition, it can be removed via wet etching after the dry etching process [159] or gas clustered ion beam smoothening [128]. To improve the sidewall angle, some processes introduce fluorine gases such as CHF_3 [160]. Therefore, the most promising structuring approach is Ar^+ plasma dry etching.

4.2.2 In-house Technology

In our group there exist a lot of knowledge regarding conventional lithium niobate and thus, the technology of titanium in-diffused waveguides and bulk poling is well developed. Based on this knowledge, we decided to extend our material portfolio by adding LNOI as a new material platform to our research. The prior knowledge aids us in comprehending the material. However, because the required structures are not the same as those for conventional lithium niobate, we had to develop an entirely new technology for LNOI from scratch. Since we developed the technology for periodic poling and waveguide fabrication for LNOI, we show the fabrication processes and their results in the next chapter 5.2.

We show that it is possible to fabricate nano-structured devices with optical-lithography. This demonstrates, that it is feasible to fabricate integrated devices on wafer-scale, by overcoming limitations in commercializing the fabrication with the need of complex lithography systems, e.g., electron-beam-lithography.

43 Characterisation

Besides the fabrication of devices, it is also beneficial to analyse the quality of the devices. There are invasive and non-invasive techniques to characterise the geometrical and optical properties of our structures. We can analyse material properties like domain inversion and waveguide geometry. For the optical properties, we can measure the transmission losses and spatial modes or coupling behaviour.

43.1 State of the Art: Material and Optical Characterisation

Characterising the properties of devices require knowledge from many other research fields. For a complete analysis we have to characterise the material properties as well as the optical properties of our structures. Therefore, we can apply knowledge of processes for material characterisation and linear optical analysis in LNOI and KTP. However, some properties go beyond previously used methods, and we need to adapt approaches from other research fields into our characterisation routine. Hence, we give an overview of the state of the art of characterisation techniques suitable for our materials.

43.1.1 Material Characterisation

The material characterisation is focusing on two main aspects, on the one hand the analysis of the domain inversion and on the other hand the characterisation of the waveguide geometries.

Domain Inversion

Visualising the domain structure is essential to characterise the quality of the poling results, in particular the duty cycle of the periodic poling and the homogeneity. Selective etching is one technique to identify ferroelectric domain structures [105]. In KTP and lithium niobate the negative dipole end surface, the -z-surface, etches more rapidly than the positive surface of a crystal [161]. In a z-cut periodically poled crystal the negative and positive surface are alternating and therefore, the domain structures can be imaged by a surface topography. In a x-cut sample it is necessary to form a trench to expose the z-surface of the crystal and etch selectively. In this way, it is possible to get information about the domains in plane and in depth of the crystal. The destructive nature of this method is a major disadvantage. By applying this technique, it is in most cases not possible to use this sample for other experiments.

A non-invasive method to visualise the domain structure is piezoresponse force microscopy (PFM). When a voltage is applied with a tip to a piezoelectric sample, the surface will be displaced due to the converse piezoelectric effect [162]. These responses

can be monitored and assigned to different polarisation directions of the crystal. This method images the domains in a contrast mechanism. One drawback of this technique is, it does not provide depth information of the domains.

Raman spectroscopy uses the inelastic scattering and gives access to several material properties. It is possible to visualise with this non-destructive technique the domain and domain walls [163].

Another non-invasive technique is second-harmonic (SH) microscopy. The SH generation efficiency is sensitive to the crystallographic structure. This results in a change in the intensity of the signal at the domain walls, because the crystal is perturbed at the domain walls. With this it is possible to image the width of the domains. Moreover, there is the possibility to determine the depth of the poled domains [164].

Waveguide Structures

It is necessary to visualise the waveguide structure and geometry, particularly the homogeneity of the structure and waveguide width and depth, in detail to improve the properties of the waveguides. For this, it is possible to use a confocal laser scanning microscope (CLSM) or a scanning electron microscope (SEM). Images with a SEM have a much higher resolution than with a CLSM. One disadvantage of the SEM is that a non-conductive substrate has to be coated with a conductive material to avoid charges due to the electron beam [165].

Secondary ion mass spectroscopy (SIMS) as well as secondary neutral mass spectroscopy (SNMS) are analytical techniques to characterise and analyse the composition of a sample. In case of SIMS an ion beam is focused onto the sample surface and the ionised secondary particles are analysed via a mass spectrometer [166]. The neutral particles are post-ionised and analysed in a mass spectrometer in case of SNMS [167]. Both methods have the disadvantage that they use a primary ion beam and therefore, are destructive methods.

Energy-dispersive X-ray spectroscopy (EDX) is another analytical approach to characterise the elemental composition. Characteristic X-rays for every element are generated in the sample by a focused electron beam. With an energy-dispersive spectrometer the intensity and the energy of the X-rays are detected [165].

Another measuring tool is a contact profilometer used to measure the topography of a surface, e.g., the curvature, step size or flatness of a surface. One drawback of this method is, due to the contact mode, the stylus scratches the sample surface.

43.1.2 Optical Characterisation

Losses imply an exponentially bad scaling of quantum photonics applications. Even the success probability of a simple transmission through a waveguide decreases exponentially in the number of photons. Therefore, low-loss waveguides are crucial for scaling quantum photonic systems and advancing them towards real-world applications. To improve the propagation losses, which are mostly caused by the fabrication process, it

is crucial to measure the losses of the waveguides precisely.

One of the simplest methods is to measure the power before and behind the waveguide and estimate the losses due to the ratio between both. However, one should be careful with this method, as it likewise involves coupling losses, which are typically unknown. Another method is the cut-back method. By measuring the intensity as a function of the waveguide length, the losses can be estimated from the slope. This is done by measuring the transmitted intensity, shorten the sample and measuring the intensity again [168]. However, there are two main drawbacks of this method. First the quality of the end-facets have to be equal for every cutting stage and second it is a destructive measurement technique.

The most common method to characterise the propagation losses is the Fabry-Pérot method, where the losses are measured by the contrast of the Fabry-Pérot resonances [169]. A challenge of this method is that it requires exact knowledge of the end-facet reflectivity. For highly confined waveguides, it is not possible to approximate the reflectivity by the Fresnel coefficient, whereas a possible approach is to estimate the reflectivity via simulations [73].

If the end-facet reflectivity is unknown, another approach to measure the losses are resonators. With different resonator sizes the link between the Q-factor and the round-trip losses allows to calculate the propagation losses [100]. For this technique it is important to know the coupling conditions of the resonator.

Until now there were no established, reliable and comparable methods for loss measurements in LNOI. Our investigations give a deeper understanding of the methods known from conventional lithium niobate and show that they are not easily transferable for LNOI.

43.2 In-house Characterisation

In the last section we introduced several techniques to characterise our devices. Here we explain the most promising characterisation methods for analysing the material properties and the optical properties of KTP or LNOI.

43.2.1 Material Characterisation

It is fundamental to understand the influences of different fabrication processes, e.g., waveguide diffusion, etching or periodic poling. Therefore, we use different approaches to characterise our samples, e.g., microscopy, electron beam microscopy or contact profilometry. Furthermore, we use a simulation tool to describe the distribution of the electric field during periodic poling of KTP and LNOI.

Contact Profilometer

With a contact profilometer (DektakXT® Stylus Profiler - Bruker) it is possible to mea-

sure the surface topography, e.g., the step height of different layer systems [170]. A stylus touches the sample with a specific contact force. Afterwards, it is moved laterally across a line along the surface for a defined time and distance. The position of the stylus along this line is converted from an analogue signal to a digital signal and displayed. From the displayed data it is possible to measure the height of the structures. The resolution of the contact profilometer is controlled by the scan speed and the stylus diameter. We use a $12.5\text{ }\mu\text{m}$ stylus and a scan speed of $5\frac{\mu\text{m}}{\text{s}}$. In our case the resolution of the DektakXT is limited to 17 nm [171].

Confocal Laser Scanning Microscope

The simplest method to visualise the waveguides is a confocal laser scanning microscope (LEXT OLS4000 - Olympus). The working principle of the LEXT is based on a conventional optical microscope but with a laser beam at 405 nm that is focused onto the sample. The beam can be scanned in the x-y plane. This results in a real-time image of the sample with a spot size (resolution) of 250 nm [172] in the x-y plane. The focused beam is reflected at the surface of the sample and detected through a pinhole that allows to detect only a small central part of the light. The resolution along the z-direction is 7 nm [171].

CLSM is a straightforward method, where we easily can analyse the sample with the microscope without any preparation and image the structures in a short amount of time.

Scanning Electron Microscope

One possibility to have a high resolution is to use a scanning electron microscope (PI-ONEER - RAITH). In this microscope an image is produced by scanning the sample with a focused electron beam. As the primary electron beam interacts with the material secondary electrons, back-scattered electrons and characteristic X-rays are generated, which can be detected and formed to images [173]. With this microscope it is possible to use the secondary electrons and back-scattered electrons to achieve images with a resolution of 10 nm [174].

For the imaging of our non-conductive samples we have to prepare the samples beforehand. We cover the sample with a conductive layer, e.g., silver or carbon, to avoid surface charges. Afterwards, we mount the sample on a holder inside the SEM. With a focused electron beam it is possible to take high resolution images.

Energy Dispersive X-ray Spectroscopy

Energy dispersive X-ray spectroscopy (JSM-6060 - JEOL) is an analytical technique used for elemental analysis and is commonly used in combination with a SEM. EDX detects the generated characteristic X-rays from the primary electron beam of the SEM. The intensity and energy of the characteristic X-rays is analysed by an energy-dispersive spectrometer. The energies are characteristic for every element as the energies between two shells of the atomic structure [165].

We use EDX to analyse our rubidium exchanged waveguides in KTP. To perform the

EDX measurements, we polish one end-facet of the sample and we sputter (SC7640 - Quorum Technologies) a thin 13 nm layer of silver on the polished end-facet. The conductive material prevents the surface charging and at the same time the characteristic X-ray energy of silver differs strongly from the elements of KTP. One more advantage of the thin layer is the possibility to see the waveguides in the SEM directly, which simplifies the measurement procedure. We mount the sample in a holder with the end-facet facing the top. We use an excitation voltage of 12 keV and a spot-size of 55. Figure 4.11 a) shows a line-scan along a waveguide.

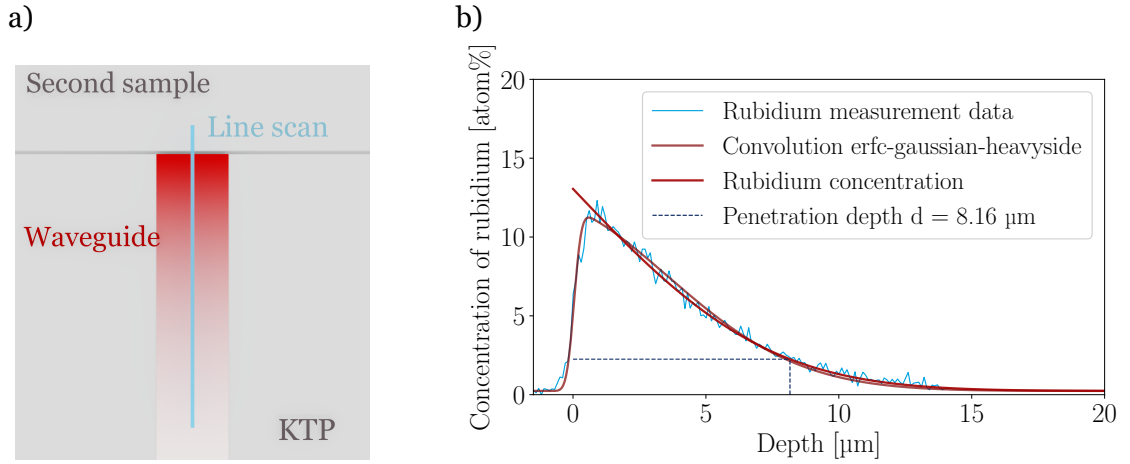


Figure 4.11 – a) Geometrical orientation of the line-scan for the EDX measurement, with respect to the waveguide at the sample end-facet. b) Measured rubidium concentration (blue) and the fit of the convolution of the predicted complementary error, Gaussian and Heaviside function (dark red). The reconstructed concentration profile is shown in red and the calculated depth is given for a $3.0 \mu\text{m}$ channel waveguide in KTP.

We take 32 measurements along a line on the end-facet of each waveguide. With this we analyse the concentration of the individual elements depending on the depth of the waveguide. In particular, we are interested in the concentration of the rubidium atoms in KTP as a function of the waveguide depth as shown in figure 4.11 b). The measured profile indicates a tendency that is consistent with the mentioned 1D diffusion model in section 3.3.1.4. The measured EDX data is a convolution of various process parameters such as the shape of the excitation beam and sample edge effects. The predicted complementary error function is convolved with a Gaussian and a Heaviside function and fitted to the measured data in dark red to determine the concentration profile. The edge of the sample is described by the Heaviside function. We use a Gaussian function that characterises a 220 nm wide excitation beam to calculate the spread of the electron

beam with a Gaussian distribution. The red line shows the reconstructed rubidium concentration profile of a waveguide. We can determine the penetration depth using this reconstructed concentration profile, which is described by equation 3.90.

Raman Spectroscopy

EDX can only detect atomic stoichiometry and not stress or other structural features such as disorder or defects in the crystal. Therefore, we use Raman spectroscopy to look for exchange-induced stress. The Raman imaging is carried out in a similar experimental configuration as the EDX measurements 4.11 at the end-facet of the waveguide. The incident light is focused on the surface, and the scattered light is collected backwards using the same objective. The incident and measured light polarisations are both parallel to the z -direction of the crystal, allowing for the detection of A_1 -TO phonons [163]. Here, the stress directly corresponds to the intensity of the Raman signal. During my PhD, we had access to Raman spectroscopy, where the measurements were performed by Dr. M. Rüsing from the group of Prof. Dr. Artur Zrenner.

Selective Etching

Selective Etching is a simple technique to visualise the domain structure, since it does not require special equipment. For many ferroelectric materials, there are chemical etchants, which etch the two crystallographic faces $+z$ and $-z$ with different rates [175]. This gives the possibility to visualise the domains with a CLSM through different height profiles.

For KTP we use a mixture of KOH and KNO_3 solved in water (weight ratio 44:33:200) at 80 °C for typically 60 min, which results in approximately 100 nm height difference between the poled and unpoled domains. The solution attacks mainly the $-z$ -face, while the $+z$ -face stays almost untouched [118].

For lithium niobate (z -cut) we typically use an ammonia solution (water, hydrogen peroxide (H_2O_2) and ammonium hydroxide (NH_4OH) with volume ratio of 70:20:10) for 20 min at 40 °C in an ultrasonic bath to softly selectively etch the domains and visualise the structure. In the case of x -cut LNOI, we cannot use selective etching, since it only reveals the domains at the polar faces of a ferroelectric crystal, which is in lithium niobate the y - and z -surface [176]. This is the reason, why we have to use other methods like SH microscopy to analyse the domain formation.

Second-Harmonic Microscopy

Second-harmonic microscopy is a method to analyse the ferroelectric domains in a non-destructive way. We use a focused pulsed laser beam at 800 nm, which generates at the surface a second-harmonic signal. The second-harmonic light is sensitive to crystallographic changes and therefore, the intensity is changed in the presence of a domain wall. The change in the sign of the nonlinear susceptibility at the domain walls and therefore, destructive or constructive interference of light generates the SH contrast pattern [177]. However, the signal does not contain information about the orientation of the domains.

Moreover, the lateral resolution is limited to 300 nm [178]. During my PhD, we had access to SH microscopy, where the measurements were performed by P. Mackwitz and Dr. G. Berth from the group of Prof. Dr. A. Zrenner.

Simulation of Electric Fields

For the electric field poling of KTP and LNOI it is of great interest to analyse the electric field distribution within the sample. We use the AC/DC Module from COMSOL to investigate the behaviour of the electric field depending on the electrode structure.

In KTP we design a bulk KTP sample ($z = 1$ mm) with a periodic insulation layer, with a period Λ and a resist thickness r . We use a uniform contact on the top of the sample with the resist structure and on the backside of the crystal to imitate the contacts during electric field poling. At this configuration we can apply a voltage V . Figure 4.12 a) shows the designed electrodes in KTP.

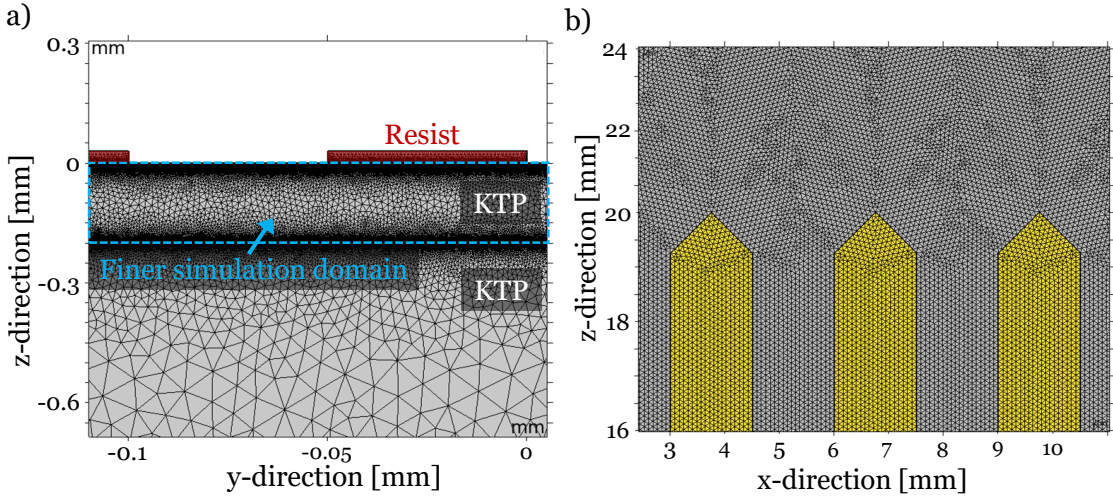


Figure 4.12 – Schematic electrode design in COMSOL of the used structures for periodic poling in KTP (a) and LNOI (b). For KTP the periodic poling proceeds in z -direction through the crystal, whereas for LNOI finger electrodes are used to apply electric fields in z -direction on the surface of the crystal. For both cases, the mesh is indicated by black triangles.

In case of LNOI we design electrode fingers facing each other with a gap g , a period Λ , a length of l and different shapes of the finger tips. We contact the fingers via contact pads to apply an uniform voltage V . Figure 4.12 b) shows the designed finger electrodes in LNOI.

We used in both cases a triangular mesh as a simulation domain. The size of the mesh is dynamically changed depending on the geometry of the objects and therefore, is more dense at interfaces.

With this program it is possible to simulate the electric field distribution depending on different electrode geometries and this allows for the optimisation of electrode shapes and thicknesses for our fabrication routine.

43.2.2 Optical Characterisation

It is necessary to examine the quality of waveguides before using them for advanced integrated circuits. For this analysis, we used for KTP an already existing setup and built a new mechanical stable optical setup for the special needs of LNOI in terms of high precision position control. Moreover, we used simulation tools to extract information about the guiding properties of our waveguides.

Simulation

There are two main properties we would like to know about our waveguides, which are the spatial modes and the corresponding effective refractive indices. We have two different software tools to model our structures. These are RSoft, which we use for modelling for KTP and Lumerical for LNOI waveguides.

RSoft

For the waveguide properties of KTP, we use the FemSIM tool from RSoft, which is a finite element model software. With this tool we can simulate the spatial modes and effective refractive index n_{wg} of our waveguides. Therefore, we implement the model presented in section 3.3.1.4 in FemSIM. Using this we can investigate different geometrical structures we fabricated and compare the measured results with the modelled ones. The model requires two geometrical parameters of the waveguide, which are the width w and the depth d of the waveguide. For the width we use the measured width of the titanium mask and for the depth d we use the measured penetration depth retrieved from the EDX measurements. Figure 4.13 shows the refractive index profile given by the previously introduced model, presented in section 3.3.1.4, as a basis for the simulation.

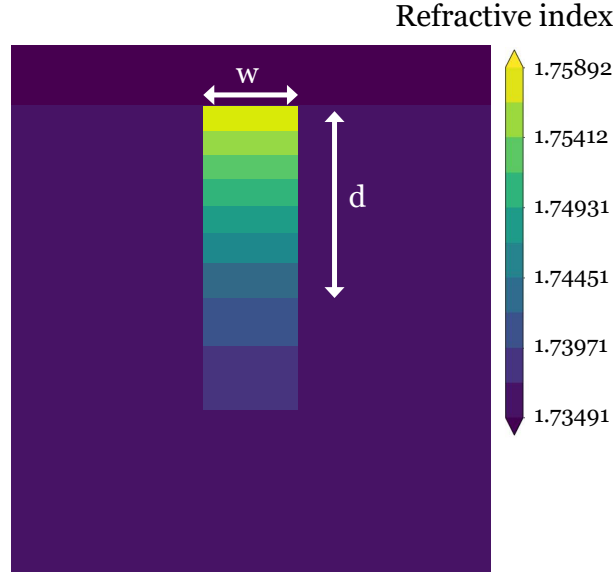


Figure 4.13 – Representation of the waveguide geometry used in RSoft to calculate the modes in KTP. With increasing depth, the refractive index of the waveguide decreases following a complementary error function profile.

As described in section 3.3.1.4 we assume an asymmetrical profile for the waveguide along the x- and y- direction. The waveguide is surrounded by a material with the refractive index of bulk KTP n_{bulk} and the crystal is surrounded by air with $n = 1$. We assume a complementary error function in y-direction and a box function along the x-direction. The simulation domain is $30 \mu\text{m} \times 22 \mu\text{m}$ discretised in steps of 100 nm along the x- and y-direction. From the simulations we retrieve the spatial mode distribution and the effective refractive index for a given polarisation and wavelength. In section 5.1.2.3 we will describe our approaches to optimise this model to our fabricated samples.

Lumerical

The simulation of waveguides in LNOI is more challenging and less established than the simulation of titanium in-diffused waveguides in conventional lithium niobate. Between these two waveguide types there is a strong reduction of the waveguide size and a transfer from micro- to nano-optics. In this case the approximation of waveguide dimensions larger than the wavelength is not true any more. Hence, the description of strongly guiding waveguides necessitates advanced numerical approaches.

For the waveguide properties of LNOI, we use Lumerical MODE Solutions. With Lumerical we can simulate the spatial modes and effective refractive indices of different waveguide geometries as a function of the wavelength. By post-processing we are able

to investigate nonlinear processes, which could be available in LNOI waveguides.

Using the MODE Solution package from Lumerical we can investigate different geometrical structures. We design a waveguide by defining the parameters for the waveguide top width w , etching depth d , thin-film thickness t , sidewall angle θ and a cladding c of SiO_2 . Figure 4.14 shows a designed waveguide.

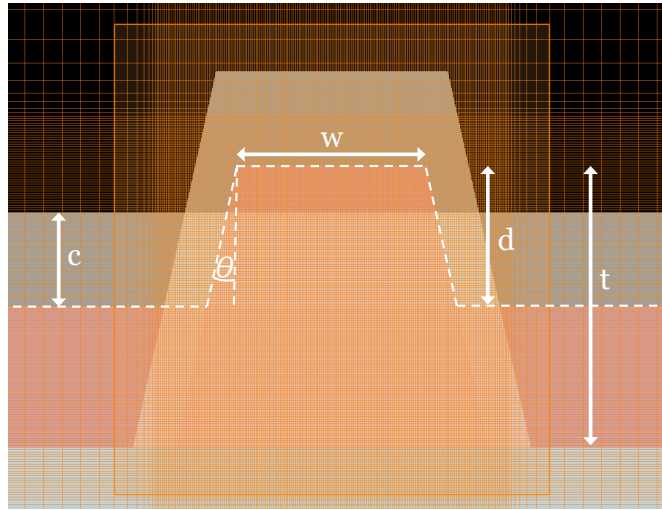


Figure 4.14 – Representation of a waveguide geometry designed in Lumerical for LNOI. The domain mesh is indicated with orange lines.

The waveguide is centred in a $6\text{ }\mu\text{m} \times 6\text{ }\mu\text{m}$ simulation domain discretised in steps of 100 nm along the x- and z-direction. We use a refined mesh in and 100 nm around of the waveguide structure with steps of 10 nm along the horizontal direction and 5 nm along the vertical direction. With this refined mesh discontinuities of the magnetic and electric field can be tracked accurately, without a larger extended refined mesh, which will increase the computational time. To avoid numerical artefacts the mesh is optimised for a mesh-independent refractive index of the modes at 1550 nm. Moreover, the simulation domain is surrounded by perfectly matching layers (PML), which is a default boundary condition available in Lumerical. PML imitates perfectly absorbing layers to also avoid numerical artefacts due to the finite extent of the simulation domain.

With this program it is possible to simulate fundamental and higher order spatial modes of different waveguide geometries. Furthermore, we get the effective refractive index of the individual modes n_{eff} and the polarisation fraction of the modes. In strongly guiding waveguides the polarisations are no longer decoupled and more complex modes can arise, such as hybrid modes, where we can have significant components along the propagation direction.

The polarisation fraction is a value, which reveals the fraction of the polarisation that is

oriented along the horizontal direction, meaning the TE polarisation. If the polarisation fraction is equal 1, it is a quasi-TE mode and if the polarisation fraction is equal to 0, the polarisation is 90 ° rotated and corresponding to a quasi-TM mode. We distribute all fractions below 0.5 to a qTM mode and all above to a qTE mode. Strictly speaking, a value differing from 0 or 1 has to be recognised as a hybrid mode. If the polarisation fraction is equal to 0.5, the mode is maximally hybridised.

We calculate the n_{eff} of the fundamental qTE and qTM modes for different geometries for wavelengths between 400 nm and 2500 nm. We fit the dispersion of each waveguide geometry to the following empirical model [73]

$$n_{\text{eff}}^{e/o}(\lambda, T) = n_{\text{bulk}}^{e/o}(\lambda, T) + A^{e/o} \cdot \lambda^3 + B^{e/o} \cdot \lambda^2 + C^{e/o} \cdot \lambda + D^{e/o} \cdot \sqrt{\lambda} + E^{e/o} + F^{e/o} \cdot \log(\lambda), (4.5)$$

where $n_{\text{bulk}}^{e/o}$ are the bulk Sellmeier equations for LN, described in section 3.3.2.2 and the Sellmeier coefficients A, B, C, D, E, F are fitted and depend on the waveguide geometry. We can also go one step further and do dispersion engineering. The unique and confined structure of LNOI waveguides allows for tuning the effective refractive index, which is highly dependent on the waveguide geometry. This opens the possibility for novel devices in LNOI, which exhibit exceptional properties.

Optical Setup

With the optical setup we analyse the propagation losses and the spatial modes of our waveguides. Figure 4.15 shows the optical setup.

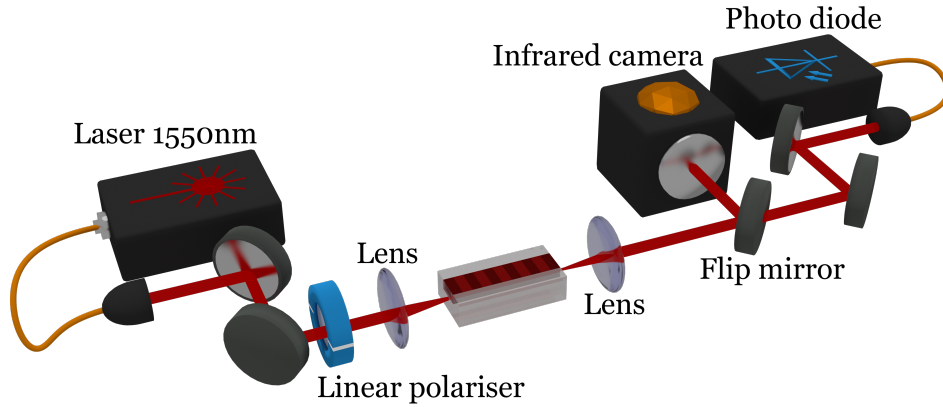


Figure 4.15 – Schematic representation of the optical setup. Laser light at a wavelength of 1550 nm is coupled with lenses in and out of the waveguide. Behind the sample, the light is either imaged on an infrared camera or detected with a photo diode.

The setup consist of a fibre-coupled laser (T100S-HP - EXFO for KTP or TSL-550 - Santec for LNOI) connected to a polarisation controller and a single-mode fibre. The light

is coupled with a lens to free space and reflected by two dielectric mirrors towards the sample. Two lenses before and behind the sample are used to couple in and out of the waveguide. In case of LNOI this setup was more challenging, because these strongly confined and geometrically very small waveguide structures necessitates a higher precision. We had to develop within this thesis a new setup that was mechanically stable and reproducible for efficient waveguide coupling. For this we used for a higher precision flexure stages (Elliot Scientific). Behind the sample, the light is either coupled with a lens in another single-mode fibre or directly detected by an infrared camera (Xeva640 IR - Xenics for KTP or Wildcat 640 U3V 200 - Xenics for LNOI). For LNOI we can replace the in-coupling lens with a lensed fibre to couple into the waveguide.

Propagation Losses

One of the most important parameters to characterise are the insertion losses, which represent the total added losses introduced due to the usage of a device. The insertion losses can be divided into coupling losses, reflection losses and propagation losses. Coupling losses occur due to a mismatch between the field and the eigenmodes of the waveguide, e.g., different spatial distributions. Reflections losses are introduced by reflections at the interface between two materials with different refractive indices, e.g., at the end-facet between the waveguiding material and air. Finally, there are propagation losses, which are due to absorption or scattering during travelling of the light field through the structure. Those losses are modelled with Lambert-Beer law

$$P(l) = P(0) \cdot e^{-\alpha \cdot l} \quad (4.6)$$

where $P(l)$ is the power depending on the propagation length l of the light field, $P(0)$ is the input power and α is the linear attenuation coefficient [22]. The propagation losses α , which are typically expressed in $\frac{\text{dB}}{\text{cm}}$, are linked to the attenuation coefficient by

$$\alpha \left[\frac{\text{dB}}{\text{cm}} \right] = 10 \cdot \log_{10}(e) \cdot \alpha \left[\frac{1}{\text{cm}} \right] \approx 4.34 \cdot \alpha \left[\frac{1}{\text{cm}} \right] \quad (4.7)$$

One of the most common techniques to measure the losses inside a system is the Fabry-Pérot method.

Fabry-Pérot

The Fabry-Pérot technique uses the waveguide as a low-finesse Fabry-Pérot resonator due to reflectivity of the polished end-facets [169]. By varying the frequency of a continuous wave (CW) laser the optical length of the cavity is scanned. The transmitted intensity is recorded as a function of the wavelength with the previously introduced optical setup, see figure 4.15. The resulting fringe contrast is used to calculate the losses of the waveguide.

The transmitted intensity is given by

$$I = \frac{(1 - R)^2 \cdot e^{-\alpha \cdot L}}{(1 - \tilde{R})^2 + 4 \cdot \tilde{R} \cdot \sin\left(\frac{\phi}{2}\right)} \cdot I_0 \cdot \eta, \quad (4.8)$$

where R is the reflectivity of the end-facet, $\tilde{R} = R \cdot e^{-\alpha \cdot L}$ is the combined loss-reflection factor, $\phi = 2 \cdot \beta \cdot L$ is the internal phase difference with the propagation constant β , I_0 is the intensity of the laser before the waveguide and η is the coupling efficiency to the waveguide mode.

By changing the wavelength, the phase changes and the intensity oscillates due to constructive and destructive interference of the light field in the resonator. Figure 4.16 shows the intensity oscillations depending on the wavelength of the resonator.

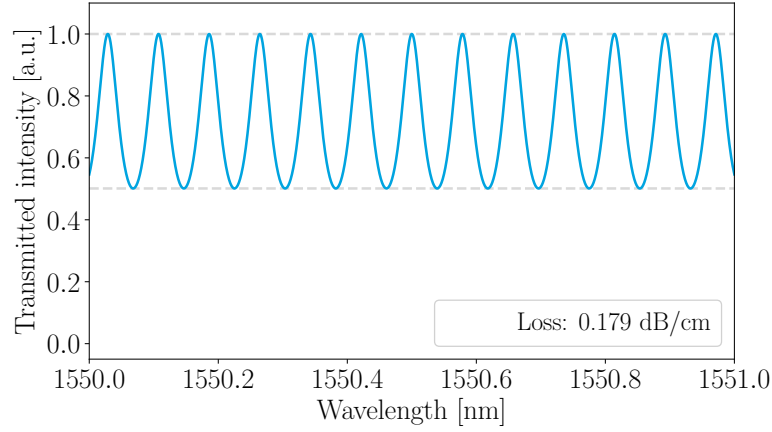


Figure 4.16 – Schematic representation of the transmitted intensity as a function of the wavelength for a Fabry-Pérot resonator. The losses can be calculated from the contrast in the intensity for a known reflectivity.

The contrast K can be calculated from the maxima I_{\max} and minima I_{\min} in the intensity signal

$$K = \frac{I_{\max} - I_{\min}}{I_{\max} + I_{\min}}. \quad (4.9)$$

The contrast is independent of I_0 and η and only a function of \tilde{R} as

$$K = \frac{2\tilde{R}}{1 + \tilde{R}^2}. \quad (4.10)$$

Solving this equation for \tilde{R} and using $\tilde{R} = R e^{-\alpha L}$ with the sample length L , we get the loss α [169] in dB/cm by

$$\alpha = \frac{4.34}{L} (\ln R - \ln \tilde{R}). \quad (4.11)$$

If we know the reflectivity of the polished end-facet and consider in a case of low-finesse waveguide resonators $\tilde{R} \approx \frac{K}{2}$, we can calculate the loss by

$$\alpha \left[\frac{\text{dB}}{\text{cm}} \right] \approx \frac{4.34}{L} (\ln R + \ln 2 - \ln K). \quad (4.12)$$

We can estimate the losses of a waveguide by measuring the transmitted intensity as a function of the wavelength.

For KTP we estimate the reflectivity using the Fresnel-reflectivity for weakly guiding waveguide structures and it can be calculated by [179]

$$R = \frac{(n_{\text{eff}} - 1)^2}{(n_{\text{eff}} + 1)^2}, \quad (4.13)$$

with the effective refractive index n_{eff} depending on the wavelength.

We can calculate the refractive index in KTP with the Sellmeier equation 3.92 introduced earlier. This leads to a reflectivity of $R_{\text{qTE}}=0.075$ and $R_{\text{qTM}}=0.086$ at a wavelength of 1550 nm. In case of LNOI we cannot use equation 4.13, because using this approximation of the reflectivity of end-facets for strongly guiding waveguides can lead to considerable errors, as discussed in [180]. As a result we need to use finite difference time domain (FDTD) simulations in Lumerical [73] to calculate the end-facet reflectivity of our waveguides. Hence, we estimate the reflectivity between 13 % - 17 % depending on the geometry of the waveguide used in this thesis.

The reflectivity R is a crucial parameter to calculate the losses, if this parameter is not known or differs strongly from the real value, it is impossible to calculate the correct losses.

Spatial Modes

Besides propagation losses, the spatial modes are a key factor to describe a waveguide. With knowledge about a spatial mode, we are able to calculate the mode overlap to an optical fibre or the mode overlap between the fundamental pump mode and second-harmonic mode.

We measure the modes at 1550 nm with the optical setup presented in previous paragraph 4.3.2.2. With a polariser before the waveguide we can select the polarisation to be qTE or qTM. The out-coupled light from the waveguide is imaged on a camera with a $100\times$ microscope objective. With this technique it is possible to distinguish between the fundamental modes and higher order modes. Moreover, we can image the shape of the mode depending on the polarisation. We use this technique to measure the modes of KTP waveguides. For LNOI we use simulations to estimate the spatial modes, see section 5.2.4.1.

Couplers

As explained in section 3.1.2 light can couple between two waveguides if the distance between them is small enough. With our technology we were able to fabricate structures down to a coupling gap G of $1\text{ }\mu\text{m}$ and measure with our optical setup waveguide top width w of $0.5\text{ }\mu\text{m}$.

Our aim is to investigate different coupler geometries by simulating the symmetric and antisymmetric modes for two waveguides next to each other in Lumerical. In section 5.2.4.2 we explain the details of the simulation.

The measurement is performed for the most promising geometry compromising fabrication limitations and desirable coupling behaviour. We investigate the fabricated coupler structures by measuring the coupling ratio in our optical setup with a camera as introduced in paragraph 4.3.2.2. We analyse different coupler structures by taking an image for each as shown schematically in figure 4.17.

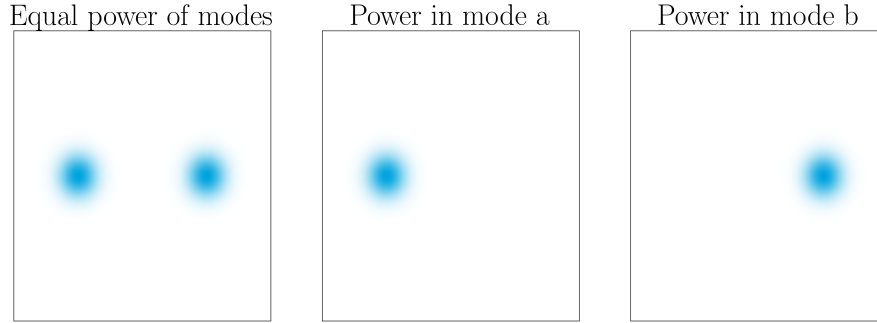


Figure 4.17 – Simulated output modes of a directional coupler. Depending on the coupling ratio between the two adjacent waveguides, spots with different intensity can be detected.

Depending on the coupling behaviour, we image two modes with different intensities. We calculate the power ratio $P_{A_{\text{norm}}}$ from the intensity I_i of the imaged modes by

$$P_{A_{\text{norm}}} = \sqrt{\frac{I_{\text{mode}_a}}{I_{\text{mode}_a} + I_{\text{mode}_b}}} \quad (4.14)$$

This calculated power is equal to the power in mode a from equation 3.40 normalised by the input power B_0 . Inserting the coupling coefficient with equation 3.45 we get

$$P_{A_{\text{norm}}} = \sin^2\left(\frac{\pi\Delta n}{\lambda} \cdot L_x\right). \quad (4.15)$$

Nonlinear Optical Setup

To characterise the nonlinear properties of our samples we analyse the phase matching spectra of the second-harmonic field. Figure 4.18 shows the setup used for the second-harmonic analysis.

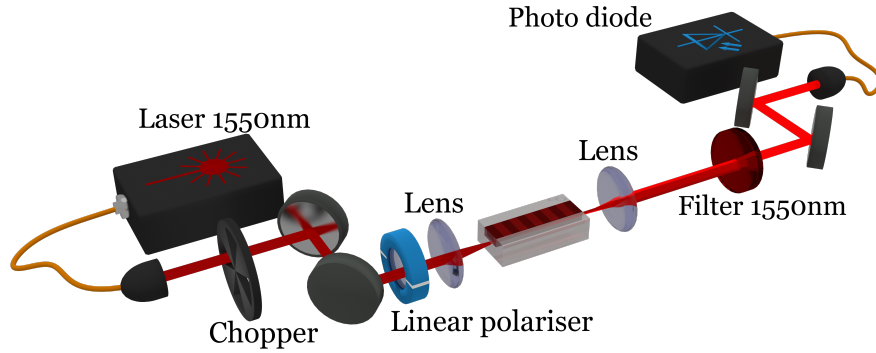
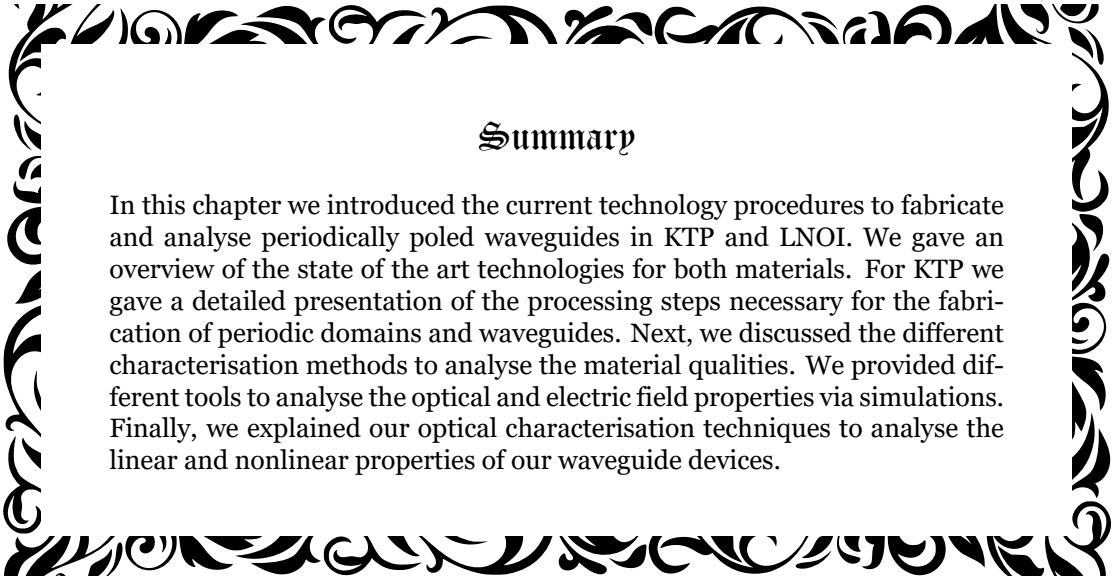


Figure 4.18 – Schematic representation of the setup for the second-harmonic measurements.

We use a fibre-coupled pump laser (Osics TUNICS - EXFO for KTP or T100S-HP - EXFO for LNOI), which is tunable in the range of 1260 nm - 1360 nm or 1490 nm - 1590 nm. The light passes through a chopper that works alongside with a lock-in amplifier (7265 - EG&G INSTRUMENTS for KTP or SR850 - Stanford Research Systems for LNOI). To set the input polarisation of the fundamental field, a polariser is placed in front of the sample. The in- and out-coupling to the waveguide is done with anti-reflection (AR) coated aspheric lenses. In case of LNOI, we use a long-pass dichroic mirror with a cut-off wavelength of 1000 nm. Finally, a silicon photodiode connected to a lock-in amplifier is used to measure the second-harmonic light. The lock-in amplifier functions as a band-pass filter, screening the background noise and enhancing the signal-to-noise ratio. This allows for measuring the phase matching spectra of the second-harmonic field as a function of the tuned fundamental wavelength. For the phase matching spectra we expect a sinc-squared shaped intensity distribution as described in the previous section 3.2.3.2.



Summary

In this chapter we introduced the current technology procedures to fabricate and analyse periodically poled waveguides in KTP and LNOI. We gave an overview of the state of the art technologies for both materials. For KTP we gave a detailed presentation of the processing steps necessary for the fabrication of periodic domains and waveguides. Next, we discussed the different characterisation methods to analyse the material qualities. We provided different tools to analyse the optical and electric field properties via simulations. Finally, we explained our optical characterisation techniques to analyse the linear and nonlinear properties of our waveguide devices.

*It's not that we use technology,
we live technology!*

Godfrey Reggio

Technology Results

Contents

5.1 Potassium Titanyl Phosphate	89
5.2 Lithium Niobate On Insulator	119
5.3 Final Remarks	165

quality technology. We show and compare the results for different fabrication procedures, discuss the most promising techniques and give final remarks for further optimisation possibilities.

In this chapter, we present our technological results for KTP and LNOI. In the following, we show the progress towards optimising and increasing the quality of periodically poled waveguides in KTP. For LNOI we present the development of a new technology and thus, the important intermediate steps to achieve a reliable and high

5.1 Potassium Titanyl Phosphate

We introduced the unique properties of KTP in section 3.3.1 and the fabrication procedures of periodically poled waveguides in KTP in section 4.1. As already mentioned this platform is still in an exploratory stage and the fabrication methods are not completely sophisticated and require individual improvement of each process step.

5.1.1 Periodic Poling

Before the fabrication of periodically poled waveguide structures, we have to analyse and understand the poling behaviour of KTP. First, we had a look at the influence of the insulation mask on the electric field distribution during periodic poling via simulations with COMSOL. After that we show our optimised optical monitoring technique for an enhanced control during periodic poling and setting a switch-off criterium for a 1:1 duty cycle. Last, we investigated the poling behaviour and back-switching characteristics of

KTP and RbKTP.

5.1.1.1 Electric Field Distribution in KTP

We model the electric field to better understand the poling process. By doing this one is able to optimise the resist layer for different poling periods and to get an ideal duty cycle. For this, we implemented a model in COMSOL, presented in section 4.3.2.2. We used this model to determine how strong the electric field strength is under the insulation layer depending on the thickness and width of the insulation layer and the applied voltage [181]. Figure 5.1 shows the parameters in blue, which we set for our simulations and in red the parameters we investigated.

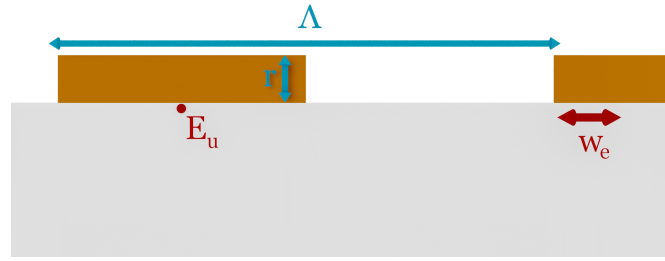


Figure 5.1 – Schematic representation of the parameters in our COMSOL model. The parameters, which we set for our simulations are blue and in red are the parameters we investigated.

As described in section 4.1.2.1 we use a $2.5\text{ }\mu\text{m}$ thick resist layer as an insulation layer for our periodic poling. We need to know if this thickness is sufficient to fulfil our requirement during poling of insulating the material, when we apply high voltage pulses. We investigated different resist thickness r namely $0.5\text{ }\mu\text{m}$, $1\text{ }\mu\text{m}$, $3\text{ }\mu\text{m}$ and $5\text{ }\mu\text{m}$, which are feasible to produce with our technology. We know from literature that the coercive field strength in KTP is $2.1\text{ }\frac{\text{kV}}{\text{mm}}$ [48], but the first nucleations already appear at electric field strength of $1.7\text{ }\frac{\text{kV}}{\text{mm}}$ [48]. Therefore, we set this value as the critical electric field strength, at which the poling starts. Figure 5.2 shows the electric field distribution in KTP for a poling period of $100\text{ }\mu\text{m}$ and different resist thickness of $0.5\text{ }\mu\text{m}$, $1\text{ }\mu\text{m}$, $3\text{ }\mu\text{m}$ and $5\text{ }\mu\text{m}$ and a voltage of 2.1 kV .

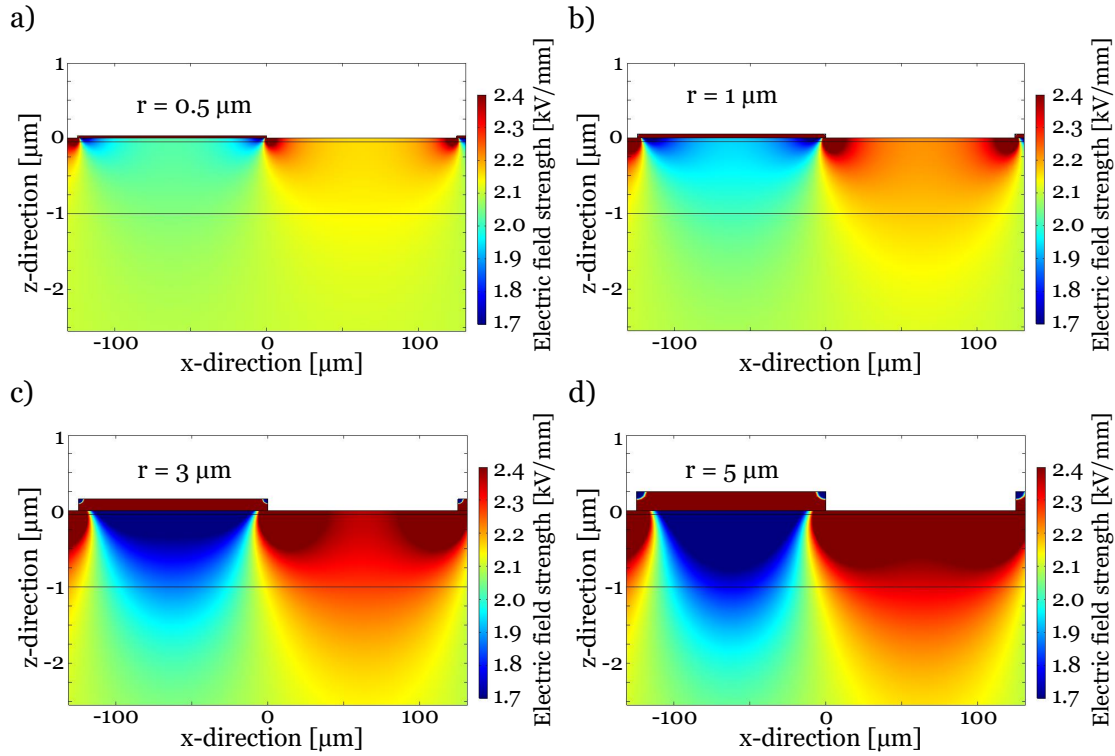


Figure 5.2 – Simulated electric field distribution for periodic poling in KTP. The poling period for all structures is 100 μm and the resist thickness is varied from a) 0.5 μm , b) 1 μm , c) 3 μm and d) 5 μm for an applied voltage of 2.1 kV.

The strength of the electric field strongly depends on the resist thickness. With increasing resist thickness, the strength of the electric fields decreases under the insulation layer and increases between the resist stripes. Due to geometrical reasons, there is extensive fringing of the electric field near the resist edges, where the polar component of the electric field can be much larger than the average field throughout the crystal. The enhanced electric field strength at the edge of the insulation layer is in good agreement with experimental results, where first domain nucleation appears at the edges of the insulation structures [118].

We had a look at the strength of the electric field E_u in the middle underneath the insulation layer, see red dot in figure 5.1. To avoid nucleation underneath the resist we set a hard limit for the electric field strength lower than $1.7 \frac{\text{kV}}{\text{mm}}$. Figure 5.3 shows the electric field strength with an uncertainty of $0.005 \frac{\text{kV}}{\text{mm}}$ underneath the resist layer in the middle depending on the resist thickness for different poling periods.

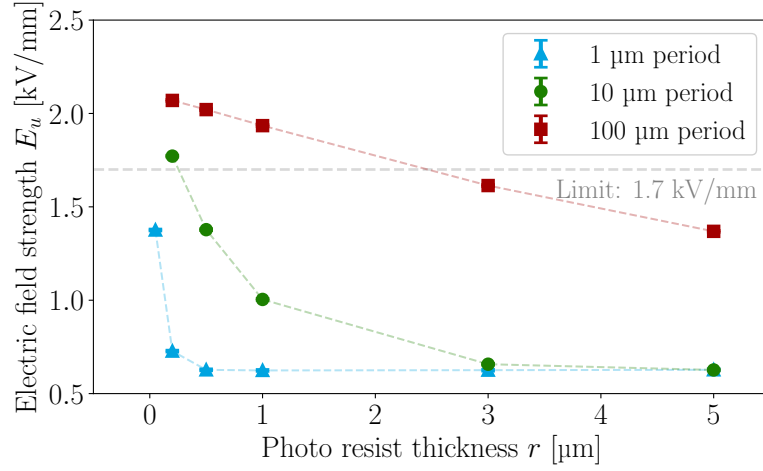


Figure 5.3 – Electric field strength E_u underneath the resist structures. Here, the electric field strength in the centre of the resist is evaluated for different poling periods and as a function of the resist thickness.

It can be seen that with decreasing resist thickness, the electric field strength increases, due to the fact that the resist no longer has an insulation effect. Depending on the poling period we have a minimum resist thickness we should use to avoid fields higher than $1.7 \frac{\text{kV}}{\text{mm}}$ underneath the resist. Especially for larger poling periods, see the red squares in figure 5.3 the resist thickness should not be below approximately $2.5 \mu\text{m}$.

Apart from the electric field strength underneath the resist we have to consider the distance under the resist w_E , where the electric field is above $2.1 \frac{\text{kV}}{\text{mm}}$. This leads to an unavoidable and uncontrollable domain broadening in the periodic poling process. The measurement uncertainty is half of the distance between two mesh points and is $0.01 \mu\text{m}$ for the poling periods $1 \mu\text{m}$, and $10 \mu\text{m}$ and $0.1 \mu\text{m}$ for the poling period $100 \mu\text{m}$. Figure 5.4 shows the distance of the coercive field strength under the resist for different poling periods depending on the thickness of the resist.

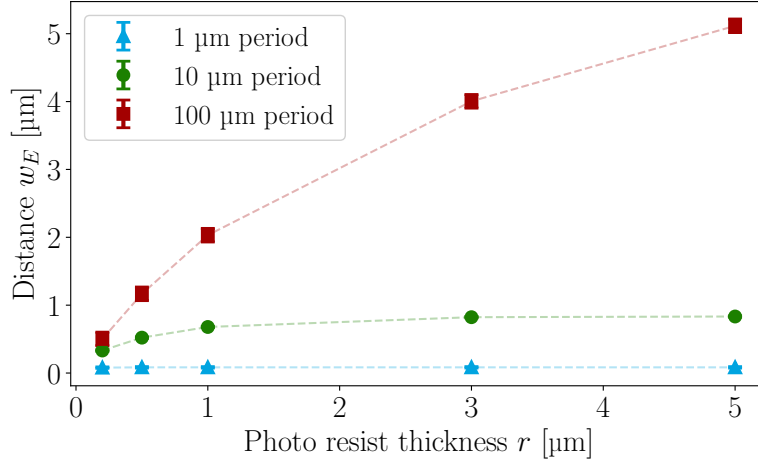


Figure 5.4 – The distance under the resist, where the electric field is above the coercive field strength, for different poling periods depending on the thickness of the resist.

This figure shows that for all poling periods the distance w_e of the electric field strength above $2.1 \frac{\text{kV}}{\text{mm}}$ under the resist increases with increasing resist thickness. Furthermore, it can be seen that the w_e saturate at a certain value depending on the poling period. To allow for fabrication errors and therefore, varying photo resist thicknesses, we should use a sufficiently thick resist layer. As a result, the fabrication errors do not influence the total distance under the resist and we get a more reproducible domain broadening. Besides that, a thicker layer has the advantage of a higher electric field extinction of the electric field below the resist. One has to note that we have to vary the resist thickness for different poling period into account. A thick resist of $2.5 \mu\text{m}$ does not have a huge impact on fabrication of poling periods of $100 \mu\text{m}$ but it is technological challenging to fabricate poling periods around $1 \mu\text{m}$ with such thick resist. But at the same time, these simulations show that for smaller periods we can use thinner photoresist layers to compensate this challenge.

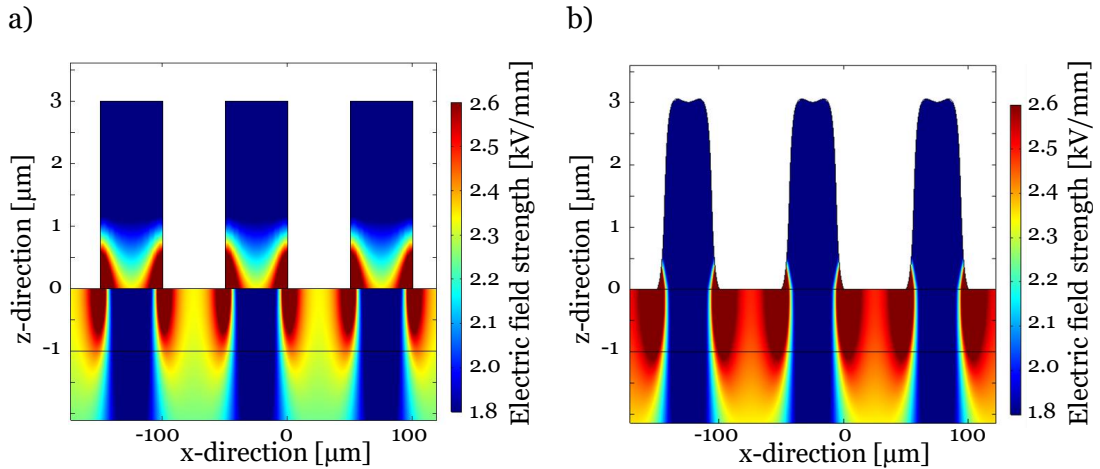
With a thicker resist layer we can tolerate the domain broadening by compensating this with an optimised duty cycle in the mask layout. For this purpose, we have to adjust the duty cycle of the resist structure and increase the length of resist strip by $2 \cdot w_e$. Table 5.6 shows the optimised mask duty cycle for the three simulated poling periods.

Table 5.6 – Optimised mask duty cycle for three simulated poling periods [181].

Poling period [μm]	Resist thickness [μm]	Duty cycle (resist : no resist)
100	3	1.16 : 0.84
10	3	1.32 : 0.68
1	3	1.34 : 0.66
1	0.5	1.34 : 0.66

This table shows that for our current resist thickness around $3\text{ }\mu\text{m}$, we need to change the duty cycle and in particular for smaller poling periods. Table 5.6 also shows the duty cycle for the smallest poling period of $1\text{ }\mu\text{m}$ for the thickness of $0.5\text{ }\mu\text{m}$. This indicates that we can optimise for the smaller poling period the mask design and still can alternate the resist thickness to find the best poling results.

It has to be noted that these simulations were done with perfectly rectangular shapes for the resist structures. From our technology procedure we know that we get a rounding of the corners during the hardbake. We simulated the behaviour of the rounded corners and see no significant changes in the distribution of the electric field strength depending on the shape of the resist structure. Figure 5.5 shows the electric field distribution for rectangular and rounded resist structures.

**Figure 5.5** – Simulated electric field distribution for KTP poling with differently shaped resist structures. The simulations are performed using COMSOL with an applied voltage of 2.1 kV for a) rectangular and b) rounded resist structures.

Only the strength of the electric field in the case of rounded resist structures is increased between the resist patterns. This was expected, since there is no sharp corner in the si-

mulation domain, which increases the local electric field. This shows that the rounded corners do not have a huge impact on the overall electric field distribution. It even shows that these types of structures benefit from a more homogeneous electric field distribution and therefore, a more homogeneous poling over the non-insulated regions. This results shows, that the unavoidable rounded resist structure during fabrication does not have a negative impact on the periodic poling process and the duty cycle for the structure dimensions in this thesis.

Besides the influence of the electrodes, we need to monitor the poling process, consequently we use an optical monitoring technique.

5.1.1.2 Optimised Optical Monitoring

To switch-off the poling process at an optimal duty cycle, we use an optical monitoring technique. During periodic poling we apply several high voltage pulses to invert the spontaneous polarisation. Until now, we analysed the optical signal in the poling pulse, which is complicated, due to the short amount of time in the rising and falling edge and at the same time additional variations in the plateau. Figure 5.6 shows the optical signal during the poling pulse for three different stages of poling of RbKTP, one pulse below coercive field strength, one poling pulse above coercive field strength and the last poling pulse resulting in a duty cycle of 1:1.

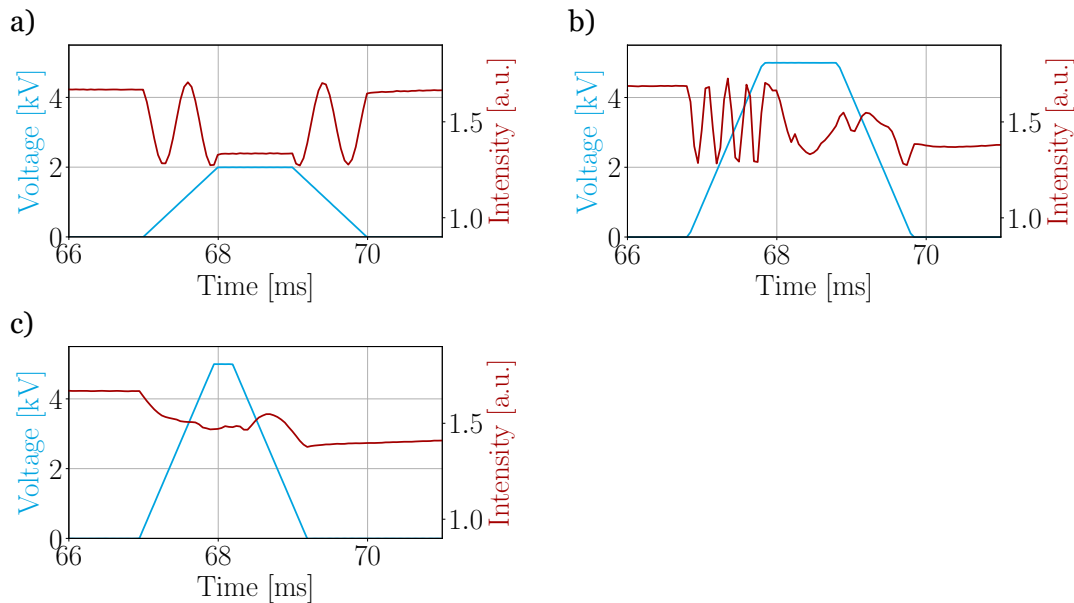


Figure 5.6 – Optical signals for different stages during the poling process. Optical signal in the a) pulse below coercive field strength, b) poling pulse above coercive field strength and c) last poling pulse resulting in a duty cycle of 1:1.

Figure 5.6 a) shows the first pulse and the optical signal is perfectly symmetric as expected, because the field strength is well below the coercive field strength of $4.2 \frac{\text{kV}}{\text{mm}}$ for RbKTP [68] and therefore, there is no poling and the phase retardation does not change. In case of domain inversion in the crystal we can observe a strong difference in the signal in figure 5.6 b) in the rising and falling edge of the plateau voltage. Moreover, we can observe variations of the signal in the plateau voltage region, introduced by the poling and thus, a change in the effective length of equation 4.4. From figure 5.6 c) we would conclude a slightly overpoled domain structure, because we counted a quarter oscillation before and a quarter oscillation after the pulse, meaning the perfect 1:1 duty cycle was reached in half of the plateau time. To analyse the optical signal directly in the poling pulse is not reliable and requires more data. To optimise the analysis we could use shorter pulses, to have more data points and be more accurate, but too many pulses lower the poling quality.

To avoid overpoling we decided to add investigation pulses at 0.5 kV before and after the poling pulse. This allows for more data points, without introducing additional poling, see figure 5.7.

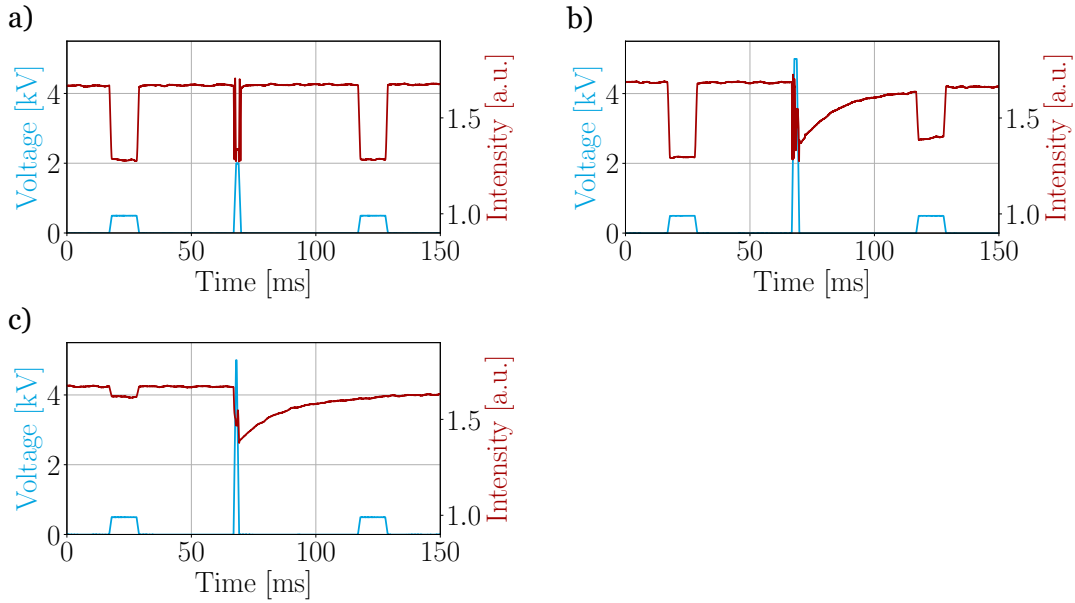


Figure 5.7 – Optical signals during the investigation pulses for different stages of the poling process. Optical signal in the investigation pulses a) with a pulse below coercive field strength, b) a poling pulse above coercive field strength and c) the last poling pulse resulting in a duty cycle of 1:1.

Figure 5.7 a) shows a symmetrical optical signal in the investigation pulses before and after the 2 kV pulse, because this is below the coercive field strength and we do not expect a domain inversion. In figure 5.7 b) we can clearly see a poling progress in the

signal, because the total height of the signal is reduced in the second investigation pulse compared to the first one. Analysing the amplitude of the signal in the investigation pulses gives us a huge improvement in the detection of the duty cycle. Shortly before a perfect 1:1 duty cycle, we can only detect a small part of a oscillations in a rising or falling edge, which is difficult to differentiate. As a result, we use the amplitude of the signal in the inspection pulses to detect these minor variations. In the last figure 5.7 c) we observe a little signal amplitude in the investigation pulse before the poling pulse and no signal amplitude variation in the second investigation pulse. This allows for the conclusion that the duty cycle is 1:1. In other samples, we can observe a switch of the signal amplitude, from a negative drop in the first investigation pulse to a positive rise in the second investigation pulse. These samples are slightly overpoled in the end.

The presented extension of the investigation pulses allows for a reliable technique to monitor the poling progress. With this technique it is possible to determine whether the sample is overpoled or not, which is not possible with a single pulse. This improves the precision of the switch-off and the quality of periodic poling.

5.1.13 Domain Stability in KTP and RbKTP

We used KTP in the last decade as an unique material for different kind of sources, like periodically poled ridge waveguides [114] for second-harmonic generation in the UV regime or periodically poled rubidium exchanged waveguides as a spatially single-mode photon pair source at 800 nm [182]. At the beginning of my PhD we discovered that the periodically poled domains in KTP tend to switch back, i.e., the poled domains invert back to its initial domain orientation, during waveguide fabrication. To improve the homogeneity of periodically poled structures, thus, to fabricate reliable samples and enhance the yield of the quantum optical devices, we investigated this back-switching behaviour in more detail. For this, we periodically poled a KTP sample with a photoresist structure and several millisecond long pulses with high voltages up to $2.7 \frac{\text{kV}}{\text{mm}}$. Afterwards, we fabricated waveguides in this material. From SH microscopy measurements in a periodically poled waveguide, we could observe the first hints of back-switching of the domains in the waveguide [183]. To verify these results we selectively etched the sample and could observe back-switching of the domains in the waveguide, see figure 5.8.

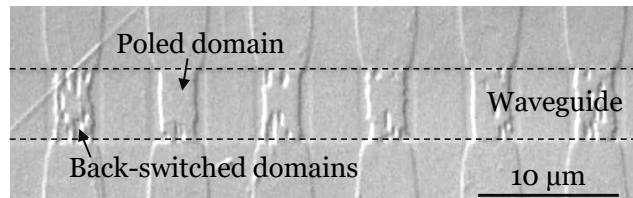


Figure 5.8 – CLSM image of back-switched domains in a selectively etched periodically poled waveguide sample.

For comparison we had a look at a second periodically poled waveguide. Figure 5.9 shows back-switching in the waveguide. Here, some domains are flipped back completely and are merged together to a big initial domain.

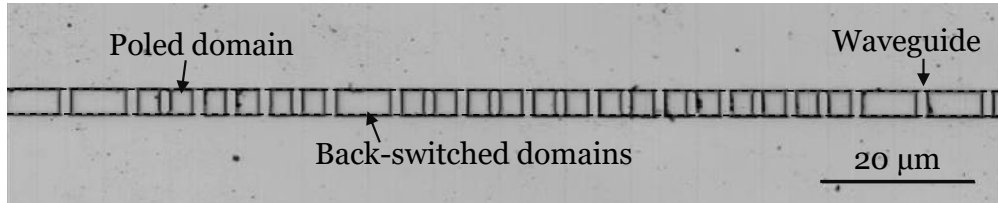


Figure 5.9 – CLSM image of back-switched domains visible in a selectively etched waveguide sample.

This is a clear indication of a domain back-switching during the Rb-exchange. Unstable domains that had grown only halfway through the sample [184] are the reason for the inversion of domains during the Rb-exchange. The exchange process is at high temperatures, which is analogue to a thermal annealing of the domains.

We could verify that the domains switch back by annealing periodically poled samples at 360 °C and at 330 °C. For this purpose we periodically poled samples and selectively etched the surface to reveal the domain structure, see figure 5.10 a).

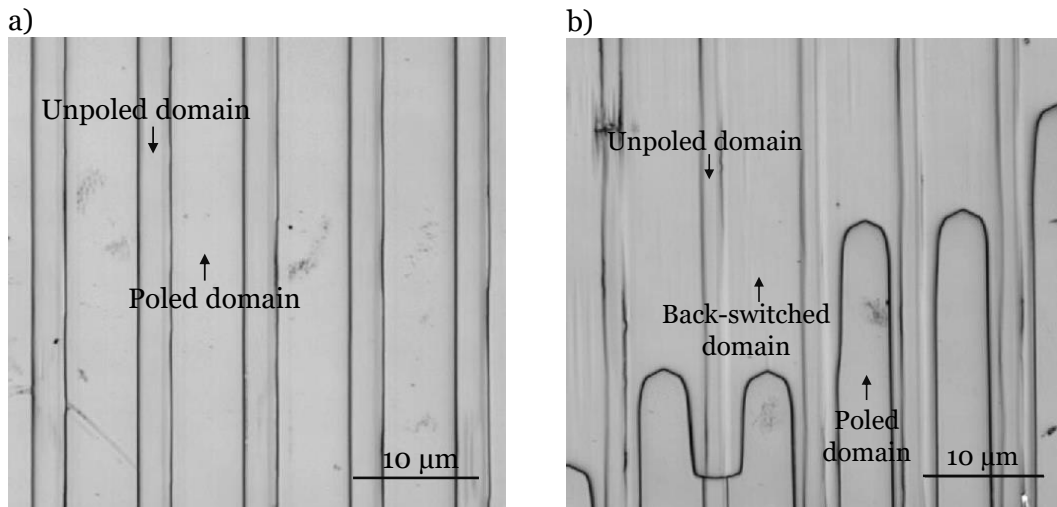


Figure 5.10 – Selectively etched surface revealing the domain structure imaged with CLSM a) after periodic poling and b) after annealing at 360 °C for 60 min.

Afterwards we annealed the samples for 60 min and selectively etched the domains again, which results in a double selectively etched surface. Figure 5.10 b) shows a double

selectively etched surface. In case of partial back-switching we can clearly see double structures, whereas in case of complete back-switching the contrast in the height between the domains stays unchanged compared to the first etching. This shows that the annealing results in a back-switching of the domains in an inhomogeneous behaviour.

To show that the domain back-switching is independent of the poling period, we studied larger poling periods. Therefore, we periodically poled a KTP sample with a poling period of $120\text{ }\mu\text{m}$. For a better visualisation of the back-switching we selectively etched the domains directly after periodic poling. Afterwards, we fabricated waveguides in that material and did a second selective etching. Figure 5.11 shows a back-switching in the waveguide.

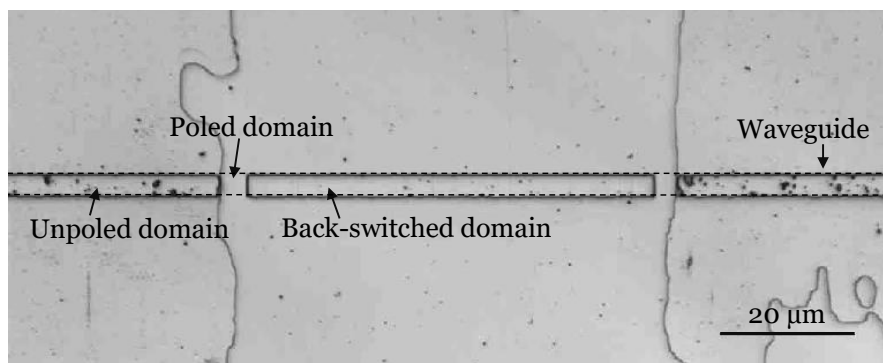


Figure 5.11 – CLSM image of selectively etched back-switched domain structure after periodic poling with a poling period of $120\text{ }\mu\text{m}$ and waveguide fabrication in KTP.

The height profile over the waveguide reveals that only the edges of the previously inverted domains are still inverted, the middle part switched back and was attacked by the selective etchant.

We know from our simulations in section 5.1.1.1 that the electric field is highest at the edges of the resist structure, resulting in an enhanced domain nucleation. The domains rapidly propagate down towards the opposite crystal face. Therefore, these domains are mostly grown completely through the crystal and are the most stable. If the domain propagation down the z -axis is hindered, for example, due to the existence of crystal defects, it is possible that before the domain tips reach the opposite face, domains start to grow sideways and merge. This means that the domains do not grow through to the other side and are more unstable.

Furthermore, we assume that the unstable domains in KTP could be due to lower coercive field strength, which allows for easier back-switching of the domains during annealing. Hence, we consider RbKTP, with a higher coercive field strength than KTP, to be more resistant for unintentional domain inversion. The fabrication technique of periodic poling and waveguides do not differ significantly between RbKTP and KTP.

For a direct comparison to the results of KTP, we periodically poled a RbKTP sample with a poling period of $120\text{ }\mu\text{m}$ and fabricated waveguides in the sample. Via double etching we revealed the change in the domains before and after the Rb-exchange. Figure 5.12 shows an etched surface of a RbKTP crystal.

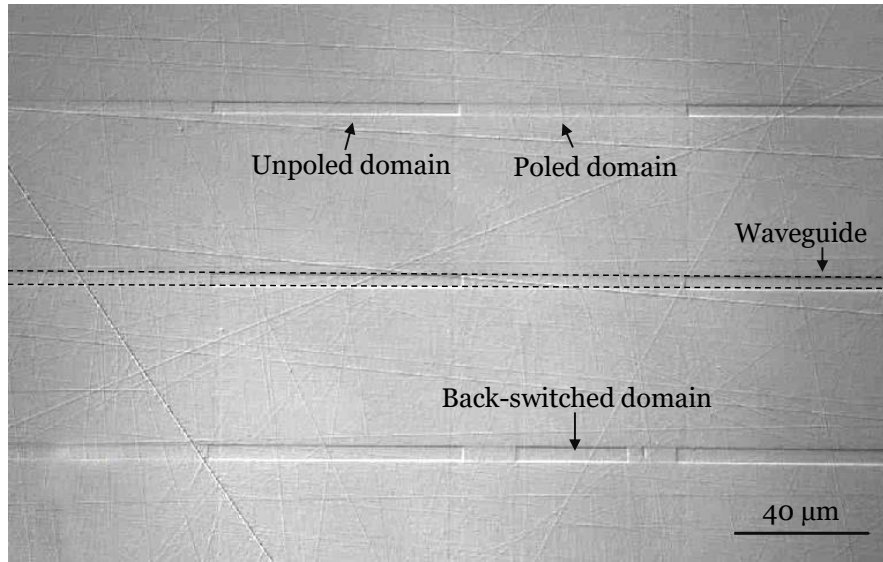


Figure 5.12 – CLSM image of selectively etched surface revealing the domain structure after periodic poling with a poling period of $120\text{ }\mu\text{m}$ and waveguide fabrication in RbKTP.

Even though this sample shows back-switching of the domains in the waveguide, some parts of the waveguides show stable domains in contrast to pure KTP, where almost all domains switched back. This leads to the assumption that in RbKTP it is possible to stabilise the domains during the exchange. We expect that if the domains are completely grown through the crystal the domains are stable against annealing.

To get an insight into the thermal activation of domains and understand the behaviour, we did a Rb-exchange on a KTP sample without periodic poling. After that we selectively etched the surface to visualise the initial domains. In that sample we could observe in the waveguides as well as in the bulk material a huge amount of unstructured nano-domains, see figure 5.13.

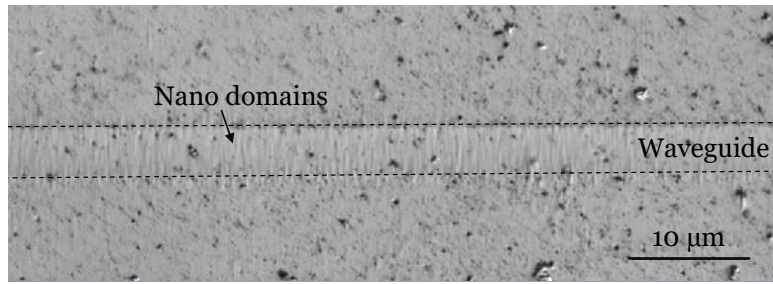


Figure 5.13 – CLSM image of selectively etched surface revealing the nano-domains in and outside of the waveguide structure in KTP.

This shows that we need to reorganise the domains in the crystal before periodic poling to allow for a homogeneous domain inversion during periodic poling. For this reason, we developed a reliable process with preconditioning pulses.

Preconditioning Poling

To homogenise and assure a single orientated domain, we contacted the unstructured sample on both sides with our poling holder. We applied four 5 kV pulses with a plateau time of 30 ms. Following this procedure, the complete sample should have the spontaneous polarisation inverted. Then, we switched the polarity and applied again four 5 kV pulses with a plateau time of 30 ms. This inverts the spontaneous polarisation to its initial orientation and we get a uniform domain in the crystal. We wanted to study the stability of periodically poled domains in preconditioning poled samples. Accordingly, we inverted the domains periodically by applying several millisecond long pulses with voltages up to 5 kV. Afterwards, we fabricated waveguides in this material and the microscope image of this sample is shown in figure 5.14.

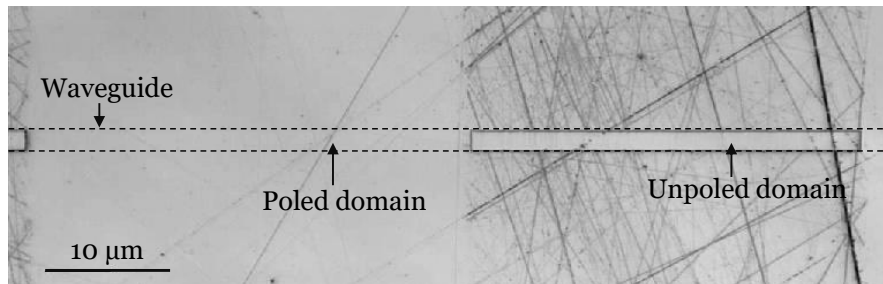


Figure 5.14 – CLSM image of selectively etched surface revealing the stable domain structure after preconditioning poling and periodic poling with a poling period of 120 μm and waveguide fabrication in RbKTP. The scratches are intrinsic in the material and are visible due to the selective etching.

This figure shows the selectively etched surface of RbKTP. The waveguide is present continuously, even though it is not visible in this image due to the selective etching. The scratches are not induced by handling issues they are intrinsic in the material and not avoidable. They are throughout the whole RbKTP surface, but they are only strongly visible due to the selective etching on the -z-face. With a closer look at the +z-face, we can see scratches, only less dominant. The quality with regard to the scratches of the RbKTP material is not as high as for KTP, which is explainable, because RbKTP crystals are not so established. Nevertheless, the domains are a lot more stable in this sample and hence, RbKTP is more favourable. This shows that the new material RbKTP as well as the preconditioning poling have an huge impact on the stability of the domains.

Our objective is to produce efficient sources, which rely on periodic poling and therefore, they rely on the uniformity of the domain structure over the sample length and propagation direction of the optical beam. Two important quality factors are the duty cycle errors as well as missing domains due to defects in the crystal. Hence, we had a coarser look at the complete sample, see figure 5.15.

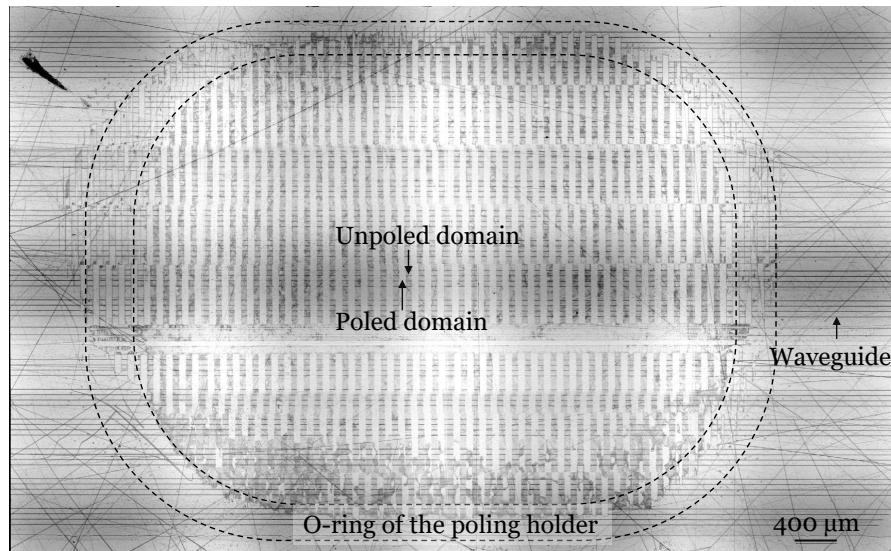


Figure 5.15 – Composite image of the selectively etched surface of a sample, revealing the domain structure after preconditioning poling and periodic poling with a poling period of $120\ \mu\text{m}$ and waveguide fabrication in RbKTP.

The inner ellipse on the sample indicates the poled area on the sample, because the holder is designed with an o-ring for a good contact with the electrolyte. Inside this region we can see the periodically poled structure with poling periods around $120\ \mu\text{m}$. From figure 5.14 we know that the poled domains in the waveguides, which are stable, are not visible after selective etching. This means that all waveguides, which show a

strong contrast, are poled well.

We fabricated another sample this time with larger poling periods between $120\text{ }\mu\text{m}$ and $150\text{ }\mu\text{m}$ in $2\text{ }\mu\text{m}$ increments, to reproduce the results. The groups in the middle of the sample are homogeneously poled over the complete waveguide length. Figure 5.16 shows a periodically poled waveguide group. The three inset-figures show a closer look that the domains are stable over the whole length.

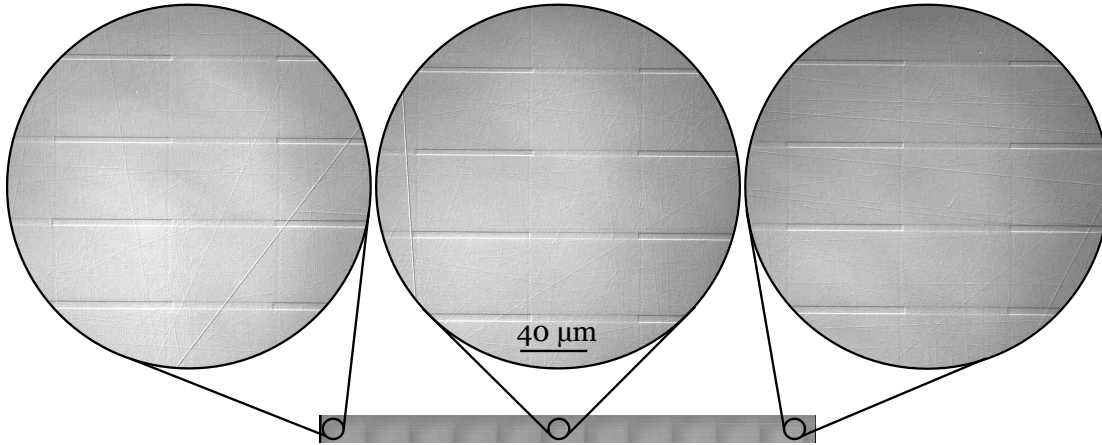


Figure 5.16 – Composite image of the selectively etched surface of a waveguide group, revealing the domain structure after pre-conditioning poling and periodic poling with a poling period of $136\text{ }\mu\text{m}$ and waveguide fabrication in RbKTP. The three insets show a closer view on the stable domain structure after waveguide fabrication over the whole sample.

We measured the variation of the duty cycle over the waveguide length for different waveguide widths of a group in the middle of the sample. Figure 5.17 shows the duty cycle obtained with optimised poling procedure. The measurement uncertainty is $0.5\text{ }\mu\text{m}$ given by the increments of the CLSM, corresponding to 0.007 uncertainty for the duty cycle.

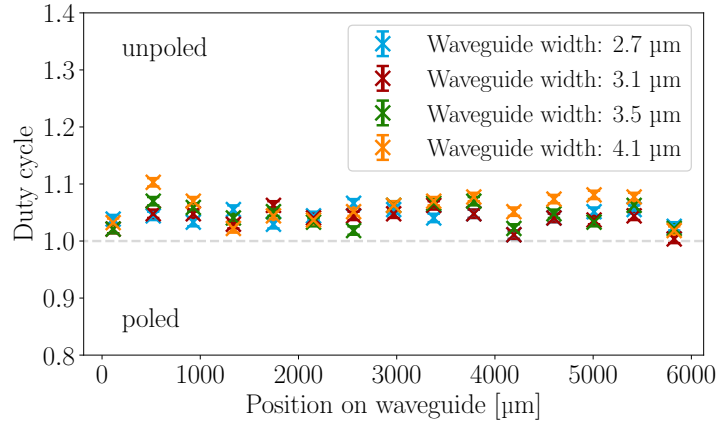


Figure 5.17 – Variation of the duty cycle over the waveguide length for a poling period of $136\ \mu\text{m}$ and different waveguide width. The measurement uncertainty is $0.5\ \mu\text{m}$ given by the increments of the CLSM, corresponding to 0.007 in this scale.

For all waveguide width, the duty cycle is homogeneous over the entire waveguide length. Moreover, the structures are slightly overpoled with a mean value of 1.058 and a standard deviation of 0.023 for the poled domains. This overpoling is not as strong as expected from the simulations with a value of 1.16 . One possible explanation for this could be that the simulations are done for KTP and not RbKTP. For RbKTP we use a higher applied voltage, because the coercive field strength is higher. This could have an influence on the overpoling and thus, a change in the duty cycle. It is not possible to measure the duty cycle for KTP, because the domains switch back and there are no continuous domains to measure.

This homogeneous poling in RbKTP is a huge improvement for the periodic poling of waveguides and the realisation of efficient sources.

5.1.1.4 Final Remarks for Periodic Poling of KTP and RbKTP

We introduced our developed techniques for periodically poling KTP or RbKTP material. To optimise the poling process, we use RbKTP as the substrate material and we take advantage of preconditioning poling to achieve a homogeneous uniform domain in the crystal for periodic poling. We established investigation pulses in the optical monitoring technique to further increase the possibility to have a reliable switch-off criterion during periodic poling for a 1:1 duty cycle. Now, we are able to fabricate reliable periodic structures in RbKTP.

Our simulation results indicated that we should optimise our mask design, to further increase our yield with perfect duty cycle poling. Given the flexibility of a laser-lithography

we could use this tool in the future to further investigate the influence of the resist width and thickness on the domain duty cycle. In the future, it would be an option to test the preconditioning poling in KTP as well.

5.1.2 Waveguides

Besides the periodic poling, we investigated the waveguide properties in KTP and RbKTP. We analysed the width via CLSM, the depth with the EDX method explained in section 4.3.2.1 and measured the modes and losses with the setup introduced in section 4.3.2.2.

5.1.2.1 EDX Analysis

We used an EDX system to characterise the exchange depth in several waveguides with varied widths to better understand the diffusion process. We introduced the technique in section 4.3.2.1 and a more detailed explanation about the technique can be found in [115]. In this section, we present the results of the EDX measurements for KTP and RbKTP, two different melt compositions for the exchange and different waveguide width.

Width-dependent Diffusion Dynamics in KTP Waveguides

For the analysis of the diffusion depth in KTP we fabricated planar waveguides and channel waveguides with different waveguide width, as introduced in section 4.1.2.2. We showed that the penetration depths of the channel waveguides are at least $2\text{ }\mu\text{m}$ deeper than planar waveguides, despite the fact that both are manufactured using the identical fabrication parameters (melt composition of 97 mol% RbNO_3 , 1 mol% $\text{Ba}(\text{NO}_3)_2$ and 2 mol% KNO_3 , $330\text{ }^\circ\text{C}$, 60 min). Furthermore, we saw a definite tendency toward increasing waveguide depth while decreasing waveguide width. These findings clearly showed that a simple model is incapable of representing the entire Rb-diffusion dynamics in KTP. The expected complementary error function is valid when a 1D model is assumed. However, we found that this is invalid when comparing different geometries as shown in figure 5.18.

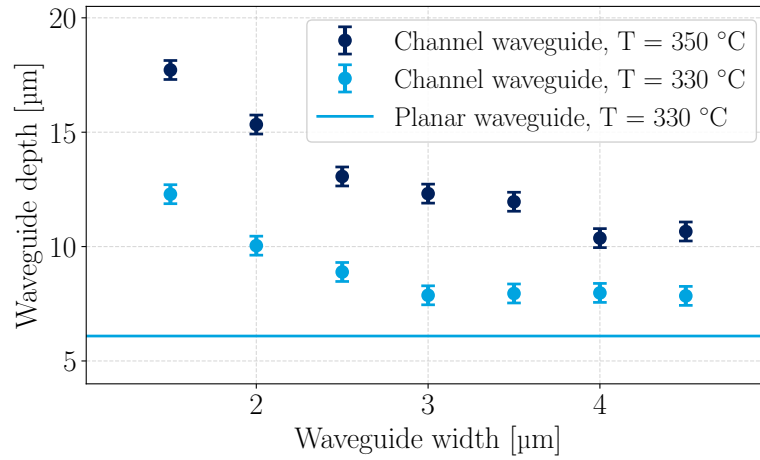


Figure 5.18 – Correlations between waveguide depth and width for different fabrication conditions. Waveguide depth depending on the waveguide width of a sample fabricated in 97 mol% RbNO_3 , 1 mol% $\text{Ba}(\text{NO}_3)_2$ and 2 mol% KNO_3 for 60 min at 330 °C in light blue and 350 °C in dark blue. The solid light blue line shows the depth of planar waveguides produced at 330 °C [185].

Furthermore, we saw that for a higher diffusion temperature at 350 °C, the trend of deeper waveguides with narrower widths is visible. In addition, we observed deeper waveguides for a higher temperature, which allowed for the conclusion that the influence of the temperature seems to follow the simple model assumptions.

For further investigations we fabricated a new set of waveguides by doing an exchange for 5 minutes at 330 °C to examine the non-trivial diffusion properties of KTP via EDX. The results are displayed in figure 5.19 a). There are two distinct characteristics that can be identified. First, for waveguides bigger than 3.0 μm, the diffusion depth is unaffected by the diffusion time. This is consistent with the findings of Bierlein et al. [69]. Second, the waveguide depths show less fluctuations and are unrelated to waveguide widths for short exchange durations.

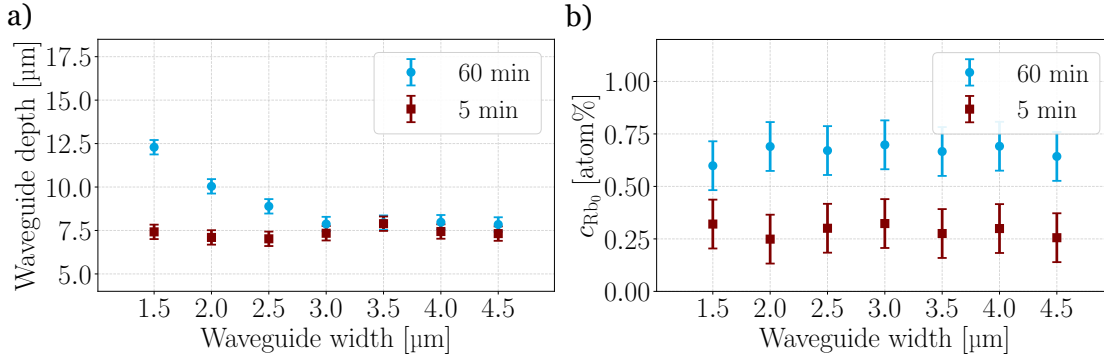


Figure 5.19 – Dependency of the diffusion depth and concentration and processing time. a) Waveguide depth depending on the waveguide width of a sample fabricated at 330 °C for 5 min (blue) and 60 min (red) in 97 mol% RbNO_3 , 1 mol% $\text{Ba}(\text{NO}_3)_2$ and 2 mol% KNO_3 . b) Ratio of exchanged potassium ions with rubidium ions at the surface depending on the waveguide width for 5 min (blue) and 60 min (red) [185].

In order to gain a better understanding, we measured via EDX the surface concentration of the waveguides, see figure 5.19 b). In a simple model, we assume that the exchanged waveguides have an infinite reservoir and therefore, the surface concentration is independent of the exchange time. This implies that the surface concentration at 5 min and 60 min should be the same, however this is not the case. We measured via EDX the potassium concentration with a second line-scan outside the waveguide. The ratio of exchanged potassium ions with rubidium ions $\frac{c_{\text{Rb}_0}}{c_{\text{K}_{\text{mean}}}}$ is for a completely exchanged surface equal to one. The concentration in the 60 min exchanged waveguides is more than twice as high as for the 5 min exchanged waveguides. We can see that the surface concentration is unaffected by the waveguide width, despite the fact that the waveguide depth varies with the width.

The existence of stress in the transition area between KTP and rubidium exchanged KTP could be the reason for the width-dependent waveguide depth. Because the rubidium ions are larger than the potassium ions, stress is expected due to the substantial lattice mismatch between KTP and RTP [44]. We anticipate that small waveguides will experience increased stress due to the proximity of the transition zones. This stress may have an impact on the diffusion properties and as a result, the diffusion depth.

We looked for exchange-induced stress using Raman spectroscopy as introduced in section 4.3.2.1. The scattering efficiency of Raman modes can be influenced by stress [186]. Figure 5.20 shows Raman images for different waveguide width.

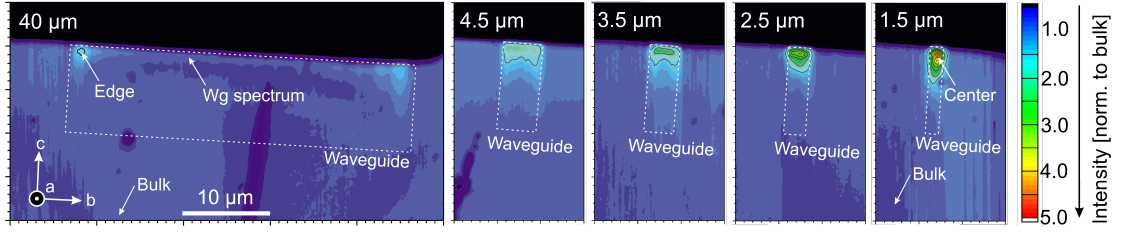


Figure 5.20 – Raman spectroscopy images for different waveguide widths visualised based on the intensity of the 264 cm^{-1} phonon [185].

When the waveguide width is reduced, the intensity in the waveguide region gradually increases. As observed for the $40\text{ }\mu\text{m}$ control channel, it is reasonable to assume that the stress is primarily concentrated at the interface between the exchanged waveguide and the pure bulk crystal and relaxes across a range of $2\text{--}3\text{ }\mu\text{m}$. As a result, it is possible that small waveguides will experience more stress, because the waveguides are smaller than the expected relaxation range.

Since the Raman investigation indicates that the stress in the waveguides is highly dependent on the waveguide width and thus, effects the diffusion dynamics, we investigated, if a stress-dependent diffusion coefficient can explain the trend shown in figure 5.18. Because a higher rubidium concentration causes more crystalline lattice distortion, a reasonable assumption is that the diffusion coefficient depends on the local concentration of Rb in the crystal and therefore, we assume an exponential dependence of the diffusion coefficient D on the concentration c

$$D(z) = D_0 e^{k(y) \cdot c(z)}, \quad (5.1)$$

where k is related to the amount of local stress. We assume that k spatially varies and is highest at the edges of the waveguides and relaxes over $2\text{--}3\text{ }\mu\text{m}$ till it is zero at the centre of the waveguide $y = 0$. The following function might be used to simulate this behaviour:

$$k(y) = k_0 \left[1 + \frac{1}{2} \cdot \operatorname{erfc}\left(\frac{y - \frac{w}{2}}{\sigma}\right) - \frac{1}{2} \cdot \operatorname{erfc}\left(\frac{y + \frac{w}{2}}{\sigma}\right) \right]. \quad (5.2)$$

The parameter σ describes how rapidly stress is relieved closer to the centre of the waveguide with width w . The strength of the stress at the waveguide edges is determined by k_0 . To match the waveguide depths for the wider waveguides and the Raman measurements, we set $D_0 = 0.25 \frac{\mu\text{m}^2}{\text{min}}$ and $\sigma = 1\text{ }\mu\text{m}$. For various nominal widths, we optimise the parameter k_0 to match the measured and simulated depth of the waveguides exchanged for 60 min. Figure 5.21 shows the comparison of simulations with measured data.

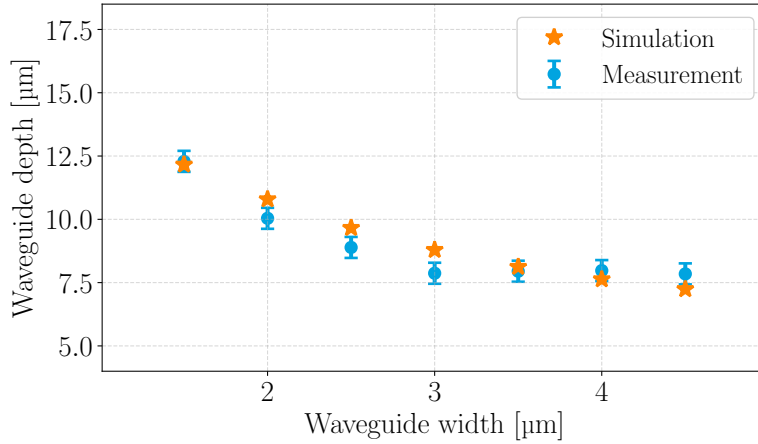


Figure 5.21 – Simulation of the waveguide depth and width using stress-dependent diffusion coefficients. It describes the trend of the measured data for a 60 min exchange that with narrower waveguide width the diffusion depth is deeper [185].

Regarding the proposed model, a few words are required. The observations for the 5 min exchanged waveguides cannot be reproduced by this model. This indicates that the overall diffusion process in our waveguide is changing with time. We suppose that in the first 5 min the diffusion is fast and stress-independent. Beyond this time, the overall diffusion is slowed down, the surface concentration increases and the stress starts to become relevant, which is described by the width-dependent diffusion depth. Additional measurements are required to verify our hypotheses and improve the modelling. In conclusion, we would suggest for the future to fabricate waveguides between 3.0 μm and 4.5 μm, since these width have a small variation in the penetration depth and are more reliable.

Corrugation Free Waveguides in KTP

Waveguides produced in periodically poled crystals may have distinct diffusion coefficients depending on the poled and unpoled sections. This leads to alternating depths along the propagation direction and result in a corrugated waveguide.

For the reduction of the corrugation, we used a mixture of 88 mol% RbNO₃, 1 mol% Ba(NO₃)₂ and 11 mol% KNO₃, in the following we refer to this as optimised melt. With an exchange temperature of 366.5 °C and time of 35 min we were able to reduce the corrugation effect. We showed that we could reduce the difference in depth, which was initially greater than 2 μm, see figure 5.22 a), to less than 1 μm, see figure 5.22 b) [1, 2, 115].

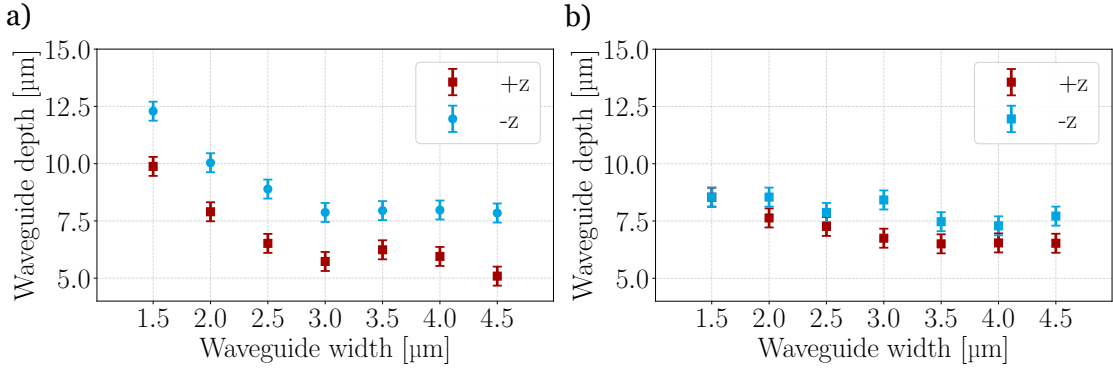


Figure 5.22 – Waveguide depth depending on the waveguide width for poled and unpoled regions. The samples are produced in a) 97 mol% RbNO₃, 1 mol% Ba(NO₃)₂ and 2 mol% KNO₃ at 330 °C for 60 min and b) optimised melt composition of 88 mol% RbNO₃, 1 mol% Ba(NO₃)₂ and 11 mol% KNO₃ at 366.5 °C for 35 min [1, 2, 115].

Corrugation Free Waveguides in RbKTP

Based on the results of reduced corrugation with optimised parameters in KTP, we decided to use the optimised parameters for the Rb-exchange to fabricate waveguides in RbKTP. We analysed the corrugation effect in RbKTP waveguides with even further optimised parameters for the Rb-exchange of 88 mol% RbNO₃, 1 mol% Ba(NO₃)₂ and 11 mol% KNO₃ at 358 °C for 43 min. For this purpose, we poled samples with poling periods between 120 μm and 150 μm, as described in section 4.1. We fabricated waveguides between 2.7 μm and 4.1 μm, for which we expected a less variation in the waveguide depth. We polished the end-facet of the sample, to reveal either the unpoled or the poled regions of the sample. After that, we used the EDX system to measure the penetration depths. Figure 5.23 shows the depths depending on the widths for the poled and unpoled waveguide sections in RbKTP.

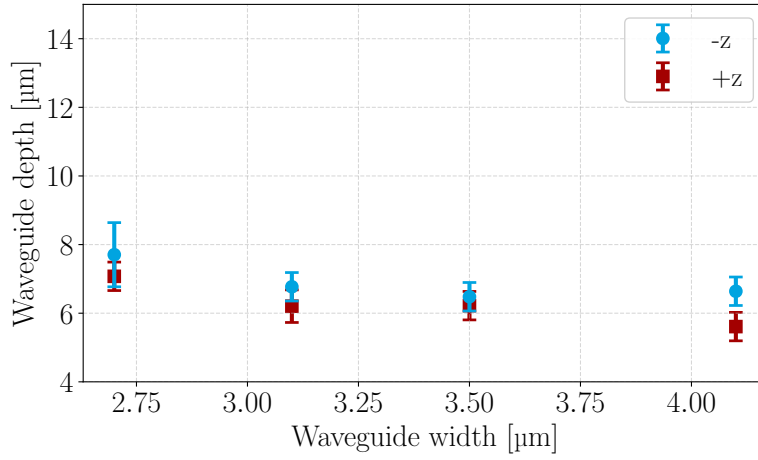


Figure 5.23 – Waveguide depth depending on the waveguide width for poled and unpoled regions of a sample produced in optimised melt. The melt has a composition of 88 mol% RbNO_3 , 1 mol% $\text{Ba}(\text{NO}_3)_2$ and 11 mol% KNO_3 in RbKTP . The data points are the mean values for different waveguide groups for each waveguide width and the uncertainty is the standard deviation.

Similar to waveguides fabricated in KTP , waveguides in RbKTP are deeper with narrower waveguide width. Moreover, the optimised melt parameters benefit comparable exchange depth within the measurement uncertainty for poled and unpoled waveguide areas. This shows that we are able to produce waveguides in periodically poled RbKTP with almost no corrugation effect.

5.1.2.2 Spatial Modes and Propagation Losses

Before using waveguides in advanced integrated circuits, it is necessary to inspect the quality of waveguides. For this reason, we measured the spatial modes of our waveguides with the setup introduced in section 4.3.2.2. Furthermore, we measured the losses. For this characterisation, we used the Fabry-Pérot method.

Spatial Modes in KTP

For the linear optical characterisation, we imaged the spatial modes of the waveguides onto an infrared camera with an $100\times$ objective at a wavelength of 1550 nm. In front of the waveguide we set the polarisation with a linear polariser. Figure 5.24 shows the fundamental modes for qTE and qTM of waveguides fabricated with the optimised melt and parameters in KTP .

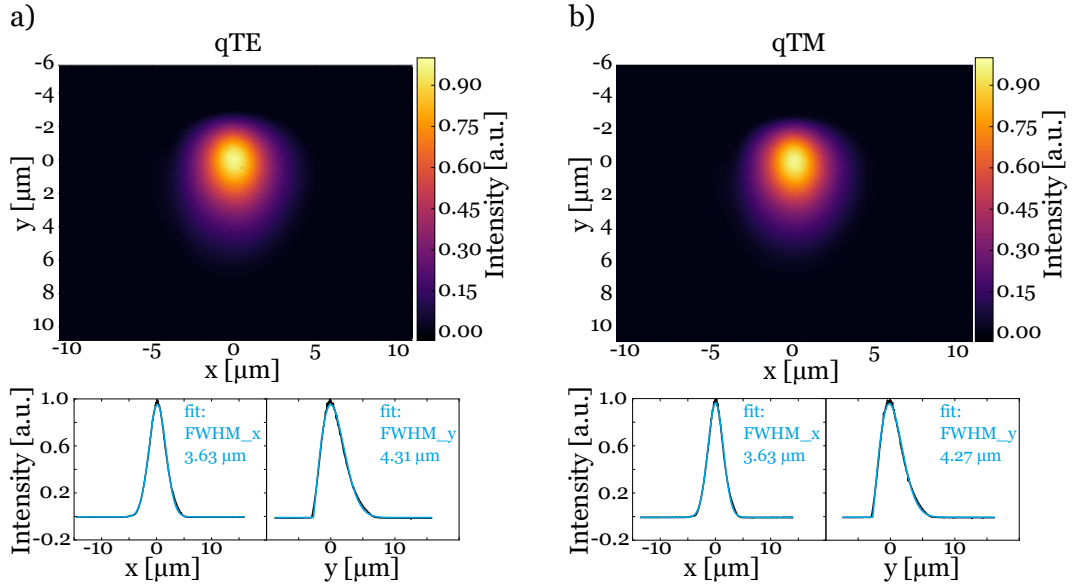


Figure 5.24 – Camera images of KTP modes and corresponding fits of mode profiles. Fundamental modes a) qTE and b) qTM for a $3.5\ \mu\text{m}$ wide waveguide produced in optimised melt composition of 88 mol% RbNO_3 , 1 mol% $\text{Ba}(\text{NO}_3)_2$ and 11 mol% KNO_3 at $358\ ^\circ\text{C}$ for 43 min in KTP.

We confirmed that all of the fabricated waveguides between $1.5\ \mu\text{m}$ and $4.5\ \mu\text{m}$ are single-mode at $1550\ \text{nm}$. To the measured data, we fitted a Gaussian profile in the width direction and a Hermite-Gaussian for the depth direction, due to a significant increase in the refractive index of air at the surface. The fitted FWHM for the qTE mode in x-direction is $3.63\ \mu\text{m}$ and in y-direction $4.31\ \mu\text{m}$. The qTM mode has a fitted FWHM of $3.63\ \mu\text{m}$ in x-direction and $4.27\ \mu\text{m}$ in y-direction.

In addition to that, we can estimate the field overlap and the coupling efficiency with a standard SMF28 telecom fibre, which has a mode field diameter of $10.4\ \mu\text{m}$ [187]. The field overlap is estimated to be above 94 % and the maximum theoretical coupling efficiency is above 89 % for both modes.

Spatial Modes in RbKTP

Analogous to KTP we measured the fundamental modes for qTE and qTM for RbKTP waveguides with the optimised melt and parameters in RbKTP, see figure 5.25.

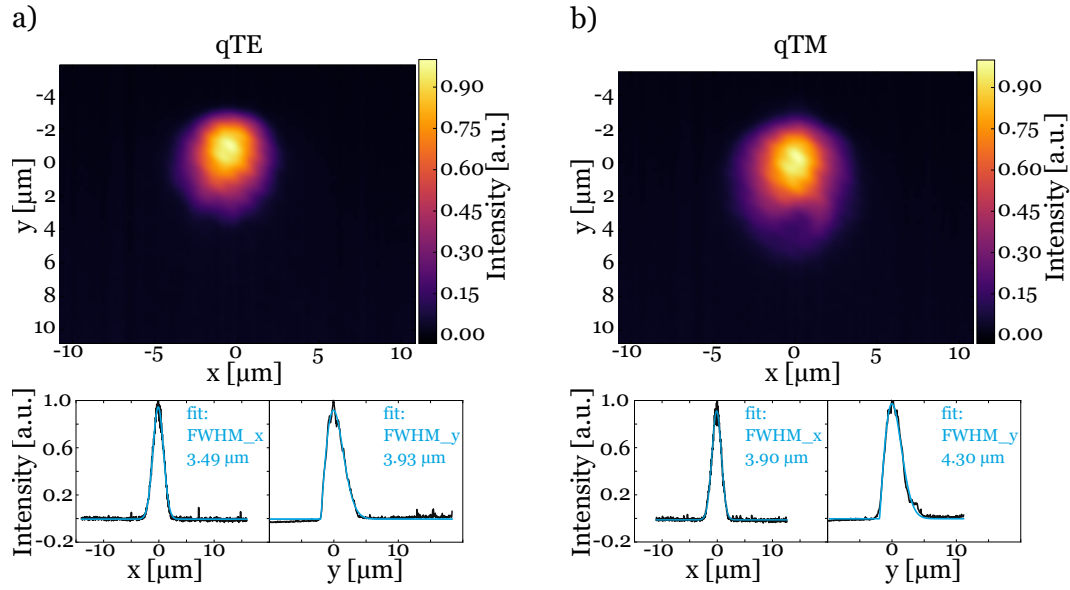


Figure 5.25 – Fundamental modes a) qTE and b) qTM for a 3.5 μm wide waveguide produced in optimised melt composition of 88 mol% RbNO_3 , 1 mol% $\text{Ba}(\text{NO}_3)_2$ and 11 mol% KNO_3 at 358 $^\circ\text{C}$ for 43 min in RbKTP.

Similar to KTP, all fabricated waveguides in RbKTP between 2.7 and 4.1 μm are single-mode at 1550 nm. The estimated field overlap with a standard SMF28 telecom fibre is above 85 % for both modes. Moreover, the maximum theoretical coupling efficiency to a SMF28 fibre is above 72 % for both modes.

If we compare the FWHM of the modes for KTP and RbKTP we can see that the values are similar and only vary in the first decimal place. The fitted FWHM for the qTE mode in x-direction is 3.49 μm and in y-direction 3.93 μm . The qTM mode has a fitted FWHM of 3.90 μm in x-direction and 4.30 μm in y-direction. This shows that the mode sizes are comparable in both materials.

Propagation Losses in RbKTP

Using the Fabry-Pérot method, we measured the losses of RbKTP waveguides at a wavelength of 1550 nm. We tuned the wavelength between 1549.7 nm and 1550.3 nm in 0.005 nm steps and measured the through coupled intensity. Figure 5.26 shows the measured intensity oscillations as a function of the wavelength measured for the fundamental qTE mode of 3.5 μm wide waveguide in RbKTP.

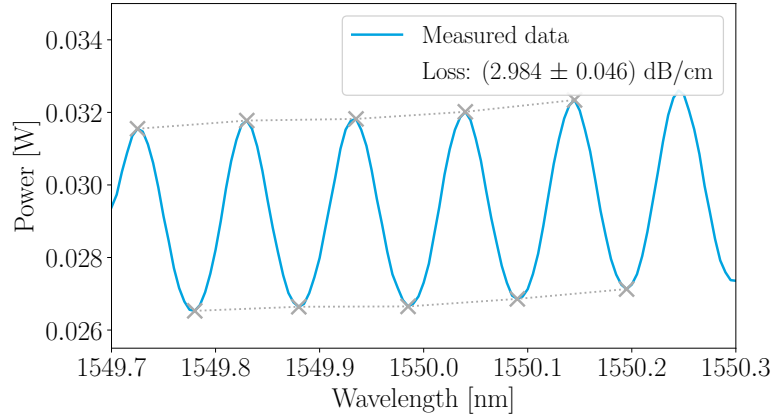


Figure 5.26 – Intensity oscillations as a function of the wavelength during Fabry-Pérot measurements of the fundamental qTE mode for a 3.5 μm wide waveguide in RbKTP.

We estimated the transmission losses of our waveguides using the contrast of the Fabry-Pérot oscillations. Figure 5.27 shows the measured losses for qTE and qTM polarisation in different waveguide groups and widths for a 7 mm long sample.

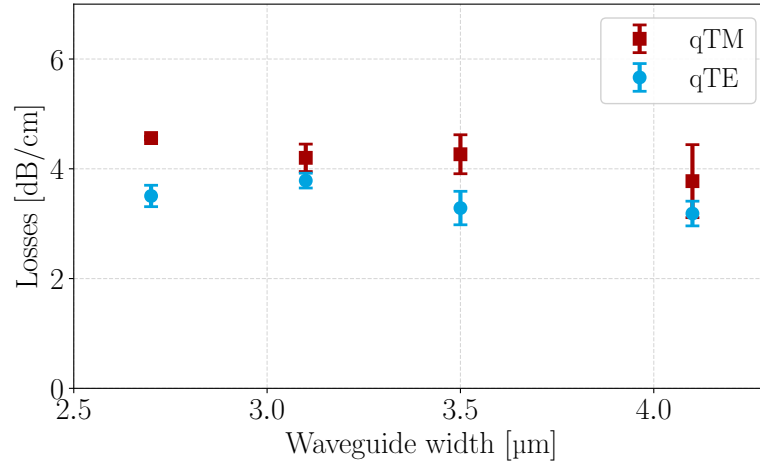


Figure 5.27 – Measured propagation losses for qTE and qTM for different waveguide width for a 7 mm long sample. The dots indicate the mean value for the losses for each waveguide width and polarisation. The uncertainty is given by the standard deviation.

The best propagation losses are 2.96 dB/cm for the qTE and 3.11 dB/cm for the qTM polarisation. These propagation losses are higher compared to losses obtained for wave-

guides produced with the optimised melt in KTP, where we measured losses down to 0.2 dB/cm.

It has to be noted that one reason for the increased losses of waveguides in RbKTP is the selective etching of the domains during the cleaning procedures. Each cleaning procedure contains an ammonia solution, which is sufficient to etch nanometres of contrast between the domains. In total the sample is cleaned at least four times after periodic poling, which results in selectively etched domains of 10 nm depth, which are visible with a microscope, see figure 5.28.

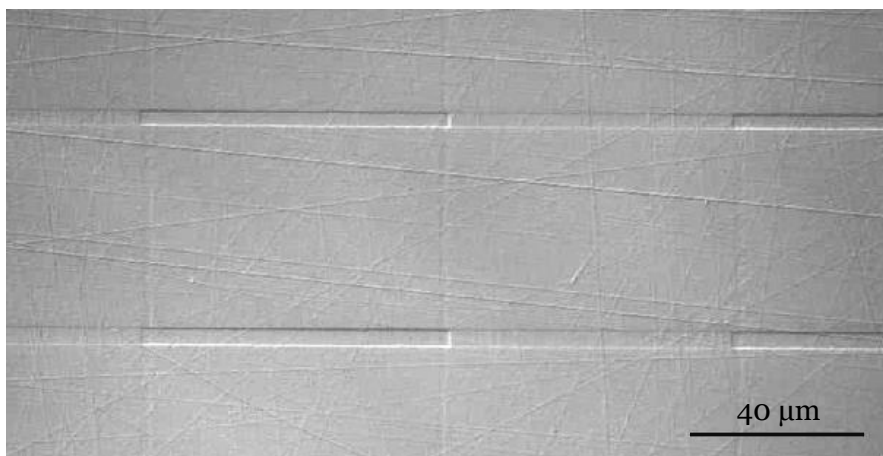


Figure 5.28 – CLSM image of the material scratches in the waveguide, which introduce propagation losses.

Moreover, the surface and the material of RbKTP itself is strongly damaged. Figure 5.28 shows visible scratches on the surface of RbKTP. As already mentioned, the only solution for less scratches are wafers with better quality from the vendor. Nevertheless, we could obtain in other RbKTP samples without a periodic poling and hence, no selective etching of domains, losses down to 0.84 dB/cm.

5.1.2.3 Modelling of Waveguides

To model our waveguides in (Rb)KTP and simulate the corresponding modes and effective refractive indices we use RSoft. We presented the model in section 4.3.2.2. There are various parameters that we must supply to the simulation software in order to simulate modes. These are the waveguide profile, for which a complementary error function in depth and a box function in width are used. The width of the waveguide measured with the CLSM and the penetration depth determined with the EDX measurements are required for the model. We assume a linear relationship between the concentration profile and the refractive index profile. Additionally, we need to know the refractive index

increase at the surface. Furthermore, we need to set the intended wavelength and polarisation to simulate our modes with the corresponding effective refractive index. From our measurements, we can specify all parameters except the refractive index increase at the surface Δn_0 . Since we lack Δn_0 , we have to determine it in a reasonable way. Therefore, we use our measured modes and compare the measured FWHM with the simulated ones. We simulated the FWHM in the x- and y-directions, with the waveguide width and depth set to $3.5\ \mu\text{m}$ and $6.35\ \mu\text{m}$ respectively. We used a wavelength of $1550\ \text{nm}$ and varied the refractive index increase at the surface Δn_0 between 0 and 0.03 in 0.001 increments for qTE and qTM mode. Figure 5.29 shows the simulated FWHM for the x- and y-direction and the fundamental qTE and qTM mode.

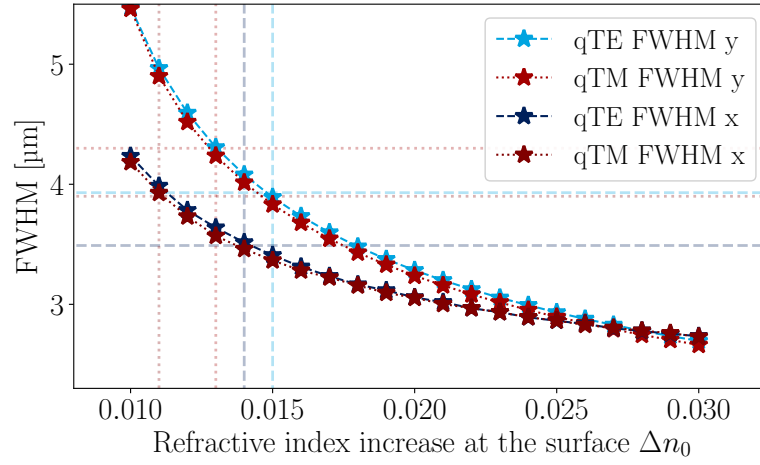


Figure 5.29 – Simulated FWHM in x- and y-direction for fundamental qTE and qTM modes. The simulations are performed for a wavelength at $1550\ \text{nm}$ and a waveguide width of $3.5\ \mu\text{m}$ and depth of $6.35\ \mu\text{m}$ depending on the refractive index increase at the surface Δn_0 .

The horizontal dashed lines indicate the measured FWHM from our fabricated modes. When we compared the measured FWHM with the simulated ones, we found the best match for the refractive index increase at the surface. We assume Δn_0 for the fundamental qTE mode between 0.014 and 0.015 and for the fundamental qTM mode between 0.011 and 0.013 at $1550\ \text{nm}$.

We repeated the simulations for a $2.7\ \mu\text{m}$ wide and $7.39\ \mu\text{m}$ deep waveguide, see figure 5.30.

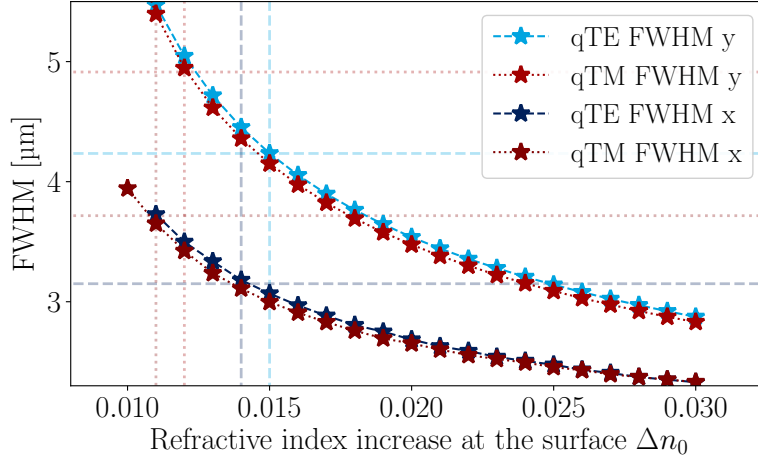


Figure 5.30 – Simulated FWHM in x- and y-direction for fundamental qTE and qTM modes. The simulations are performed for a wavelength at 1550 nm and a waveguide width of 2.7 μm and depth of 7.39 μm depending on the refractive index increase at the surface Δn_0 .

The dashed lines represent the corresponding FWHM of our measured modes. By comparing the measured FWHM with the simulated ones for this geometry at 1550 nm, we get similar results for the Δn_0 , which is between 0.014 and 0.015 for the fundamental qTE and between 0.011 and 0.012 for the fundamental qTM mode.

We investigated, if the Rb doping of the crystal with 0.015 Rubidium in RbKTP does change the simulated modes in comparison to pure KTP. The resulting effective refractive indices are similar, and only differ with a fixed offset in the fourth decimal place.

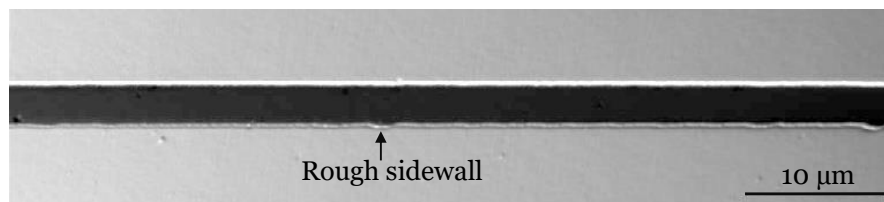
In conclusion, it is possible to simulate the spatial modes of our waveguides in RbKTP with RSoft with reasonable numbers for the refractive index increase at the surface. For future simulations, it is sufficient to estimate a surface refractive index increase Δn_0 between 0.011 and 0.015 for the fundamental modes at 1550 nm in KTP and RbKTP.

5.1.2.4 Final Remarks for KTP/RbKTP Waveguides

For waveguides in KTP we developed a model that could explain the influence of stress on the penetration depth and that narrow waveguides are deeper, in good agreement with our measured data. We started with a new material RbKTP. For this reason, we investigated the corrugation and width dependence depth behaviours of the waveguides fabricated in RbKTP. As a result, we are able to produce waveguides in periodically poled RbKTP with almost no corrugation effect.

In the future, we should optimise the corrugation in RbKTP waveguides and optimise the exchange parameters for symmetrical circular spatial modes for a higher field overlap to fibres and lower propagation losses. One possibility to reduce the losses is to polish the surface of the samples, to reduce the impact of scratches on the waveguides. Moreover, the mask-lithography has the disadvantage that dust and particles are easily trapped in the small slits of the chromium mask, therefore, introduce imperfections in the titanium mask, thus, increasing the losses of the waveguides. First investigations showed, we should be able to reduce the losses, by optimising the edge roughness of the titanium mask. This is possible by using the laser-lithography, see figure 5.31.

a)



b)

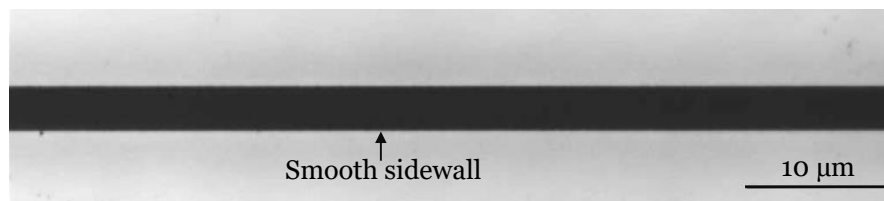


Figure 5.31 – CLSM image of titanium mask fabricated with a) mask-lithography and b) laser-lithography.

5.2 Lithium Niobate On Insulator

In this section, we introduce our developed technologies for periodic poling and waveguide fabrication in LNOI. The research field of LNOI is a new field and was rapidly expanding in the recent years. In the following, we present our most important results in developing a new technology. Building up a new technology is accompanied by several pitfalls and failures, which would overload this written work. Therefore, the resulting recipes to fabricate periodically poled waveguides are shown in this section. Moreover, we present our simulations for the influence of the waveguide geometry on the modes and effective refractive index and show developed model to simulate coupler structures.

5.2.1 Wafer Quality

The wafer quality has a huge impact on the technology procedures and device quality, but it depends only on the vendor technology. The quality of the material, e.g., changes in the total thickness of the layers or the homogeneity of the layer thickness itself lead to different periodic poling behaviour for every sample and wafer. Moreover, the variation of the thin-film thickness has a huge impact on the waveguide properties, see section 5.2.4.

Figure 5.32 shows a heat-map of the thin-film thickness with respect to the position on the wafer, measured from the vendor and specified in the specification sheet.

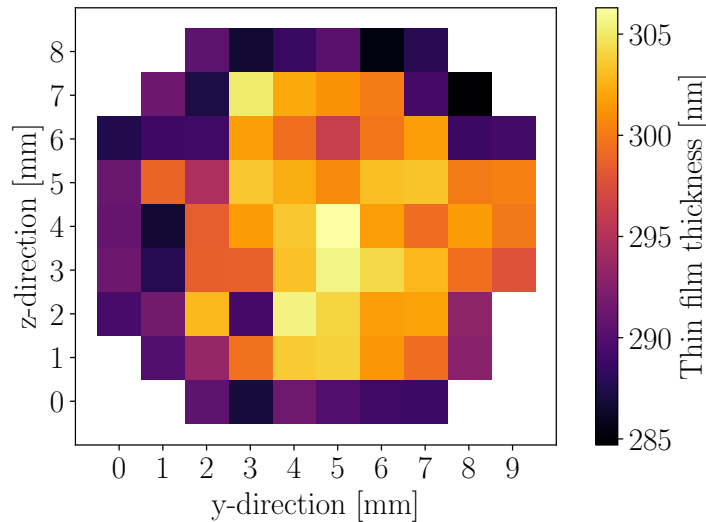


Figure 5.32 – Heat-map of the thin-film thickness with respect to the position on the wafer. The thickness is measured by the vendor and specified in the specification sheet.

This shows that the wafer is varying from a minimal thickness of 284.7 nm at the edges to a maximal thickness of 306.3 nm in the centre of the wafer. Moreover, the maximal difference between two neighbouring points is 17.8 nm. This allows us to suggest that the strongest thin-film variation can be around 18 nm. The mean value for the thin-film thickness is 296.2 nm with a standard deviation of 6.4 nm. This variation can only be improved by the vendor and their thin-film wafer production technique. For us the best approach in future would be to measure the height of the wafer with ellipsometry and to pick out the most homogeneous areas and to cut the samples from these areas for the production.

5.2.2 Periodic Poling

Periodic poling of x-cut LNOI was a completely new challenge we had to face. In section 4.2.1.1 we introduced different techniques for periodic poling in LNOI. For our technology we decided to use electric field poling, since we already had experience in this technique with other materials like bulk lithium niobate or KTP. Moreover, this technique has recently become the most popular technique to periodically invert domains in the community. The time we started with LNOI, periodic poling was only shown in x-cut LNOI. Efficient periodic poling of z-cut LNOI was shown in late 2019 [132].

We decided to do the periodic poling in x-cut before the waveguide fabrication to have an unstructured surface for the structuring of the electrodes. The electrodes are fabricated as finger electrodes facing each other along the z-direction of the crystal, see figure 5.34. With needles the electrodes are contacted and one high voltage pulse is applied to invert the ferroelectric domains between the fingers.

The first step towards good periodic poling recipes, was to investigate different electrode shapes for the finger electrodes. After that, we used different lithography systems to improve the quality of the finger tips and the general structure of the electrodes. Next, we tested different electrode configurations and materials for periodic poling. Last, we investigated the poled domains via SH microscopy.

5.2.2.1 Electrode Geometry

Before the actual periodic poling process, we have to choose a geometry for the electrodes. Since we are using x-cut LNOI and the spontaneous polarisation is along the z-direction, we need two electrodes on the top surface to define the periodic poling area. For a periodic domain inversion we need a periodic structure, which can be designed by fingers connected to a big rectangular electrode, in the following referred to as contact pad.

As introduced in section 4.3.2.2, we build a model in COMSOL to simulate the electric field strength depending on the finger electrode structure. Figure 5.33 shows three different finger tip shapes and their simulated electric field distribution with an applied voltage of 700 V.

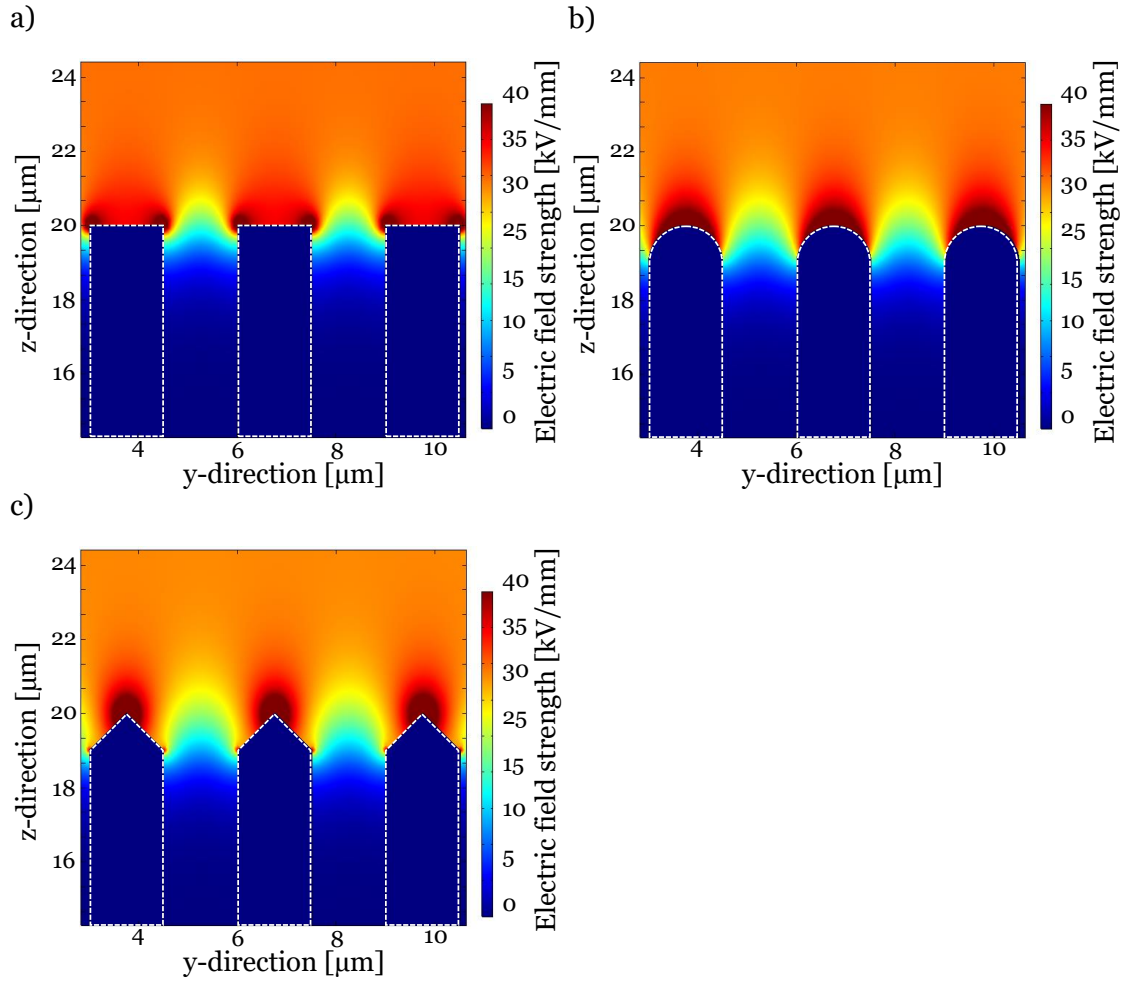


Figure 5.33 – Simulated electric field distribution for different finger tip shapes: a) rectangular, b) round and c) tapered. The finger shape is indicated by the white dashed lines.

The shape of the finger tip influences drastically the domain growth along the z-direction. A rectangular finger electrode, as shown in figure 5.33 a), has an increased field strength at both corners and therefore, intrinsically introduces wider domains. In comparison, figure 5.33 b) shows the case of rounded finger tips, where the electric field is concentrated in the middle of the finger and decreases to the sides continuously. With a tapered finger tip, as shown in figure 5.33 c), the highest field components are located at the tip, which accelerates the domain growth along the z-direction. Moreover, tapered finger shapes suppress the domain merging, which is more prominent in the case of rectangular tips [188].

The width of the finger influences the width of the domain. For the highest conversion efficiency we need a 1:1 duty cycle of the poled and unpoled domains with respect to the

poling period. To precompensate the lateral domain growth, we design the finger width with 30 % of the poling period, which is smaller than the desired 50 % of the poled domains.

Depending on the length of the fingers, the distinction of the electric field between the finger tips and the contact pads can be maximised to avoid poling directly between the contact pads. Therefore, the electric field between the contact pads needs to be well below the coercive field strength of lithium niobate. This can be achieved by using 10 μm long fingers.

Besides the lateral domain growth, we need to control the growth in the depth of the LNOI thin-film. This can be controlled by a separation gap between the opposite finger electrodes, which should be higher than 20 μm to assure a growth through the complete film thickness [164].

Therefore, we designed our electrodes with 20 μm separation gap, 10 μm for the finger length and 30 % of the poling period for the tapered finger width, see figure 5.34.

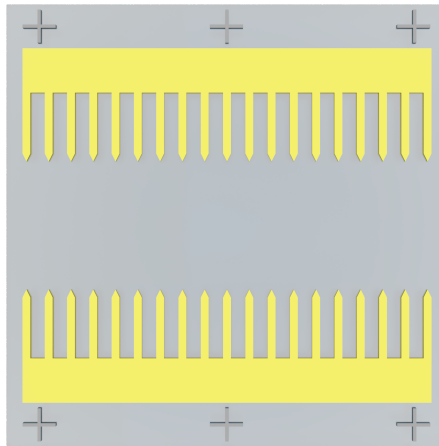


Figure 5.34 – Design of finger electrodes for periodic poling. The fingers are connected to bigger contact pads. The crosses indicate the alignment marker.

5.2.2.2 Electrode Lithography

During this thesis we had the opportunity to test different lithography systems for our fabrication of finger electrodes, namely laser-lithography and electron-beam-lithography. In the following we will show the results for the finger electrodes fabricated with different lithography approaches.

Sample Preparation

The very first step before doing any periodic poling or waveguides is to prepare the samples. The x-cut LNOI is a 3 inch wafer diced in 10 mm × 10 mm samples. The top of the sample is the positive x-surface, referring to a right handed coordinate system in relation to the +z-direction.

The first step is to clean the surface of the sample. We are using the same cleaning procedure as in KTP introduced in section 4.1.2.1. Since the periodic poling is done before the waveguide fabrication it is necessary to have alignment markers to match the waveguides to the periodically poled region. The alignment markers are fabricated with a lift-off process. The progress of a lift-off is explained in detail in the following. For the alignment markers we use 100 nm of sputtered titanium (Sputtering System 518 - Prevac).

Electrodes via Laser-Lithography

In the following, we describe the process steps, which are necessary to structure our designed electrodes on the surface of LNOI, see figure 5.34.

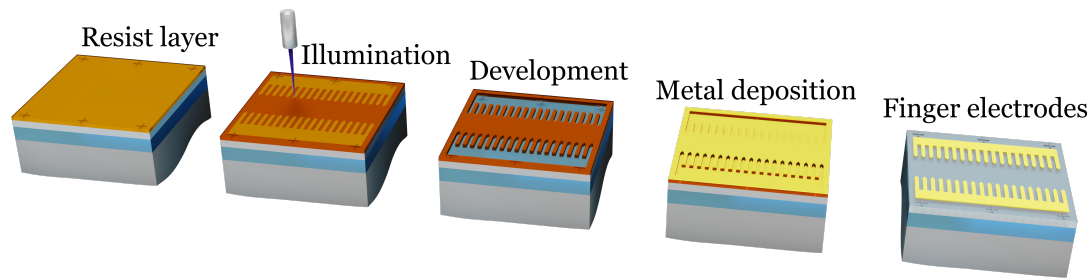


Figure 5.35 – Schematic of the distinct steps of the fabrication process to fabricate finger electrodes for periodic poling. Here, the electrode patterning is performed by means of laser-lithography.

Before structuring the electrodes, we rinse the sample with isopropyl alcohol and dry it with nitrogen before spin-coating to ensure good adhesion between the sample and the resist since the resist is hydrophobic. We use a negative photoresist (AZ nLoF 2020 - MicroChemicals), which we spin-coat at 6000 rounds per minute (rpm) for 5 seconds. This results in a 1 μm thick resist layer, which is sufficient to lift-off electrodes of 200 nm thickness. Following spin coating we do a softbake of the resist at preheated 110 °C for 15 min.

After the sample is completely cooled down, we clean the backside of the sample with acetone and a swab to assure a plain surface during lithography. The sample size of LNOI is small and the resist forms a bulge at the edges of the sample. Nevertheless, since we use a laser-lithography (DWL 66+ - Heidelberg Instruments) to structure the

resist, we do not need to remove it like we do in the case of KTP. Depending on the material system, we use fixed parameters to illuminate our desired structures (MgO doped LNOI: 38 mW, focus, -25 % intensity 35 %, filter 1 %; congruent LNOI: power 40 mW, focus -10 %, intensity 35 %, filter 1 %).

Afterwards, we do a post exposure bake (UF30plus - Memmert) to cross-link the exposed areas. Besides the illumination, the post exposure bake is a critical step, where a too hot or too long baking process cross-links the whole resist layer. To achieve the strict temperature requirements we are using a computer controlled oven with following temperature profile shown in figure 5.36 a). The procedure is to preheat the samples in the oven to 23.2 °C, ramp up the temperature to 124.8 °C and open the oven to let the samples cool down to room temperature.

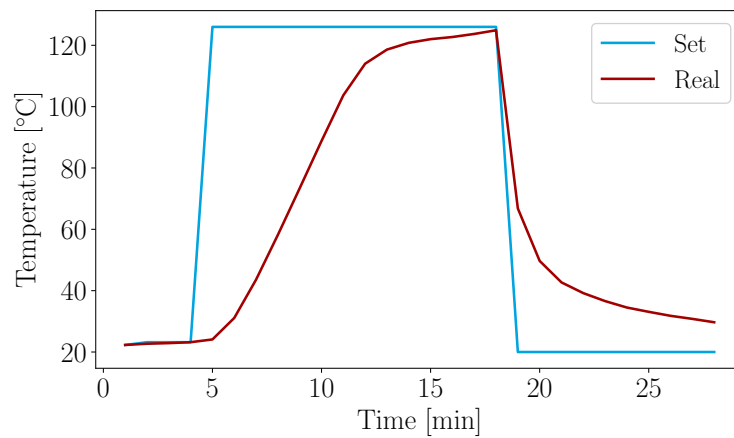


Figure 5.36 – a) Temperature in the oven depending on the time. The blue line shows the set temperature and the red line the real temperature during the post exposure bake.

During development (AZ 726 MIF - MicroChemicals mixed with water at ratio 78:22) all the non-exposed areas vanish and we get an undercut of the remaining resist structures, which benefit the lift-off process. The development of the resist is the third critical step. It is important to develop long enough to get an undercut in the resist, see figure 5.37 a), but at the same time not too long to avoid undesirable removal of the resist areas, thus, a too low resist thickness to lift the structures.

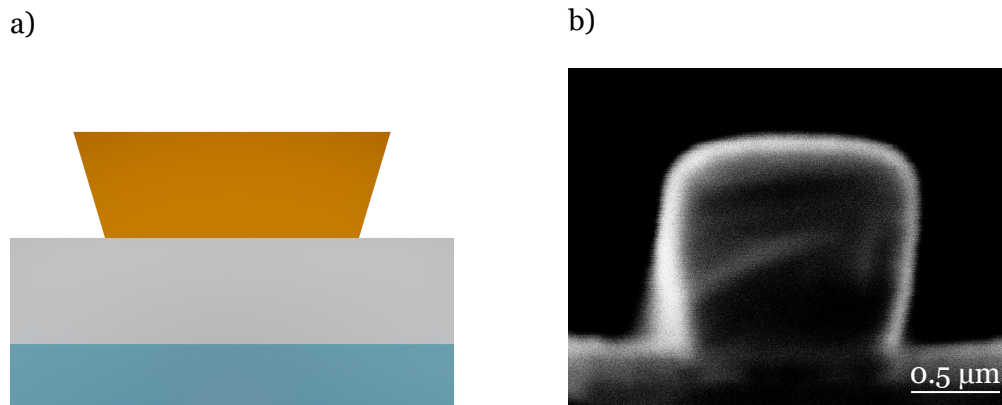


Figure 5.37 – a) Trapezoidal cross-section of the negative resist after development. b) SEM image of the resist cross-section from the laser-lithography with a trapezoidal shape.

Using the previously described optimised parameters for fabricating the lift-off structure, we achieve a trapezoidal cross-section can be realised and figure 5.37 b) shows our fabricated cross-section via laser-lithography analysed with a SEM.

For the electrodes we sputter (Sputtering System 518 - Prevac) 170 nm chromium on top of the LNOI surface for a homogeneous conductivity and 30 nm gold to prevent the chromium from oxidation. We lift the metal layer on top of the resist, by solving the resist in TechniStrip (TechniStrip NI555 - MicroChemicals) in a warm ultrasonic bath at 65 °C over night and a following step in acetone for 10 min and isopropyl alcohol for 10 min.

In a fabrication process with optimised parameters it is possible to fabricate finger electrodes with width of around 1 μm. Figure 5.38 shows finger electrodes with a width of 1 μm and a poling period of 3.0 μm on a MgO doped LNOI sample. The resulting finger electrodes on congruent LNOI are the same and this method is suited for a variety of thin-film thicknesses.

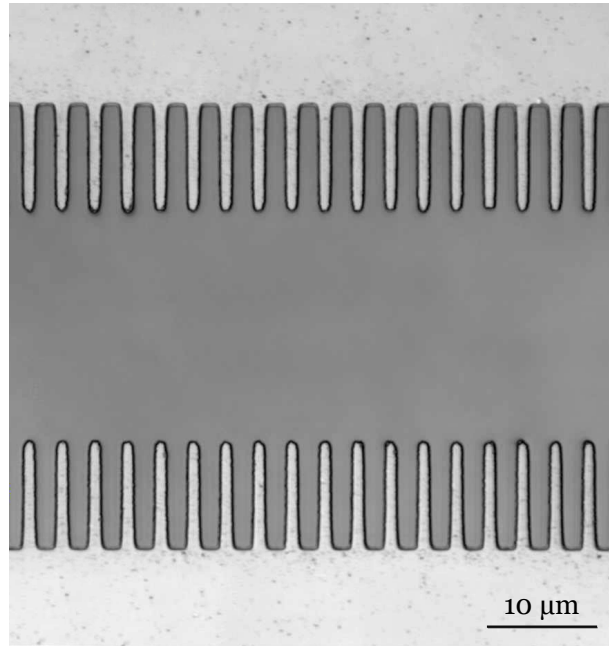


Figure 5.38 – Finger electrode structure fabricated with laser-lithography imaged via CLSM.

The resulting finger tip edges are homogeneous. At the same time we can see that the desired tapered tip is strongly rounded. We investigated different finger tip shapes from the mask design, and the resulting finger tips did not differ from each other. The reason for this is that for the size of the finger tips, we reach the resolution limit of the laser-lithography.

Nevertheless, these lifted structures were appropriate to periodically pole LNOI. To test different poling parameters, we decided to fabricate several 400 μm long electrode structures with a poling period of 3 μm on one sample. Figure 5.39 shows an overview of an LNOI sample structured with laser-lithography.

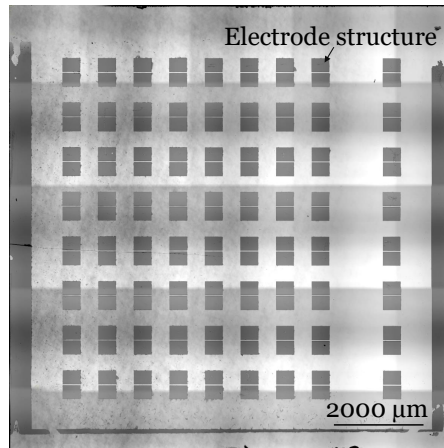


Figure 5.39 – Composite overview of a sample with several 400 μm long electrode structures. The image is acquired by a CLSM and the electrodes are patterned by use of laser-lithography.

Our objective is to fabricate periodically poled waveguides for frequency conversion and single photon sources. The efficiency of nonlinear processes is depending on the length of the QPM structure. To increase the efficiency, we need to increase the total length of our electrodes. Therefore, we increased the electrode length to 7.5 mm. This is the maximal length we can achieve for 10 mm long samples, because the electrodes need to be shorter than the dimension of the resist bulge at the two edges of the sample. In figure 5.40 we show a sample with 7.5 mm long electrodes.

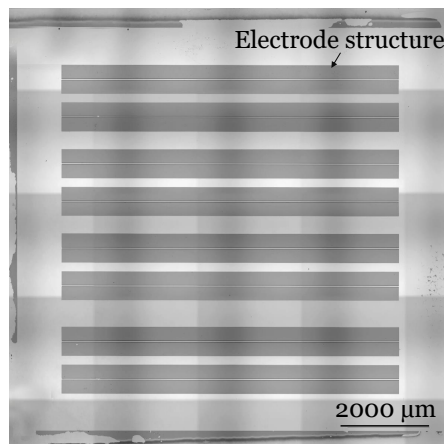


Figure 5.40 – Composite overview image of a sample with 7.5 mm long electrode structures the electrodes are patterned by use of laser-lithography and imaged via CLSM.

Electrodes via Electron-Beam-Lithography

In the last month of my PhD, we had the opportunity to use a new electron-beam-lithography (EBL). Hence, we developed a process to fabricate high quality finger electrodes on LNOI, to further push our technology to a next level.

For the lift-off with EBL, we use a two layer resist lift-off process. Therefore, we spin-coat two different resists on the sample, illuminate and develop only the top resist and use a second development to achieve an undercut for the lift-off. Figure 5.41 shows the double resist structure for the lift-off.



Figure 5.41 – Illustration of a cross-section of the two resist layers and undercut for the lift-off after development.

Figure 5.42 shows the fabrication steps for finger electrodes with EBL lithography.

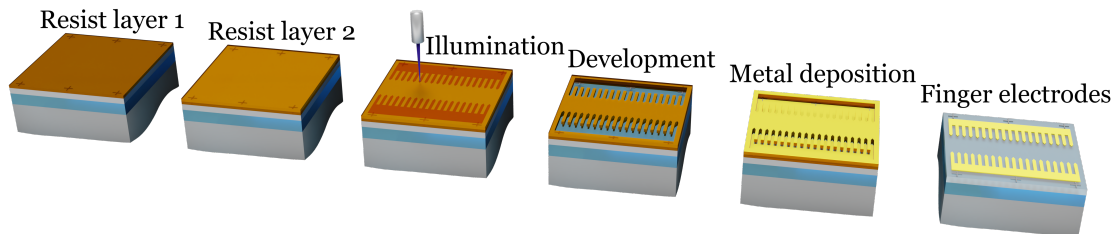


Figure 5.42 – Schematic of the distinct steps of the fabrication process to fabricate periodic electrodes. Here, the electrode patterning is performed by means of electron-beam-lithography.

The first step is to spin-coat a resist for the undercut, which is not sensitive to the electron beam. We use LOR3A (Kayaku Advanced Materials), which we spin-coat at 4000 rpm for 45 s. This results in a 300 nm thick resist layer, which is sufficient to lift electrodes of 200 nm thickness. We do a controlled softbake in an oven (UF30plus - Memmert), which heats up the sample to 190 °C holds the temperature for 10 min and slowly

cools down the sample to room temperature. Afterwards, we spin-coat a positive resist (CSAR 62 - Allresist) on the first resist layer with 4000 rpm for 60 s and do a controlled second softbake at 150 °C for 30 min.

We fix the sample on the holder for the EBL (VOYAGER - Raith) with a carbon tape touching the sample surface to avoid charging effects that occur due to the high energy of the electron beam on the sample.

We illuminate the areas of the contact pads with a high current and a dose of $250 \frac{\mu\text{C}}{\text{cm}^2}$. For the fingers we use a 'zero stitching error' approach that is called modulated beam moving stage (MBMS). This technology allows continuous writing of elongated paths with the combination of patterning, resulting in stitch-free periodic structures. For this we use a low current and a dose of $225 \frac{\mu\text{C}}{\text{cm}^2}$.

After the illumination, we develop the first resist layer for 70 s (AR 600-546 - Allresist) and stop the development process in Stopper (AR 600-60 - Allresist) for 30 s and water for 30 s. Through the free trenches in the resist, we can develop the lower resist for 17 s (AZ 726 MIF - MicroChemicals) for a sufficient undercut for the lift-off. Analogue to the lift-off process, which is done via laser-lithography, we sputter 170 nm chromium and 30 nm gold on the LNOI surface. We lift the structures by moving the sample in TechniStrip (TechniStrip Micro D350 - MicroChemicals). Afterwards, we put the samples in new TechniStrip in a warm ultrasonic bath at 65 °C to solve the parts between the fingers. When all the structures are lifted, we use isopropyl alcohol and water each for 10 min to finally clean the samples. As a result, we have finger electrodes as schematically shown in figure 5.34, which are ready for poling.

Since we use a two layer resist lift-off process, we need an undercut resist structure for the lift-off. For the analysis of the cross-section of the resist structures we cleave our samples in the centre to reveal the cross-sections. Moreover, we need to coat the cross-section to compensate for surface charges. The cleaving and the metal coating results in an inhomogeneous surface. Figure 5.43 shows the cross-section of the two layers after development for the lift-off of the electrodes.

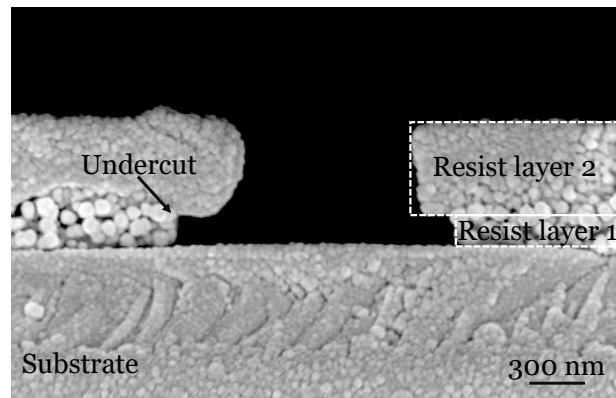


Figure 5.43 – Resist cross-section from the electron-beam-lithography with a trapezoidal shape imaged with a SEM. The dirt at the cross-section is due to the cleaving and metal-coating.

We can see an undercut in the double resist structure, which is well pronounced compared to laser-lithography. Thus, this enables a reliable lift-off. By carefully choosing the electron beam current during MBMS illumination and subsequent metal deposition, we can achieve high quality fingers with a tapered finger tip, see figure 5.44.

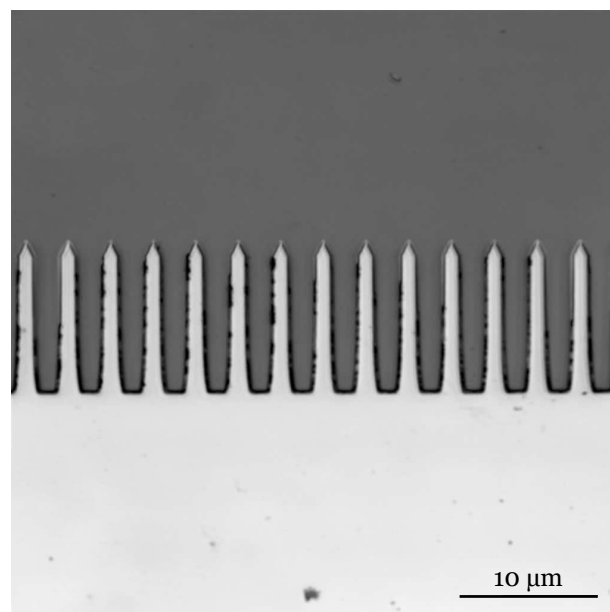


Figure 5.44 – CLSM image of a finger electrode structure fabricated with electron-beam-lithography.

If we would use a standard EBL system and fabricate test-structures for periodic poling, it normally would take days to illuminate the complete sample. But if we combine the unique properties of the Voyager system, namely the MBMS in low current mode for the finger and standard writing-fields and high current for the contact pads, it is possible to write the same areas in less than nine hours. Figure 5.45 shows identical lifted electrodes structures for testing poling parameters.

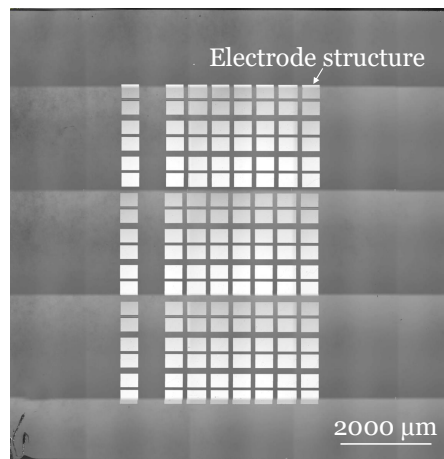


Figure 5.45 – Composite overview imaged with CLSM of a sample with 400 μm long electrode structures fabricated with electron-beam-lithography.

Therefore, this process allows us to fabricate high quality finger electrodes in an acceptable amount of writing time.

5.2.2.3 Periodic Poling

With the fabricated electrodes we are able to periodically pole our samples by applying a high voltage pulse to the electrodes. We investigated different plateau times and plateau voltages for the pulses and analysed the poled domains via SH microscopy.

Periodic Poling Setup

For the electric field poling a new poling setup was required. Due to the x-cut and two top electrodes, the setup for conventional z-cut bulk lithium niobate is not suitable. Figure 5.46 shows the new setup we build with micro-manipulators and needles to directly contact the electrodes.

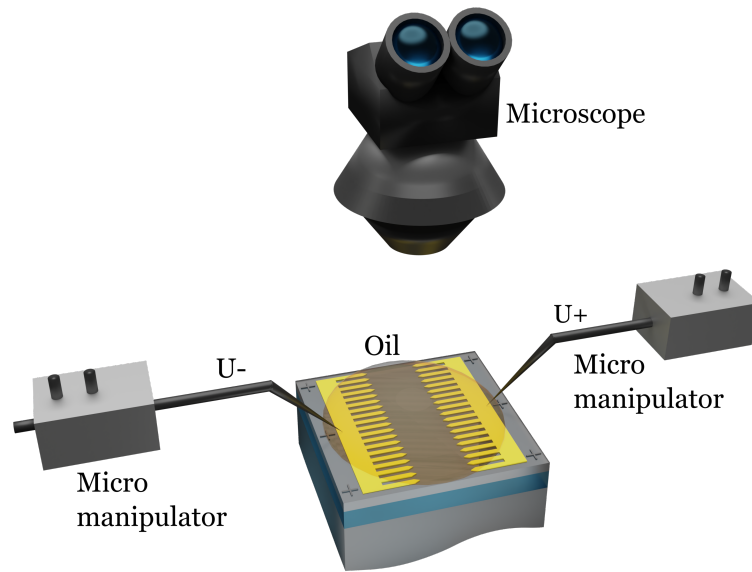


Figure 5.46 – Schematic representation of the periodic poling setup for LNOI. The electrodes are contacted by means of high voltage probes.

The LNOI sample is immersed in oil (ELBESIL TRANSFORMATORENÖL BTR 50 - Silikon Profis) to prevent arcing due to the high voltage between the electrodes. The sample is placed below an optical microscope to align the needles directly to the contact pads. The contact pad is used to contact all finger electrodes. We use micro-manipulators to hold and align precisely the needles manually. Moreover, the needles are contacted to a high voltage amplifier (20/20C - Trek), which is controlled by a computer program to define the pulse shape and voltage amplitude of the poling pulses. The software records simultaneously the applied voltage and the current from the amplifier. Nevertheless, it is not possible to monitor the poling process by controlling the charge as it is normally done in conventional lithium niobate [189]. In the case of LNOI, the areas we pole are much smaller, implying a lot lower charge and, as a result, a lower current in the micro ampere range. For this reason, the poling signal is small compared to the noise in the system.

We use one single-voltage pulse to pole LNOI periodically. Hence, we need to design the poling pulse to our needs. Figure 5.47 shows our well-experienced poling pulse from bulk lithium niobate, which shape we adapted for LNOI. We need a fast ramp up to a maximum voltage, which is hold for a specific amount of time. In this plateau time, the voltage is higher than the coercive field strength and the spontaneous polarisation is inverted. After that, the voltage drops to 80 % of the maximum voltage to stop the poling process. We have a discharge time, where we slowly decrease the voltage to zero to stabilise the domains and avoid back-switching of the domains.

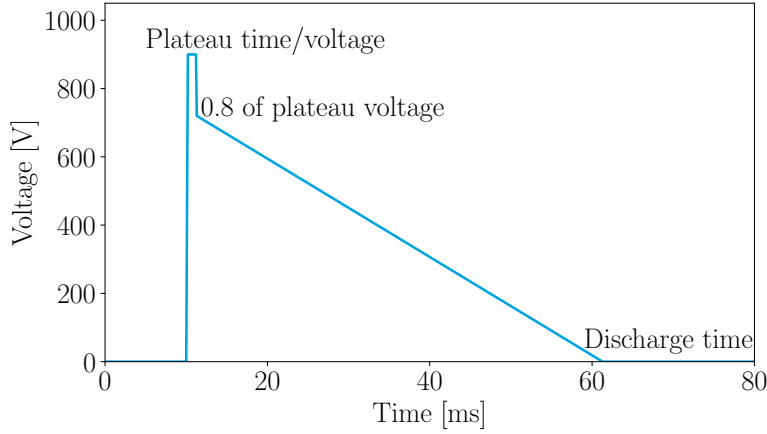


Figure 5.47 – Graph of the applied high voltage pulse used for poling. A rapid reduction of the voltage after the poling stops the poling process and simultaneously a long discharge time stabilises the domains.

For x-cut LNOI we fix the rise time to 0.2 ms, the voltage drop to 80 %, the fall time to 0.1 ms and the discharge time to 300 ms [190]. During this work, we varied the maximum voltage (between 500 V and 1300 V) and the plateau time (between 1 ms and 10 ms) to achieve perfect periodic poling depending on the material system and poling period. For simplicity, the plateau voltage and plateau time will be referred to as voltage and time in the following.

Before the waveguide fabrication, the finger electrodes have to be removed in a gold etchant (TechniEtch ACl2 - MicroChemicals) for 10 min and chromium etchant (TechniEtch Cro1 - MicroChemicals) for 10 min.

Initial Poling Tests

The first poling tests were done with block electrodes without fingers to narrow the possible parameter range for the applied pulses to achieve domain inversion in MgO doped LNOI. The following results are for electrodes fabricated with laser-lithography on MgO doped LNOI with a thin-film thickness of 300 nm. We used testing block electrodes with a separation gap of 40 μm , a length of 400 μm , and a width of 300 μm , see figure 5.48.

We applied to each structure a single-voltage pulse with voltages ranging from 0.8 kV to 2 kV in 0.2 kV increments and times from 1 ms to 10 ms in 1 ms steps.

For the investigation we used SH microscopy. We started with line-scans, where we expected a change in the intensity at the domain walls and thus, peaks in the spectrum. However, it turned out that line-scans did not give enough information about the domain growth from electrode to electrode, since it depends on the exact position of the line-scan relative to the electrodes.

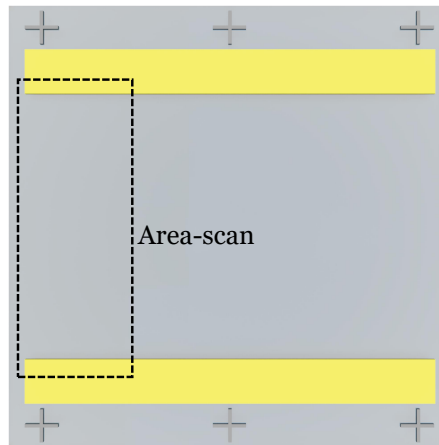


Figure 5.48 – Schematic representation of block electrodes. The dashed rectangular indicates the area-scan with the SH microscopy.

Therefore, we decided to use only area-scans for the analysis, even though the generation of this scan is more time consuming. Figure 5.49 shows a SH microscopy area scan for a poled block electrode with a 40 μm distance and an applied voltage of 1.4 kV for 9 ms.

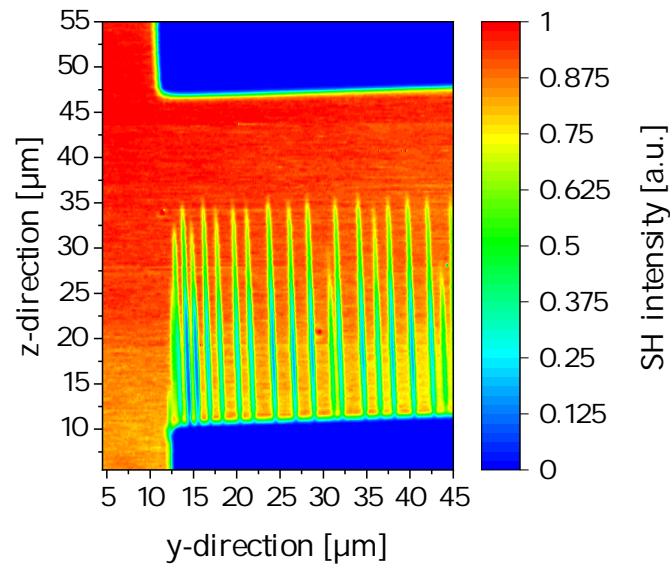


Figure 5.49 – SH microscopy area-scan of block electrodes poled with a voltage of 1.4 kV and a time of 9 ms. The domains are growing from the positive electrode to the negative electrode.

In this figure and all the following SH microscopy area-scans the negative electrode is

on top and the positive electrode is at the bottom. The domain walls are shown in green. The domain inversion starts at the positive electrode, which is in good agreement with the findings of Rüsing et al. [164]. Despite the fact that the block electrodes have no periodic structure, these domain walls tend to nucleate in a periodic manner. Even though we can observe an intrinsic periodic behaviour of the domain growth, we did not further investigate that, because we did not want to use this uncontrolled effect. As a result of this initial test, we know that we need voltages above 1.4 kV for 40 μm separation gaps to invert the spontaneous polarisation.

Because the size of the separation gap as well as the finger electrodes themselves have a large impact on the poling results, these preliminary poling tests are simply a rough study for the poling parameters. Therefore, we did a similar parameter study with finger electrodes.

Finger Electrodes

For the investigation of finger electrodes, we fabricated finger electrodes with a poling period of 3 μm , finger widths of 1.2 μm and finger lengths of 10 μm . We used a separation gap of 20 μm , a total periodic poling length of 400 μm and contact pads with a width of 300 μm , see figure 5.50.

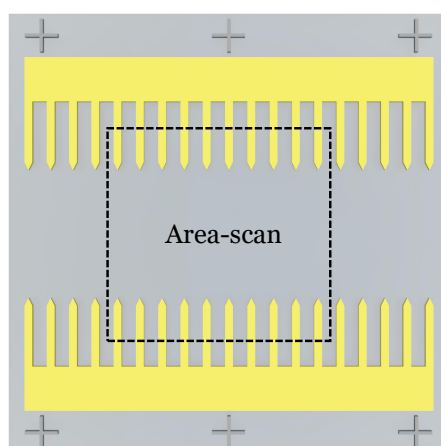


Figure 5.50 – Schematic representation of finger electrodes. The dashed rectangular indicates the area-scan with the SH microscopy.

From the initial poling tests we know that the best voltage for block electrodes is above 1400 V for a 40 μm separation gap. For this reason, we decided to use values around 700 V for a 20 μm separation gap and extended the voltage range to find the optimal parameter for finger electrodes. We applied single-voltage pulses with voltages ranging from 500 V to 1300 V in 100 V increments and times of 1 ms, 4 ms, 7 ms and 10 ms. Voltages below 800 V are not sufficient for a homogeneous poling from one electrode to

the other and voltages above 1000 V lead to a strong overpoling of the structure. Figure 5.51 shows a SH microscopy area-scan (logarithmic scale) of a periodically poled sample with a poling period of $3.0\text{ }\mu\text{m}$ with a voltage of 900 V and a time of 1 ms yielding the best duty cycle and homogeneous poling result.

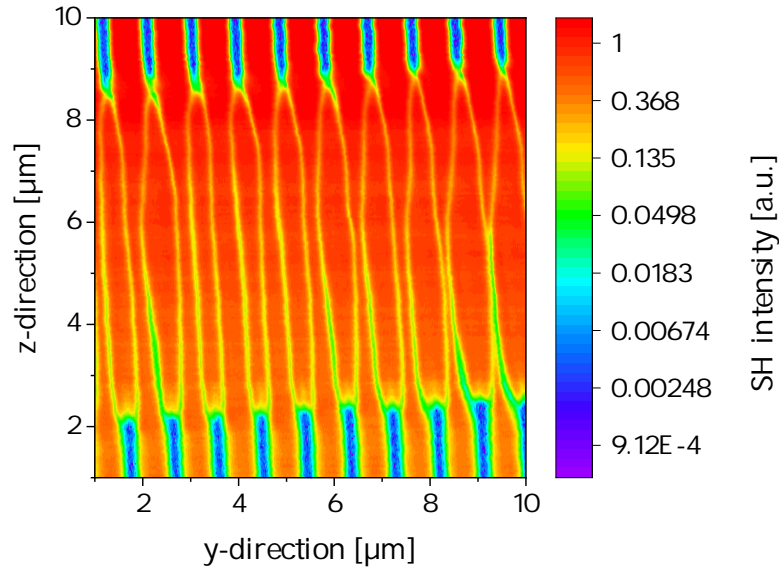


Figure 5.51 – SH microscopy area-scan (logarithmic scale) of finger electrodes poled with a voltage of 900 V and a time of 1 ms.

The yellow-green lines display the domain walls. All poled domains have grown from one electrode to the other. The domain walls at the positive electrode on the bottom are more angular than the tapered domain wall shape at the negative electrode. This indicates again a domain growth from the positive to the negative electrode, which means the domains grow from $+z$ to $-z$. Moreover, the duty cycle of the poled and unpoled domains is close to 1:1. In some areas the poled domains have a stronger lateral domain growth, which corresponds to overpoling induced by local imperfections and nano-domains in the material itself.

For efficient devices, we have to increase the overall length of the electrodes and pole these homogeneously over the entire length.

Longer Finger Electrodes

In a first step, we increased the total length to 5 mm long electrodes, because the efficiency of a nonlinear process increases quadratically with the length. We fixed the time to 1 ms and tested voltages between 870 V up and 950 V in 10 V steps. We contacted the long electrodes in the centre to allow for a homogenous distribution of the voltage over the entire electrode structure.

A voltage of 870 V results in the best poling behaviour, measured with a SH microscopy area-scan. To get information about the homogeneity of the poling over the electrode length, a second area-scan was done on one of the ends of the electrode. Figure 5.52 shows the two area-scans with respect to their position on the electrode.

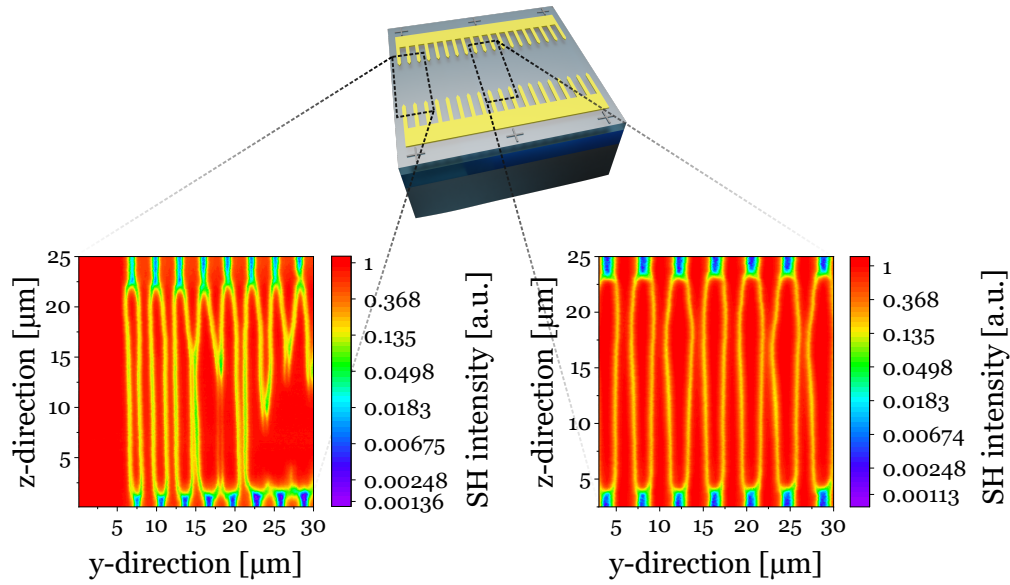


Figure 5.52 – SH microscopy area-scan (logarithmic scale) of 5 mm long finger electrodes with a poling period of 3 μm on the edge and in the middle of the electrode. The sample is poled with a voltage of 870 V and a time of 1 ms.

The area-scan in the middle of the electrode shows homogeneous domain inversion between the finger electrodes. The domain walls are straight, with only partly and little overpoling. In comparison, the area-scan at the edge of the electrode structure reveals certain domains that are grown together. As a result, the sample is overpoled in this area. Inhomogeneities in the thin-film layer, such as nano-domains or variations in the thin-film thickness, do have a huge influence on the homogeneity of the duty cycle. Nonetheless, this shows that we are able to periodically pole 5 mm long electrodes with a poling period of 3 μm homogeneous over the entire electrode length.

After the successful poling of 5 mm we extended the electrodes to 7.5 mm length. We used the same poling parameters as for poling of the 5 mm long electrode samples. In addition, the poling period of the finger electrodes was varied in steps of 0.1 μm from 2.7 μm to 2.9 μm to evaluate the effect of the poling period. Figure 5.53 shows area-scans in the middle and at the edge of the electrode for a poling period of 2.7 μm .

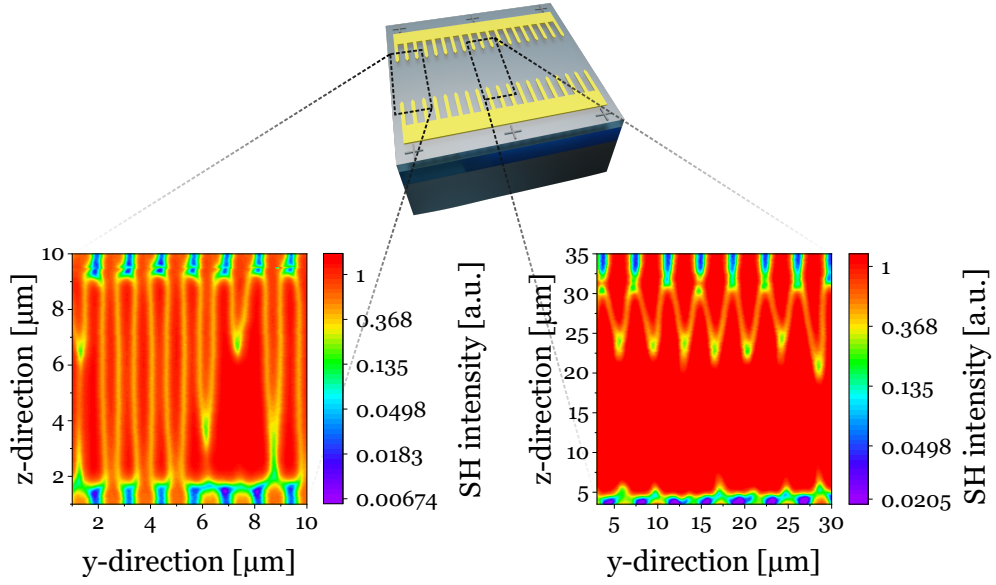


Figure 5.53 – SH microscopy area-scan (logarithmic scale) of 7.5 mm long finger electrodes with a poling period of $2.7\mu\text{m}$ on the edge and in the middle of the electrode. The sample is poled with a voltage of 870 V and a time of 1 ms.

In the middle of the area-scan the domain walls are only visible near the top negative electrode. Since we know that the domains grow from the $+z$ to $-z$, we can conclude that this sample is overpoled. The reason for this could be a change in the total thickness of the sample, compared to the previous one. As already mentioned, the thickness of thin-film layers varies, within the sample and between different samples, and has a huge influence on the required voltage for periodic poling. Even though the structure is overpoled in the middle, the area-scan at the edge of the electrode shows no overpoling except from the inhomogeneity induced overpoling. This indicates a voltage drop along the electrodes and an decreased external electric field at the edges of the electrodes, since we contact in the middle. This can be compensated by modifying the electrode and poling parameters.

5.2.2.4 Final Remarks for Periodic Poling of LNOI

We have developed the technology for the fabrication of finger electrodes as well as the poling technique. We successfully periodically poled MgO doped LNOI with a poling period of $3\mu\text{m}$ for $400\mu\text{m}$ and 5mm long electrodes. Beyond that we poled 7.5mm long electrodes with poling periods between $2.7\mu\text{m}$ to $2.9\mu\text{m}$. These structures are overpoled, but can be optimised with some adaptations in the poling process.

In the future, we can reduce the voltage drop, by increasing the thickness of the electrodes by a factor of 1.5 to 255 nm chromium and 45 nm gold, to compensate the 1.5 longer electrode length compared to the 5 mm electrodes. Moreover, we need to observe the influence of the thin-film thickness on the overall poling behaviour.

One reason for the overpoling is the poling pulse shape itself. The voltage drops to 80 % of the maximum voltage and this was adapted from the conventional lithium niobate poling technology. Since we use much higher electric field strengths as needed for lithium niobate we are with 80 % and a voltage of 696 V far above the coercive field strength (for a 20 μm the voltage is 420 V) and this will introduce further poling during the discharge time. Hence, we suggest to reduce the voltage to 10 % of the maximum voltage to avoid any poling during the discharge time.

Additionally, we can get rid of nano-domains by preconditioning pulses similar to those we do in RbKTP for stable domains and to homogenise the substrate material and avoid local overpoling.

The fabricated finger electrodes with the electron-beam-lithography show much more tapered finger tips, thus, will concentrate the electric field at the finger tip and this will allow for directed domain growth between the electrodes and less domain broadening. An open question that remains and needs to be answered in the future is the growth of the domains into the depth of the thin-film for our specific poling parameters. This is possible to analyse with a SH microscope [164].

5.23 Waveguides

Waveguides in LNOI are rib waveguides and require a surface structuring. As introduced in section 4.2.1.2 the most promising approach for structuring LNOI is using dry etching with an Ar^+ plasma. The fabrication of waveguides in LNOI was a completely new challenge. The first step was to investigate different mask materials for the dry etching. Then, we had a look at the dry etching process itself. After that, we explored different techniques to remove the redeposition material during dry etching. Last, we developed a technique to polish the end-facets of the waveguides.

5.23.1 Dry Etching

The waveguides are fabricated via dry etching. We have chosen pure argon as the etching material, because using reactive ions of other gases selectively react to crystal orientations and etch them differently. Since our goal is to make integrated devices and sources, we need periodically poled structures. A reactive ion, thus, a gas that reacts to the orientation of the domains would induce corrugated waveguides. To prevent this, we use only argon and physical dry etching. Our first step was to decide on a mask material that would meet our requirements and withstand the physical etching process.

Mask Material

There are different ways to fabricate the mask for the dry etching. Either the photoresist is used directly as an etching mask, or we use the photoresist structure to produce a hard mask through a lift-off. We have tested both, for the resist we used AZ MIR 701 (Micro-Chemicals) for mask-lithography as well as for laser-lithography. This resist has a high resolution and is advertised by the manufacturer as stable in dry etching processes. The advantage of photoresist as a direct etching mask is that the amount of process steps are significantly reduced. However, we noticed that the photoresist formed bubbles during the etching process. Figure 5.54 shows the resist strip with the induced bubbles after dry etching.

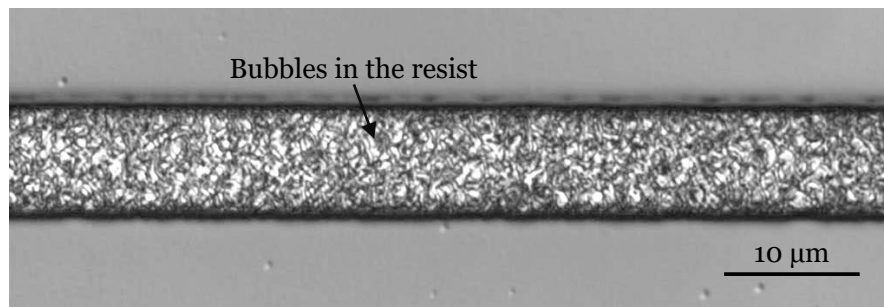


Figure 5.54 – CLSM image of a photo resist stripe after usage as a dry etching mask. After the process distinct bubbles, which were formed during the etching process, are visible.

These bubbles increased the sidewall roughness and thus, the losses of the waveguides. So, we investigated the origin of the bubbles to check, if they were induced by the vacuum or by the high temperatures during etching. We have exposed the photoresist structure to both high pressures around 10^{-7} mbar and high temperatures of 300°C and have not seen any bubble formation. Therefore, the only possibility is that the process reacts to all factors simultaneously directly in the etching. In order to avoid bubble formation due to the outgassing of the photo resist, we tried flood exposure of the resist after development, but this did not lead to the desired result. The only way to prevent bubble formation is to cool the sample during dry etching. To do this, the holder plate is cooled with helium (30 mTorr). To cool the sample, the sample must be thermally contacted. Vacuum grease has proven to be the best material for this, and it can be wiped off very well with isopropyl alcohol afterwards. Figure 5.55 shows the resist and waveguide structure after dry etching with helium back-side cooling and vacuum grease.

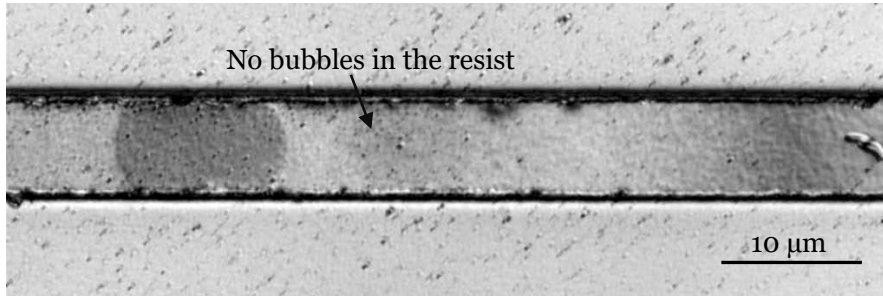


Figure 5.55 – Photoresist and waveguide structure after dry etching with helium back-side cooling and vacuum grease imaged via CLSM.

Due to the helium cooling, it is possible to reduce the formation of bubbles. However, the helium cooling reduces the pressure in the chamber and the etching rate decreases. As a result, using photoresist as a hard mask is attractive because of the reduced amount of process steps, but we would prefer a hard mask, which does not require cooling to be stable during the dry etching.

As an alternative, we investigated different materials as suitable materials for a physical dry etching process and we fabricated hard masks with a lift-off process [171]. We investigated the etch mask materials in terms of their etch rates as well as the homogeneity of the structure. Table 5.7 shows different mask materials and their etch rates and selectivity, which is the ratio between the etch rate of the material and lithium niobate, as a mask material.

Table 5.7 – Etching rates for different materials with process parameters during dry etching of argon gas flow rate of 20 sccm, a pressure of 2 mTorr, a RF power of 70 W and an ICP power of 100 W [171].

Material	Etch rate [nm/min]	Etch selectivity to LN
Lithium niobate	11.5 ± 1.6	-
Chromium	14.4 ± 0.1	0.8 : 1
Silicon dioxide	7.5 ± 1.1	1.5 : 1
Titanium	9.1 ± 0.1	1.3 : 1

Chromium has a high etch rate and therefore, a lower selectivity during the etch process, which makes it harder to produce deeper waveguide structures. SiO₂ and titanium have comparable etching rates. Even though our first investigations showed a higher homogeneity of the sidewalls for titanium, we decided to use SiO₂ as an etching mask material, because the best waveguides, with the lowest losses at that time, were fabricated

with hydrogen silsesquioxane (HSQ) resist and physical dry etching [123]. HSQ offers the advantages of a photoresist as a dry etching mask, but is at the same time stable as SiO_2 during dry etching. Therefore, we decided to optimise our fabrication process with SiO_2 as an etching mask, to facilitate the transfer to HSQ resist and electron-beam-lithography in the future.

The thickness of SiO_2 depends on the desired etching depth. Since we have a physical etching process, the selectivity between the mask and lithium niobate is 1.5:1. Consequently, the mask has to be at least 1.5 times thicker than the desired etching depth. Moreover, since we use a physical etching, the sidewalls of the waveguides are slanted. Therefore, the width of the SiO_2 mask design has to be equal to the bottom width of the etched waveguide. Figure 5.56 shows the difference between the mask definition and the etched waveguide with slanted sidewalls.

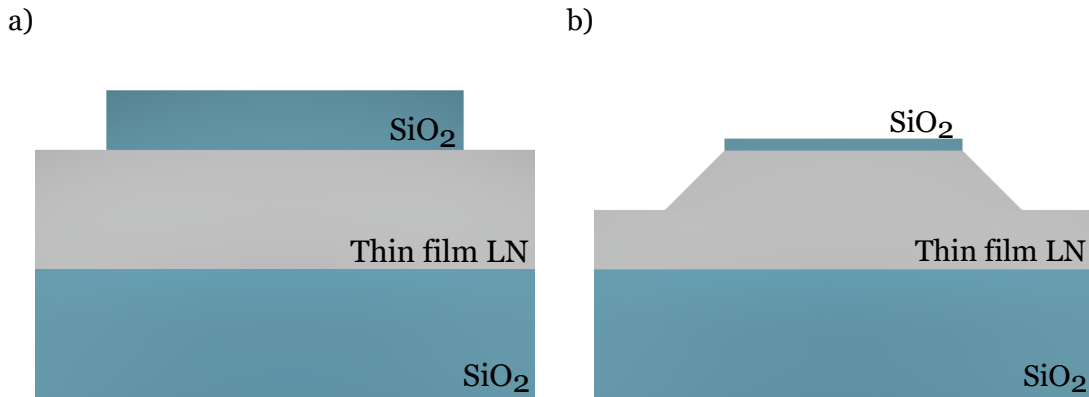


Figure 5.56 – Schematic representation of the mask a) before and b) after dry etching the waveguide with slanted sidewalls.

Dry Etching

To transfer the SiO_2 mask into the lithium niobate thin-film, we use inductively coupled plasma - reactive ion etching (ICP-RIE - Oxford Plasmalab 100). Figure 5.57 shows the ICP-RIE and its parameters to tune the dry etching behaviour with the gas flow rate, the ICP power, the RF power and the chamber pressure.

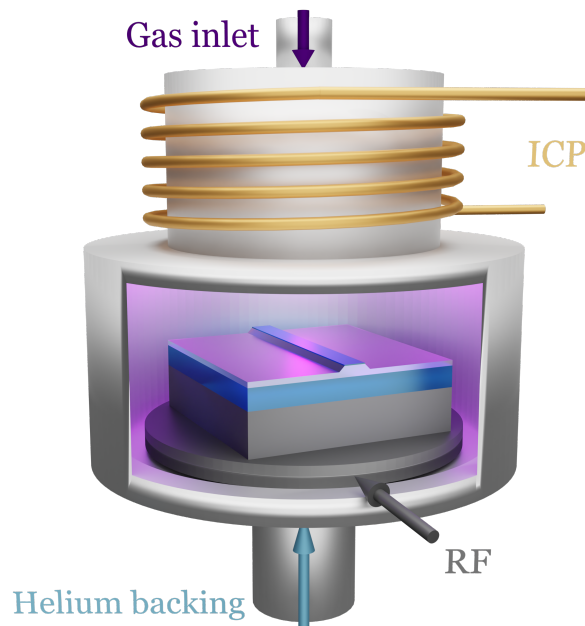


Figure 5.57 – Schematic representation of the dry etching system and parameters in an ICP-RIE.

During the dry etching process the incident ions lead to a cascade of collisions on the surface on LN. If the kinetic energy of the ions is higher than the binding energy of the etched material, atoms are knocked out of the substrate surface and material is removed from the surface.

The larger the gas flow rate, the more argon plasma can be activated by the ICP. The higher the ICP power, the more atoms will be ionised, which can be accelerated to the sample by the RF. The higher the RF power, the higher the DC bias voltage and therefore, the acceleration speed will be larger as the electric field is stronger. This corresponds to a stronger ion bombardment, thus, increasing the etching rate. Nevertheless, with a high gas flow rate, ICP and RF power, side wall roughness will be reduced but at the same time redeposition is increased, which means a higher side wall angle. Moreover, the selectivity between the mask and the lithium niobate decreases [159]. The lower the chamber pressure, the longer the mean free path of the gas molecules and the accelerated ions have more energy before collision, thus, we achieve higher etch rates. For the best results the chamber pressure has to be as low as possible and the gas flow rate, ICP and RF power have to be balanced with respect to the sidewall roughness and angle.

Physical dry etching as a versatile procedure can be used for different kind of structures, e.g., straight waveguides or couplers with a bottom gap from edge to edge down to 1 μm , see figure 5.58.

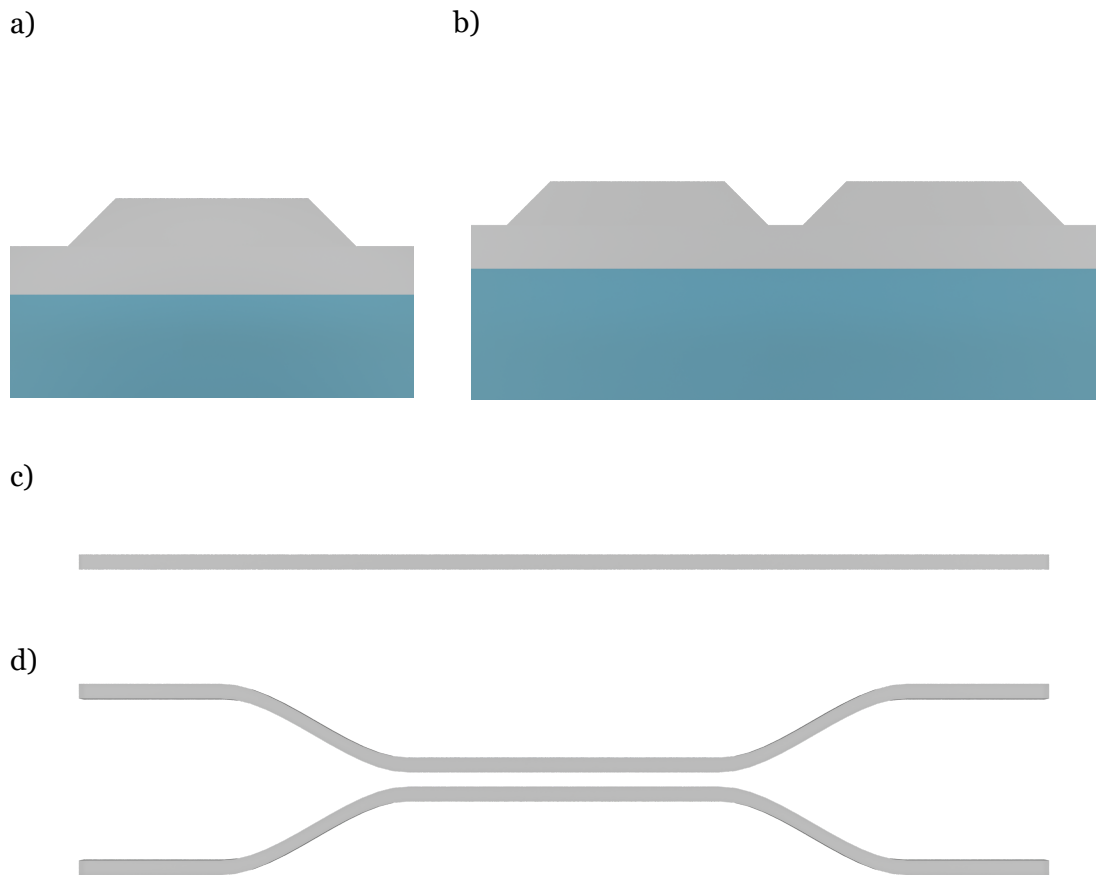


Figure 5.58 – Schematic representation of different kind of structures we are able to fabricate with our developed fabrication techniques. Cross-section of a) one waveguide and b) a directional coupler. Top view of c) one waveguide and d) a directional coupler.

Dry Etched Waveguide

In the following, we show our dry etched waveguides for a SiO_2 etching mask. To define the SiO_2 mask, we adapted the lift-off process (via laser-lithography or electron-beam-lithography) explained in section 5.2.2. After the lift-off we end up with a SiO_2 mask ready for the dry etching. Figure 5.59 shows a lifted SiO_2 structure for the waveguide dry etching.

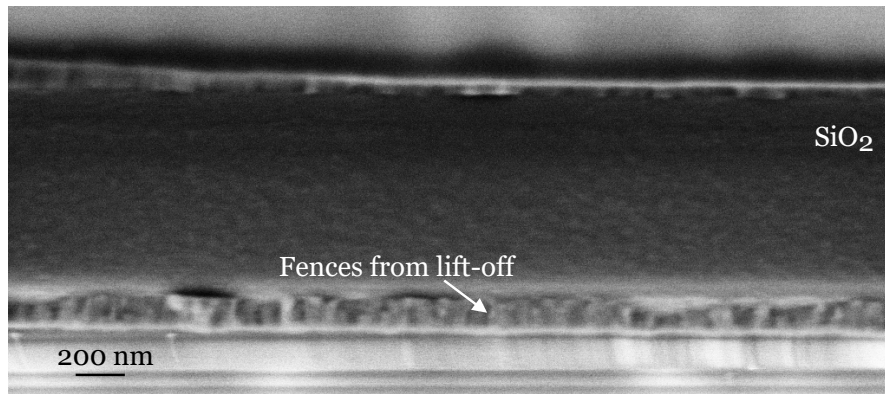


Figure 5.59 – SEM image of a lifted SiO_2 structure for dry etching.

We can see rough sidewalls, which are introduced by fences from the lift-off process itself. These structures are directly transferred into the waveguide after dry etching, see figure 5.60.

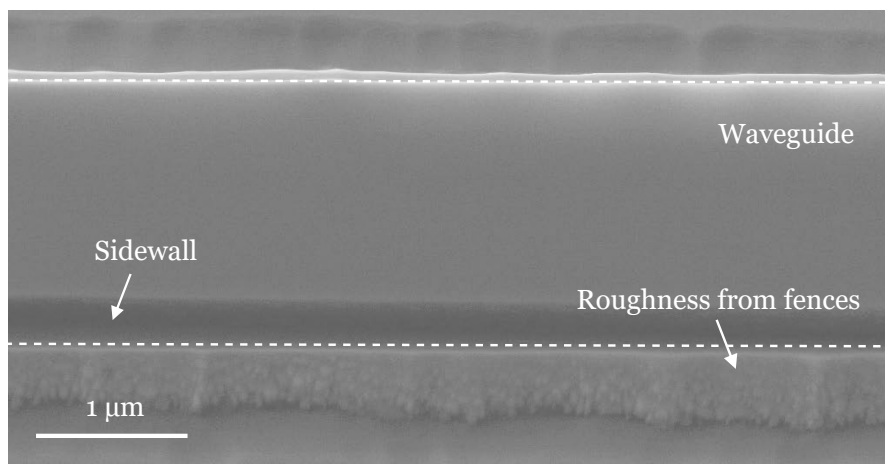


Figure 5.60 – SEM image of a waveguide after dry etching with a SiO_2 mask.

Nevertheless, these waveguides show a promising surface with a low variation, which

represents a huge improvement of the first waveguides we fabricated. Figure 5.61 a) shows one of the first fabricated waveguides. This waveguide shows a lot of inhomogeneities in the width along the propagation direction and at the sidewalls a lot of damages.

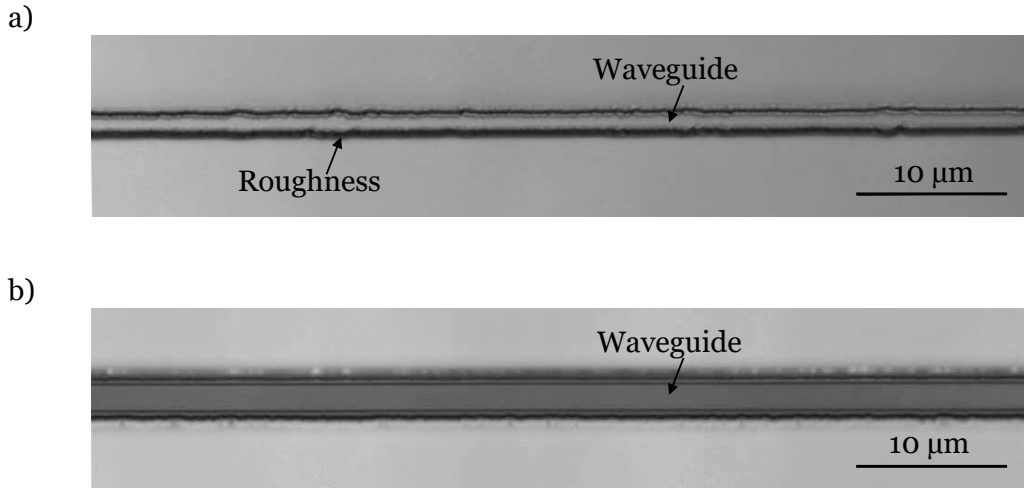


Figure 5.61 – a) The first fabricated waveguides in LNOI. b) Fabricated waveguides after optimisation of process steps and parameters.

We were able to improve the fabrication of the etching mask itself and etching procedure to reduce the inhomogeneities and damages at the sidewalls, see figure b).

Besides the sidewall roughness, the other important parameter is the waveguide geometry, which we can analyse from the cross-section.

Waveguide Geometry

The geometry of the waveguide can be described by different parameters, which are the width, the depth and the angle. The width is set by the etch mask and results in the bottom width of our waveguide. To evaluate the top width of our waveguides, we need to know the etching depth and angle of the waveguide. We can adjust the etching depth by the time in the etching process. For our chamber parameters (argon gas flow rate of 60 sccm, pressure of 7.3 mTorr, RF power of 70 W and ICP power of 100 W) we obtain an etch rate of 6.26 nm/min. The angle of the waveguide depends on the parameters in the chamber and is in our case around 60°. Figure 5.62 shows an etched and polished waveguide end-facet.

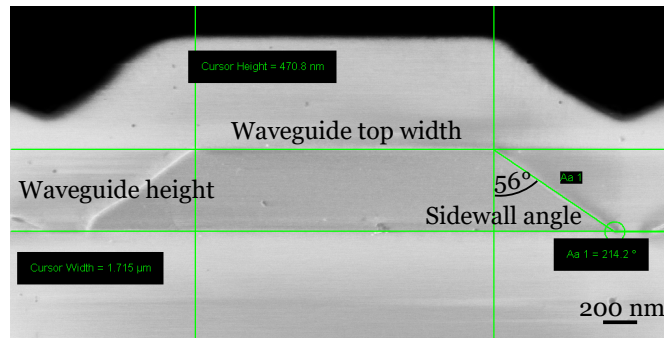


Figure 5.62 – SEM image of a dry etched and polished waveguide end-facet. The etching conditions had an argon gas flow of 60 sccm, a pressure of 7.3 mTorr, a RF power of 70 W and an ICP power of 100 W, resulting in an 56° angle of the sidewall.

With the SEM we can analyse the geometry of the waveguide. This waveguide in figure 5.62 has a height of 470.8 nm, a top width of $1.715\ \mu\text{m}$ and a sidewall angle of 56° . The ideal case would be an waveguide structure with a 0° angle of the sidewalls, which is not possible with an anisotropic etching process, like we have in the case of ICP dry etching. Nevertheless, the etching conditions have much more room for improvement to decrease the angle.

First tests show that if we use SiO_2 as a mask material instead of photoresist and reduce the argon flow rate to 20 sccm, we can increase the pressure to 12.7 mTorr. This allows for much steeper angles, see figure 5.63.

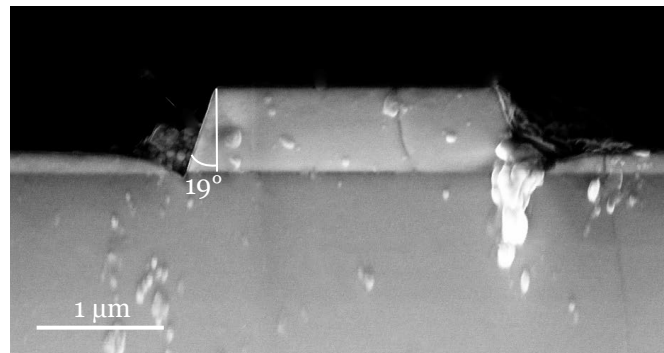


Figure 5.63 – SEM image of a dry etched and polished waveguide end-facet. The etching conditions had an argon gas flow rate of 20 sccm, a pressure of 2 mTorr, a RF power of 70 W and an ICP power of 100 W, resulting in an 19° angle of the sidewall.

The particles on the waveguide and next to the waveguide are remaining residuals from the end-facet polishing. Moreover, this image shows on both sides of the waveguide trenches. These trenches are induced by additional etching from reflected ions from the sidewalls of the waveguide. Up to now we reduced the argon flow rate to 20 sccm, which enabled us to reduce the angle from 56° to 19° degrees, due to the higher pressure in the chamber. This comparable to demonstrated sidewall angles with 15° in literature [191]. When we further reduce the flow rate, we still need to see if more optimisation is possible. The fact that we can change the angle through the etching conditions, gives us completely new possibilities for modelling and a huge parameter range. We can adjust our sources according to your needs, by tuning not only width and depth of a waveguide but the angle of the sidewalls. This gives us the possibility of designing and fabricating unique sources with special requirements.

After the dry etching we clean the sample in a cleaning procedure. To reduce the propagation losses of our waveguides we need to minimize the the sidewall roughness.

5.23.2 Sidewall Roughness Minimisation

During dry etching LN molecules are ejected in all directions and some of these sputtered molecules deposit on the sidewalls of the waveguide. As a result of this redeposition, the optical performance of the etched ridges is reduced. Figure 5.64 a) shows waveguide with redeposition after dry etching.

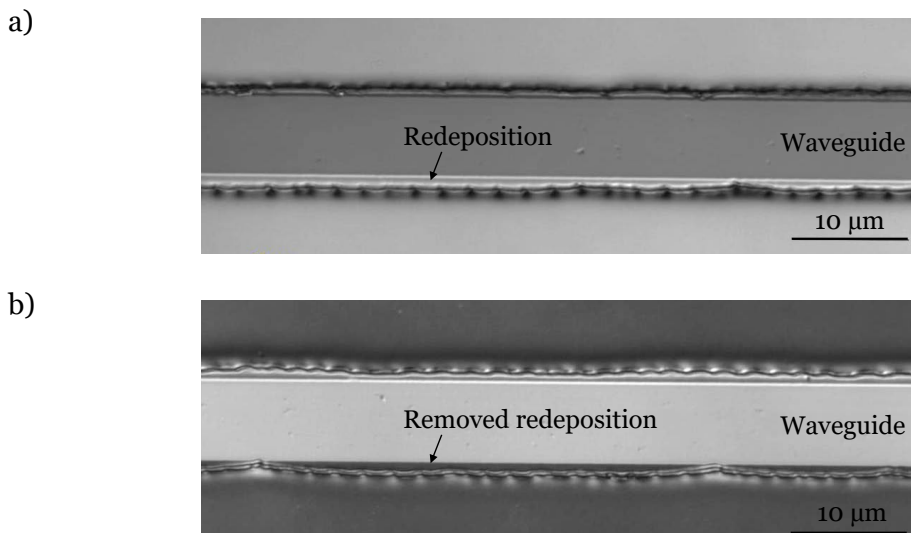


Figure 5.64 – CLSM images of a) dry etched waveguide with redeposition and b) waveguide after removing of the redeposition with an ammonia solution (NH_4OH , H_2O_2 , H_2O volume ratio 2:2:1) for 90 min at 75°C .

To remove this redeposition, we can use chemical etching in an ammonia solution (NH_4OH , H_2O_2 , H_2O volume ratio 2:2:1) for 90 min at 75 °C in an ultrasonic bath. Figure 5.64 b) shows the same waveguide with removed redeposition. Nevertheless, one has to mention that this solution is similar to the one we use to selectively etch domain structures, which makes this approach problematic for periodically poled waveguides, because the sidewalls are attacked selectively to the domain orientation.

To avoid chemical etching, we started to investigate top surface polishing via CMP technique to remove the redeposition. The waveguide tops are protected with a chromium layer that we avoid polishing of the top surface of the waveguide. The sample is facing with the top surface upwards and fixed to a sample holder, which we turn upside down and mount into a second holder on the polishing plate with an velvet polishing cloth. We choose an amorphous colloidal silica suspension (MasterMet - Buehler) with a 60 nm diameter of the particles. We move the sample holder manually back and forth parallel to the direction of the waveguide, to avoid strong polishing lateral to the waveguide. Afterwards, we remove the chromium in a chromium etchant (TechniEtch Cr01 - Microchemicals) and clean the samples in a cleaning procedure. The samples get a cladding layer of 600 nm SiO_2 to facilitate the end-facet polishing.

We used four waveguide samples with identical waveguide structures and increased with each sample the polishing time. With longer polishing, we expected to remove more redeposition material and get smoother sidewalls. As a result, we expected to see a decrease in the losses with increasing polishing time. We measured the losses with the Fabry-Pérot method and contrary to our expectations, the losses increased with the polishing time. Moreover, the sample that was not polished at all had the lowest losses [192].

SEM images of each sample were taken to better understand the increasing losses with the polishing duration. Figure 5.65 shows SEM images of the waveguide cross-section at the polished end-facet from each sample.

The four pictures show the end-facet of a waveguide with increasing polishing time. Waveguide a) with no polishing looks like we expected after dry etching. Waveguide b) - d) show all damages at the sidewalls due to the surface polishing. This explains the higher losses in these waveguides. Moreover, the waveguide d) with the longest polishing time is decreased in total height, which gives an indication that the chromium layer was not thick enough for 90 s polishing time and we directly polished the waveguide top.

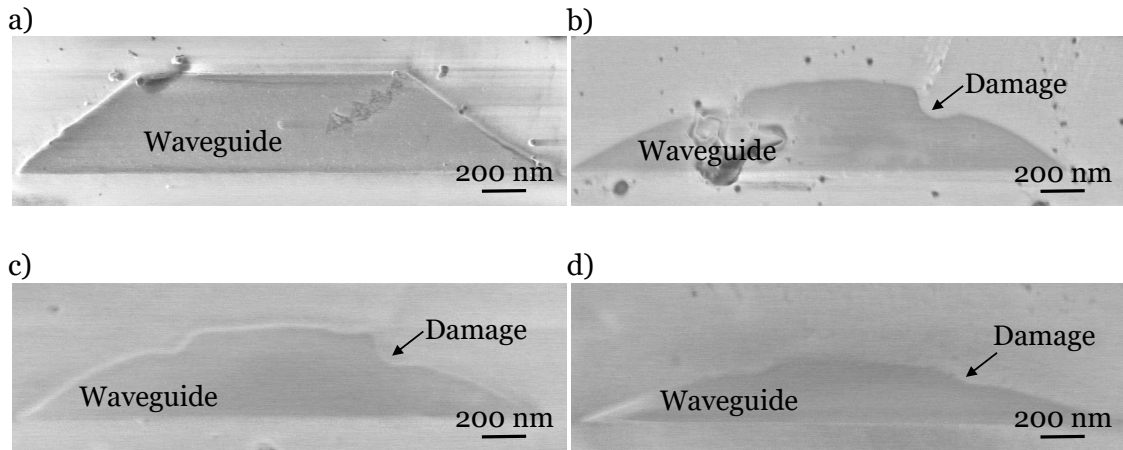


Figure 5.65 – SEM images of waveguide end-facets for different degrees of surface polishing. The degree of polishing is determined by the used time. For a) no additional polishing was conducted. The used polishing times are b) 30 s, c) 60 s and d) 90 s.

As a result of these measurements, we can conclude that polishing the surface in this manner does not reduce our losses, in fact it increases them. Therefore, we suggest for the future to reduce the polishing time to remove the redeposited material without chemical etching and at the same time avoid damage at the sidewalls.

Following the removing of the redeposition, we need to polish the end-facets, with a method similar as described in section 4.1.2.2, for the in-coupling of the waveguides.

5.233 Polishing

We have many years of experience in polishing end-facets in conventional LN and KTP. Therefore, we have chosen this method to prepare the end-facets of LNOI. For polishing, we use the method presented in section 4.1.2.2. Instead of photoresist between the samples, we use a cladding layer of SiO_2 on the waveguides of the LNOI sample to improve the polishing results. This distributes the pressure from the individual waveguides over the entire substrate, if we press a second sample onto the LNOI sample. We examine the polishing result in the holder under the CLSM for an efficient and quick study of the polished end-facets. Figure 5.66 a) shows one of our polished end-facet with a cladding layer.

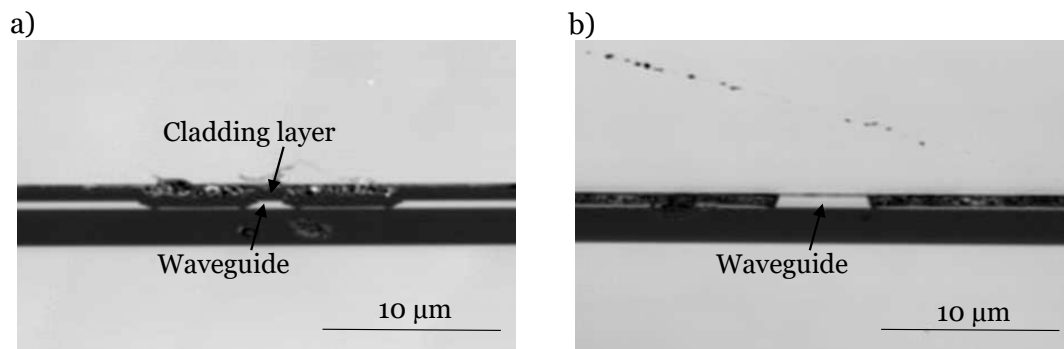


Figure 5.66 – CLSM image of a polished end-facet with a) a cladding layer and b) without a protection layer.

Our objective is to develop dispersion engineered sources and most of our simulations show that we need to avoid the cladding layer to realise desired source designs [73]. Therefore, we started to investigate the possibility of polishing without a cladding. From conventional lithium niobate we know that it is possible to polish samples without any protection layer between the substrates. Thus, we tested polishing LNOI without any protection. It takes some attempts to polish the end-facet without breaking small parts of the waveguides end-facet. Figure 5.66 b) shows a polished end-facet without a protection layer imaged with the CLSM.

Even though it is possible to polish the waveguides without a protection layer, we get a lot of residuals from the polishing on top of the sample, see figure 5.67.

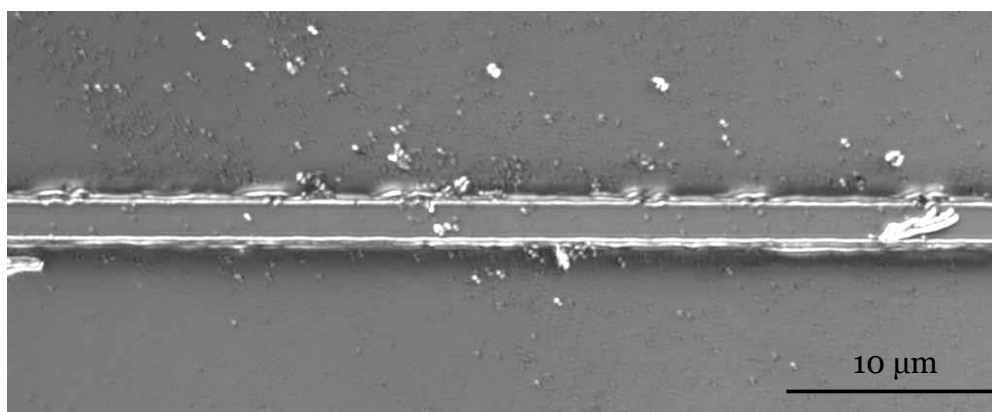


Figure 5.67 – Residuals from the end-facet polishing on top of the sample imaged with a CLSM.

The dirt settles between the two samples due to the spaces between them. These particles can introduce additional scratches on the waveguides and these lead to higher

losses. It is possible to avoid this, by using a thin layer of photoresist on the LNOI sample, which we can remove with a cleaning procedure after the polishing.

Polishing Residuals

One important point we would like to mention is that the dirt from the polishing at the end-facet is not visible with the CLSM. If we image the same sample as figure 5.66 a) with a SEM, we see a lot of polishing residuals on the end-facet, see figure 5.68 a).

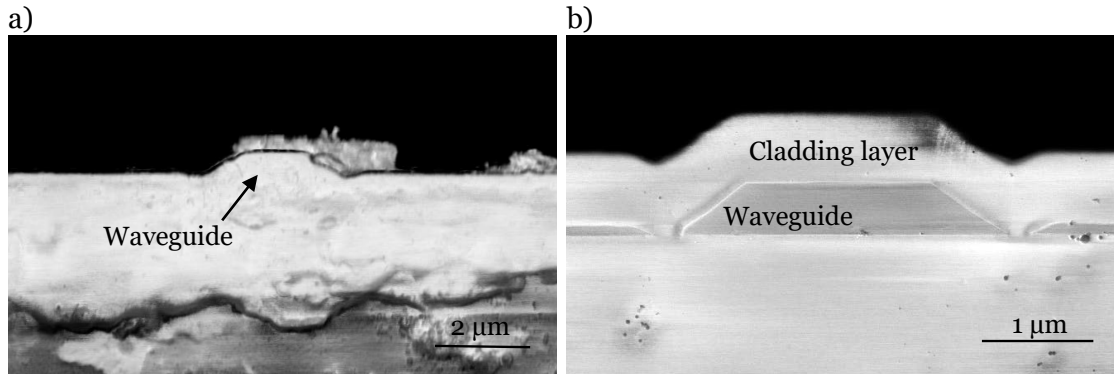


Figure 5.68 – a) SEM image of an end-facet in LNOI directly after polishing. b) SEM image of an polished end-facet in LNOI after an extended cleaning procedure.

It is possible to clean the end-facet with an extended cleaning procedure. Therefore, we first immerse the samples for 10 min in an ammonia solution and then, we do a standard cleaning procedure afterwards. Another solution could be to clean the samples directly after the end-facet polishing in hot tickopur. Figure 5.68 b) shows the same end-facet after cleaning.

As a result, we highly recommend to clean the samples independent of the substrate (LNOI, KTP or LN) with an extended cleaning procedure.

5.23.4 Propagation Losses

We used the Fabry-Pérot method described in section 4.3.2.2 to measure the losses in LNOI. We measured the losses of LNOI waveguides at a wavelength of 1550 nm using the Fabry-Pérot method. We measured the through coupled intensity while tuning the wavelength between 1550.0 nm and 1550.5 nm in 0.005 nm steps. The measured intensity oscillations as a function of wavelength for the fundamental qTE mode of a 1 μm top width waveguide is shown in figure 5.69.

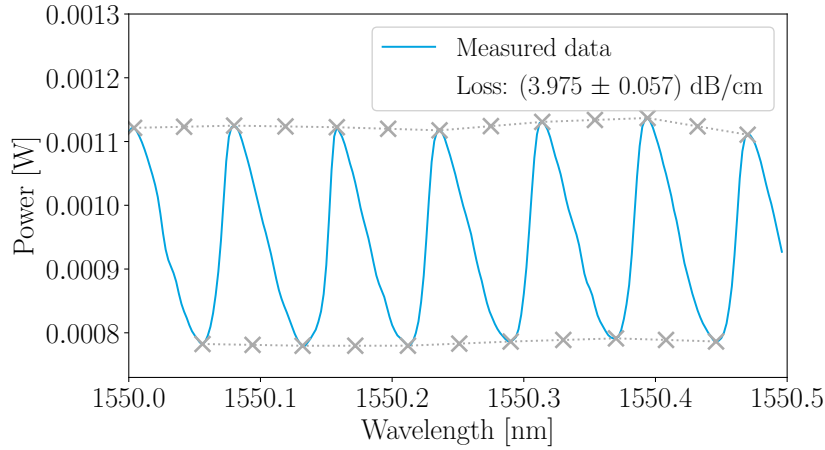


Figure 5.69 – Intensity oscillations as a function of the wavelength during Fabry-Pérot measurements of the fundamental qTE mode of a 1 μm top width waveguide in LNOI.

We measured propagation losses in our waveguides down to 2 dB/cm for a reflectivity of $R = 0.135$. As mentioned in section 4.3.2.2, we can not calculate the reflectivity using the Fresnel-reflectivity and hence, we estimate the reflectivity via FDTD simulations. Nevertheless, we do not know the reflectivity for sure and this introduces an uncertainty in the loss definition.

The only way to make an accurate statement about the losses is not to assume a value for the reflectivity, but to determine the losses by the measurement itself. This is possible via the transmission spectrum of a ring resonator. Therefore, the next logical step would be to develop ring resonators in the future and use them first to determine the losses of our waveguides.

5.23.5 Final Remarks for LNOI Waveguides

We developed the technology for LNOI to fabricate a mask for dry etching and the dry etching process itself. We extended our knowledge in the polishing for removing the redeposition from dry etching and polish our end-facet for waveguide in-coupling.

In the future, we can use the electron-beam-lithography to either lift-off SiO_2 as a dry etching mask or directly use HSQ resist for a higher resolution and smoother edges of the mask and thus, smoother sidewalls of the waveguides. This enables us to fabricate waveguides with lower losses. One more important point we have to mention is that the stability of the ICP system has a huge impact on the reproducibility of waveguides, the more stable the etching conditions in the chamber are, the more reliable is the waveguide fabrication.

5.2.4 Modelling of LNOI Structures

LNOI has unique features that make it an ideal technological platform for the fabrication of waveguides for quantum optical applications. However, LNOI is a new material platform such that first a systematic investigation of the dispersion is essential to properly understand its possibilities and limitations. For this reason, we studied the influence of the waveguide geometry on the dispersion relation. Moreover, we simulated a coupler structure, which we fabricated and characterised to improve and validate our simulations.

5.2.4.1 Modelling of Waveguides

To investigate the influence of the waveguide geometry on the spatial modes and effective refractive indices, we simulated various geometries via Lumerical. Especially the influence of fabrication errors on the phase matching is important for us. For this reason, we performed a study of the dispersion relation of congruent LNOI and MgO doped LNOI.

We used the model introduced in section 4.3.2.2 and designed a waveguide by defining the waveguide top width w , etching depth d , thin-film thickness t , sidewall angle θ and a cladding thickness c of SiO_2 . We fixed the thin-film thickness to 600 nm, because preliminary studies showed that this is the most promising thin-film thickness for future sophisticated quantum optical devices. Moreover, we set the cladding layer to zero, as a cladding layer lowers the difference in refractive index between the waveguide core and its cladding, bringing it closer to a weakly guiding regime [73]. For all simulation we set the temperature to 20 °C for operations at room temperature. Figure 5.70 shows an exemplary simulated qTE mode for a 600 nm thin-film, 300 nm etching depth, 0.75 nm top width and a sidewall angle of 60 °.

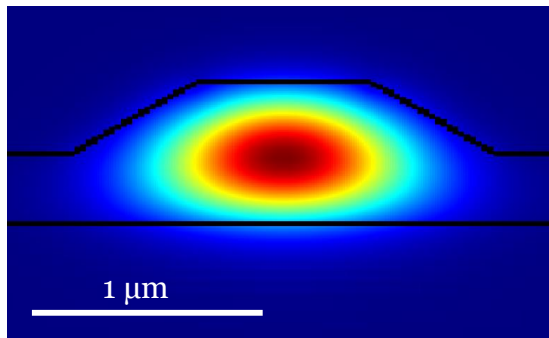


Figure 5.70 – Simulated qTE mode, for a 600 nm thin-film, 300 nm etching depth, 0.75 nm top width and a sidewall angle of 60 °.

The simulations in Lumerical give us the fundamental and higher order modes of different waveguide geometries including their polarisation and their corresponding effective refractive index n_{eff} of the individual modes.

For the first analysis, we studied the influence of the width and depth for congruent LNOI. Therefore, we fixed the angle to 60° . We varied the etching depth between 25 nm and 600 nm in 25 nm steps and the waveguide top width between $0\ \mu\text{m}$ and $2.0\ \mu\text{m}$ in $0.25\ \mu\text{m}$ steps. Moreover, we scanned a wavelength range from 400 nm to 2500 nm. Figure 5.71 shows the effective refractive index for the fundamental qTE (blue) and qTM (red) modes depending on the wavelength for a fixed etching depth of 500 nm and varying waveguide width. The colour gets darker with increasing waveguide width.

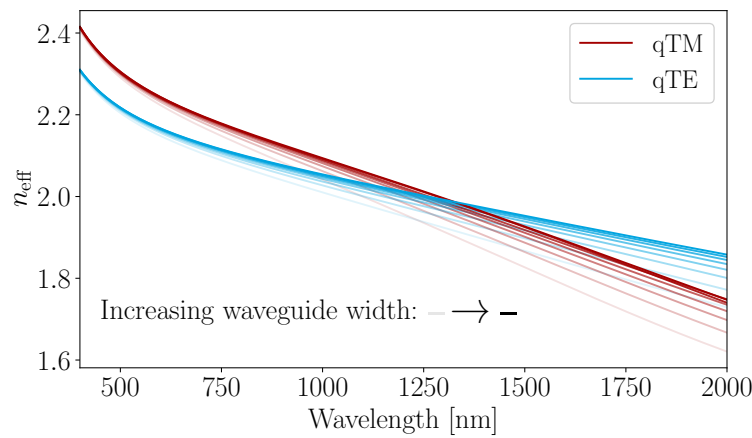


Figure 5.71 – Effective refractive index n_{eff} for the fundamental qTE (blue) and qTM (red) modes depending on the wavelength for a fixed waveguide depth of 500 nm. The waveguide top width varies from $0\ \mu\text{m}$ (light) to $2\ \mu\text{m}$ (dark).

This figure shows that the waveguide width has a huge influence on n_{eff} for both polarisations, in particular for longer wavelengths.

In contrast to that the effective refractive index for the fundamental qTE (blue) and qTM (red) modes for a etching depth variation and a fixed waveguide width of $1\ \mu\text{m}$ is shown in figure 5.72. For increasing etching depths the colour gets darker.

In general the etching depth has a stronger influence on the effective refractive index for higher wavelength, in particular for the qTM mode. Nonetheless, the dependence on the etching depth is not as strong as on the waveguide width for n_{eff} .

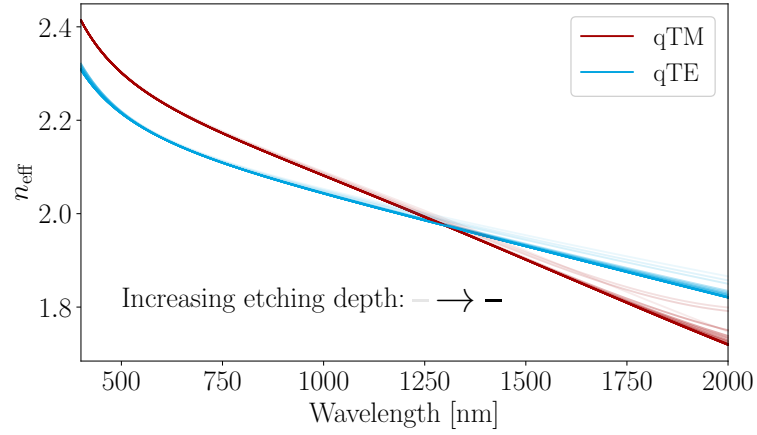


Figure 5.72 – Effective refractive index n_{eff} for the fundamental qTE (blue) and qTM (red) modes depending on the wavelength for a fixed waveguide top width of $1\ \mu\text{m}$. The etching depth varies from 25 nm (light) to 600 nm (dark).

For our fabrication and future reliable devices, it is important to find geometry ranges, which do not have a strong variation in the effective refractive index to be more resistant to fabrication errors. Figure 5.73 shows the effective refractive index of the qTE (blue) and qTM (red) mode for the fixed wavelength of 775 nm and 1550 nm. With darker colour we increased the etching depth.

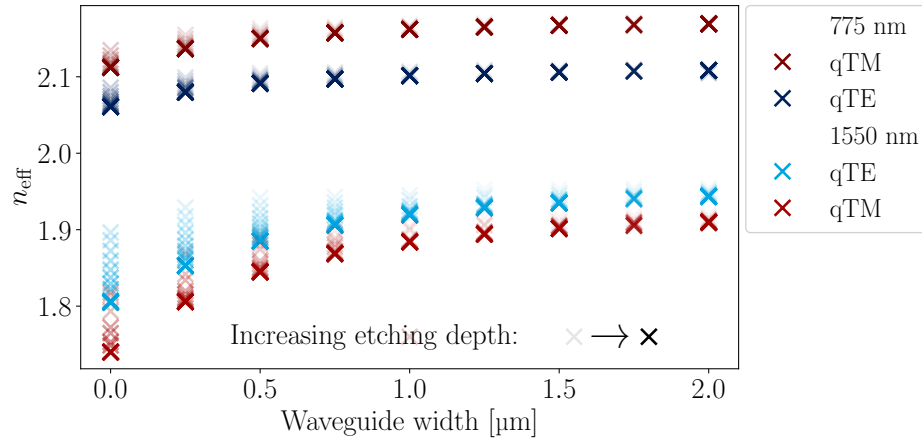


Figure 5.73 – Effective refractive index n_{eff} for the fundamental qTE (blue) and qTM (red) modes depending on the waveguide top width for the fixed wavelength of 775 nm and 1550 nm. The etching depth varies from 25 nm (light) to 600 nm (dark) in 25 nm steps.

Analogue to figure 5.71, figure 5.73 shows that the waveguide width has a higher impact for longer wavelength. Moreover, the effective refractive index increases for wider waveguides, which is more prominent at 1550 nm. Furthermore, the shallower the waveguides are etched, the less pronounced in the variation in the refractive index depending on the waveguide width. In addition, for the wider waveguides, the variation of n_{eff} reduces to a change in the second decimal place, which still has a major impact on the phase matching.

We also had a look at the influence of the angle on the effective refractive index. Hence, we varied the sidewall angle from 0° to 85° . Figure 5.74 shows the influence of the sidewall angle, the steeper the sidewalls the darker is the colour, for the qTE (blue) and qTM (red) mode for the fixed wavelength of 775 nm and 1550 nm.

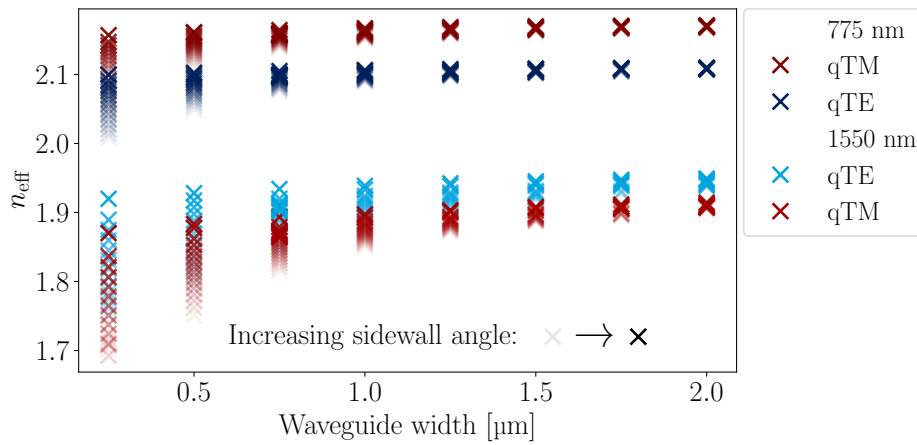


Figure 5.74 – Effective refractive index n_{eff} for the fundamental qTE (blue) and qTM (red) modes depending on the waveguide top width for the fixed wavelength of 775 nm and 1550 nm. The sidewall angle varies from 0° (light) to 85° (dark).

We can see that the angle has the most influence at waveguides with a smaller width. Moreover, the steeper the waveguide and the more the waveguide becomes similar to a rectangular shape, the less does the angle impact the effective refractive index. This is comparable with the results for the etching depth.

This strong dependence on the geometry shows the huge opportunities of LNOI and possibilities for dispersion engineering for novel phase matching processes.

Since we use two material versions of LNOI, namely congruent and MgO doped, we are interested in the influence of the material on the dispersion relation. Therefore, we simulated the same width and depth dependence for MgO doped LNOI. We could not see a huge difference between the two materials in the form of presentation from

figure 5.71. Therefore, we calculated the difference in the refractive indices to visualise the dissimilarities. Figure 5.75 shows the difference between the effective refractive of MgO doped LNOI and congruent LNOI for a variation in the waveguide width.

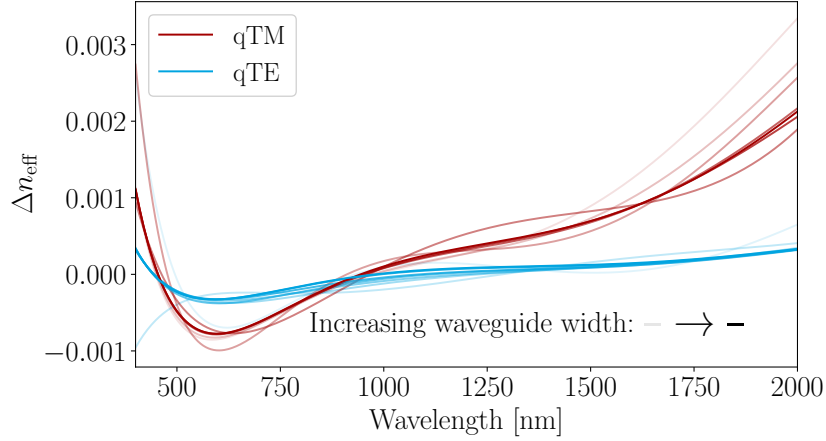


Figure 5.75 – Difference between the effective refractive index Δn_{eff} of MgO doped LNOI and congruent LNOI for the fundamental qTE (blue) and qTM (red) modes depending on the wavelength for a fixed waveguide depth of 300 nm. The waveguide top width varies from 0 μm (light) to 2 μm (dark).

The variation in the Δn_{eff} between the materials is for the qTE mode in the fifth decimal place and lower than 0.0005. Moreover, it does not vary much over the presented wavelength range. This is strongly different for the qTM mode. The variation is in the fourth decimal place, which has an effect on the phase matching. Nevertheless, the impact of the material is much lower, than the geometry of the waveguide itself. This is reasonable, because the dispersion of strongly guiding waveguides is more influenced by the waveguide geometry.

Analogue to the variation in the waveguide width, figure 5.76 shows the difference between the effective refractive of MgO doped LNOI and congruent LNOI for a variation in the waveguide depth.

This analysis shows the same result as for the variation of the width that the qTE mode is not as strongly influenced by the difference between the materials as the qTM mode. This study implies that we can employ both materials and pick out the best geometries for dispersion engineering, which are feasible to fabricate and less critical to fabrication errors.

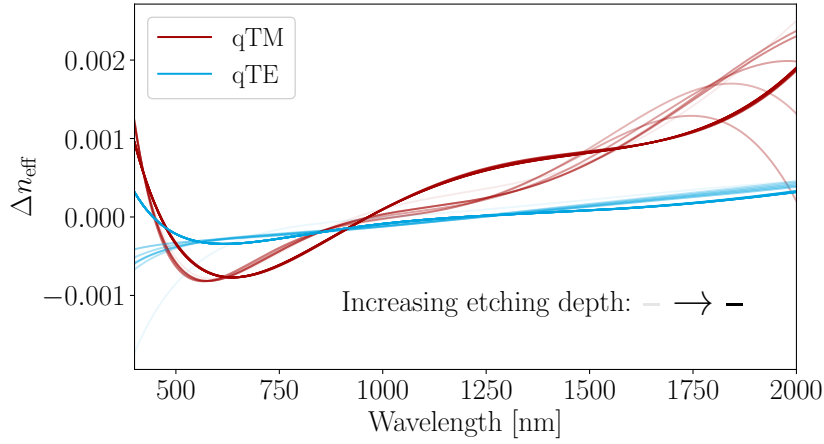


Figure 5.76 – Difference between the effective refractive index n_{eff} of MgO doped LNOI and congruent LNOI for the fundamental qTE (blue) and qTM (red) modes depending on the wavelength for a fixed waveguide top width of $1\text{ }\mu\text{m}$. The etching depth varies from 25 nm (light) to 600 nm (dark).

To investigate the influence of fabrication errors, we have chosen an exemplary geometry, which is single mode at 1550 nm . We define the waveguide top width to $0.75\text{ }\mu\text{m}$, etching depth to 300 nm , thin-film thickness to 600 nm , sidewall angle to 60° . For this geometry we get for a type II process a poling period, calculated with equation 3.75, of $2.869\text{ }\mu\text{m}$.

To represent the influence of the fabrication we estimated a maximal fabrication error for the top width between $0.65\text{ }\mu\text{m}$ and $0.85\text{ }\mu\text{m}$. The mean poling period is $(2.867 \pm 0.028)\text{ }\mu\text{m}$. The uncertainty is the standard deviation and gives us an indication of the extent, to which the fabrication errors have an impact on the poling period. For a variation in the etching depth between 250 nm and 350 nm we get a poling period of $(2.871 \pm 0.006)\text{ }\mu\text{m}$. This shows that the fabrication errors in the etching depth are more tolerable than in the waveguide width. This is the same result we got from figure 5.73. By varying the angle of the sidewalls between 55° and 65° , we calculated a poling period of $(2.873 \pm 0.027)\text{ }\mu\text{m}$, which shows that the phase matching is sensitive to errors in the fabrication of the sidewall angle. Finally, we investigated thin-film thickness variations between 582 nm and 618 nm . This results in a poling period of $(2.868 \pm 0.049)\text{ }\mu\text{m}$. This shows that the thin-film thickness has the highest impact on the phase matching.

In conclusion, this study shows that very small changes in the fabrication lead to variations in the phase matching. This demonstrates that LNOI waveguides are ideal for dispersion engineering, but at the same time it demands a high precision in the fabrication. To counteract fabrication errors, we suggest to vary the poling period in small steps of 1 nm .

5.2.4.2 Modelling of Couplers

Light can couple between two waveguides, when they are placed close together, as explained in section 3.1.2. The distance between the waveguides, also known as the gap, and the coupling length are the two most essential geometrical factors that must be optimised in order to facilitate coupling between them. We performed a simulation analysis with Lumerical of different coupler geometries to identify a coupler geometry, which we could fabricate. For the study of couplers, we extended the template of Dr. M. Santandrea [73] for waveguides in LNOI to coupler structures. Therefore, we added a second waveguide and adapted the cladding layer for the two waveguides. The coupler template consist of two straight waveguides, imitating the coupling region of the coupler. The centre-to-centre distance between the two waveguides is defined as a new parameter, which we will refer to as the gap in the following. This gives us the possibility to adjust the gap between the waveguides in addition to the parameters for the waveguide geometry and cladding. We can define the waveguide top width w , etching depth d , thin-film thickness t , sidewall angle θ , coupling gap G and a cladding layer thickness c of SiO_2 . Figure 5.77 shows a designed coupler geometry in Lumerical with the different parameters to change.

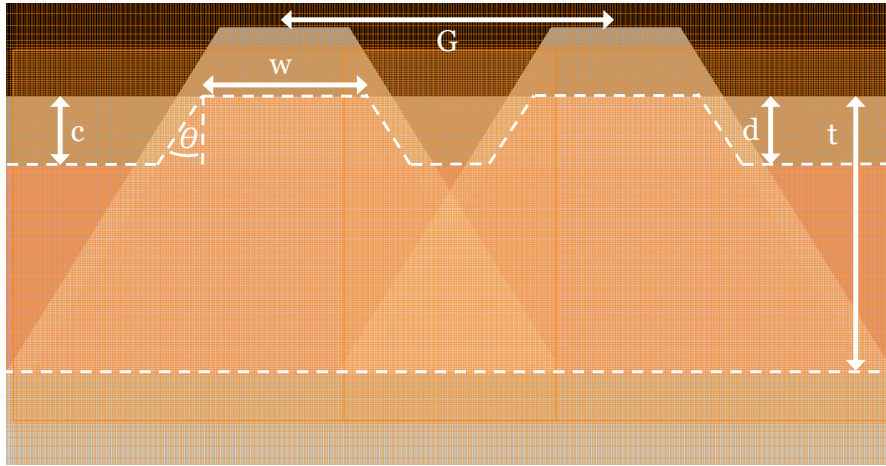


Figure 5.77 – Representation of the coupler geometry designed in Lumerical for LNOI and the domain mesh, indicated with orange lines.

Our goal is to find a coupler geometry, which is producible via optical-lithography enabling an upscaling to wafer scale fabrication. Moreover, in best case the individual waveguides in the coupler are single mode and the coupling length is not too long enabling dense integration. Due to the high confinement of the mode in LNOI waveguides, the gap needs to be small in order to realise a coupler with an adequate coupling length. In the coupling zone, it is critical that the two waveguides are well separated. If this is not the case, the coupler transforms into a multimode-interference (MMI) coupler,

which functions differently than a directional coupler. For this reason, we did a preliminary study on the minimal possible coupling gap that we can fabricate with a lift-off structure with the laser-lithography. We are able to fabricate a minimal coupling gap of $1\ \mu\text{m}$.

For different geometries of the waveguides and different gap values we studied various parameter sets that allow for the guiding of the symmetric and antisymmetric mode in the coupler. Only if both modes are guided, a coupling between the waveguides takes place. Figure 5.78 shows the symmetric and antisymmetric mode of the coupler.

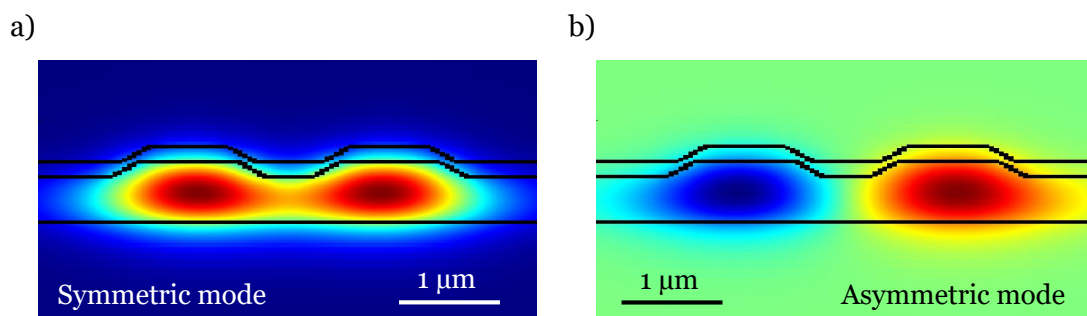


Figure 5.78 – Simulated a) symmetric mode and b) antisymmetric mode of a coupler.

Lumerical gives us the effective refractive indices of the two modes and with this we can calculate the cross-over length with equation 3.44.

Due to the fabrication limitations we decided to go to shallower etched waveguides, because the modes are less confined and couple easier between adjacent waveguides. For single-mode waveguides, we fixed the etching depth to $150\ \text{nm}$, the top width to $1\ \mu\text{m}$, the angle to 60° and added a $150\ \text{nm}$ SiO_2 cladding layer. After that we looked for the best value for the centre-to-centre gap, which compromises fabrication limitations and desirable coupling behaviour. A gap of $2.3\ \mu\text{m}$ allows for small deviations of the centre-to-centre gap, width, etching depth, angle and thin-film thickness, which are within the fabrication errors, without big impact on the single-mode and coupling behaviour. The theoretical cross-over length L_x of this coupler is $120\ \mu\text{m}$. We fabricated this coupler geometry and investigated the coupling behaviour.

5.2.5 Couplers

Based on the simulation results from Lumerical, we designed a mask for the laser-lithography with different length of the coupling region varied from $30\ \mu\text{m}$ to $580\ \mu\text{m}$. With these different couplers, we could measure the coupling ratio and calculated the cross-over length L_x .

We used for the fabrication the lift-off process via laser-lithography described in section 5.2.2. Figure 5.79 a) shows an etched coupler structure and b) shows an overview

of etched coupler structures with different lengths.

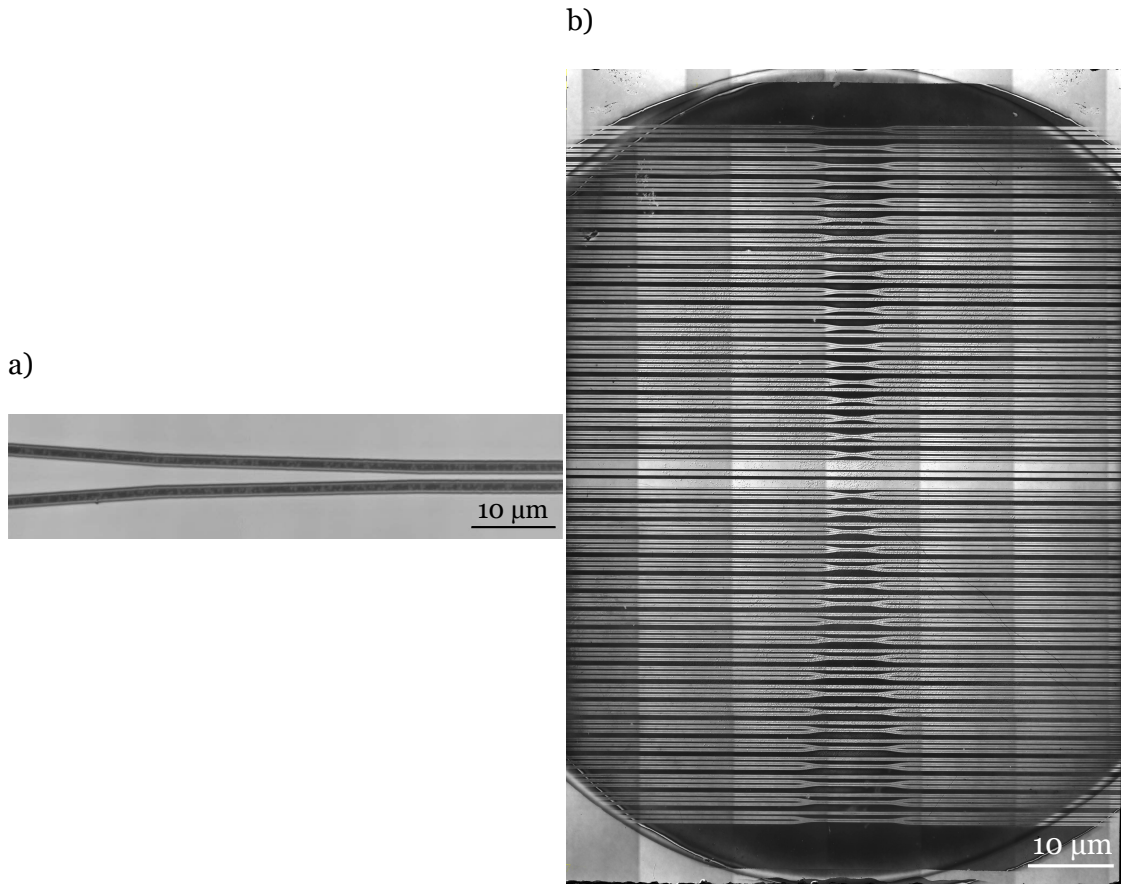


Figure 5.79 – a) Coupler structure with centre-to-centre gap of 2.3 µm.
b) Overview of coupler structures with different coupling length.

We studied the fabricated coupler structures in our optical setup with the method as introduced in section 4.3.2.2. We couple into one waveguide, in this case waveguide *b*, and image the output of the coupler. Figure 5.80 shows images for the power of the qTE modes in the coupler for three different coupling length. It was not possible to take mode images of the couplers for the qTM polarisation, since the qTM mode was not guided properly. For further details see [192].

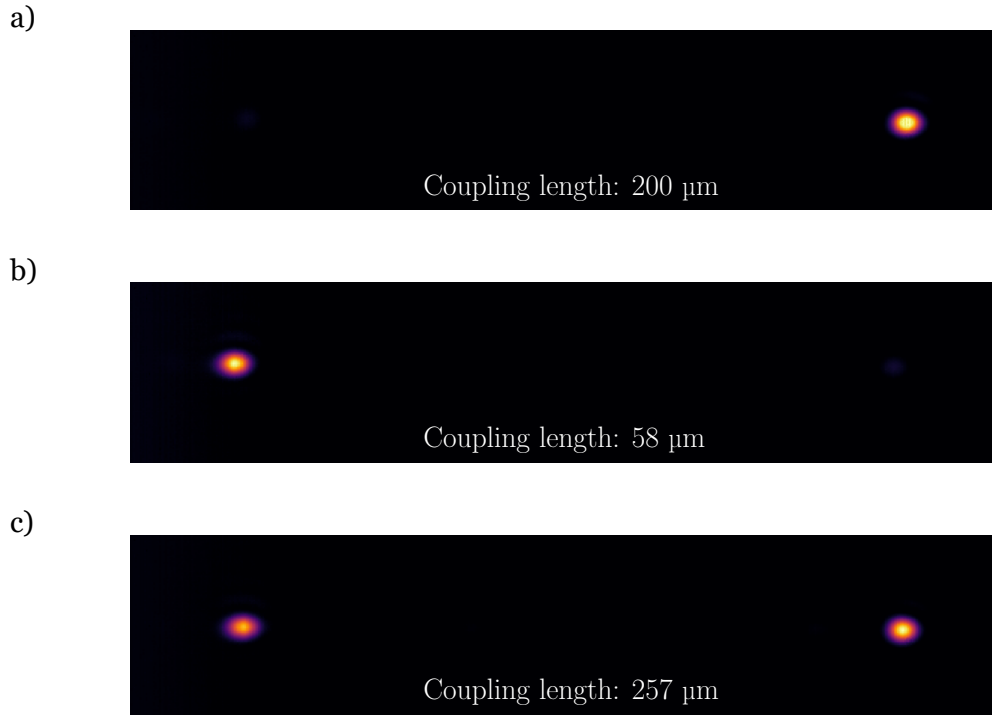


Figure 5.80 – Images of the power of the qTE modes of couplers with different coupling length: a) 200 μm - Almost all light remains in waveguide *b*. b) 58 μm - Almost all light couples to waveguide *a*. c) 257 μm - Almost 50 % of the light couples from waveguide *b* to waveguide *a*.

For a coupling length of 200 μm almost all light remains in waveguide *b*. For a coupling length of 58 μm almost all of the light couples from the input waveguide *b* to the other waveguide *a*. In the case of 257 μm coupling length, light is partially coupled into the second waveguide *a*, thus, we can image two modes with almost equal intensity.

As explained in section 4.3.2.2 we measured the power of the two modes, calculated the power ratio and plotted it against the corresponding length of the coupler. Figure 5.81 shows the normalised power against the coupling length for both waveguides *a* and *b* of a coupler for the qTE modes.

The data show that the light oscillates between the two waveguides as expected. With a sine-fit using equation 4.15 we calculated the cross-over length. For waveguide *a* we calculate a cross-over length of $(114.81 \pm 1.57) \mu\text{m}$ and $(110.7 \pm 1.57) \mu\text{m}$ for waveguide *b*. We measured the waveguide geometry with a SEM, see figure 5.82, and seeded the geometry information back into the simulations.

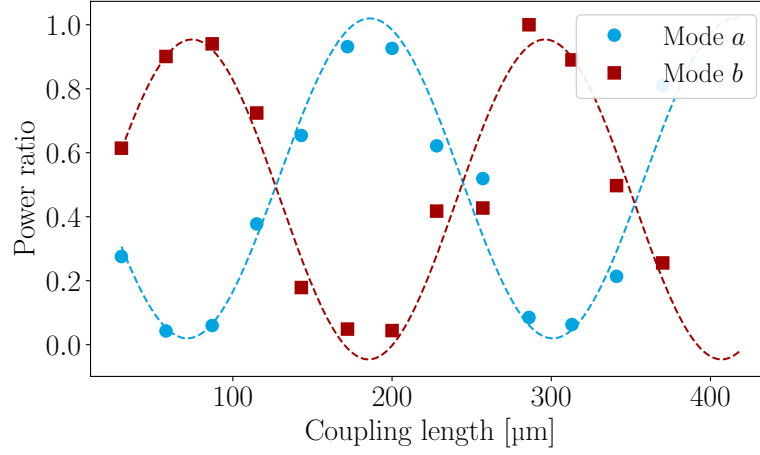


Figure 5.81 – Measured power ratio as a function of the coupling length for a set of directional couplers. The coupling is measured for both, mode *a* and *b*. The uncertainty of the acquisition is less than the size of the symbols.

We aimed with our initial values for a cross-over length of 120 μm . With the fabrication corrected values we simulated a cross-over length of 120.29 μm . The coupler performs as expected for the qTE mode and the simulations correlate well with the fabricated results. This shows that our fabrication is reliable to produce targeted waveguide geometries, which is necessary for designing and fabricating dispersion engineered sources.

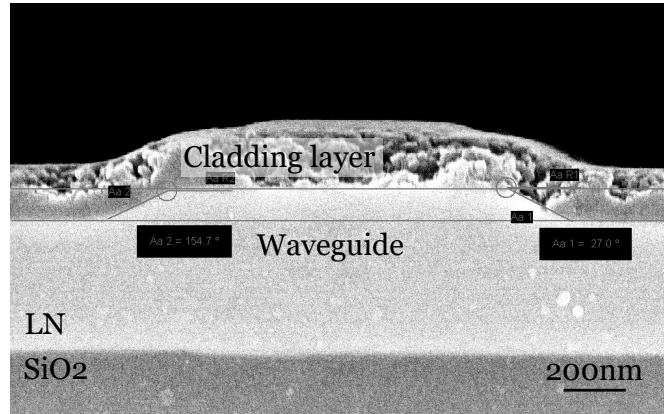


Figure 5.82 – SEM image of one of the waveguides from the coupler sample. The damaged cladding layer is due to the low SiO_2 deposit quality.

53 Final Remarks

For our technology, we presented novel developments for the fabrication of periodic poling and waveguides in RbKTP and LNOI. The aim of this thesis was to enhance the existing technology and overcome the obstacles in the fabrication for KTP and develop a functioning technology for LNOI.

At the beginning of this thesis, we had to deal with irregularities in the diffusion of waveguides and instable domains after periodic poling in KTP. To understand the diffusion dynamics, we developed a model for waveguides in KTP that explain the influence of stress on the waveguide depth and that narrow waveguides are deeper. The developed model showed good agreement with our measured data. To achieve a 1:1 duty cycle, we added investigation pulses to the optical monitoring technique during periodic poling. In order to stabilise and homogenise domains in RbKTP, we established preconditioning pulses. We improved the exchange process and showed that we are able to fabricate waveguides with nearly no corrugation. Furthermore, we extended the existing model in RSoft to model our waveguides in RbKTP. As a result, we are able to reliably fabricate periodically poled waveguides in RbKTP.

For LNOI, we started from a blank page and developed an entirely new technology. For periodic poling, we established the poling setup with needles for contacting the new developed finger electrodes. We successfully periodically poled MgO doped LNOI with a poling period of $3\text{ }\mu\text{m}$ for 5 mm long electrodes. For the waveguide fabrication, we investigated different possible fabrication routines. We extended our knowledge in the polishing, and used this technique to remove the redeposition from dry etching. Moreover, we demonstrated that it is possible in LNOI to polish the end-facets for waveguide in-coupling. Waveguides with sidewall angles as low as 19° can be produced using our developed fabrication technique for dry etched waveguides. It may be possible to alter the etching conditions to fine-tune the angle. This opens up entirely new possibilities for the modelling and source engineering and expands our parameter range for fine-tuning sources to meet our specific requirements. For a full understanding of the waveguides in LNOI, we have analysed various geometries to comprehend the influence of the geometry on the modes and effective refractive indices. In particular, variations in the thin-film of nanometres have a huge impact on the phase matching. In addition, we simulated, fabricated and analysed coupler structures. The calculated coupling length matches the simulations extremely well. As a result, we are in a position to fabricate periodically poled waveguides in LNOI.

With the results presented in this work, we have now laid the foundations for a toolbox to realise novel and engineered devices. With this toolbox we are ready to design and fabricate advanced complex components on a single chip in KTP and LNOI. In addition, together with our developed simulations we can start sophisticated dispersion

engineering to design, fabricate and demonstrate unique sources.

Summary

In this chapter, we explained our solution to overcome challenges for the periodic poling and waveguide fabrication in KTP. We showed that we are able to fabricate with preconditioning pulses stable and homogeneous domains in RbKTP and waveguides with almost no corrugation in this material. Moreover, we extended the existing model in RSoft to model our waveguides in RbKTP. We provided a detailed overview of our developed processing procedures required to fabricate periodic domains and waveguides in LNOI. We successfully periodically poled LNOI with a poling period of $3\text{ }\mu\text{m}$ over 5 mm long electrodes. We developed the technology to fabricate a mask for dry etching and the dry etching process itself. We extended our knowledge in CMP for removing the redeposition at waveguides caused by dry etching. Moreover, we showed that it is possible to polish the end-facet of waveguide. We can produce sidewall angles as small as 19° using our developed fabrication procedure for dry etched waveguides. Beyond that, the etching parameters allow for fine-tuning the sidewall angle. This opens up entirely new modelling possibilities and expands our parameter set for tailoring sources to your own requirements. Finally, we simulated, fabricated and analysed coupler structures. The simulated coupling length matches the simulated ones extremely well. With this work, we have laid the foundations for a toolbox to realise novel and engineered devices in RbKTP and LNOI.

*Any sufficiently advanced technology
is indistinguishable from magic!*

Arthur C. Clarke

Tailored Waveguide Sources

Contents

6.1	Potassium Titanyl Phosphate	167
6.2	Lithium Niobate On Insulator	178

For LNOI we show a SHG analysis of our first in-house fabricated periodically poled waveguides.

In this chapter, we demonstrate and analyse the performance of our tailored sources in KTP and LNOI. We give for both materials an overview of the state of the art of special sources. Furthermore, we present our SHG analysis, JSI characterisation and modelling in periodically poled RbKTP waveguides.

6.1 Potassium Titanyl Phosphate

In this section, we characterise the nonlinear optical properties of our periodically poled waveguides in RbKTP. We give an overview of the state of art decorrelated sources in KTP and present our nonlinear characterisation for one of our sources.

6.1.1 State of the Art: Decorrelated Sources in KTP

Fundamental to the realisation of complex photonic systems for quantum communication or quantum simulation applications is the generation and the interference between different quantum states of light at a beam splitter [9–11]. This means it requires near perfect interference between photons of multiple sources. An established standard for the generation of photon pairs are PDC sources, where we can detect one photon to herald the second one. It is necessary to have separable PDC sources, defined as having no time-frequency correlations between signal and idler, because correlations introduce

mixedness in the heralded photons [38] and this decreases the visibility of the interference. Every photon that is not pure is described as mixed and possesses correlations between the signal and the idler photon. One can describe the correlations between the signal and idler photon using the JSI. A decorrelated JSI is represented by either a symmetric shape, i.e., a circle, or by an ellipsoid aligned to either axis. For a symmetric JSI, the projection of the JSI on the axis gives identical spectral shapes for signal and idler. This is possible with an angle of the phase matching function at 45° and equal bandwidth between the phase matching function and the pump function. As soon as there are correlations between the two photons, the JSI deviates from the ideal circular shape and heralding results in a mixed state. Every angle between 0° and 90° gives partly decorrelated photons for a tailored bandwidth of the pump compared to the bandwidth of phase matching. Individual photons in the form of light pulses can only interfere with each other, if the wave is totally coherent and there are no wildly mixed frequencies. Thus, for the performance of such applications the purity and indistinguishability of these states is crucial. Indistinguishable photons must have the same wavelength, polarisation, and temporal and spatial extent.

For this reason, we need to create quantum state sources, which are bright and efficient, but at the same time generate pure and indistinguishable photons. One possible approach is to use a type II source with identical central frequencies of signal and idler and rotate the polarisation of one of the photons for the interference.

Using a PDC source it is possible to generate separable two-photon states for heralding single photons [12–15]. Nevertheless, very often spectral filtering is used in order to increase the purity of heralded photons [193, 194], which on the one hand reduces the brightness of the source and on the other hand breaks the photon number correlations [195].

By dispersion engineering it is possible to tailor the dispersion properties of the nonlinear medium in such a way that the PDC process produces decorrelated states directly [38, 196] without the need for narrowband filtering.

In periodically poled KTP waveguides, a decorrelated source was realised for telecom wavelengths [197]. Indistinguishability between signal and idler has been realised in bulk KTP [198]. The next logical step was to exploit the dispersion properties and combine decorrelation and indistinguishability in periodically poled waveguides in KTP [16].

For a perfect decorrelated source, we would need sGVM and thus, an angle in the phase matching of 45° . However, the presented decorrelated source with indistinguishable photons has an angle of 59° [16]. Therefore, our objective is to use our developed technology from the two previous chapters 4 and 5 to overcome the limitations of the presented source and decrease the angle of the phase matching function to 45° , which is important for a really high purity.

6.1.2 KTP Source

In order to produce the desired decorrelated source type II at 1550 nm with indistinguishable photons using the unique properties of KTP, precise control over the periodic poling of the sample is required.

For this reason, we periodically poled RbKTP samples and fabricated waveguides in the poled material, the technological steps are described in section 4.1. In the case of bulk KTP, we would need a poling period of $46.55\text{ }\mu\text{m}$ [198] to generate two photons at 1550 nm. For periodically poled waveguides in KTP this poling period shifts to $104\text{ }\mu\text{m}$ [197] or even further away from the bulk value to $117\text{ }\mu\text{m}$ [16]. Previous investigations have shown that we should use poling periods above $120\text{ }\mu\text{m}$. For this reason, we periodically poled samples with a variation in the poling periods between $120\text{ }\mu\text{m}$ and $150\text{ }\mu\text{m}$ in $2\text{ }\mu\text{m}$ steps. We have chosen a wide range, because we did not know, at which wavelength the momentum is conserved, since our simulations deviated from the fabricated devices. We fabricated waveguides in the periodically poled material.

In addition to the variation of the poling period, we have a small variation of the waveguide width nominally $2.0\text{ }\mu\text{m}$ - $3.5\text{ }\mu\text{m}$ in $0.5\text{ }\mu\text{m}$ steps. In the following, we refer to these, with increasing waveguide width, as A,B,C,D. The waveguide width has an influence on the penetration depth and both of them have an influence on the phase matching due to the change in the geometry. The flexibility in the poling periods and waveguide width allows us to tune the central wavelength of the phase matching. Moreover, we also made several samples to check the reproducibility.

6.1.2.1 Second-Harmonic Generation

In the following, we want to compare the central wavelengths of the SHG phase matching spectrum depending on different poling periods. Via second-harmonic generation, we analysed the nonlinear behaviour with the setup introduced in section 4.3.2.2. We scanned the wavelength between 1490 nm and 1590 nm for 45° polarised light to excite the fundamental qTE and qTM modes simultaneously. Second-harmonic light polarised along qTE is generated in a type II process in the waveguide at half of the pump wavelength, for further details see section 3.3.1.2. We determined the phase matching spectrum for the type II process for four equally fabricated samples to investigate the influence of fabrication errors. We determined that we are within the wavelength range of our laser system and match our desired wavelength only for poling periods between $144\text{ }\mu\text{m}$ and $148\text{ }\mu\text{m}$. For this reason, we investigated the different samples and their waveguides for this poling period further. Figure 6.1 shows the central wavelength of the different waveguide width and samples for the three poling periods.

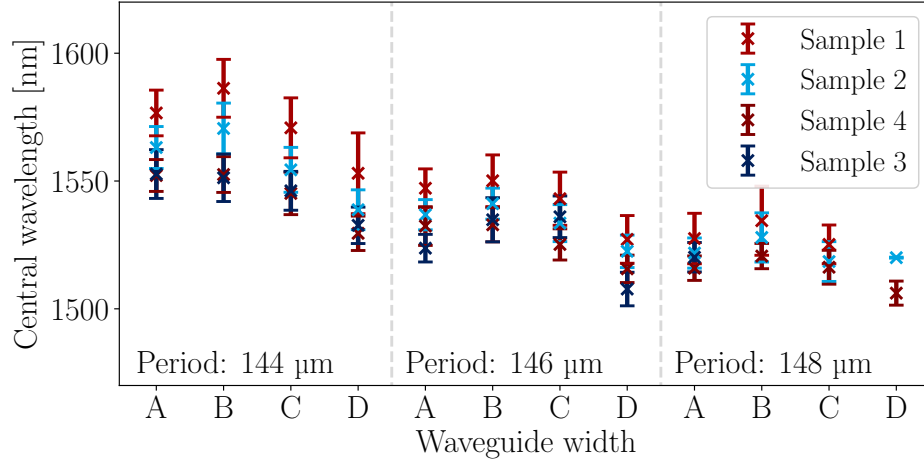


Figure 6.1 – Central wavelength of the SHG phase matching spectrum depending on different waveguide width and poling periods for four different samples indicated by the coloured crosses.

Each colour represents a different sample with nominally the same fabrication parameters. We can see that there are deviations in the central wavelength of the SHG phase matching spectrum for a fixed poling period and nominal waveguide width, for various sample batches. Two fundamental factors that may have an impact on the deviations, are the waveguide width and the exchange parameters. A deviation in the width of the titanium mask during mask fabrication can introduce a different waveguide width than the nominal width. Additionally, deviations in the temperature during the exchange lead to different penetration depths. As we know the geometry of the waveguide changes the effective refractive index of the modes and thus, the phase matching.

Despite this, we see that the central wavelength of SHG phase matching spectrum decreases as the grating of the periodic poling increases. This demonstrates the importance of varying the poling period in order to compensate for geometric fabrication errors. For long poling periods the term $\frac{m}{\Lambda}$ from equation 3.74 gets small and therefore, the effective refractive indices and thus, the geometry of the waveguide has a major influence on the phase matching.

The central wavelength of the phase matching spectrum in RbKTP waveguides is around 1550 nm for waveguides between 2.0 μm and 3.5 μm and a Rb-exchange in 88 mol% RbNO₃, 1 mol% Ba(NO₃)₂ and 11 mol% KNO₃ at 358 °C for 43 min, the poling period should be investigated in future in smaller steps around 144 μm-146 μm. One possible reason for this lack of the reproducibility is variations in the fabrication from run to run. Automating the exchange, especially the lowering, immersing into the melt and raising of the sample can enhance the reproducibility. Moreover, we can increase the accuracy of the exchange, by including an automatic temperature stabilisation, to ensure a constant temperature distribution.

From the width of the phase matching spectrum, we can gain information about the quality of the waveguide and periodic poling. As a result of analysing the phase matching spectra of all the waveguides, we concentrate our efforts on the one that showed phase matching in close proximity to the target process at 1550 nm. For a more detailed analysis, we looked at the waveguide with a measured width of $2.7\text{ }\mu\text{m}$ and depth of $7.39\text{ }\mu\text{m}$ and with poling period of $146\text{ }\mu\text{m}$. Figure 6.2 shows the measured SHG spectrum for this waveguide.

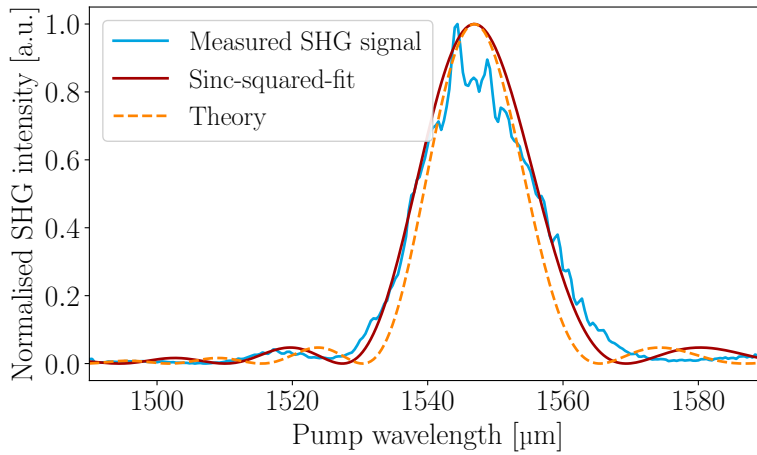


Figure 6.2 – Measured SHG spectrum for a periodically poled KTP waveguide. Measured SHG intensity in blue as the pump wavelength is varied for a waveguide with a measured width of $2.7\text{ }\mu\text{m}$ and depth of $7.39\text{ }\mu\text{m}$ and with poling period of $146\text{ }\mu\text{m}$. The sinc-squared-fit is shown in red and the dashed orange curve shows the theoretical spectrum.

The SHG intensity follows an expected sinc-squared-function with the central wavelength at 1547 nm at room temperature. With the help of a fit, see equation 3.73, we can determine the FWHM of the spectrum and from this the effective poling length. The broadened width of the phase matching bandwidth is associated with fabrication imperfections, e.g., that the periodic poling or that dispersion properties vary along the waveguide. Any poling inhomogeneities, e.g., missing domains or imperfections, or any waveguide inhomogeneities, e.g., variations in the width of depth, broadens it. The fit results in an effective poling length of 3.9 mm . This is equal to 27 poling periods of $146\text{ }\mu\text{m}$ resulting in a total length of $3942\text{ }\mu\text{m}$. Whereas the theoretical function has an effective poling of length of $L=4818\text{ }\mu\text{m}$. A possible explanation for this reduced effective poling length is that six out of 33 poling periods are not completely inverted or missing. This fits very well with our investigations of the surface topography of the domains investigated with the CLSM, comparable to the analysis in section 5.1.1.3. The higher poling periods of $120\text{ }\mu\text{m}$ - $150\text{ }\mu\text{m}$, particularly the poling periods $144\text{ }\mu\text{m}$, $146\text{ }\mu\text{m}$, $148\text{ }\mu\text{m}$,

are at the edge of the sample. This means that these waveguides are fabricated in the periodically poled regions, which were at the edge of the o-ring during the poling period. This leads to inhomogeneous poling behaviour, because the electrolyte does not reach the poling periods at the edge to contact these areas properly. In future, it would be preferable to use the desired poling periods in the middle of the sample to enhance the duty cycle homogeneity over the entire waveguide length, see our analysis about the homogeneous duty cycle in section 5.1.1.3.

The next parameter to study the quality of the periodically poled waveguides, is to analyse the conversion efficiency of a process. To investigate the conversion efficiency we measured the generated output power P_{SHG} and the pump power P_{pump} after the waveguide with a power meter (PM100 - Thorlabs). We can calculate the SHG efficiency with the following equation

$$\eta_{\text{eff}} = \frac{P_{\text{SHG}}}{P_{\text{pump}}^2 \cdot L^2} \cdot 100\%, \quad (6.1)$$

where L is the length of the periodic poling in the crystal as retrieved from the phase matching bandwidth. We corrected the pump and SHG power by the reflection losses at the end-facet and out-coupling lens and transmission losses in the waveguide, which are 4.53 dB/cm. This results in a SHG efficiency of $\eta_{\text{eff}} = (2.6 \pm 1.4) \cdot 10^{-2} \text{ \%}/(\text{W} \cdot \text{cm}^2)$.

In addition, we calculated the theoretically normalised conversion efficiency [199] with

$$\eta_{\text{norm}} = \frac{8 \cdot \pi^2 \cdot d_{24,\text{eff}}^2 \cdot |\Theta|^2}{n_{\text{pump, qTE}} \cdot n_{\text{pump, qTM}} \cdot n_{\text{SHG, qTE}} \cdot c \cdot \epsilon_0 \cdot \lambda_{\text{pump}}^2} \quad (6.2)$$

where c is the speed of light, ϵ_0 is the permittivity of free space, λ_{pump} the pump wavelength, $d_{24,\text{eff}}^2 = \frac{2}{\pi} \cdot d_{24} = \frac{2}{\pi} \cdot 7.9 \frac{\text{pm}}{\text{V}}$ [65]. The refractive indices n_i of the pump modes and SH mode are simulated with RSoft given the geometry of the waveguide and the poling period. The overlap integral Θ is between the three normalised involved modes and is equal to $7.9 \cdot 10^9 \text{ m}^{-1}$. This value was determined using RSoft and modelling the fundamental and second-harmonic modes. This yields a normalised conversion efficiency of $\eta_{\text{norm}} = (4.4 \pm 0.9) \text{ \%}/(\text{W} \cdot \text{cm}^2)$, where we estimated the error assuming uncertainties for the mode overlap of 10 %. These estimation is justified, because it is difficult to precisely evaluate the field overlap with simulations, since we know that we have still deviations from the real waveguide.

There is a large deviation between the experimental and theoretical efficiency, which is not solely explainable by waveguide and poling inhomogeneities and the reduced effective poling length. Possible reasons for this deviation could be that there are changes in the nonlinearity of the substrate, or the overlap of the modes is not as expected. Moreover, on the experimental side, it is possible that we underestimated the losses for the 775 nm light, because we assumed the same losses as for light at 1550 nm.

For comparison we also measured the SHG efficiency for a commercially available sample from AdvR. For the commercial sample, we could only correct the pump power for the reflection losses at the lens and we obtained a maximal SHG efficiency of $\eta_{\text{eff,AdvR}} = (2.3 \pm 0.4) \cdot 10^{-2} \text{ \%}/(\text{W} \cdot \text{cm}^2)$. With the same corrections our sample has an efficiency of $\eta_{\text{eff,IQO}} = (3.4 \pm 0.6) \cdot 10^{-2} \text{ \%}/(\text{W} \cdot \text{cm}^2)$. This shows that even though our measured SHG efficiency is far below the normalised conversion efficiency, we already outperformed commercially available sources with our in-house technology.

6.12.2 Joint Spectral Intensity Measurements

As introduced in section 3.2.4.2 the spectral properties of a PDC source can be characterised by the JSI. To evaluate our fabricated source, we measured the JSI spectrum by using difference-frequency generation using the setup shown in figure 6.3.

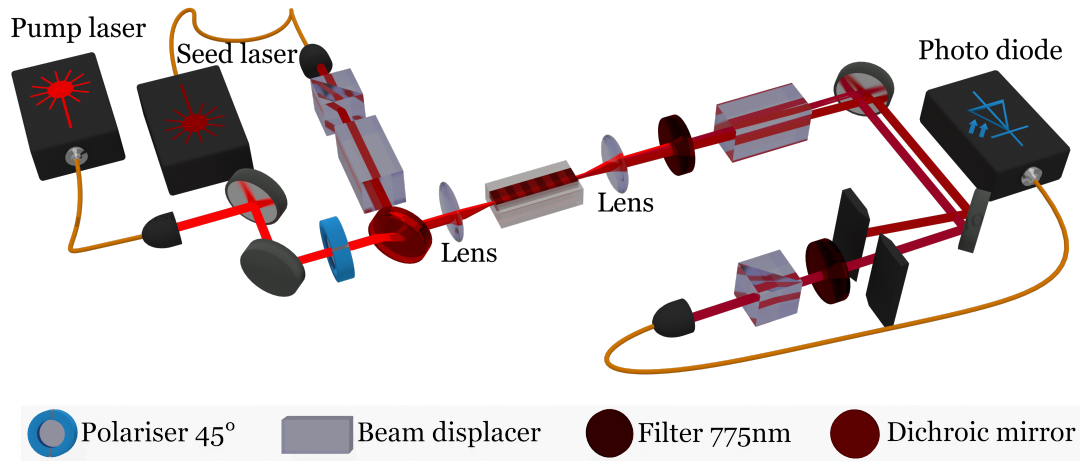


Figure 6.3 – Setup to measure the JSI spectrum of our periodically poled waveguide source in RbKTP.

We used for the pump femtosecond ($<100\text{fs}$) pulses at 775 nm and scanned the signal frequency ω_s to stimulate the generation of the idler frequency ω_i in the waveguide [200]. By using a broad pump we can project the ω_i by measuring the generated signal spectrum by an optical spectrum analyser (OSA - Anritsu). By varying the ω_s we can map the ω_i and reconstruct the JSI spectrum. Since we have a type II process, we use a pump, which is polarised along 45° and use a seed field along one polarisation. Therefore, we can generate a signal in the KTP waveguides with seeding at ω_s polarised along qTE to generate the idler light ω_i at the other polarisation qTM. We blocked the pump after the sample via a wavelength filter and displaced the seeded signal ω_s with a beam displacer in order to get a huge amount of suppression of the seed field. The generated field is launched into a fibre and analysed with an OSA.

In the spectrum we can detect two peaks, one from the external cavity diode lasers (ECDL, T100-HP - EXFO) ω_s , which is not completely blocked, and one from the generated signal, which is much weaker. By tuning the seeded signal we see a change in the ω_i frequency. Figure 6.4 shows the measured JSI by using a broad pump bandwidth and scanning the signal frequency. For visualisation, we show the measured JSI spectrum in wavelength (signal λ_s , idler λ_i) and not in frequency, as they are inversely proportional to each other. The residual seed field shows up as a thin yellow line along the 45° .

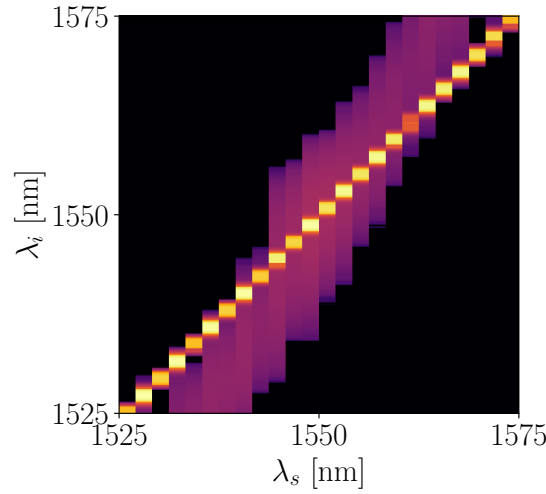


Figure 6.4 – Measured phase matching function for a type II process. The waveguide is $2.7\ \mu\text{m}$ wide and $7.39\ \mu\text{m}$ deep and the polarizing period is $146\ \mu\text{m}$.

The figure shows a second line with a higher intensity than background level, which crosses the yellow line at $1550\ \text{nm}$. This is our measured JSI spectrum from the phase matching in the waveguide. The measured JSI spectrum has an angle of $(58 \pm 2)^\circ$ for the phase matching function. The measured angle deviates 13° from our desired 45° for symmetric group velocity matching, see section 3.2.4.2.

To see if we can reconstruct the measured phase matching function with our modelling, we did simulations on exactly this waveguide geometry.

6.1.2.3 Modelling

To simulate our source, there are some parameters, e.g., geometry of the waveguide, wavelength or polarisation, we need to put into the simulation. One issue of this modelling is that we cannot estimate parameters ab-initio. As long as our fabrication is not

completely reliable, we need to measure the waveguide geometry beforehand to incorporate the collected data into the simulation. Moreover, we are missing the refractive index increase at the surface Δn_0 , which we cannot measure, as outlined in section 5.1.2.3. Nevertheless, we can conclude from the simulation in the last chapter that describing the fundamental qTM and qTM modes with a refractive index increase at the surface Δn_0 between 0.011 and 0.015 is feasible. However, at this point we were missing the Δn_0 for 775 nm, so we decided to do a large parameter scan.

We simulated the fundamental modes for qTE and qTM at wavelengths of 775 nm and 1550 nm and calculated the effective refractive indices by varying Δn_0 between 0 and 0.04 in 0.001 steps. With the effective refractive indices of the modes, we could calculate with equation 3.75 the poling period for a type II process at 1550 nm. We studied all 26100 combination of the effective refractive indices, which gave us the poling period of 146 μm . Only one combination remained in the end, which was likewise for the fundamental qTE and qTM mode at 1550 nm within our prior simulations with $\Delta n_0=0.012$ from section 5.1.2.3. At 775 nm, the refractive index increase at the surface qTE mode was 0.039.

For this specific parameter set, we calculated the effective refractive indices for the modes by doing a wavelength scan in the immediate vicinity of our target wavelengths. This allows us to reconstruct the phase matching function. Figure 6.5 shows the phase matching function plotted as a function of signal and idler.

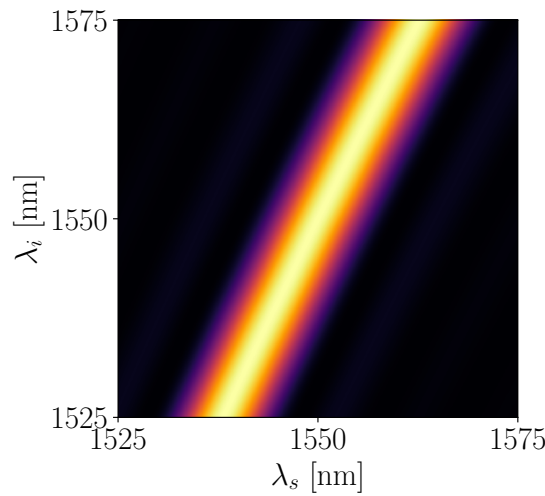


Figure 6.5 – Simulated phase matching function for a type II process. The waveguide is 2.7 μm wide and 7.39 μm deep and the poling period is 146 μm .

The angle of phase matching is 64° and thus, deviates 6° from our measured JSI. If we now multiply this phase matching function with a broadband pump function, we get for

our simulated JSI, see figure 6.6, a comparable result to our measured JSI, see figure 6.4.

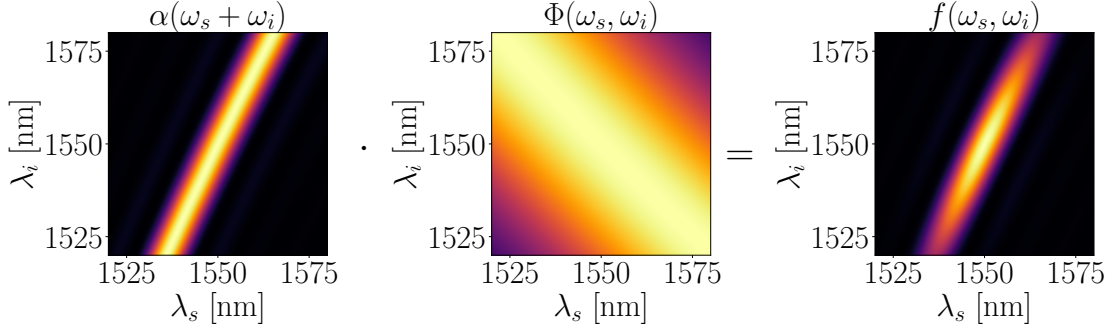


Figure 6.6 – Pump envelope function, phase matching function and the resulting JSI of our simulated waveguide geometry for a type II process at 1550 nm.

Even though, we are not under an angle of 45° , we can reduce the pump bandwidth and achieve a single-mode profile with low correlations between signal and idler, see figure 6.7.

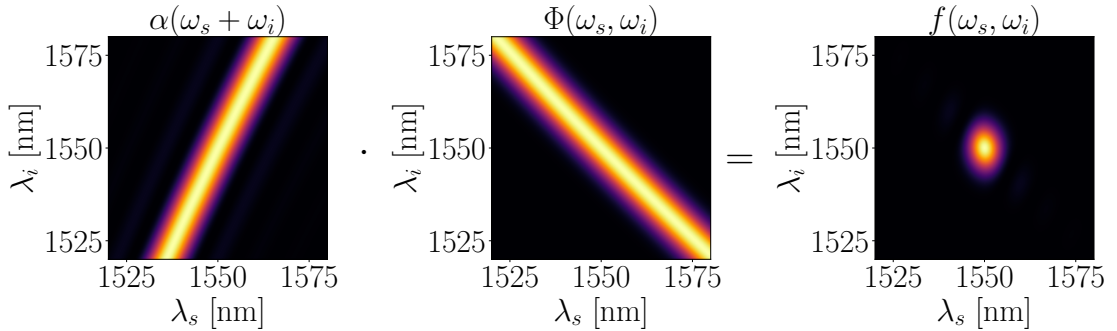


Figure 6.7 – Pump function with a narrow bandwidth results together with the phase matching function in an almost circular JSI for our simulated waveguide geometry for a type II process at 1550 nm.

At this point we would like to note that even though we can reconstruct the phase matching function with our simulations, the modelling of RbKTP waveguides is a hard task, because we need to estimate the refractive index increase at the surface Δn_0 . Further measurements are needed to improve the modelling, especially we need a larger parameter set of JSI measurements for different poling periods and waveguide widths to investigate the influence of the geometry of the waveguides on the angle of the phase matching function.

However, our presented work takes us one step further in describing our waveguide sources. The work presented in chapter 5 laid the foundation for the technology to produce the first in-house fabricated decorrelated source at 1550 nm. We have developed all the tools to start dispersion engineering and optimise the source. To change the angle of the JSI we need to adapt the waveguide geometry or the melt composition during the exchange. Our source paves the way for future tunable quantum devices with dispersion engineering.

6.2 Lithium Niobate On Insulator

With the development of the technological procedures described in the previous chapter, we pave the way for a large variety of devices for classical and quantum optical applications. In the following, we provide an overview of the state of the art sources in LNOI and show our first periodically poled waveguides analysed with second harmonic generation.

6.2.1 State of the Art: Sources in LNOI

The second order nonlinearity of lithium niobate in LNOI enables frequency conversion, as well as the generation of non-classical states of light through PDC. In the following, we give an overview of recently demonstrated periodically poled straight waveguide sources, which are continuously pushing the nonlinear efficiency to higher records.

In comparison to conventional LN waveguides, the process efficiency of frequency conversion processes is considerably improved in LNOI waveguides, since the efficiency depends mainly on the spatial mode overlap, the effective mode area and the effective nonlinear susceptibility [201]. In LNOI the modes areas are more than one order of magnitude smaller than those in conventional LN and therefore, the conversion efficiency can be much higher in LNOI waveguides. Periodic poling up to 4.2 mm is shown with normalised conversion efficiencies of $33000 \text{ } \%/(\text{W} \cdot \text{cm}^2)$ [20].

Besides classical processes, the first quantum processes via PDC have been demonstrated on LNOI in microdisks [202], in periodically poled waveguides [78–80, 203] and in periodically poled rings [204]. One of the main objectives is to do dispersion engineering, which was recently demonstrated in this system with a source for spectrally pure heralded single photons [205].

6.2.2 LNOI Source

Our intention is to identify and produce unique sources for our applications through dispersion engineering. Bringing simulation and experiment together is the first step in source engineering. Hence, to improve our simulations we used our manufactured samples, the technological procedures are presented in section 5.2.

For this purpose, we poled a sample similar to the sample from figure 5.53. The periodic poling length was 7.5 mm with poling periods of $2.7 \mu\text{m}$ and $2.8 \mu\text{m}$. Afterwards, we fabricated two waveguides with a top width of $1 \mu\text{m}$ and etching depth of 60 nm in the poled region. To facilitate end-facet polishing, the sample was given a cladding layer of 150 nm SiO_2 . With this approach, we created our first periodically poled waveguides in LNOI, which we used for a nonlinear characterisation.

6.2.2.1 Second-Harmonic Generation

In order to gain the first insights into the properties of our periodically poled waveguides, we measured the generated second-harmonic light. We employed the setup described in section 4.3.2.2 for the SHG measurements. Figure 6.8 shows the measured SHG intensities as the pump wavelength was varied for the two waveguides with poling periods of $2.7\ \mu\text{m}$ and $2.8\ \mu\text{m}$.

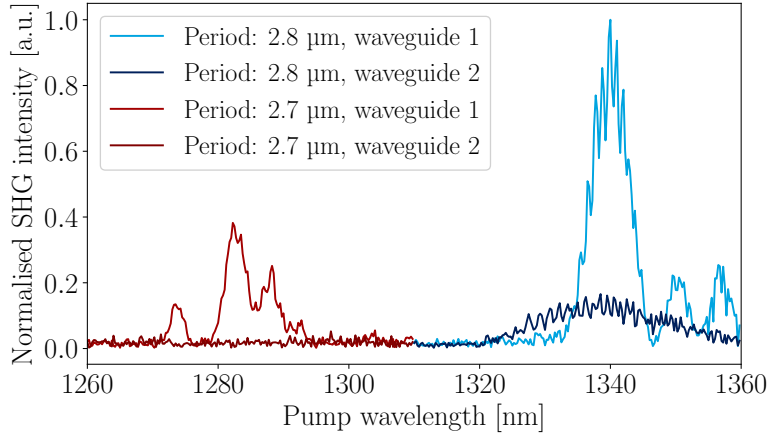


Figure 6.8 – Measured SHG spectrum for two waveguides with different poling period of $2.7\ \mu\text{m}$ in red and $2.8\ \mu\text{m}$ in blue.

The red traces represent the two waveguides with a poling period of $2.7\ \mu\text{m}$, whereas the blue signal corresponds to the two waveguides with a poling period of $2.8\ \mu\text{m}$. This shows that a change in the poling period of $0.1\ \mu\text{m}$ leads to a shift of $58\ \text{nm}$ in the central frequency of the SHG signal. The waveguide 1 (red and blue) describes the waveguides, whose position is closer to the negative electrodes, whereas the waveguide 2 (dark red and dark blue) are closer to the positive electrode. The dark red and dark blue curves show low to no SHG signal, which indicates no periodic domain inversion. If we assume that this sample poled similar to the previously analysed $7.5\ \text{mm}$ poled sample, we know that with a voltage of $870\ \text{V}$ the domains are probably completely inverted near the positive electrodes. A complete inversion of the domains is equivalent to no domain inversion, where we do not expect a generated SHG signal. Waveguide 2 for a poling period of $2.8\ \mu\text{m}$ shows a little increase in the SHG intensity. We assume that there are over the length of $7.5\ \text{mm}$ remaining domains, which contributed to the SHG generation. These domains did not completely merge together due to crystal inhomogeneities or defects in the contacts of the finger electrodes and contributed to the effective poling length.

For this sample, we had the possibility to analyse the poled structure in the waveguides via piezoresponse force microscopy (PFM), see figure 6.9.

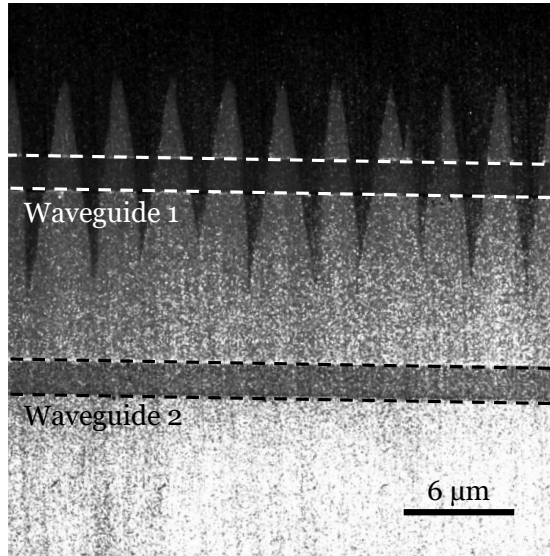


Figure 6.9 – PFM area scan of two waveguides in periodically poled domains with a length of 7.5 mm and a poling period of $2.7\ \mu\text{m}$. The PFM area-scan was measured with a Dimension Icon XR SPM-System of Bruker.

This image shows the inverted domains in light and initial domains in dark with respect to the position of the two waveguides, where waveguide 1 is on top and waveguide 2 at the bottom. This measurement shows similar results as the SH microscopy area scan from figure 5.53. The PFM measurements confirm our assumption that waveguide 2 is overpoled and that only waveguide 1 is periodically poled. Moreover, we can also validate that the domains are stable and do not switch back, even after the processing of the waveguides, where the sample is exposed to high temperatures or after several weeks. If we have a closer look at waveguide 1 with a poling period of $2.8\ \mu\text{m}$, we see the expected sinc-squared-function, see figure 6.10.

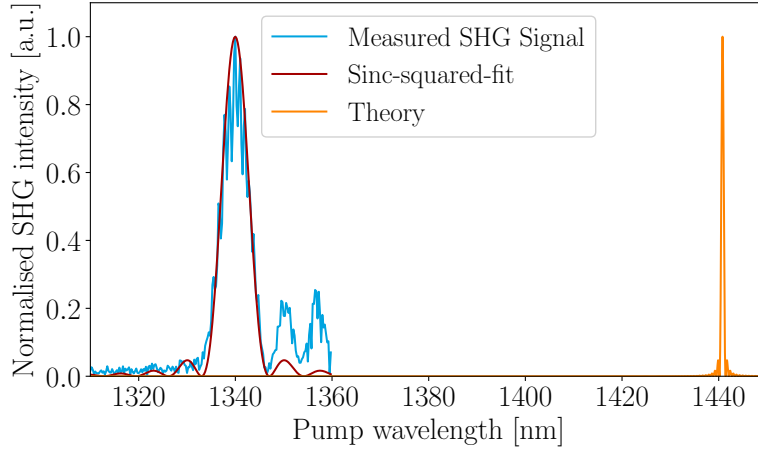


Figure 6.10 – Comparison of the measured SHG spectrum and our simulations (orange). Measured SHG intensity depending on the pump wavelength for a poling periods of $2.8\ \mu\text{m}$ in blue and a sinc-squared-fit in red.

Inhomogeneities and variations in the poling and the waveguide itself could explain the deviations of the envelope of the measured phase matching signal from an ideal sinc-squared-function.

If we compare this spectrum with the theory from our Lumerical simulations, we can clearly see a discrepancy in the central frequency of 101 nm. We can fit the phase matching with equation 3.73 to the measured data and use as the fitting parameters the poling period and the effective length of the periodically poled domains. We get a poling period of $2.63\ \mu\text{m}$ from the fit, which deviates $0.17\ \mu\text{m}$ from our fabricated poling period. This shows, how sensitive the central wavelength of the SHG phase matching spectrum is to the changes in poling period. Furthermore, this comparison between the fabricated and measured sample and the simulations shows us that our simulations deviate from the real fabricated device in the first decimal place of the poling period. This is under the assumption that the real waveguide geometry is equal to the simulated one, because we cannot exclude deviations in the fabrication process. This demonstrates how the high confinement in LNOI waveguides makes the entire system extremely sensitive to changes in waveguide geometry, poling period or adopted Sellmeier equations. Furthermore, we can say that our current simulations require adjustments for modelling the phase matching in LNOI waveguides and hence, poling periods. However, the developed model is suitable for modelling linear relationships such as the couplers, as shown in section 5.2.5. This means for us, in the future that we have to adjust the simulations and at the same time provide a variation of the poling periods in small steps of 10 nm to vary our phase matching.

Furthermore, the theoretical spectrum is noticeably narrower than the measured spectrum. A narrower phase matching bandwidth is associated with longer effective poling

lengths and lack of imperfections in the waveguide. Any fabrication imperfections that reduce the overall effective length broadens the bandwidth as well as imperfections and variations of the waveguide geometry. For our fabricated periodically poled waveguides this results in an effective poling length of $0.567\text{ }\mu\text{m}$, instead of $7.5\text{ }\mu\text{m}$. This indicates that in addition to correcting the overpoling, we have to optimise the homogeneity of our periodically poled structures.

Nevertheless, we have shown at this point that we successfully implemented technologies for periodic poling and waveguides in LNOI. Moreover, we produced the first in-house source and achieved the first proof of principle SHG measurement in LNOI. We have laid the foundations for future periodically poled sources in LNOI and our technology is ready to take nonlinear and quantum sources to a whole new level.

Summary

In this chapter, we demonstrated our in-house fabricated decorrelated source in RbKTP for indistinguishable photons for heralded single photons. It is possible to tune the centre of the phase matching spectrum via the poling period and the waveguide geometry. We achieved for a type II process at 1550 nm the highest conversion efficiency of $\eta_{\text{eff}} = (2.6 \pm 1.4) \cdot 10^{-2} \text{ } \%/(\text{W} \cdot \text{cm}^2)$ in our source with a poling period of $146\text{ }\mu\text{m}$ and outperformed commercially available sources. Additionally, we characterised the phase matching as a function of the signal and idler wavelength with a JSI measurement. This waveguide shows an angle of $(58 \pm 2)^\circ$ for the phase matching. With our model we could find a parameter set to reconstruct the phase matching function with an angle of 64° . Narrowing the pump bandwidth would allow us to achieve a decorrelated source with low correlations between signal and idler photons. Furthermore, we have used our new developed techniques for periodic poling and waveguides in LNOI as a tool box to produce a source in LNOI. The successfully performed SHG measurements in in-house periodically poled waveguides in LNOI show that we have developed a working toolbox for LNOI.

*All the shine of a thousand spotlights
All the stars we steal from the night sky
Will never be enough*

Loren Allred

Conclusion and Outlook

7.1 Conclusion

Through this work we had the opportunity to explore two material platforms, namely RbKTP and LNOI. One of our main driving motivators was to create a unique synergistic environment of simulation, technological development and application, in order to pave the way for novel integrated quantum optical devices.

Integrated photonics has outstanding potential for realising low-cost and scalable optical solutions, e.g., for communication and computation. For both classical and quantum applications, materials with a rich component toolbox and design versatility, will become the material platform of choice for realising multi-functional, high-performance photonic integrated circuits. For integrated photonics, a variety of material systems have been investigated and two of the most popular materials are RbKTP and LNOI. The work of this thesis demonstrates our technological developments in RbKTP and LNOI, as well as our ability to apply this knowledge to create adaptable and unique quantum light sources.

For the technology, we gave an overview over the current state of the art of techniques to fabricate and analyse periodically poled waveguides in (Rb)KTP and LNOI. We presented a full overview of the processing procedures required for the fabrication of periodic domains and waveguides in (Rb)KTP. We explained our solution to overcome challenges for the periodic poling and waveguides fabrication in (Rb)KTP. For waveguides in KTP, we developed a model that could explain the influence of stress on the diffusion process and thus, on the waveguide depth. We demonstrated that by using preconditioning pulses, we can fabricate stable and homogeneous domains and waveguides with nearly no corrugation in RbKTP. Furthermore, we extended the existing model in RSoft to model our waveguides in RbKTP. We are now able to reliably fabricate periodically poled waveguides in RbKTP.

Apart from this, we extended our material portfolio by adding LNOI as a new platform

to our research. We developed an entirely new technology for LNOI from scratch. We presented the developed techniques for periodic poling and waveguide fabrication in LNOI. We successfully poled LNOI periodically with a period of $3\text{ }\mu\text{m}$ for 5 mm long electrodes. Our developed fabrication procedure for the dry etched waveguides allows us to produce waveguides with sidewall angles down to 19° . Beyond that, we are able to tune the angle by adjusting the etching conditions. This gives us completely new possibilities for modelling and enhances our parameter range to adjust sources according to our needs. To fully comprehend the waveguides in LNOI we simulated various waveguide geometries and fabrication errors to see how they affected the modes and effective refractive indices. In addition, we simulated, fabricated and analysed coupler structures. The calculated coupling length matches the simulations extremely well.

By taking advantage of the technology and the toolbox we have developed, we succeeded in producing sources in RbKTP and LNOI. We demonstrated our in-house fabricated decorrelated source in RbKTP for indistinguishable photons. We characterised our device via SHG measurements for a type II phase matching process at 1550 nm and achieved a conversion efficiency of $\eta_{\text{eff}} = (2.6 \pm 1.4) \cdot 10^{-2} \text{ } \%/(\text{W} \cdot \text{cm}^2)$ in our source, outperforming commercially available sources. A JSI measurement was used to characterise the phase matching as a function of signal and idler wavelength and we obtained an angle of $(58 \pm 2)^\circ$ for the phase matching function. The poling period and waveguide geometry can be used to modify the angle of the phase matching. We derived a model for the waveguides in RbKTP and we could reconstruct the phase matching function with an angle of 64° . We have developed all the tools to start sophisticated dispersion engineering and source optimisation. In addition, we used our new developed techniques for periodic poling and waveguides in LNOI as a toolbox to generate a source in LNOI. Successful SHG measurements demonstrate that we have established a functional toolbox for in-house periodically poled waveguides and thus, sources in LNOI.

The work presented in this thesis lays a strong foundation for the realisation of integrated devices in the future. In conclusion, we developed and established a technology for periodically poled waveguide structures in RbKTP and LNOI. We provide a fully developed and sophisticated tool box for both material platforms. This thesis is a concrete starting point for the design, fabrication and investigation of novel devices in RbKTP and LNOI.

7.2 Outlook

The results of this work opens up a wide range of possible continuations and even completely new technological possibilities. There are certainly further investigations that could optimise our technology for periodically poled waveguides in RbKTP. Based on our simulation results, we need to improve our mask design to further optimise the duty cycle of periodically poled domains. For a higher field overlap to fibres and lower propa-

gation losses, we should optimise the corrugation in RbKTP waveguides and the shape of the spatial modes, by optimising the exchange parameters and edge roughness of the titanium mask. Note that we have developed all the tools to start dispersion engineering and optimise the type II source in RbKTP. We could implement aperiodic poling, utilising different duty cycles and poling periods. This would aid in the improvement of the sources, e.g., resulting phase matching would change from a sinc-squared shape to a Gaussian. We expect to improve the source in the future by tuning the waveguide geometry or the melt composition during the exchange or modify the periodic poling.

In contrast to RbKTP, LNOI is still in its early stages of development. We have created the basis, but there is still a lot of work to be done to optimise the components. For a better control of the poling behaviour, we suggest to get rid of nano-domains by preconditioning pulses, similar to those used with RbKTP, to homogenise the substrate material and avoid local overpoling. We can overcome limitations in the waveguide fabrication by using the electron-beam-lithography to either lift-off SiO_2 as a dry etching mask or directly use HSQ resist for a higher resolution and smoother sidewalls of the waveguides and thus, waveguides with lower losses. For this task it would be beneficial to be able to estimate the performance of our devices, e.g., measure the losses of our waveguides. Therefore, we suggest to investigate ring resonators, since they do not require assumptions for the end-facet reflectivity of the waveguide. Moreover, this new tool would give us the possibility to exploit resonant sources. In LNOI we plan to extend our toolbox and add active modulation to our passive routing and generation. Together with our developed simulation methods, we will be able to exploit the full potential of LNOI in the near future.

*Two arms around me. heaven to ground me.
And family that always calls me home.
Four wheels to get there. enough love to
share.
And a sweet. sweet. sweet song.*

*At the end of the day.
Lord I pray.
I have a life that is good.*

Charles Esten

Acknowledgements

Who would have thought that in particular this part would be the hardest for me. I have just written a 190 page thesis and I am struggling with the last pages of the acknowledgements. It is not that I do not have anyone to thank, it is much more that I do not know how to say thank you for the incredible help.

First and foremost, I want to express my gratitude to my supervisor, Professor Christine Silberhorn, without whom this work would not have been possible. I can still remember the situation, when I applied as a student helper many years ago. When I think back, to how I was then and what she already saw in me at that time, I do not know how to thank her. She senses potential in people that they themselves or others do not see yet, and she assists them in realising their full potential. This is reflected in our work group as well. We are a one-of-a-kind group with a strong desire to collaborate. Whenever there is a need for assistance, one only requires to go through one or two more doors, and everyone takes the time to assist the other. All of this served to ignite my passion for science and quantum optics.

I would like to honour two of my greatest passions in life: Science, especially technology, and my husband. I love to invest my time and energy in technological development, but who would have guessed that I would like to go even further? This work has contributed significantly to my realisation that I want to be present and work on the first demonstrations of quantum optical applications of my devices. Although my roots stay always in technology, the quantum world sparked my interest.

I would like to thank my husband from the bottom of my heart. You are the one person who knows me the best and always covers my back. My mind is constantly looking for solutions, yet you have managed to shift my focus to other things and free my mind when I am with you. If there is a work-life-balance, then you are my life in this equation.

I am so grateful for you in my life and I am looking forward to many more adventures with you.

At the end of this four-and-a-half-year adventure, I need to express my wholehearted gratitude to all the people that accompanied me throughout this journey.

I want to express my gratitude to Christof Eigner and Raimund Ricken, two people from whom I learned the majority of what I know about technology. Many thanks to Sebastian Lengeling and Viktor Quiring for help with sample preparations. In addition, I would like to thank my colleagues in technology for stimulating discussions and assistance. It is amazing how many different solutions may emerge when everyone is committed in the development process and brings their own knowledge and strengths to the table.

Apart from technology, I would like to express my gratitude to those individuals who have taken me beyond the clean room and helped me with their expertise. Many thanks to Matteo Santandrea for many hours of theory and simulation explanations and Michael Stefszky for his explanations and assistance with the nonlinear optical analyses. I want to thank Benjamin Brecht for the numerous illustrations that have helped me to better understand the theory.

I want to thank two young co-workers, Laura Bollmers and Silia Babel, who have shown me that it is a pleasure for me to accompany others on their journeys. Laura and Silia, working with you both is so much fun and productive at the same time.

A huge thank you goes to all other colleagues of the IQO group for this amazing time: Felix vom Bruch, Christian Kießler, Olga Brecht, Michelle Kirsch, Johannes Otte, Ellen Wecker, Harald Herrmann, Kai Hong Luo, Marcello Massaro, Melanie Engelkemeier, Sonja Barkhofen, Sebastian Brauner, Dana Echeverria, Patrick Folge, Frederico Pegoraro, René Pollmann, Nidhin Prasannan, Franz Roeder, Fabian Schlue and Laura Serino. And of course thanks to Rita Prevora and Petra Bobe for all administrative help and non-scientific conversations.

Last but not least, I would like to express my gratitude to all members of my family. Thank you for providing me with the chance to study physics, for your unwavering support and for always being there.

I want to emphasise at this point that I am grateful to all of you and I can say with pride: *I have a life that is good!*

Appendix

A.1 Patents

(1) Herstellung von Wellenleitern aus Materialien der KTP-Familie

Laura Padberg, Christof Eigner, Matteo Santandrea und Christine Silberhorn
Az. 10 2018 108 636.9. (2018)

(2) Gradientenfilter zur strahlversatzfreien, wellenlängenselektiven Modifikation der Lichteigenschaften

Laura Padberg, Christof Eigner, Viktor Quiring, Johannes Tiedau und Christine Silberhorn
Az. 10 2019 130 532.2 (2018)

(1) Production of waveguides made of materials from the KTP family

Laura Padberg, Christof Eigner, Matteo Santandrea und Christine Silberhorn
US 11.181.802 B2 (2021)

A.2 Publications

(1) Characterisation of width-dependent diffusion dynamics in rubidium-exchanged KTP waveguides

Laura Padberg, Matteo Santandrea, Michael Rüsing, Julian Brockmeier, Peter Mackwitz, Gerhard Berth, Artur Zrenner, Christof Eigner and Christine Silberhorn
Opt. Express, 28(17), 24353-24362. (2020)

(2) Non-Invasive Visualization of Ferroelectric Domain Structures on the Non-Polar y-Surface of KTiOPO_4 via Raman Imaging

Julian Brockmeier, Peter Walter Martin Mackwitz, Michael Rüsing, Christof Eigner, Laura Padberg, Matteo Santandrea, Christine Silberhorn, Artur Zrenner, and Gerhard Berth
Crystals 11(9), 1086 (2021)

(3) Spatially single mode photon pair source at 800 nm in periodically poled Rubidium exchanged KTP waveguides

Christof Eigner, Laura Padberg, Matteo Santandrea, Harald Herrmann, Benjamin Brecht, and Christine Silberhorn
Opt. Express 28(22), 32925-32935 (2020)

(4) Periodically poled ridge waveguides in KTP for second harmonic generation in the UV regime

Christof Eigner, Matteo Santandrea, Laura Padberg, Martin F. Volk, Christian E. Rüter, Harald Herrmann, Detlef Kip, and Christine Silberhorn
Opt. Express 26(22), 28827-28833 (2018)

(5) Heralded generation of high-purity ultrashort single photons in programmable temporal shapes

Vahid Ansari, Emanuele Roccia, Matteo Santandrea, Mahnaz Doostdar Kejdehi, Christof Eigner, Laura Padberg, Ilaria Gianani, Marco Sbroscia, John M. Donohue, Luca Mancino, Marco Barbieri, Christine Silberhorn
Opt. Express 26(3), 2764-2774 (2018)

(6) Fabrication of low-loss Rb-exchanged ridge waveguides in z-cut KTiOPO₄

Martin F. Volk, Christian E. Rüter, Matteo Santandrea, Christof Eigner, Laura Padberg, Harald Herrmann, Christine Silberhorn, and Detlef Kip
Opt. Mater. Express 8(1), 82-87 (2018)

Preprints

(7) DC ionic conductivity in KTP and its isomorphs: properties, methods for suppression and its connection to gray tracking.

Laura Padberg, Viktor Quiring, Adriana Bocchini, Matteo Santandrea, Uwe Gerstmann, Wolf Gero Schmidt, Christine Silberhorn and Christof Eigner
in preparation (2022)

(8) Optimisation of corrugation-free Rb-exchanged waveguide in periodically poled KTiOPO₄

Laura Padberg, Christof Eigner, Matteo Santandrea, and Christine Silberhorn
in preparation (2022)

(9) Decorrelated photon pair source at 1550 nm in periodically poled Rb doped KTiOPO₄ waveguides

Laura Padberg, Michael Stefsky, Matteo Santandrea, Christof Eigner, and Christine Silberhorn
in preparation (2022)

A3 Conference Contributions

- International Workshop on Polar Oxides: Lithium Niobate and Related Compounds, 2022, *talk*
- Max Planck School of Photonics - Autumn School, Virtual/ Suhl, 2021, *poster*
- Max Planck School of Photonics - Virtual Spring School, Virtual, 2021, *poster/talk*
- SFB-TRR 142 PhD workshop, Virtual, 2020, *poster*
- Max Planck School of Photonics - Virtual Spring School, Virtual, 2020, *poster*
- Deutschen Gesellschaft für angewandte Optik (DGaO), Darmstadt, 2019, *talk*
- European Conference on Integrated Optics (ECIO), Ghent, 2019, *poster*
- 5th SFB/TRR 142 workshop “Tailored Nonlinear Photonics, Bad Sassendorf, 2018, *talk*
- European Conference on Integrated Optics (ECIO), Valencia, 2018, *poster*
- Projekt Meeting QcomQ, Bad Honnef, 2018, *poster*

References

- [1] L. Padberg, C. Eigner, M. Santandrea, and C. Silberhorn. “Herstellung von Wellenleitern aus Materialien der KTP-Familie”.
- [2] L. Padberg, C. Eigner, M. Santandrea, and C. Silberhorn. “Production of waveguides made of materials from the KTP family”.
- [3] L. Padberg, M. Stefsky, M. Santandrea, C. Eigner, and C. Silberhorn. “Decorrelated source at 1550 nm in periodically poled Rb doped KTiOPO₄ waveguides”. (2022).
- [4] B. Mullanuri, D. Davis, and Y. Banadaki. “Simulation of Quantum Cheques Circuits in Five-qubit IBM Quantum Computer”. In: *Research Conference*. 2021.
- [5] G. Czelusta and J. Mielczarek. *Secure quantum communication through a worm-hole*. 2021.
- [6] C. D. Bruzewicz, J. Chiaverini, R. McConnell, and J. M. Sage. “Trapped-ion quantum computing: Progress and challenges”. *Applied Physics Reviews* **6**, 021314 (2019).
- [7] M. Kjaergaard, M. E. Schwartz, J. Braumüller, et al. “Superconducting qubits: Current state of play”. *Annual Review of Condensed Matter Physics* **11**, 369–395 (2020).
- [8] S. Takeda and A. Furusawa. “Toward large-scale fault-tolerant universal photonic quantum computing”. *APL Photonics* **4**, 060902 (2019).
- [9] E. Knill, R. Laflamme, and G. J. Milburn. “A scheme for efficient quantum computation with linear optics”. *Nature* **409**, 46–52 (2001).
- [10] T. Ralph. “Quantum optical systems for the implementation of quantum information processing”. *Reports on Progress in Physics* **69**, 853 (2006).
- [11] J. B. Spring, B. J. Metcalf, P. C. Humphreys, et al. “Boson sampling on a photonic chip”. *Science* **339**, 798–801 (2013).
- [12] A. B. U’Ren, C. Silberhorn, K. Banaszek, and I. A. Walmsley. “Efficient conditional preparation of high-fidelity single photon states for fiber-optic quantum networks”. *Physical review letters* **93**, 093601 (2004).
- [13] T. Pittman, B. Jacobs, and J. Franson. “Heralding single photons from pulsed parametric down-conversion”. *Optics communications* **246**, 545–550 (2005).
- [14] K. Laiho, K. Cassemiro, and C. Silberhorn. “Producing high fidelity single photons with optimal brightness via waveguided parametric down-conversion”. *Optics express* **17**, 22823–22837 (2009).

- [15] P. J. Mosley, J. S. Lundeen, B. J. Smith, et al. “Heralded generation of ultrafast single photons in pure quantum states”. *Physical Review Letters* **100**, 133601 (2008).
- [16] G. Harder, V. Ansari, B. Brecht, et al. “An optimized photon pair source for quantum circuits”. *Optics express* **21**, 13975–13985 (2013).
- [17] M. Fiorentino, S. M. Spillane, R. G. Beausoleil, et al. “Spontaneous parametric down-conversion in periodically poled KTP waveguides and bulk crystals”. *Optics express* **15**, 7479–7488 (2007).
- [18] D. S. Hum and M. M. Fejer. “Quasi-phasematching”. *Comptes Rendus Physique* **8**, 180–198 (2007).
- [19] K. R. Parameswaran, R. K. Route, J. R. Kurz, et al. “Highly efficient second-harmonic generation in buried waveguides formed by annealed and reverse proton exchange in periodically poled lithium niobate”. *Optics Letters* **27**, 179–181 (2002).
- [20] T. Park, H. S. Stokowski, V. Ansari, et al. *High efficiency second harmonic generation of blue light on thin film lithium niobate*. 2021.
- [21] Y. Hu, M. Yu, D. Zhu, et al. “On-chip electro-optic frequency shifters and beam splitters”. *Nature* **599**, 587–593 (2021).
- [22] A. Yariv and P. Yeh. *Photonics: Optical Electronics in Modern Communications*. Oxford series in electrical and computer engineering. Oxford University Press, 2007. ISBN: 9780195179460.
- [23] E. A. Marcatili. “Dielectric rectangular waveguide and directional coupler for integrated optics”. *Bell System Technical Journal* **48**, 2071–2102 (1969).
- [24] C. Grossmann, H.-G. Roos, and M. Stynes. *Numerical treatment of partial differential equations*. Vol. 154. Springer, 2007.
- [25] A. Yariv. “Coupled-mode theory for guided-wave optics”. *IEEE Journal of Quantum Electronics* **9**, 919–933 (1973).
- [26] L. Chrostowski and M. Hochberg. *Silicon Photonics Design: From Devices to Systems*. Cambridge University Press, 2015.
- [27] P. Kumar. “Quantum frequency conversion”. *Opt. Lett.* **15**, 1476–1478 (1990).
- [28] J. Rarity, P. Tapster, and E. Jakeman. “Observation of sub-poissonian light in parametric downconversion”. *Optics Communications* **62**, 201–206 (1987).
- [29] R. W. Boyd. *Nonlinear optics*. Academic press, 2008. ISBN: 9780123694706.
- [30] N. Kamanina. *Nonlinear Optics*. BoD–Books on Demand, 2012.
- [31] M. M. Fejer, G. Magel, D. H. Jundt, and R. L. Byer. “Quasi-phase-matched second harmonic generation: tuning and tolerances”. *IEEE Journal of quantum electronics* **28**, 2631–2654 (1992).
- [32] C. Couteau. “Spontaneous parametric down-conversion”. *Contemporary Physics* **59**, 291–304 (2018).

-
- [33] A. Christ, K. Laiho, A. Eckstein, K. N. Cassemiro, and C. Silberhorn. “Probing multimode squeezing with correlation functions”. *New Journal of Physics* **13**, 033027 (2011).
 - [34] B. Brecht. “Engineering ultrafast quantum frequency conversion”. PhD thesis. Paderborn University, 2014.
 - [35] A. Christ, K. Laiho, A. Eckstein, et al. “Spatial modes in waveguided parametric down-conversion”. *Physical Review A* **80**, 033829 (2009).
 - [36] A. Christ. “Theory of ultrafast waveguided parametric down-conversion: from fundamentals to applications”. PhD thesis. Paderborn University, 2013.
 - [37] W. P. Grice and I. A. Walmsley. “Spectral information and distinguishability in type-II down-conversion with a broadband pump”. *Physical Review A* **56**, 1627 (1997).
 - [38] A. B. U’Ren, C. Silberhorn, K. Banaszek, et al. “Generation of pure-state single-photon wavepackets by conditional preparation based on spontaneous parametric downconversion”. *Laser Physics* **15**, 146–161 (2005).
 - [39] A. Eckstein, B. Brecht, and C. Silberhorn. “A quantum pulse gate based on spectrally engineered sum frequency generation”. *Optics express* **19**, 13770–13778 (2011).
 - [40] T. E. Keller and M. H. Rubin. “Theory of two-photon entanglement for spontaneous parametric down-conversion driven by a narrow pump pulse”. *Physical Review A* **56**, 1534 (1997).
 - [41] V. Ansari, J. M. Donohue, B. Brecht, and C. Silberhorn. “Tailoring nonlinear processes for quantum optics with pulsed temporal-mode encodings”. *Optica* **5**, 534–550 (2018).
 - [42] V. Ansari, E. Roccia, M. Santandrea, et al. “Heralded generation of high-purity ultrashort single photons in programmable temporal shapes”. *Optics express* **26**, 2764–2774 (2018).
 - [43] L. Ouvrard and M. Troost. “Recherches sur les phosphate double de titane, d’étain et de cuivre”. *Journal of applied physics* **111**, 177–179 (1890).
 - [44] F. Zumsteg, J. Bierlein, and T. Gier. “ $\text{K}_x\text{Rb}_{1-x}\text{TiOPO}_4$: a new nonlinear optical material”. *Journal of Applied Physics* **47**, 4980–4985 (1976).
 - [45] G. Hansson, H. Karlsson, S. Wang, and F. Laurell. “Transmission measurements in KTP and isomorphic compounds”. *Applied optics* **39**, 5058–5069 (2000).
 - [46] J. D. Bierlein and H. Vanherzeele. “Potassium titanyl phosphate: properties and new applications”. *JOSA B* **6**, 622–633 (1989).
 - [47] J. Hellström, V. Pasiskevicius, H. Karlsson, and F. Laurell. “High-power optical parametric oscillation in large-aperture periodically poled KTiOPO_4 ”. *Optics letters* **25**, 174–176 (2000).

- [48] C. Canalias, J. Hirohashi, V. Pasiskevicius, and F. Laurell. “Polarization-switching characteristics of flux-grown KTiOPO_4 and RbTiOPO_4 at room temperature”. *Journal of applied physics* **97**, 124105 (2005).
- [49] G. Dhanaraj, K. Byrappa, V. Prasad, and M. Dudley. *Springer handbook of crystal growth*. Springer Science & Business Media, 2010.
- [50] P. I. Tordjman, E. Masse, and J. Guitel. “Structure cristalline du monophosphate KTiPO_5 ”. *Zeitschrift für Kristallographie* **139**, 103–115 (1974).
- [51] R. Masse and J.-C. Grenier. “Étude des monophosphates du type MITiOPO_4 avec $\text{MI} = \text{K, Rb et Tl}$ ”. *Bulletin de Minéralogie* **94**, 437–439 (1971).
- [52] J. Bierlein and C. Arweiler. “Electro-optic and dielectric properties of KTiOPO_4 ”. *Applied physics letters* **49**, 917–919 (1986).
- [53] K. Momma and F. Izumi. “VESTA 3 for three-dimensional visualization of crystal, volumetric and morphology data”. *Journal of applied crystallography* **44**, 1272–1276 (2011).
- [54] M. Satyanarayan, A. Deepthy, and H. Bhat. “Potassium titanyl phosphate and its isomorphs: Growth, properties, and applications”. *Critical Reviews in Solid State and Materials Sciences* **24**, 103–191 (1999).
- [55] D. Allan, J. Loveday, R. Nelmes, and P. Thomas. “A high-pressure structural study of potassium titanyl phosphate (KTP) up to 5 GPa”. *Journal of Physics: Condensed Matter* **4**, 2747 (1992).
- [56] B. Mohamadou, G. Kugel, F. Brehat, et al. “High-temperature vibrational spectra, relaxation and ionic conductivity effects in KTiOPO_4 ”. *Journal of Physics: Condensed Matter* **3**, 9489 (1991).
- [57] O. Driesner. “Vergrabene Lichtwellenleiter in Kalium Titanyl Phosphat”. Master Thesis. Paderborn University, 2014.
- [58] P. Thomas, R. Duhlev, and S. Teat. “A comparative structural study of a flux-grown crystal of $\text{K}_{0.86}\text{Rb}_{0.14}\text{TiOPO}_4$ and an ion-exchanged crystal of $\text{K}_{0.84}\text{Rb}_{0.16}\text{TiOPO}_4$ ”. *Acta Crystallographica Section B: Structural Science* **50**, 538–543 (1994).
- [59] P. Urenski, N. Gorbatov, and G. Rosenman. “Dielectric relaxation in flux grown KTiOPO_4 and isomorphous crystals”. *Journal of Applied Physics* **89**, 1850–1855 (2001).
- [60] L. Padberg, C. Eigner, V. Quiring, et al. “DC ionic conductivity in KTP and its isomorphs: properties, methods for suppression and its connection to gray tracking.” *in preparation*, (2022).
- [61] G. Lindgren, A. Zukauskas, V. Pasiskevicius, F. Laurell, and C. Canalias. “Studies of sub-millisecond domain dynamics in periodically poled Rb-doped KTiOPO_4 , using online in situ second harmonic generation”. *Optics express* **23**, 20332–20339 (2015).

-
- [62] J. Jacco, G. Loiacono, M. Jaso, G. Mizell, and B. Greenberg. “Flux growth and properties of KTiOPO_4 ”. *Journal of Crystal Growth* **70**, 484–488 (1984).
- [63] K. Kato and E. Takaoka. “Sellmeier and thermo-optic dispersion formulas for KTP”. *Applied optics* **41**, 5040–5044 (2002).
- [64] B. Boulanger, J. P. Fève, G. Marnier, et al. “Relative sign and absolute magnitude of $d(2)$ nonlinear coefficients of KTP from second-harmonic-generation measurements”. *JOSA B* **11**, 750–757 (1994).
- [65] L. Cheng, L. Cheng, J. Galperin, P. M. Hotsenpiller, and J. Bierlein. “Crystal growth and characterization of KTiOPO_4 isomorphs from the self-fluxes”. *Journal of crystal growth* **137**, 107–115 (1994).
- [66] D. Xue and S. Zhang. “The origin of nonlinearity in KTiOPO_4 ”. *Applied physics letters* **70**, 943–945 (1997).
- [67] R. A. Stolzenberger and M. P. Sripsick. “Recent advancements in the periodic poling and characterization of RTA and its isomorphs”. In: *Laser Material Crystal Growth and Nonlinear Materials and Devices*. Vol. 3610. International Society for Optics and Photonics. 1999, 23–35.
- [68] C. Eigner. “Periodically poled waveguides in potassium titanyl phosphate: from technology development to applications”. PhD thesis. Universitätsbibliothek, 2019.
- [69] J. D. Bierlein, A. Ferretti, L. H. Brixner, and W. Y. Hsu. “Fabrication and characterization of optical waveguides in KTiOPO_4 ”. *Applied Physics Letters* **50**, 1216–1218 (1987).
- [70] W. Jost. “Diffusion in solids”. *Liquid, Gases* **73**, (1960).
- [71] J. Crank. *The mathematics of diffusion*. Oxford university press, 1979.
- [72] P. T. Callahan, K. Safak, P. Battle, T. D. Roberts, and F. X. Kärtner. “Fiber-coupled balanced optical cross-correlator using PPKTP waveguides”. *Optics express* **22**, 9749–9758 (2014).
- [73] M. Santandrea. “Design of Nonlinear Integrated Devices for Quantum Optics Applications”. PhD thesis. Universitätsbibliothek, 2019.
- [74] G. Poberaj, H. Hu, W. Sohler, and P. Guenter. “Lithium niobate on insulator (LNOI) for micro-photonic devices”. *Laser & photonics reviews* **6**, 488–503 (2012).
- [75] F. Zachariasen. “Standard x-ray diffraction powder patterns”. *Naturv-Idensk. Kl* **4**, 1–8 (1928).
- [76] B. Matthias and J. Remeika. “Ferroelectricity in the ilmenite structure”. *Physical Review* **76**, 1886 (1949).
- [77] L. Kovács and G. Corradi. *New Trends in Lithium Niobate: From Bulk to Nanocrystals*. 2021.

- [78] J.-y. Chen, Y. M. Sua, Z.-h. Ma, et al. “Efficient parametric frequency conversion in lithium niobate nanophotonic chips”. *OSA Continuum* **2**, 2914–2924 (2019).
- [79] B. S. Elkus, K. Abdelsalam, A. Rao, et al. “Generation of broadband correlated photon-pairs in short thin-film lithium-niobate waveguides”. *Optics express* **27**, 38521–38531 (2019).
- [80] J. Zhao, C. Ma, M. Rüsing, and S. Mookherjea. “High quality entangled photon pair generation in periodically poled thin-film lithium niobate waveguides”. *Physical review letters* **124**, 163603 (2020).
- [81] S. Abrahams, J. M. Reddy, and J. Bernstein. “Ferroelectric lithium niobate. 3. Single crystal X-ray diffraction study at 24 C”. *Journal of Physics and Chemistry of Solids* **27**, 997–1012 (1966).
- [82] R. Weis and T. Gaylord. “Lithium niobate: summary of physical properties and crystal structure”. *Applied Physics A* **37**, 191–203 (1985).
- [83] M.-L. Hu, L.-J. Hu, and J.-Y. Chang. “Polarization switching of pure and MgO-doped lithium niobate crystals”. *Japanese journal of applied physics* **42**, 7414 (2003).
- [84] T. Volk and M. Wöhlecke. *Lithium niobate: defects, photorefraction and ferroelectric switching*. Vol. 115. Springer Science & Business Media, 2008.
- [85] D. H. Jundt. “Temperature-dependent Sellmeier equation for the index of refraction, n_e , in congruent lithium niobate”. *Optics letters* **22**, 1553–1555 (1997).
- [86] G. Edwards and M. Lawrence. “A temperature-dependent dispersion equation for congruently grown lithium niobate”. *Optical and quantum electronics* **16**, 373–375 (1984).
- [87] O. Gayer, Z. Sacks, E. Galun, and A. Arie. “Temperature and wavelength dependent refractive index equations for MgO-doped congruent and stoichiometric LiNbO_3 ”. *Applied Physics B* **91**, 343–348 (2008).
- [88] D. N. Nikogosyan. *Nonlinear optical crystals: a complete survey*. Springer Science & Business Media, 2006.
- [89] Y. S. Kuz'minov. *Lithium niobate crystals*. Cambridge Int Science Publishing, 1999.
- [90] S. Kim, V. Gopalan, and A. Gruverman. “Coercive fields in ferroelectrics: A case study in lithium niobate and lithium tantalate”. *Applied Physics Letters* **80**, 2740–2742 (2002).
- [91] M. Wengler, B. Fassbender, E. Soergel, and K. Buse. “Impact of ultraviolet light on coercive field, poling dynamics and poling quality of various lithium niobate crystals from different sources”. *Journal of applied physics* **96**, 2816–2820 (2004).
- [92] J. T. Nagy and R. M. Reano. “Periodic poling of ion-sliced x-cut magnesium oxide doped lithium niobate thin films”. In: *2018 Conference on Lasers and Electro-Optics (CLEO)*. IEEE. 2018, 1–2.

-
- [93] J. T. Nagy and R. M. Reano. “Reducing leakage current during periodic poling of ion-sliced x-cut MgO doped lithium niobate thin films”. *Optical Materials Express* **9**, 3146–3155 (2019).
 - [94] A. Rao, M. Malinowski, A. Honardoost, et al. “Second-harmonic generation in periodically-poled thin film lithium niobate wafer-bonded on silicon”. *Optics express* **24**, 29941–29947 (2016).
 - [95] L. Chang, Y. Li, N. Volet, et al. “Thin film wavelength converters for photonic integrated circuits”. *Optica* **3**, 531–535 (2016).
 - [96] L. Gui. “Periodically poled ridge waveguides and photonic wires in LiNbO₃ for efficient nonlinear interactions”. *Paderborn University*, (2010).
 - [97] H. Hu, R. Ricken, W. Sohler, and R. Wehrspohn. “Lithium niobate ridge waveguides fabricated by wet etching”. *IEEE Photonics Technology Letters* **19**, 417–419 (2007).
 - [98] M. Fukuma, J. Noda, and H. Iwasaki. “Optical properties in titanium-diffused LiNbO₃ strip waveguides”. *Journal of Applied Physics* **49**, 3693–3698 (1978).
 - [99] A. Boes, B. Corcoran, L. Chang, J. Bowers, and A. Mitchell. “Status and potential of lithium niobate on insulator (LNOI) for photonic integrated circuits”. *Laser & Photonics Reviews* **12**, 1700256 (2018).
 - [100] D. Zhu, L. Shao, M. Yu, et al. “Integrated photonics on thin-film lithium niobate”. *Advances in Optics and Photonics* **13**, 242–352 (2021).
 - [101] M. F. Volk, S. Suntsov, C. E. Rüter, and D. Kip. “Low loss ridge waveguides in lithium niobate thin films by optical grade diamond blade dicing”. *Optics express* **24**, 1386–1391 (2016).
 - [102] H. Hu, R. Ricken, and W. Sohler. “Etching of lithium niobate: micro-and nanometer structures for integrated optics”. In: *Topical Meeting” Photorefractive Materials, Effects, and Devices—Control of Light and Matter, Bad Honnef*. 2009.
 - [103] M. C. Gupta, W. Risk, A. C. Nutt, and S. Lau. “Domain inversion in KTiOPO₄ using electron beam scanning”. *Applied physics letters* **63**, 1167–1169 (1993).
 - [104] C. Van der Poel, J. Bierlein, J. Brown, and S. Colak. “Efficient type I blue second-harmonic generation in periodically segmented KTiOPO₄ waveguides”. *Applied physics letters* **57**, 2074–2076 (1990).
 - [105] F. Laurell, M. Roelofs, W. Bindloss, et al. “Detection of ferroelectric domain reversal in KTiOPO₄ waveguides”. *Journal of applied physics* **71**, 4664–4670 (1992).
 - [106] W. Risk and S. Lau. “Periodic electric field poling of KTiOPO₄ using chemical patterning”. *Applied physics letters* **69**, 3999–4001 (1996).
 - [107] H. Karlsson and F. Laurell. “Electric field poling of flux grown KTiOPO₄”. *Applied Physics Letters* **71**, 3474–3476 (1997).

- [108] P. Bindner, A. Boudrioua, J. Loulergue, and P. Moretti. “Formation of planar optical waveguides in potassium titanyl phosphate by double implantation of protons”. *Applied Physics Letters* **79**, 2558–2560 (2001).
- [109] F. Laurell, T. Calmano, S. Müller, et al. “Laser-written waveguides in KTP for broadband Type II second harmonic generation”. *Optics express* **20**, 22308–22313 (2012).
- [110] S. Müller, T. Calmano, P. W. Metz, et al. “Highly efficient continuous wave blue second-harmonic generation in fs-laser written periodically poled Rb:KTiOPO₄ waveguides”. *Optics Letters* **39**, 1274–1277 (2014).
- [111] S. Campbell, R. Thomson, D. Hand, et al. “Frequency-doubling in femtosecond laser inscribed periodically-poled potassium titanyl phosphate waveguides”. *Optics Express* **15**, 17146–17150 (2007).
- [112] V. Boutou, A. Vernay, C. Félix, et al. “Phase-matched second-harmonic generation in a flux grown KTP crystal ridge optical waveguide”. *Optics Letters* **43**, 3770–3773 (2018).
- [113] M. F. Volk, C. E. Rüter, M. Santandrea, et al. “Fabrication of low-loss Rb-exchanged ridge waveguides in z-cut KTiOPO₄”. *Optical Materials Express* **8**, 82–87 (2018).
- [114] C. Eigner, M. Santandrea, L. Padberg, et al. “Periodically poled ridge waveguides in KTP for second harmonic generation in the UV regime”. *Optics express* **26**, 28827–28833 (2018).
- [115] L. Padberg. “Analysis and optimisation of rubidium in-diffused waveguides in KTP”. Master Thesis. Paderborn University, 2017.
- [116] H. Karlsson, F. Laurell, and L. Cheng. “Periodic poling of RbTiOPO₄ for quasi-phase matched blue light generation”. *Applied physics letters* **74**, 1519–1521 (1999).
- [117] J. Hellström, R. Clemens, V. Pasiskevicius, H. Karlsson, and F. Laurell. “Real-time and in situ monitoring of ferroelectric domains during periodic electric field poling of KTiOPO₄”. *Journal of Applied Physics* **90**, 1489–1495 (2001).
- [118] C. Canalias. “Domain engineering in KTiOPO₄”. PhD thesis. KTH, 2005.
- [119] R. Wellendorf. “Kationenaustausch in K(TiO)PO₄ - Einkristallen im Kontakt mit Rb-haltigen Nitratschmelzen zur Erzeugung von mikrooptischen Strukturen”. (1999).
- [120] R. Wellendorf, C. Kaps, and R. Kriegel. “On the Rb⁺ and K⁺ counterdiffusion in single crystals of K(TiO)PO₄ - a quasi-one-dimensional superionic conductor”. *Ionics* **2**, 222–230 (1996).
- [121] N. Yamada and Y. Yamamoto. “Effects of alkaline-earth elements on refractive index profile and domain inversion of Rb-exchanged waveguide in KTiOPO₄”. *Japanese journal of applied physics* **34**, 6407 (1995).

-
- [122] A. Guarino, G. Poberaj, D. Rezzonico, R. Degl’Innocenti, and P. Günter. “Electro-optically tunable microring resonators in lithium niobate”. *Nature photonics* **1**, 407–410 (2007).
 - [123] M. Zhang, C. Wang, R. Cheng, A. Shams-Ansari, and M. Lončar. “Monolithic ultra-high-Q lithium niobate microring resonator”. *Optica* **4**, 1536–1537 (2017).
 - [124] R. Wu, M. Wang, J. Xu, et al. “Long low-loss-litium niobate on insulator waveguides with sub-nanometer surface roughness”. *Nanomaterials* **8**, 910 (2018).
 - [125] R. Wolf, I. Breunig, H. Zappe, and K. Buse. “Scattering-loss reduction of ridge waveguides by sidewall polishing”. *Optics express* **26**, 19815–19820 (2018).
 - [126] B. Desiatov, A. Shams-Ansari, M. Zhang, C. Wang, and M. Lončar. “Ultra-low-loss integrated visible photonics using thin-film lithium niobate”. *Optica* **6**, 380–384 (2019).
 - [127] M. Xu, M. He, H. Zhang, et al. “High-performance coherent optical modulators based on thin-film lithium niobate platform”. *Nature communications* **11**, 1–7 (2020).
 - [128] S. Y. Siew, E. J. H. Cheung, H. Liang, et al. “Ultra-low loss ridge waveguides on lithium niobate via argon ion milling and gas clustered ion beam smoothening”. *Optics express* **26**, 4421–4430 (2018).
 - [129] A. J. Mercante, P. Yao, S. Shi, et al. “110 GHz CMOS compatible thin film LiNbO₃ modulator on silicon”. *Optics express* **24**, 15590–15595 (2016).
 - [130] C. Wang, X. Xiong, N. Andrade, et al. “Second harmonic generation in nano-structured thin-film lithium niobate waveguides”. *Optics express* **25**, 6963–6973 (2017).
 - [131] L. Wang, L.-Q. Li, X.-T. Zhang, and F. Chen. “Type I phase matching in thin film of lithium niobate on insulator”. *Results in Physics* **16**, 103011 (2020).
 - [132] J. Lu, J. B. Surya, X. Liu, et al. “Periodically poled thin-film lithium niobate microring resonators with a second-harmonic generation efficiency of 250,000%/W”. *Optica* **6**, 1455–1460 (2019).
 - [133] G. Lin, J. U. Fürst, D. V. Strekalov, and N. Yu. “Wide-range cyclic phase matching and second harmonic generation in whispering gallery resonators”. *Applied Physics Letters* **103**, 181107 (2013).
 - [134] J. Lin, Y. Xu, J. Ni, et al. “Phase-Matched Second-Harmonic Generation in an On-Chip LiNbO₃ Microresonator”. *Physical Review Applied* **6**, 014002 (2016).
 - [135] R.-R. Xie, G.-Q. Li, F. Chen, and G.-L. Long. “Microresonators in Lithium Niobate Thin Films”. *Advanced Optical Materials*, 2100539 (2021).
 - [136] C. Wang, Z. Li, M.-H. Kim, et al. “Metasurface-assisted phase-matching-free second harmonic generation in lithium niobate waveguides”. *Nature communications* **8**, 1–7 (2017).
 - [137] I. Krasnokutskaya, J.-L. J. Tambasco, and A. Peruzzo. *Submicron domain engineering in periodically poled lithium niobate on insulator*. 2021.

- [138] Z. Hao, L. Zhang, W. Mao, et al. “Second-harmonic generation using d 33 in periodically poled lithium niobate microdisk resonators”. *Photonics Research* **8**, 311–317 (2020).
- [139] Y. Niu, C. Lin, X. Liu, et al. “Optimizing the efficiency of a periodically poled LNOI waveguide using in situ monitoring of the ferroelectric domains”. *Applied Physics Letters* **116**, 101104 (2020).
- [140] A. Rao, K. Abdelsalam, T. Sjaardema, et al. “Actively-monitored periodic-poling in thin-film lithium niobate photonic waveguides with ultrahigh nonlinear conversion efficiency of $4600\%/W^{-1}\text{ cm}^{-2}$ ”. *Optics express* **27**, 25920–25930 (2019).
- [141] J. Zhao, M. Rüsing, M. Roeper, L. M. Eng, and S. Mookherjea. “Poling thin-film x-cut lithium niobate for quasi-phase matching with sub-micrometer periodicity”. *Journal of Applied Physics* **127**, 193104 (2020).
- [142] Y. Wang, Z. Chen, L. Cai, et al. “Amorphous silicon-lithium niobate thin film strip-loaded waveguides”. *Optical Materials Express* **7**, 4018–4028 (2017).
- [143] P. Rabiei, J. Ma, S. Khan, J. Chiles, and S. Fathpour. “Heterogeneous lithium niobate photonics on silicon substrates”. *Optics express* **21**, 25573–25581 (2013).
- [144] N. Courjal, B. Guichardaz, G. Ulliac, et al. “High aspect ratio lithium niobate ridge waveguides fabricated by optical grade dicing”. *Journal of Physics D: Applied Physics* **44**, 305101 (2011).
- [145] R. Takigawa, E. Higurashi, T. Kawanishi, and T. Asano. “Lithium niobate ridged waveguides with smooth vertical sidewalls fabricated by an ultra-precision cutting method”. *Optics express* **22**, 27733–27738 (2014).
- [146] R. Geiss, S. Saravi, A. Sergeyev, et al. “Fabrication of nanoscale lithium niobate waveguides for second-harmonic generation”. *Optics letters* **40**, 2715–2718 (2015).
- [147] R. Geiss, J. Brandt, H. Hartung, et al. “Photonic microstructures in lithium niobate by potassium hydroxide-assisted ion beam-enhanced etching”. *Journal of Vacuum Science & Technology B, Nanotechnology and Microelectronics: Materials, Processing, Measurement, and Phenomena* **33**, 010601 (2015).
- [148] L. Cai, Y. Wang, and H. Hu. “Low-loss waveguides in a single-crystal lithium niobate thin film”. *Optics letters* **40**, 3013–3016 (2015).
- [149] L. Cai, Y. Kang, and H. Hu. “Electric-optical property of the proton exchanged phase modulator in single-crystal lithium niobate thin film”. *Optics express* **24**, 4640–4647 (2016).
- [150] L. Cai, R. Kong, Y. Wang, and H. Hu. “Channel waveguides and y-junctions in x-cut single-crystal lithium niobate thin film”. *Optics Express* **23**, 29211–29221 (2015).
- [151] S.-M. Zhang, Y.-P. Jiang, and Y. Jiao. “Clean waveguides in lithium niobate thin film formed by He ion implantation”. *Applied Physics B* **123**, 1–5 (2017).

-
- [152] G. Si, A. J. Danner, S. L. Teo, et al. “Photonic crystal structures with ultrahigh aspect ratio in lithium niobate fabricated by focused ion beam milling”. *Journal of Vacuum Science & Technology B, Nanotechnology and Microelectronics: Materials, Processing, Measurement, and Phenomena* **29**, 021205 (2011).
 - [153] Z. Fang, Y. Xu, M. Wang, et al. *Monolithic integration of a high-quality factor lithium niobate microresonator with a free-standing membrane waveguide using femtosecond laser assisted ion beam writing (FLAIBW)*. 2017.
 - [154] H. Hu, A. Milenin, R. Wehrspohn, H. Hermann, and W. Sohler. “Plasma etching of proton-exchanged lithium niobate”. *Journal of Vacuum Science & Technology A: Vacuum, Surfaces, and Films* **24**, 1012–1015 (2006).
 - [155] H. Nagata, N. Mitsugi, K. Shima, M. Tamai, and E. Haga. “Growth of crystalline LiF on CF₄ plasma etched LiNbO₃ substrates”. *Journal of crystal growth* **187**, 573–576 (1998).
 - [156] D. Jun, J. Wei, C. Eng Png, et al. “Deep anisotropic LiNbO₃ etching with SF₆/Ar inductively coupled plasmas”. *Journal of Vacuum Science & Technology B, Nanotechnology and Microelectronics: Materials, Processing, Measurement, and Phenomena* **30**, 011208 (2012).
 - [157] S. Y. Siew, S. S. Saha, M. Tsang, and A. J. Danner. “Rib microring resonators in lithium niobate on insulator”. *IEEE Photonics Technology Letters* **28**, 573–576 (2015).
 - [158] C. Shen, C. Wang, Y. Zhu, et al. “A comparative study of dry-etching nanophotonic devices on a LiNbO₃-on-insulator material platform”. In: *4th Optics Young Scientist Summit (OYSS 2020)*. Vol. 11781. International Society for Optics and Photonics. 2021, 117810X.
 - [159] G. Ulliach, V. Calero, A. Ndao, F. Baida, and M.-P. Bernal. “Argon plasma inductively coupled plasma reactive ion etching study for smooth sidewall thin film lithium niobate waveguide application”. *Optical Materials* **53**, 1–5 (2016).
 - [160] I. Krasnokutskaya, J.-L. J. Tambasco, X. Li, and A. Peruzzo. “Ultra-low loss photonic circuits in lithium niobate on insulator”. *Optics express* **26**, 897–904 (2018).
 - [161] N. Ohnishi and T. Iizuka. “Etching study of microdomains in LiNbO₃ single crystals”. *Journal of Applied Physics* **46**, 1063–1067 (1975).
 - [162] A. Kholkin, S. Kalinin, A. Roelofs, and A. Gruverman. “Review of ferroelectric domain imaging by piezoresponse force microscopy”. In: *Scanning probe microscopy*. Springer, 2007, 173–214.
 - [163] M. Rüsing, C. Eigner, P. Mackwitz, et al. “Identification of ferroelectric domain structure sensitive phonon modes in potassium titanyl phosphate: A fundamental study”. *Journal of Applied Physics* **119**, 044103 (2016).
 - [164] M. Rüsing, J. Zhao, and S. Mookherjee. “Second harmonic microscopy of poled x-cut thin film lithium niobate: Understanding the contrast mechanism”. *Journal of Applied Physics* **126**, 114105 (2019).

- [165] J. I. Goldstein, D. E. Newbury, J. R. Michael, et al. *Scanning electron microscopy and X-ray microanalysis*. Springer, 2017.
- [166] A. Benninghoven. “Surface analysis by secondary ion mass spectrometry (SIMS)”. *Surface Science* **299**, 246–260 (1994).
- [167] H. Oechsner. “Recent applications of secondary neutral mass spectrometry for quantitative analysis of homogeneous and structured samples”. *Nuclear Instruments and Methods in Physics Research Section B: Beam Interactions with Materials and Atoms* **33**, 918–925 (1988).
- [168] R. G. Hunsperger. *Integrated optics*. Vol. 4. Springer, 1995.
- [169] R. Regener and W. Sohler. “Loss in low-finesse Ti:LiNbO₃ optical waveguide resonators”. *Applied physics B* **36**, 143–147 (1985).
- [170] Bruker. *DektakXT Stylus Profiler*. Booklet. 2020.
- [171] L. Bollmers. “Herstellung und Optimierung von Wellenleiterstruktur in LNOI”. Bachelor Thesis. Paderborn University, 2019.
- [172] Olympus. *OLS4000 - Ultimate Measurement Performance*. Booklet. 2021.
- [173] L. Reimer. *Scanning Electron Microscopy: Physics of Image Formation and Microanalysis*. Springer Series in Optical Sciences. Springer Berlin Heidelberg, 2013. ISBN: 9783662135624.
- [174] R. Pease and W. Nixon. “High resolution scanning electron microscopy”. *Journal of Scientific Instruments* **42**, 81 (1965).
- [175] M. E. Lines and A. M. Glass. *Principles and applications of ferroelectrics and related materials*. Oxford university press, 2001.
- [176] W. L. Holstein. “Etching study of ferroelectric microdomains in LiNbO₃ and MgO: LiNbO₃”. *Journal of crystal growth* **171**, 477–484 (1997).
- [177] K. Spychala, P. Mackwitz, M. Rüsing, et al. “Nonlinear focal mapping of ferroelectric domain walls in LiNbO₃: Analysis of the SHG microscopy contrast mechanism”. *Journal of Applied Physics* **128**, 234102 (2020).
- [178] G. Berth. “Visualization of ferroelectric domain structures in lithium niobate by means of confocal nonlinear microscopy”. *Paderborn University*, (2010).
- [179] D. Rabus. *Integrated Ring Resonators: A Compendium*. Springer-Verlag Berlin Heidelberg, 2007. ISBN: 13 978-3-540-68786-3.
- [180] D. Khalil. “Extension of the radiation spectrum method for the reflection calculation at the end of a strongly guiding optical waveguide”. *Optical and quantum electronics* **35**, 801–809 (2003).
- [181] J. Otte. “Analyse der elektrischen Feldverteilung in KTP zur Domäneninversion”. Bachelor Thesis. Paderborn University, 2020.
- [182] C. Eigner, L. Padberg, M. Santandrea, et al. “Spatially single mode photon pair source at 800 nm in periodically poled Rubidium exchanged KTP waveguides”. *Optics Express* **28**, 32925–32935 (2020).

-
- [183] P. Mackwitz. “Nonlinear analysis of periodically poled waveguides in KTP: A fundamental study”. Master Thesis. Paderborn University, 2017.
- [184] J. Brockmeier, P. W. M. Mackwitz, M. Rüsing, et al. “Non-Invasive Visualization of Ferroelectric Domain Structures on the Non-Polar y -Surface of KTiOPO_4 via Raman Imaging”. *Crystals* **11**, 1086 (2021).
- [185] L. Padberg, M. Santandrea, M. Rüsing, et al. “Characterisation of width-dependent diffusion dynamics in rubidium-exchanged KTP waveguides”. *Optics Express* **28**, 24353–24362 (2020).
- [186] M. Fontana, R. Hammoum, P. Bourson, S. Margueron, and V. Y. Shur. “Raman probe on PPLN microstructures”. *Ferroelectrics* **373**, 26–31 (2008).
- [187] “Single Mode Fiber with 900 μm Hytrel Jacket”. SMF-28-J9. Thorlabs. 2015.
- [188] B. J. Stanicki, M. Younesi, F. J. F. Löchner, et al. “Surface domain engineering in lithium niobate”. *OSA Continuum* **3**, 345–358 (2020).
- [189] L. E. Myers, R. Eckardt, M. Fejer, et al. “Quasi-phase-matched optical parametric oscillators in bulk periodically poled LiNbO_3 ”. *JOSA B* **12**, 2102–2116 (1995).
- [190] M. Younesi, R. Geiss, S. Rajaei, et al. “Periodic poling with a micrometer-range period in thin-film lithium niobate on insulator”. *JOSA B* **38**, 685–691 (2021).
- [191] I. Krasnokutskaya, J.-L. J. Tambasco, and A. Peruzzo. “Tunable large free spectral range microring resonators in lithium niobate on insulator”. *Scientific reports* **9**, 1–7 (2019).
- [192] S. Babel. “Exploring precise loss characterization methods in LNOI waveguides”. Master Thesis. Paderborn University, 2021.
- [193] E. Bimbard, N. Jain, A. MacRae, and A. Lvovsky. “Quantum-optical state engineering up to the two-photon level”. *Nature Photonics* **4**, 243–247 (2010).
- [194] P. Tapster and J. Rarity. “Photon statistics of pulsed parametric light”. *Journal of Modern Optics* **45**, 595–604 (1998).
- [195] E. Meyer-Scott, N. Montaut, J. Tiedau, et al. “Limits on the heralding efficiencies and spectral purities of spectrally filtered single photons from photon-pair sources”. *Physical Review A* **95**, 061803 (2017).
- [196] C. Law, I. A. Walmsley, and J. Eberly. “Continuous frequency entanglement: effective finite Hilbert space and entropy control”. *Physical Review Letters* **84**, 5304 (2000).
- [197] A. Eckstein, A. Christ, P. J. Mosley, and C. Silberhorn. “Highly efficient single-pass source of pulsed single-mode twin beams of light”. *Physical Review Letters* **106**, 013603 (2011).
- [198] T. Gerrits, M. J. Stevens, B. Baek, et al. “Generation of degenerate, factorizable, pulsed squeezed light at telecom wavelengths”. *Optics express* **19**, 24434–24447 (2011).

- [199] R. V. Roussev, C. Langrock, J. R. Kurz, and M. M. Fejer. “Periodically poled lithium niobate waveguide sum-frequency generator for efficient single-photon detection at communication wavelengths”. *Optics letters* **29**, 1518–1520 (2004).
- [200] M. Liscidini and J. Sipe. “Stimulated emission tomography”. *Physical review letters* **111**, 193602 (2013).
- [201] R. Luo, Y. He, H. Liang, M. Li, and Q. Lin. “Highly tunable efficient second-harmonic generation in a lithium niobate nanophotonic waveguide”. *Optica* **5**, 1006–1011 (2018).
- [202] R. Luo, H. Jiang, S. Rogers, et al. “On-chip second-harmonic generation and broadband parametric down-conversion in a lithium niobate microresonator”. *Optics express* **25**, 24531–24539 (2017).
- [203] U. A. Javid, J. Ling, J. Staffa, et al. “Ultrabroadband Entangled Photons on a Nanophotonic Chip”. *Physical review letters* **127**, 183601 (2021).
- [204] Z. Ma, J.-Y. Chen, Z. Li, et al. “Ultrabright quantum photon sources on chip”. *Physical Review Letters* **125**, 263602 (2020).
- [205] C. J. Xin, J. Mishra, C. Chen, et al. *Spectrally separable photon-pair generation in dispersion engineered thin-film lithium niobate*. 2022.